Cosserat Rod Modeling of Continuum Robots : Application to Concentric Agonist-Antagonist Robots

Matthias Tummers

THESIS

For the degree of

DOCTOR OF PHILOSOPHY OF UNIVERSITÉ GRENOBLE ALPES

Doctoral school: ISCE - Ingénierie pour la Santé la Cognition et l'Environnement
Specialization: CIA - Ingénierie de la Cognition, de l'interaction, de l'Apprentissage et de la création
Research unit: Translational Innovation in Medicine and Complexity

Cosserat Rod Modeling of Continuum Robots: Application to Concentric Agonist-Antagonist Robots

Modélisation de Robots Continus par la Théorie de Cosserat : Application aux Robots Concentriques Agonistes-Antagonistes

Dissertation presented by

Matthias TUMMERS

Thesis supervision

Jocelyne TROCCAZ Directrice de Recherche, CNRS, TIMC	Thesis director
M. Taha CHIKHAOUI Chargé de Recherche, CNRS, TIMC	Thesis co-supervisor
Benoît ROSA Chargé de Recherche, CNRS, ICube	Thesis co-supervisor

Reviewers

Christian DURIEZ
Directeur de Recherche, INRIA, CRIStAL
Jérôme SZEWCZYK
Professeur des Universités, Sorbonne Université, ISIR

Thesis defended in public on the **26th of April 2023**, before the examining committee

Jocelyne TROCCAZ Directrice de Recherche, CNRS, TIMC	Thesis director
Christian DURIEZ Directeur de Recherche, INRIA, CRIStAL	Reviewer
Jérôme SZEWCZYK Professeur des Universités, Sorbonne Université, ISIR	Reviewer
Jessica BURGNER-KAHRS Associate Professor, University of Toronto, Canada	Examiner
Grégory CHAGNON Professeur des Universités, Université Grenoble Alpes, TIMC	Examiner
Christine CHEVALLEREAU Directrice de Recherche, CNRS, LS2N	President
M. Taha CHIKHAOUI Chargé de Recherche, CNRS, TIMC	Invited
Benoît ROSA Chargé de Recherche, CNRS, ICube	Invited

THÈSE

Pour obtenir le grade de

DOCTEUR DE L'UNIVERSITÉ GRENOBLE ALPES

École doctorale : ISCE - Ingénierie pour la Santé la Cognition et l'Environnement
Spécialité : CIA - Ingénierie de la Cognition, de l'interaction, de l'Apprentissage et de la création
Unité de recherche : Translational Innovation in Medicine and Complexity

Modélisation de Robots Continus par la Théorie de Cosserat : Application aux Robots Concentriques Agonistes-Antagonistes

Cosserat Rod Modeling of Continuum Robots: Application to Concentric Agonist-Antagonist Robots

Présentée par :

Matthias TUMMERS

Direction de thèse :

Jocelyne TROCCAZ Directeur de recherche, CNRS Délégation Alpes	Directrice de thèse
M. Taha CHIKHAOUI Chargé de Recherche, CNRS	Co-encadrant de thèse
Benoît ROSA CNRS	Co-encadrant de thèse

Rapporteurs :

CHRISTIAN DURIEZ
Directeur de recherche, INRIA CENTRE DE LILLE-NORD EUROPE
JERÔME SZEWCZYK
Professeur des Universités, SORBONNE UNIVERSITE

Thèse soutenue publiquement le **26 avril 2023**, devant le jury composé de :

JOCELYNE TROCCAZ Directeur de recherche, CNRS DELEGATION ALPES	Directrice de thèse
CHRISTIAN DURIEZ Directeur de recherche, INRIA CENTRE DE LILLE-NORD EUROPE	Rapporteur
JERÔME SZEWCZYK Professeur des Universités, SORBONNE UNIVERSITE	Rapporteur
GREGORY CHAGNON Professeur des Universités, UNIVERSITE GRENOBLE ALPES	Examinateur
CHRISTINE CHEVALLEREAU Directeur de recherche, CNRS BRETAGNE ET PAYS DE LA LOIRE	Présidente
JESSICA BURGNER-KAHRS Professeur associé, University of Toronto	Examinatrice

Invités :

MOHAMED TAHA CHIKHAOUI
Chargé de Recherche, CNRS DELEGATION ALPES
BENOÎT ROSA
Chargé de Recherche, CNRS DELEGATION ALSACE

To my first research partners Benoît and Xavier
for taking me under their wings
and having given a home to
my lust for learning.

Contents

Aknowledgements

I would like to commence by expressing my heartfelt gratitude to my esteemed supervisors, Taha, Joce, and Benoît. The wealth of knowledge and guidance you have imparted upon me during our time together has been invaluable. Through your vast experience and unwavering commitment to rigor, you have consistently pushed the boundaries of my intellectual capabilities, propelling my growth in all facets of the scientific method. For these aspects, I could not have been more fortunate than to have three passionate researchers from the National Center for Scientific Research (CNRS) guiding me along this academic journey. Moreover, I am deeply appreciative of your inclination to involve me in projects and subjects that, while sometimes tangential to my thesis, broadened my horizons. I am appreciative that you consistently included me in captivating scientific events, demonstrating your thoughtfulness and consideration.

This endeavor has not only been intellectually stimulating but also a profound human experience. For those observing from afar, it is imperative to note that our thesis meetings were a collective effort, involving the four of us. The out-and-out availability you exhibited throughout my thesis was awe-inspiring, especially evident during the intense and very short period when I was writing my manuscript. Your prompt and rapid feedback during that period was nothing short of astonishing. I still can't believe it.

Furthermore, throughout the entirety of my thesis, you consistently managed to motivate me, even during the year-long period of stumbling and wrestling with the Cosserat rod modeling of CAARs using the Newtonian approach, where results seemed elusive. In summary, I could not have envisioned a more ideal support.

Additionally, I would be remiss not to acknowledge the indispensable collaboration I have enjoyed with my special and familiar colleagues at LS2N in Nantes, Frédéric Boyer and Vincent Lebastard. Countless meetings and various informal yet equally enjoyable moments shared together have played a pivotal role in shaping the work I present in this document. To both of you, I extend my deepest gratitude.

Furthermore, I must express my sincere appreciation to my two esteemed rapporteurs, Christian Duriez and Jérôme Szewczyk, for their invaluable contributions. Your vast expertise and experience have provided me with a comprehensive vision of my work, enabling me to perceive its significance in a more profound manner. Your meticulous reading, paying meticulous attention to even the minutest details, has been instrumental in refining the quality of my research.

The efforts of the remaining members of the jury, Christine Chevallereau, Jessica Burgnerkahrs, and Grégory Chagnon, are also deserving of profound gratitude. I extend my heartfelt thanks for your keen interest and unwavering commitment to thoroughly examining my work. It is a matter of immense pride for me to have individuals of your competence serving on my thesis jury.

Besides, I would like to seize this opportunity to emphasize that Jérôme Szewczyk has been an integral part of my thesis committee throughout my research journey, alongside Yohan Payan. Their attentive guidance and invaluable advice have also significantly contributed to the body of work presented in this manuscript.

In addition to the assessment and continuous support provided towards the advancement of my research, I would like to extend my heartfelt appreciation to the entire GMCAO team for their warm reception and inclusive environment. Beyond your remarkable scientific aptitude, which continually fueled my curiosity across a broad spectrum of subjects, you transformed my thesis journey into an unforgettable human adventure.

Furthermore, I would like to include and acknowledge the wider community at TIMC. Despite being a laboratory comprising over 400 individuals, the sense of conviviality and genuine connection between teams is palpable.

While it would be impossible to individually mention everyone, I must make a special exception for Pablo, Baptiste, and Quentin, with whom I shared not only an office but also the daily rigors of research. Working alongside all of you was an absolute pleasure. I am deeply grateful for the assistance rendered, moments of shared laughter, and the occasional challenge of solving chess problems during our day-to-day activities.

I would also like to extend special recognition to two dedicated colleagues, Emmanuel Promayon and Guillaume Thomann, who played pivotal roles as my mentors in the courses I taught throughout my thesis. With Guillaume, I invested considerable time and effort in crafting the course structure and determining the pertinent topics to be covered. Our collaborative efforts resulted in a comprehensive and engaging learning experience for our students. Emmanuel, on the other hand, demonstrated exceptional flexibility by willingly adjusting his lecture plan to allow me to conduct my own experimental teaching interventions with his students. This remarkable display of support further reinforces the notion that I have been surrounded by exceptional individuals throughout these past three years.

To my dear friends who warmly welcomed me to Grenoble, I must express my profound gratitude. While it is impossible to mention everyone individually, my thoughts are particularly with my roommates from my initial two years in Grenoble, namely Nana, Kéké, Laulau, and Simon. You have become akin to a second family to me. It is largely due to our bond that we all succeeded on our diverse personal itineraries. I emphasize this aspect because, in addition to a conducive professional environment, I firmly believe that being surrounded by a supportive network is of utmost importance to the successful completion of a doctoral thesis.

In addition to the presence and support of my adoptive host family in Grenoble, I was fortunate enough to embark upon the journey of starting my own family during the course of my thesis. Many inquire as to how I managed to navigate both realms simultaneously. In truth, the process of building a family, although certainly not without its challenges, pales in comparison to the arduous task of completing a thesis. But I guess I am very fortunate, it is thanks to them that the integration of these two facets of my life has felt like a natural progression. Éléonore, your exceptionally easy-going nature and ever-present enthusiasm and cheerfulness have made you an extraordinary presence in my life. It comes as no surprise that our daughter, Zélie, reflects the same remarkable qualities. To both of you, I extend my deepest gratitude for the boundless reservoir of energy you embody, which has proven indispensable on this journey. Moreover, I am profoundly grateful for the permanent support you provided during the intense month of manuscript writing, a period that demanded dedication and focus.

The culmination of a thesis necessitates a copious amount of character and perseverance. These qualities are not acquired overnight but are instilled within an individual over time, often under the nurturing guidance of their parents. I am immensely grateful to my parents for imparting upon me these invaluable attributes, which have propelled me forward on this arduous academic journey. Moreover, I am compelled to thank you for your support during my studies at the École Polytechnique de Louvain. The academic grounding I received from this institution served as solid foundation upon which I have constructed the complex framework of this thesis.

To conclude this note, I wish to convey my profound gratitude, tempered with a sense of humility, towards my first research partners, Benoît Herman and Xavier Bollen, for graciously guiding me and providing a nurturing environment for my eagerness to learn. It is with deep appreciation and reverence that I dedicate this manuscript to them.

Notations

		Dim	Units
l	Length of the rod/robot	$\mathbb{R}$	m
$X \in [0,\, l]$	Reference length parameter	$\mathbb{R}$	m
$r(X)$	Position	$\mathbb{R}^3$	m
$R(X)$	Orientation	$\mathbb{R}^{3\times3}$	
$g(X) = (R, r)(X)$	Cross-sectional frame homogeneous transform.	$\mathbb{R}^{4\times4}$	
$\mathcal{F}(X) = (r, b_X, b_Y, b_Z)(X)$	Cross-sectional frame		
$\mathcal{F}_s = (O, e_x, e_y, e_z)$	Inertial frame		
(E_X, E_Y, E_Z)	Canonical (numerical) base of $\mathbb{R}^3$ $E_X = (1,0,0)^T$ $E_Y = (0,1,0)^T$ $E_Z = (0,0,1)^T$		
$\bullet^0$	Initial value or prior to deformation		
$\bullet', \bullet''$	First and second derivative wrt. X		
$\Gamma(X)$	Linear rate of change (shear & extension)	$\mathbb{R}^3$	
$K(X)$	Angular rate of change (bending & torsion)	$\mathbb{R}^3$	m^{-1}
$\xi = (K^T, \Gamma^T)^T$	Space-rate twist	$\mathbb{R}^6$	$(\mathrm{m}^{-1}, -)$
$\epsilon = \xi - \xi^0$	Strain	$\mathbb{R}^6$	$(\mathrm{m}^{-1}, -)$
$c(X),\ C(X)$	Stress (bending & torsion)	$\mathbb{R}^3$	Nm
$n(X),\ N(X)$	Stress (shear & extension)	$\mathbb{R}^3$	N
$\Lambda(X) = \left(C(X)^T, N(X)^T\right)^T$	Stress (wrench)	$\mathbb{R}^6$	(Nm, N)
$\bar{c}(X),\ \bar{C}(X)$	Total external distributed couples	$\mathbb{R}^3$	Nm/m
$\bar{n}(X),\ \bar{N}(X)$	Total external distributed forces	$\mathbb{R}^3$	N/m
$\bar{F}(X) = \left(\bar{C}(X)^T, \bar{N}(X)^T\right)^T$	Total external distributed wrench	$\mathbb{R}^6$	(Nm/m, N/m)
$c_+,\ C_+$	External tip couples	$\mathbb{R}^3$	Nm
$n_+,\ N_+$	External tip forces	$\mathbb{R}^3$	N
$F_+ = \left(C_+^T, N_+^T\right)^T$	External tip wrench	$\mathbb{R}^6$	(Nm, N)
$\mathcal{H}_{ang}(X), \mathcal{H}_{lin}(X)$	Angular and linear stiffness matrices	$\mathbb{R}^{3\times3}$	N, Nm^2
$\mathcal{H}(X)$	Hookean stiffness matrix	$\mathbb{R}^{6\times6}$	(N, Nm^2)
$\mathcal{K}_{\epsilon\epsilon}$	Generalized stiffness	$\mathbb{R}^{k\times k}$	$*$

* The units of these quantities depend on the choice of the shape functions.

			Dim	Units
$\mathcal{E}$		Young's modulus	$\mathbb{R}$	Pa
$\mathcal{G}$		Shear modulus	$\mathbb{R}$	Pa
ν		Poisson's ratio	$\mathbb{R}$	
a_g		Gravitational acceleration field	$\mathbb{R}^3$	N/kg
μ		Equivalent density	$\mathbb{R}$	kg/m^3
$\mathcal{A}$		Cross-sectional area	$\mathbb{R}$	m^2
$\mathcal{I}$		Cross-sectional inertia moment	$\mathbb{R}$	m^4
$\bullet_a$		active components, allowed by the model		
$\bullet_c$		constrained components, restricted by the model		
n_a		number of active components	$\mathbb{R}$	
B		selection matrix for active components	$\mathbb{R}^{n_a \times 6}$	
$\bar{B}$		selection matrix for active components	$\mathbb{R}^{(6-n_a)\times 6}$	
m		Number of tendons	$\mathbb{R}$	
$\bullet_i$		Related to the i^{th} element (tube, tendon, rod)		
	Chap.3:	Related to the i^{th} tendon ($i = 1 \,..\, m$)		
	Chap.4:	Related to the i^{th} tube/neutral line ($i = 1 \,..\, 2$)		
l_i		Length of the i^{th} element (tube, tendon, rod)	$\mathbb{R}$	m
	Chap.3:	Length of the i^{th} tendon	$\mathbb{R}$	m
	Chap.4:	Length of the i^{th} neutral line	$\mathbb{R}$	m
$D_i(X)$	Chap.3:	Cross-sectional frame position of the i^{th} tendon	$\mathbb{R}^3$	m
	Chap.4:	Offset of the i^{th} neutral line	$\mathbb{R}^+$	m
$D(X)$		Distance between neutral lines	$\mathbb{R}^+$	m
$r_i(X) = r + RD_i$		Inertial frame tendon position	$\mathbb{R}^3$	m
$t_i = r_i'/\|r_i'\|$		Tangent to the path of the i^{th} tendon	$\mathbb{R}$	
$[\![t_i]\!]_j$		Tendon slope discontinuity step	$\mathbb{R}$	
τ_i		Tension in the i^{th} tendon	$\mathbb{R}$	N
$\tau = (\tau_1 \,..\, \tau_m)^T$		Vector of tensions	$\mathbb{R}^m$	N
T_+		Push/pull force applied at the inner tube base	$\mathbb{R}$	N
a		Translation of the inner tube at the baseplate	$\mathbb{R}$	m
θ		Rotation of the inner tube at the baseplate	$\mathbb{R}$	m
L		Matrix of actuation	$\mathbb{R}^{k\times m}$	*

* The units of these quantities depend on the choice of the shape functions.

		Dim	Units
R_t	Tendon offset	$\mathbb{R}$	m
R_b	Backbone radius	$\mathbb{R}$	m
$\underline{\rho}_i$	Inner radius of the i^{th} tube	$\mathbb{R}$	m
$\overline{\rho}_i$	Outer radius of the i^{th} tube	$\mathbb{R}$	m
$d = 2\overline{\rho}_1$	Robot outer diameter	$\mathbb{R}$	m
$\gamma_i = \alpha_i - \overline{\rho}_i$	Notch depth of the i^{th} tube	$\mathbb{R}$	m
h_i	Notch height of the i^{th} tube	$\mathbb{R}$	m
c_i	Inter-notch height of the i^{th} tube	$\mathbb{R}$	m
$\mathcal{B}_i$	Body of the i^{th} tube	$\mathbb{R}$	m
$\mathcal{M}$	Centerline of the robot and tubes	$\mathbb{R}$	m
$\mathcal{N}_i$	Neutral line of the i^{th} tube	$\mathbb{R}$	m
$\beta_i = \frac{dD_i}{dX_i}$	Tilt of the neutral line of the i^{th} tube	$\mathbb{R}$	m
$\widetilde{\bullet}$	Face-to-face operator/pull-back function	$\mathbb{R}$	m
$h = d\widetilde{X}_2/dX_1$	Tangent pull-back function	$\mathbb{R}$	m
$\bullet_{ext}$	Relative to external loads (not tendons)		
$\bar{n}_{ext}(X)$	External distributed forces (not tendons)	$\mathbb{R}^3$	N/m
$\bar{c}_{ext}(X)$	External distributed couples (not tendons)	$\mathbb{R}^3$	Nm/m
$\bullet_{rod}$	Relative to rod elastics		
$\bullet_{act}$	Relative to actuation by the tendons		
$\bar{n}_{act}(X)$	Distributed forces applied by the tendons	$\mathbb{R}^3$	N/m
$\bar{c}_{act}(X)$	Distributed couples applied by the tendons	$\mathbb{R}^3$	Nm/m
$\bar{n}_i(X)$	Distributed forces applied to the i^{th} tendon	$\mathbb{R}^3$	N/m
$\Lambda_{act}(X)$	Stress of actuation	$\mathbb{R}^6$	(Nm, N)
k	Number of shape functions	$\mathbb{R}$	
$\Phi(X) = (\Phi_1 \,..\, \Phi_k)^T$	Shape functions	$\mathbb{R}^{6\times k}$	$*$
$q = (q_1 \,..\, q_k)^T$	Generalized strain coordinates	$\mathbb{R}^k$	$*$
δW	Virtual work	$\mathbb{R}$	J
$\delta\zeta$	Absolute variation of the configuration	$\mathbb{R}^6$	$(\mathrm{m}^{-1}, -)$
$\delta\xi = \delta\epsilon$	Relative variation or strain variation	$\mathbb{R}^6$	$(\mathrm{m}^{-1}, -)$
δq	Variation of the generalized strain coordinates	$\mathbb{R}^k$	$*$
δl_i	Variation of the length of the i^{th} tendon	$\mathbb{R}$	m
Q_{ext}	Generalized external forces	$\mathbb{R}^k$	$*$
Q_{rod}	Generalized restoring forces	$\mathbb{R}^k$	$*$
Q_{act}	Generalized forces of actuation	$\mathbb{R}^k$	$*$

$*$ The units of these quantities depend on the choice of the shape functions.

		Dim	Units
$\bullet^\star$	Guessed value for an unknown BC		
$\mathfrak{Res}$	Residual vector		
$J(q) = \partial\mathfrak{Res}/\partial q$	Jacobian matrix of the residual	$\mathbb{R}^{k\times k}$	$*$
$\bullet_j$	Related to the j^{th} segment		
χ	Number of segments	$\mathbb{R}$	
l_j	Length of the j^{th} segment	$\mathbb{R}$	m

* The units of these quantities depend on the choice of the shape functions.

List of Abbreviations

BC	Boundary Condition
BVP	Boundary Value Problem
CAAR	Concentric Agonist-Antagonist Robot
CAMI	Computer Aided Medical Interventions
CE	Conformité Européenne (French for "European conformity")
CTCR	Concentric Tube Continuum Robot
DoF	Degree of Freedom
FDA	Food And Drug Administration
FDM	Fused Deposition Modeling
FEM	Finite Element Method
GIC	General Intermediate Constraint
MBCR	Multi-Backbone Continuum Robots
NTCR	Notched Tube Continuum Robot
ODE	Ordinary Differential Equation
PCR	Parallel Continuum Robot
PDE	Partial Differential Equation
PLA	Polylactic Acid
TACR	Tendon Actuated Continuum Robot
TBVP	Tangent Boundary Value Problem

Introduction

Robots for improving clinical outcomes

Medical robotics is, since roughly 40 years, a continuously flourishing field that combines the advances in robotics and healthcare to provide improved patient outcomes and enhance the delivery of medical services. The integration of robotics into healthcare has led to significant advances in surgical procedures, enabling minimally invasive procedures with enhanced navigation, dexterity, sensing, and safety. Surgical robots have gained widespread acceptance, with an estimated 4000 robots being employed daily in worldwide medical procedures [Fiorini et al. 2022]. Research teams are studying the clinical benefit with an expanding literature. Since 1998, over 29 000 peer-reviewed studies have been published on *da Vinci* surgery alone [Haidegger et al. 2022]. Regardless, many challenges remain and there is still work to be done to further improve quality of care.

Today, most robots used in clinic are rigid-link robots, characterized with mechanical rigidity and limited degrees-of-freedom. For certain applications, there might be a mismatch between the robots and the soft human tissues. Hence, in recent years, there has been a growing trend towards the development of robots that are designed to interact with the human body in a more compliant manner and offer increased dexterity to the clinicians. Moreover, to further reduce surgical invasiveness, a search has started for ways to access the body through natural orifices (see Figure I.1). This has led to the advent of continuum robots in the medical robotics field.

Figure I.1: Example of an endoluminal surgical procedure, here in bariatric surgery with access through the throat. Image adapted from: https://consultqd.clevelandclinic.org

Continuum robots and new challenges

Continuum robots are composed of elastic materials such that their body bends continuously when actuated, providing infinite degrees of freedom. Such degrees of freedom give continuum robots the ability to conform to the shape of lumens of the human anatomy and access regions that are difficult to reach with traditional robots. In many cases, continuum robots can be scaled down to very small sizes, yet further opening the range of possible applications. Additionally, the compliance of continuum robots make them especially suited for safe interactions in medical applications.

While continuum robots commit to be an answer to the shortcomings of rigid-link robots, this emerging type of robots present a series of new challenges to the community. First, structurally, due to their flexible nature and depending on their architecture, continuum robots can be subject to a number of physical phenomenons that limit their performances (elastic instabilities, insufficient payload, backlash etc.). Second, in order to deploy continuum robots, precise models that link actuation variables to the full robot shape are required. In this second challenge, the modeling of continuum robots is drastically different from the modeling of rigid-link robots by the fact that no discrete joints can be identified. The elasticity of the constituting materials must be taken into account, along with interaction forces from the environment.

To answer these challenges, the continuum robotics community is continuously developing *novel robot structures* and hence *new models*. The multidisciplinary nature of continuum robots favors new and unconventional scientific approaches. A prime illustration is the symbiosis that arose between continuum mechanics and robotics in the quest for capturing their unique behavior.

In particular, the over 100 years old Cosserat rod theory has found a leading application with the geometrically exact modeling of long, slender continuum robots. Since their first occurrence in the continuum robotics community in the late 2000s, Cosserat rod models have imposed themselves as the gold standard in the field. Such models were initially derived through a Newtonian approach, by isolating the robot constituents and considering their interactions (Newton's Laws of motion). Despite its success, the Newtonian approach may be arriving at its limits and face difficulties to fully capture the behavior of newborn continuum robot structures that are increasingly complex. On that account, another approach for deriving Cosserat rod models, based on a Lagrangian viewpoint, has recently gained interest from the community. This alternative approach considers the system as a whole and derives the robot models through a canonical application of the principle of virtual work. By considering the system in its entirety, this approach promises to provide a more comprehensive understanding of the behavior of continuum robots, and may open the door to the development of even more advanced and capable robots in the future.

In a more general way, models of continuum robots are the first building block of many aspects of their implementation and use. Models are evidently used for control but also for design optimization, path planning, feedback, and the analysis of their stability, compliance, manipulability etc. The more precise and capable continuum robot models are, the more advantageously they can be exploited for these various tasks.

Objectives of this thesis

The main objective of this thesis is to contribute to the development of innovative continuum robots to answer the current challenges (improved payload, enhanced downscalability, elastic instabilities, backlash). As stated above, these emerging continuum robot structures require new model considerations and developments to further promote their technological transfer to medical applications.

Scientific contributions and structure of the document

Driven by the desire to contribute to medical care, this dissertation addresses the above detailed objectives as follows:

- In **chapter 1**, continuum robots are re-contextualized and the structure of some prevalent types is analyzed, leading to the identification of a promising emerging type of continuum robots, namely concentric agonist-antagonist robots (CAARs). These robots, at the intersection between three standard continuum robot types, are put forward for their assets. The potential added value of CAARs in medical applications is highlighted. Currently, the available models for CAARs are geometry based models that are not capable of modeling the interactions of the robot with its environment. The following chapters will contribute to the development of a mechanical model that meets this requirement.

- To this end, in **chapter 2**, the Cosserat rod theory with its complex network of interrelated elements is rederived in a unique mathematical framework. All the ingredients for modeling continuum robots through either the Newtonian or Lagrangian approach are laid out in a single structured picture as a strong basis for modeling various types of continuum robots.

- To gain further insight as to the similarities and differences between the Newtonian and Lagrangian modeling approaches, **chapter 3** presents the case study of the modeling of tendon actuated continuum robots (TACRs). The two approaches are derived side-by-side, which allows an in-depth and objective analysis of both.

- It is this in-depth comprehension that enabled the development of a new planar model for CAARs, which is presented in **chapter 4**. This geometrically exact model is derived through a canonical application of the Lagrangian approach by considering the unique mechanics of CAARs.

- The derived model is subsequently validated in **chapter 5** through an extensive set of experiments and corresponding simulations involving versatile CAAR designs and external loading. Additionally, **chapter 5** details the design of 3D CAAR designs and experimentally assesses their capabilities.

- The manuscript ends with a terse summary of the developments and an in depth discussion of perspectives for future work. Perspectives include considerations for upgrading the maturity of the developed prototypes and numerous model extensions that will enable to further transfer CAARs to clinical applications.

This document is the result of the research projects funded by grants ANR-11-LABX-0004-01 (CAMI Labex) and ANR-19-P3IA-0003 (3IA MIAI@Grenoble Alpes) within the context of a collaboration between the TIMC Laboratory in Grenoble, France, and the ICube Laboratory in Strasbourg, France, both part of the computer aided medical interventions (CAMI) Laboratory of Excellence (LABEX) network. Another, unforeseen, collaboration with Frédéric Boyer and Vincent Lebastard from the LS2N Laboratory in Nantes, France, within the ANR COSSEROOTS project, emerged during the second half of this thesis. The contributions of the external collaborators will be detailed at the end of the corresponding chapters.

1

Continuum Robots

1.1 Foreword

The purpose of this chapter is to explain in more details what continuum robots are. To define continuum robots, their history is presented briefly, starting over from pioneer industrial robots. It will cover different types of existing continuum robots and position concentric agonist-antagonist robots (CAARs) with respect to other types of continuum robots. The exposed perspectives will provide the rationale behind the choice for studying CAARs. The chapter also provides a literature review of research related to CAARs over recent years. Finally, the medical applications in which continuum robots are investigated are discussed and the potential of CAARs in these applications is analyzed.

1.2 Definition and Origin

Today, the presence of robots in our society is ubiquitous. They can be found in many fields like industry, healthcare, and agriculture just to name a few. The vast majority of these robots are rigid-link robots (see Figure 1.1a). They are the first and best known type of robots. Rigid-link robots consist of a finite number of joints with rigid links in between. As such, their main characteristics are that they are rigid and can be very precise.

When the number of joints of traditional rigid-link robots increases, they fall under the category of hyper-redundant robots (see Figure 1.1b) [Hong et al. 2020, Feng et al. 2021, Sartoretti et al. 2021]. Hyper-redundant robots have many more degrees of freedom than their task space and thus allow to control the shape of the robot in addition to the position of its end effector. When hyper-redundant robots feature a great number of links, it is possible to approach curvilinear paths. The tensor arm displayed in Figure 1.2 is considered as one of the ancestors of continuum robots [Anderson 1967].

Going one step further in this direction, as the number of joints approaches infinity or, said differently, when no more distinct joints can be observed, a new category of robots is found: continuum robots (see Figure 1.1c). A continuum robot is an elastic structure that bends continuously when actuated.

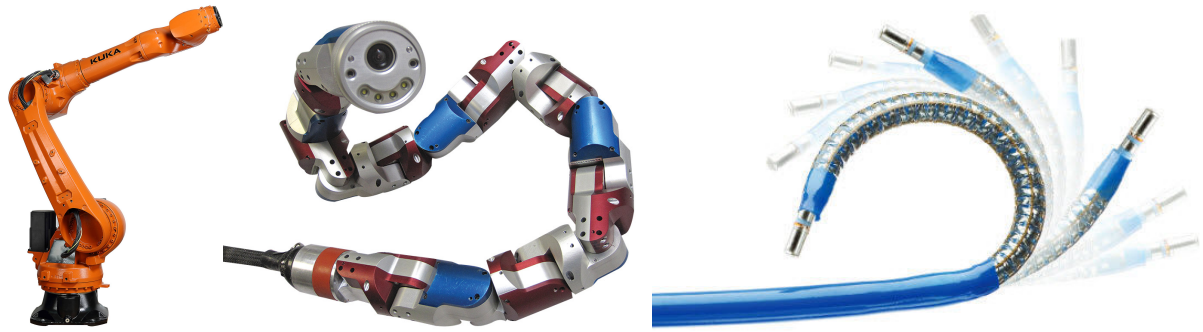

(a) (b) (c)

Figure 1.1: Examples from three categories of robots (inspired by [Burgner-Kahrs et al. 2015]). (a) A rigid-link robot: an industrial robot from Kuka Robotics Corp. (b) A hyper-redundant robot: a modular snake-robot from the Biorobotics Lab of Carnegie Mellon University. (c) A continuum robot: a steerable catheter developed by Hansen Medical [Camarillo et al. 2008].

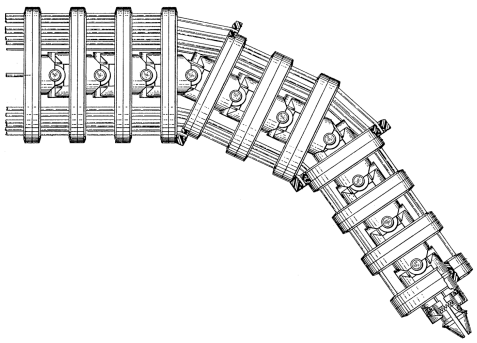

Figure 1.2: The Tensor Arm presented in [Anderson 1967]. Featuring many joints, this hyper-redundant robot can approach continuously curving shapes.

Table 1.1: Advantages and environment characteristics of continuum robots

Advantages of continuum robots		Environment constraints
• structural compliance	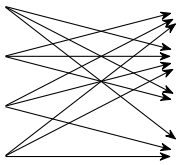	• confined spaces
• ease of miniaturization		• obstacle avoidance
• enhanced dexterity		• safe and soft interaction
• curvilinear paths		• unstructured environments

Robotics research has greatly sought inspiration in nature [Rus and Tolley 2015]. This is why it is interesting to make an analogy between the above described robots and animal structures. In this analogy, rigid-link robots can be compared to skeletal structures where the rigid-links replace the bones between the joints. In the same way, hyper-redundant robots can be compared to snakes that have numerous vertebrae, enabling them to conform their body to curved shapes [Gautreau et al. 2022]. The first biologically inspired hyper-redundant robots were probably those investigated by Hirose et al. in the 1970s [Hirose 1987]. Finally, completely removing the vertebrae, continuum robots can be compared to elephant trunks [Yang et al. 2006], octopus arms [Renda et al. 2012], or squid tentacles [Kim et al. 2013].

From the definition above, it is clear that continuum robots are very different from rigid-link robots. They can conform to curvilinear paths and are inherently compliant. In addition, their designs often offer ease of miniaturization and enhanced dexterity. These advantages enable them to have potentially safe and soft interactions with unstructured environments [Graule et al. 2022] and to evolve in confined spaces or avoid obstacles [Torres et al. 2014, Torres et al. 2015]. The advantages of continuum robots over rigid-link robots and the characteristics of the environments they are suited for are summarized in Table 1.1. For each advantage in the left column, it is possible to connect some or all of the environment constraints in the right column and vice versa.

Rigid-link robots are known for their rigidity, precision, and suitability to highly structured environments. As continuum robots have new advantages, it is evident that the environments they are best suited for also differ. This opens possibilities for applications that have not previously been approachable with robots [Cieślak and Morecki 1999]. Such applications include undersea applications, nuclear decontamination, nuclear reactor repair, inspection of unstructured environments, and search and rescue [Wolf et al. 2003]. More recently, but today also most notably, continuum robots have found their way into many medical applications [Burgner-Kahrs et al. 2015, Dupont et al. 2022]. Indeed, looking at the right column of Table 1.1, the environments of medical application are characterized by all four constraints: (i) minimally invasive surgery and endoluminal procedures require evolving in confined spaces; (ii) during these procedures, it is often crucial to avoid bones, organs, or sensitive structures; (iii) the surrounding and operated tissue and structures are soft and fragile; and finally (iv) it is clear that the human body is a highly unstructured environment from a robotics point of view.

The next section dives into more details about various continuum robots, providing some examples, to help position CAARs among these different types. Section 1.4 gives a more formal definition of the CAAR concept and provides a brief literature review on the topic. Further, section 1.5 will present some recent medical applications in continuum robotics and the potential of CAARs in these applications will be highlighted.

1.3 Different Types of Continuum Robots

Many types of continuum robots exist. The first major distinction that can be made between these numerous types regards the actuation of the robots. Some robots have their actuators distributed within their active part. This type of actuation is called intrinsic actuation. Other robots rely on actuators located at the proximal end of the robots, conveying movement through a mechanical transmission. This second type of robots fall under the extrinsic actuation category.

1.3.1 Intrinsically Actuated Continuum Robots

Intrinsic actuation in continuum robots can be achieved by embedding active materials as shape-memory alloys [Szewczyk et al. 2001, Szewczyk et al. 2011, Shao et al. 2020], shape-memory polymers [Mattmann et al. 2022], or electroactive polymers [Chikhaoui et al. 2016a, Chikhaoui et al. 2016b, Bartkowski et al. 2022]. Such embedded actuators enable to construct very small manipulators without the need for bulky actuation units.

Another possibility is to use fluidic actuation systems. This type of robots feature one or several chambers distributed radially and along the length of the robots. The chambers extend when actuated, defining the curvature of the robot. Fluidic actuated continuum robots can further be categorized in hydraulic actuated robots [Ikuta et al. 2006, Nguyen et al. 2022a] and pneumatic actuated robots [Falco et al. 2017, Zhang et al. 2021a, Eugster et al. 2022, Fang et al. 2022, Hu et al. 2022, Treratanakulchai et al. 2022]. Generally, pneumatic actuated continuum robots are softer than their hydraulic counterpart.

Instead of making use of distinct bellows, some fluidic robots are composed of one single pouch that prolapses when it is pressurized [Hawkes et al. 2017, Abrar et al. 2021, Exarchos et al. 2022]. Some such eversion robots are capable of sensing [Bryant et al. 2022] or mapping their position while navigating [Watson and Morimoto 2020]. A last actuation possibility that falls under the fluidic systems is the use of a water jet at the tip of the robots. The tip is subject to a point force and couple, deforming the whole shape of the robot [Campisano et al. 2020, Campisano et al. 2021].

A completely different strategy is to include permanent magnets [Lin et al. 2021] or ferromagnetic materials [Gan et al. 2020] into manipulators to enable controlling them with an external electromagnetic field [Nelson et al. 2022]. While the electromagnetic field is external to the robots, they are here categorized as intrinsically actuated robots because, according to the definition in [Burgner-Kahrs et al. 2015], the final conversion of power to the mechanical energy domain occurs in the active part. Often, it is convenient to manufacture the core or backbone of electromagnetically actuated continuum robots with elastomeric polymers which are electromagnetically transparent. Applying selective magnetization profiles allows actuating the robot according to a desired target shape [Lloyd et al. 2022].

Three more notable intrinsic actuation systems are the use of McKibben muscles [McMahan et al. 2006, Maloisel et al. 2021] or super-coiled polymers [Tsabedze et al. 2020, Yang et al. 2020, Sun and Zhao 2022] and the use of embedded micro-motors [Noonan et al. 2011].

Overall, the common benefits of intrinsically actuated continuum robots are a reduced footprint and the fact that they address problems like friction, hysteresis, and elastic instabilities sometimes encountered in the extrinsically actuated types. On the downside, their fabrication can be more complex, and it is difficult to construct smaller diameter robots that exhibit a high output force range.

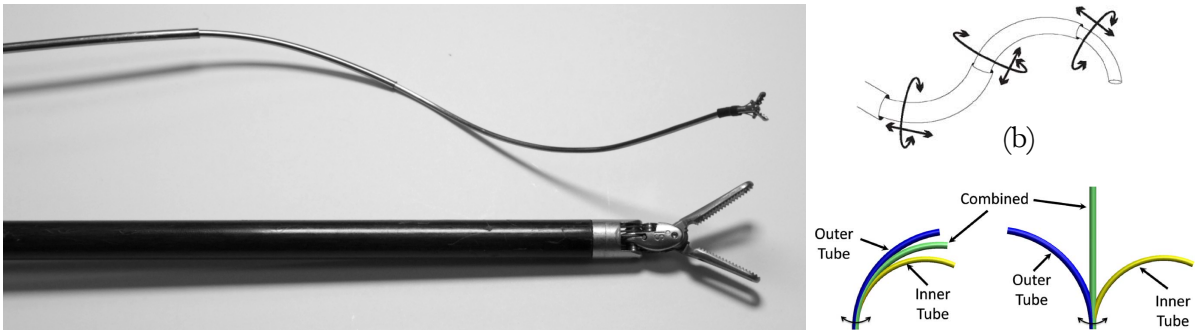

Figure 1.3: Concentric tube continuum robots. (a) A concentric tube robot next to a *da Vinci Pro-Grasp*™ laparoscopic forceps (8 mm) from [Gilbert et al. 2016b]. (b) Actuator space input movement of the tubes of a CTCR. Adapted from [Webster et al. 2009a]. (c) Elastic interaction of precurved tubes in a CTCR. Each elastic tube has a different precurvature. When the tubes are assembled, the resultant shape (green) is somewhere in between the individual initial precurvatures. Adapted from [Dupont et al. 2010].

1.3.2 Extrisically Actuated Continuum Robots

Extrinsically actuated continuum robots often require a larger external footprint but can be an answer to the limitations encountered with intrinsic actuation. As this thesis primarily deals with extrinsically actuated continuum robots, the following sections will dive into some standard types of such robots with more details. Concentric tube continuum robots (CTCRs), tendon actuated continuum robots (TACRs), and multi-backbone continuum robots (MBCRs) are presented, including an analysis of their systems. Building upon these standard robots, the category of hybrid continuum robot designs is presented with some examples. All these perspectives will enable position CAARs with respect to their counterparts.

Concentric tube continuum robots

CTCRs are composed of multiple, precurved elastic tubes arranged concentrically, i.e. telescoping (see Figure 1.3a). The tubes can be rotated and translated with respect to one another (see Figure 1.3b) and the bending comes from the precurvature of the tubes. In a given configuration, the tubes interact elastically to determine the shape of the robot (see Figure 1.3c) [Sears and Dupont 2006]. CTCRs are a highly miniaturizable type of continuum robots thanks to the fact that they consist of a single backbone [Li et al. 2017]. Also, their most interesting advantage is that, compared to other continuum robots, they have the best lumen diameter over robot diameter ratio.

One of the major drawbacks of CTCRs is that they can be subject to undesirable elastic instabilities. Due to the torsional twisting associated with rotating curved tubes, elastic energy builds up in the system and can suddenly be released when, for a given actuation input, multiple minimal energy configurations exist. Several studies reported ways of model based predicting instabilities or providing design constraints for preventing such phenomenons [Peyron et al. 2019]. Another approach is to reduce the ratio of flexural rigidity to torsional rigidity of the tubes. Such tubes can be obtained through anisotropic patterning of the tubes [Kim et al. 2014a, Lee et al. 2015, Luo et al. 2018] or by using multi-layer helical tubes [Azimian et al. 2014]. Recently, transverse anisotropic patterning has also been investigated and likewise allowed stabilization of CTCRs while preserving overall robot stiffness [Rucker et al. 2022b]. Extensive reviews of CTCR can be found in [Gilbert et al. 2016b, Mahoney et al. 2018].

Figure 1.4: A tendon actuated continuum robot (the METABot (Magnetically Extensible TACR)) presented in [Amanov et al. 2021].

Tendon actuated continuum robots

TACRs consist of a central elastic backbone that is pulled upon by tendons (i.e. cables) attached at its end. The tendons are generally routed through holes in disks, distributed along the length of the backbone (see Figure 1.4). When a tendon is pulled, the backbone bends continuously. By attaching tendons at different angles around the backbone and combining their actuation, a 3D workspace can be reached. To obtain multiple segments with different bending, sets of tendons can be attached at intermediate lengths along the backbone [Pogue et al. 2022]. Converging tendon routing allows obtaining a variable curvature and reduce overall deflection when the robot is subject to tip loads [Wang et al. 2021, Xu et al. 2021, Yuan et al. 2021]. Tendons can also be routed helically around the backbone to obtain more complex shapes [Liu and Alambeigi 2022]. Compared to CTCRs, this type of continuum robots has the advantage to reach a larger range of curvatures. However, they often require tedious assembly and can experience backlash.

TACRs are definitively the most studied and widespread type of continuum robots. Many variations have been explored. In particular, several TACR designs that do not comprise a backbone have been explored. The backbone can be replaced with springs [Hu et al. 2019b, Zhang et al. 2021c], pneumatic chambers [Jones et al. 2004], rolling joints [Kim et al. 2014b], hinge joints [Kong et al. 2022], or notched tubes [Francis et al. 2018, Alambeigi et al. 2020, Zeng et al. 2021]. Regarding this last category, using a single tendon located opposite to the remaining backbone limits the bending to one side but enables scaling down the manipulators to less than 0.5 mm [Swaney et al. 2016, Jeong et al. 2020].

Multi-backbone continuum robots

MBCRs feature multiple backbones and can thus be regarded as parallel robots. The rods are attached at their distal end and are either routed through disks along a backbone or left free in space.

The first type, also called push-pull robots, very much resembles TACR but with the main differences that tendons can only be pulled whereas rods can also be pushed and that the rods will not form line segments between routing points but bend continuously (see Figure 1.5a) [Simaan et al. 2004, Zhang et al. 2019a]. Advantages include backlash elimination, enhanced down-scalability, and increased payload. In these robots, the central backbone carrying the disks can thus be distinguished from the secondary backbones that serve for actuation.

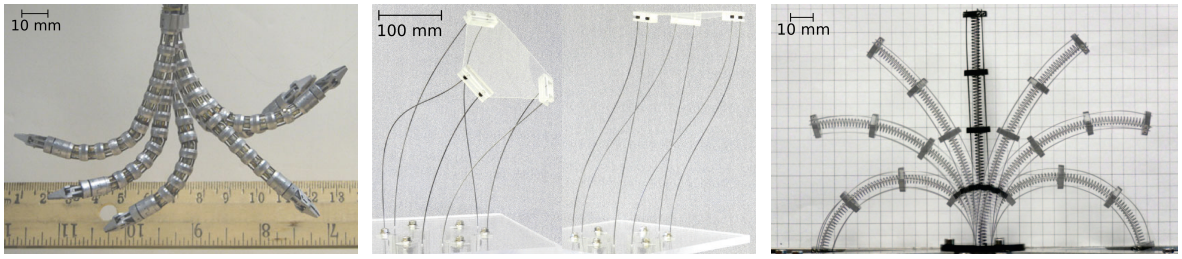

(a) (b) (c)

Figure 1.5: Multi-backbone continuum robots. (a) The push-pull actuator developed in [Simaan et al. 2009]. (b) The parallel continuum robot presented in [Bryson and Rucker 2014]. (c) The parallel continuum robot studied in [Orekhov et al. 2017].

The type where the rods are left in free-space between the base of the robot and its end are called parallel continuum robots (PCRs) (see Figure 1.5b) [Bryson and Rucker 2014, Black et al. 2018]. By attaching the rods in different configurations at the base and the end of the robot, interesting movements can be created. However, the robot diameter increases when it is actuated and the reachable workspace is limited by the fact that large deflections are transmitted to single rods instead of the whole system. To solve this issue, routing disks can be added to PCRs [Orekhov et al. 2017, Wang and Zhang 2021]. The difference with push-pull robots described above is that the rods do not necessarily run parallel and that individual rotation of the rods is used in addition to the push-pull motion (see Figure 1.5c).

Note that, for this dissertation, the concept of PCRs is limited to the multi-backbone case in the sense that the multiple parallel elements are supposed to be rods or tubes. Beyond the scope of this document, other research activities explore PCRs where each chain can be any type of continuum robot [Huang et al. 2022, Russo et al. 2022, Lilge and Burgner-Kahrs 2023].

Hybrid continuum robots

With the ambition to combine the advantages of the standard continuum robots described above, the community has seen the development of continuum robots with hybrid structures mixing two or three of the standard types. Figure 1.6 schematically summarizes how the strengths of each standard type plug into the various combinations. Examples include: the METABot [Nguyen and Burgner-Kahrs 2015, Amanov et al. 2021], a TACR but with extensible segments thanks to multiple concentrically arranged backbones that can move axially like CTCR and to loose magnetic disks (see Figure 1.6d); the manipulator developed by the authors of [Amanov et al. 2017] that concentrically arranges two tendon actuated segments, letting the distal segment slide on the proximal segment, enabling true follow-the-leader motion (see Figure 1.6a); the interlaced continuum robot developed in [Kang et al. 2016] that combines multi-backbone designs and concentrically arranged tubes (see Figure 1.6 (f)); a robot nesting a distal tendon actuated segment in a CTCR [Wu et al. 2017] (see Figure 1.6b); a TACR with segments that can extend thanks to additional cables and sliding backbone segments [Zhang et al. 2018] (see Figure 1.6c); a MBCR that utilizes a sliding concentric tube to modify its configuration and stiffness independently of the end effector pose [Zhao et al. 2020] (see Figure 1.6 (g)); the robot developed by the authors of [Gu et al. 2019] where a TACR is traversed by two MBCRs (see Figure 1.6 (h)); and the concentric agonist-antagonist robot [Oliver-Butler et al. 2017] (see Figure 1.7). Section 1.4 is devoted to the description of CAARs and an analysis of the literature covering the topic.

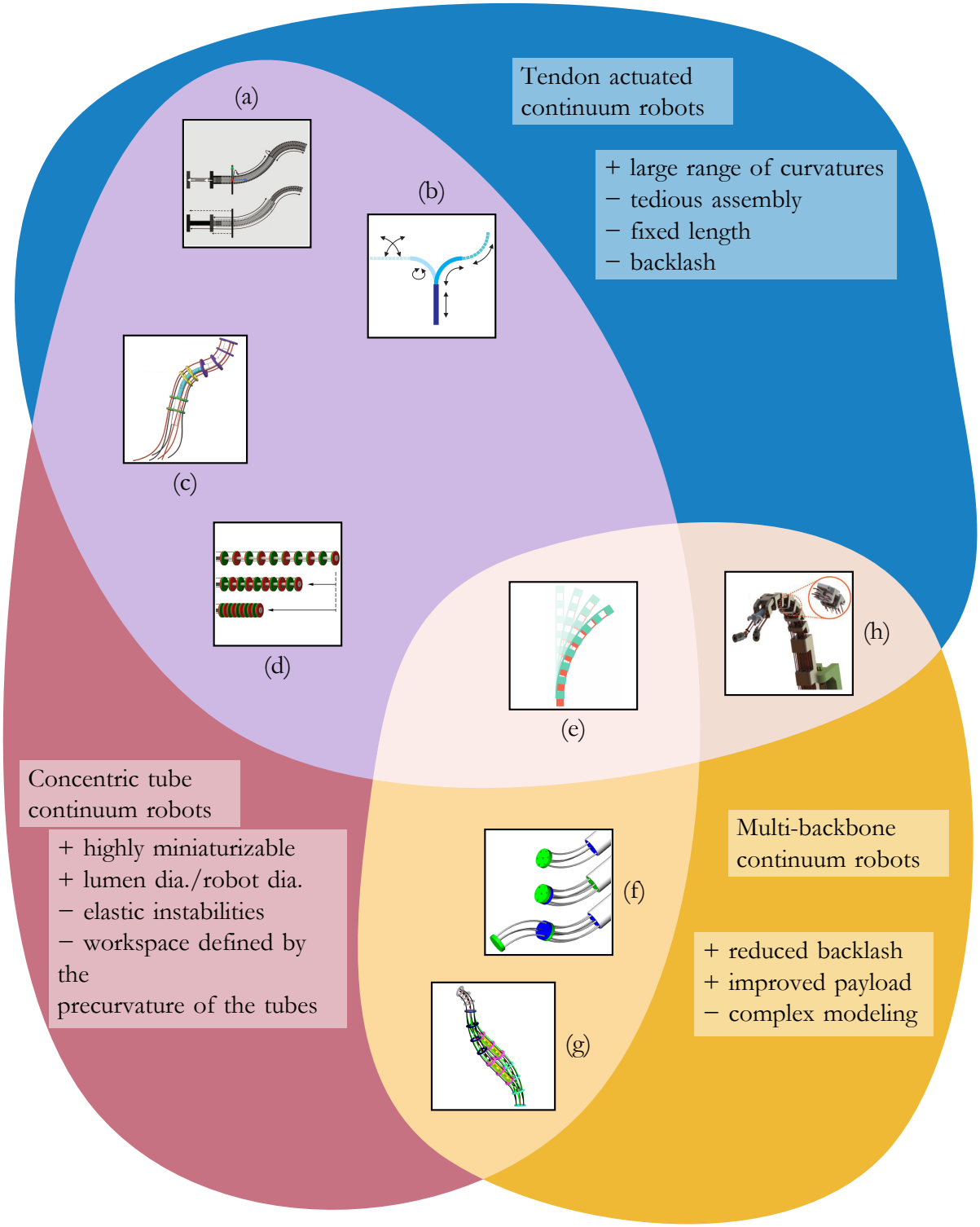

Figure 1.6: Hybrid continuum robots at the crossing of standard continuum robot types. Top left, the hybrid designs (a), (b), (c), and (d) combine TACRs and CTCRs. Bottom, the hybrid designs (f) and (g) combine MBCRs and CTCRs. Right, the hybrid design (h) combines MBCRs and TACRs. In the middle, CAARs (e) are a combination of all three standard continuum robot types TACRs, MBCRs, and CTCRs. (a), (b), (c), (d), (f), (g), and (h) are adapted respectively from [Amanov et al. 2017], [Wu et al. 2017], [Zhang et al. 2018], [Nguyen and Burgner-Kahrs 2015], [Kang et al. 2016], [Zhao et al. 2020], and [Gu et al. 2019].

State-of-the-art hybrid continuum robots have shown to effectively combine several advantages of the robots they are based on. Follow-the-leader motion or the increase of the payload of robots while preserving an interesting ratio of lumen diameter over outer diameter are two examples of capabilities of hybrid continuum robots over their standard counterparts. Combining structures may however also bring in some drawbacks as, for instance, the fact that hybrid continuum robots often require more effort on the modeling side.

1.3.3 Other Notable Continuum Robot Features

Remarkably, some continuum robots try to take advantage of both intrinsic and extrinsic actuation by combining them. Some notable examples include the CTCR made out of electro-active polymers investigated by the authors of [Chikhaoui et al. 2018]; the concentric tube robot introduced by the authors of [Peyron et al. 2022] that features a magnetically steerable inner tube; the hybrid magnetically- and tendon actuated continuum robot proposed by the authors of [Zhang et al. 2021b]. Other examples of magnetically steerable hybrid intrinsic-extrinsic actuated continuum robots can be found in the review by the authors of [Yang et al. 2023] that focuses on magnetic continuum robots for medical applications.

Parallel to the actuation system, the specifics of continuum robots have led to the development of interesting features, some of which are detailed below.

First, as continuum robots are compliant, it naturally comes to mind that the compliance presents both advantages and disadvantages, sometimes within a single application. This observation has led to the development of systems that enable to vary the stiffness of the manipulators or even lock their shape in certain configurations. Granular jamming [Wei et al. 2022, Wockenfuß et al. 2022] or layer jamming [Li et al. 2021, Clark and Rojas 2022] consists in locking together particles or flaps by compacting them together in a vacuum chamber such that friction prevents further motion [Langer et al. 2018]. The authors of [Moses et al. 2013] propose some additional jamming methods utilizing electro-rheological, phase transition, or magneto-rheological fluids.

Globally, the jamming approach may suffer from leaks and needs continuous energy supply to function. To circumvent these issues, the stiffening of continuum robots can also be achieved with pure mechanisms. To completely block certain parts of continuum robots, the authors of [Zhong et al. 2020, Lin et al. 2022a] use bi-stable mechanisms while the authors of [Wang et al. 2022a] use vertebrae that can lock together.

A different objective for variable stiffness robots is to enable continuously varying stiffness without completely locking the shapes. Such stiffness control has been studied in [Kim et al. 2019] through specific alignment of patterned tubes. The authors of [Misra and Sung 2022] investigate the use of springs made out of tunable stiffness polymers, while in [Chen et al. 2022] shape-memory alloy rods are used.

Continuum robots being hyper-redundant in the sense that their shapes have infinite degrees of freedom (DoF), another feature that naturally comes to mind is the ability to sense their own shape. This path has been investigated in [Li et al. 2022, Orekhov et al. 2023] and [Yin et al. 2022] where shape sensing is achieved, respectively, with extra passive tendons and embedded ultrasound transducers. In [AlBeladi et al. 2021], shape sensing is achieved through vision while in [Huang et al. 2022], a model based approach is proposed. In the 'proprioception' sensing domain, force sensing is also an active field of continuum robotics research [Aloi et al. 2022, Cangan et al. 2022, Lin et al. 2022c, Wooten and Walker 2022].

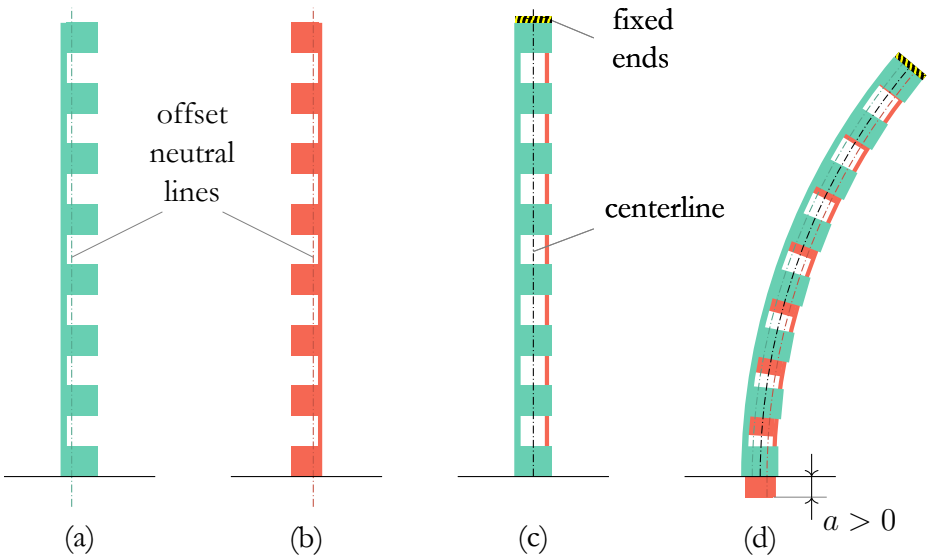

Figure 1.7: Composition and working principle of a CAAR. Two asymmetrically notched tubes are arranged concentrically and attached at their tip. To actuate the CAAR the tubes are translated axially at their base. (a) The outer tube, in its undeformed configuration (b) The inner tube, in its undeformed configuration. (c) The tubes assembled forming the CAAR in its undeformed configuration. (d) Example of an actuated configuration of the CAAR where the axial translation of the inner tube $a > 0$.

1.4 Concentric Agonist Antagonist Robots

1.4.1 Definition and Principle

CAARs are continuum robots that consist of concentric tubes attached at their distal ends. The tubes have an asymmetric geometry that offset their bending plane from the tube centerlines. The tubes can be translated axially at their base to induce a bending movement by the difference in length of the offset neutral lines (see Figure 1.7).

Looking at Figure 1.6, this type of robots can be seen as a hybrid type of continuum robots, between CTCRs where tubes are arranged concentrically and TACRs or MBCRs where the offset neutral lines (i.e. neutral axis) of the tubes can be compared to secondary backbones fixed at the distal extremity of the robots. Like CTCRs, CAARs can be constructed at very small scales, are easy to assemble, and take advantage of the interesting lumen diameter over robot diameter ratio. But where CTCRs curvatures are defined by the precurvature of the tubes and are subject to elastic instabilities, CAARs can bend over a large range of curvatures, like TACRs and MBCRs, and do not rely on counter rotation of the tubes, thus such instabilities. Moreover, as for MBCRs, the actuation of CAARs is transmitted through solid material, leading to an increased payload with respect to their TACRs counterpart. One can see how this type of robots is a perfect example of a hybrid structure that combines strengths of the robots it is based on. It is exactly this analysis that has led to an interest in investigating and enhancing these robots, which is the main objective of this dissertation.

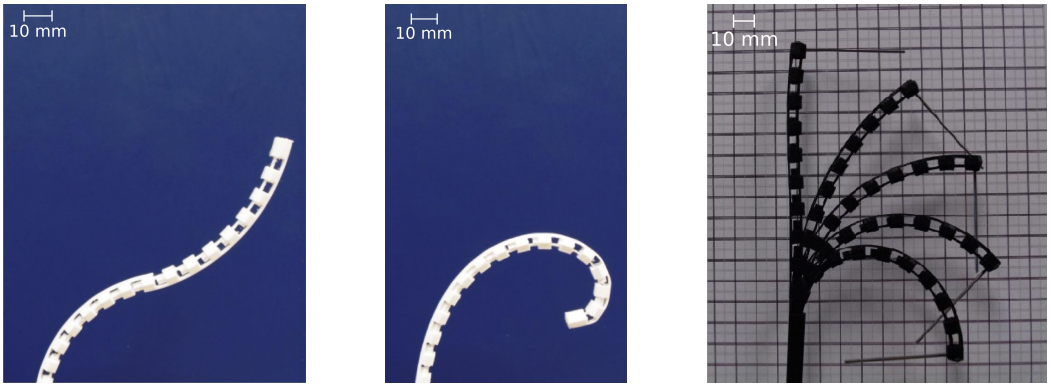

(a) (b) (c)

Figure 1.8: CAAR design variations. (a) Shifting the orientations of the notches 180° midway creates an 'S'-shape. (b) By varying the notch depth of the notches in the tubes, variable curvature can be achieved. (c) Precurving the tubes increases the maximum reachable curvature while still allowing the tubes to be actuated to a straight position. (a), (b), and (c) are adapted from [Oliver-Butler et al. 2017].

1.4.2 State-of-the-art CAARs

This section gives an overview of the scientific literature devoted to CAARs. A thorough search of the relevant work yielded only seven occurrences of CAARs in the literature. The concept was first introduced in [Oliver-Butler et al. 2017] and a first constant curvature model was derived. The same year, the topic is studied in a master thesis [Ponten 2017]. The following year, a small scale manipulator was constructed and utilized in an endoscope as a preliminary step towards medical applications [Rox et al. 2018]. Specifically, the prototype was designed for use in bronchoscopy. In 2019, a patent was released [Riojas et al. 2019]. In 2020, K. Oliver-Butler published her PhD dissertation [Oliver-Butler 2021], which is currently under embargo. More recently, the same team published a journal paper with an extension of the initial constant curvature model to a piecewise constant curvature model [Oliver-Butler et al. 2022]. In these references, the CAAR general concept is described, as well as some possible design variations.

The first model that was developed is a constant curvature geometry based model [Oliver-Butler et al. 2017]. It relates the tube axial displacement actuation variable with the in-plane end effector angle or, equivalently, the curvature of the robot. With this initial model, it is thus not possible to model CAARs with design variations, such as CAARs with variable curvatures (see Figure 1.8).

The second model that was developed extends the first constant curvature model to a piecewise constant curvature model [Oliver-Butler et al. 2022]. It takes the individual geometry of each notch into account. With the input of elementary beam mechanics, it enables to relate a force or displacement actuation variable to the shape of the robot. The modeling of CAARs with variable notches is possible as long as the neutral lines of the robots lie in-plane and opposite to each other.

The piecewise constant curvature model also served as a building block for the implementation of a CAAR design algorithm. Starting at the input from a desired target shape, the algorithm uses the model to determine robot parameters (depth and height of the notches) such that, when actuated, the robot fits the target shape.

For both models, the main limitation is that they are based on geometry, which does not allow taking external efforts into account. This is a crucial shortcoming that prevents the use of CAARs beyond free-space swaying, i.e. in interaction with an actual environment. Moreover, the

constant curvature method relies on very restrictive hypotheses, which are hampering precision of the models (maximum reported errors are above 18% of the length of the manipulator).

All six references discussed above are from the University of Tennessee, Knoxville, USA. One outside reference is to be found in the literature [Gulotta et al. 2020]. It is a master thesis project that explored an integrated and application-oriented design of CAARs.

1.5 Continuum Robots for Medical Applications

Without the aim of being exhaustive, this section scans medical applications of continuum robots. The idea is rather to provide an overview and to point out the suitability of continuum robots to medical applications linking with the inherent advantages of such robots, identified in section 1.2. Further, perspectives for the propitious use of CAARs in some of these applications are discussed.

Continuum robots in vessels and the heart

The inherent compliance of continuum robots make them particularly suited for endoluminal navigation inside the vessels of the circulatory system. Several vascular applications have been assessed. In [Jayender et al. 2008], the authors are interested in the treatment of angioplasty with a shape-memory alloy actuated active catheter and conduct a preliminary study on a test bed. Devices have also been developed for insertion reaching up to the heart [Back et al. 2017, Jeong et al. 2020, Lis et al. 2022] for interventions like atrial fibrillation treatment [Sheng et al. 2018] or ablation tasks [Yip et al. 2017]. These devices are mainly TACRs and have been evaluated in studies ranging from anatomical phantoms to cadaver studies. Of course, the applications are not restricted to blood vessels only, other circulatory systems are concerned. Even, navigation inside the ducts of the breast has been considered and assessed with a hybrid fluidic TACR on an anatomical phantom for early cancer detection [Berthet-Rayne et al. 2021]. The authors of [Kim et al. 2022] provide a review of endoluminal robots.

Most of these robots can bend their tip in only a single direction through the attachment of a single tendon (strings can only transmit tension). Some of them are actually made out of notched tubes. By adding a second tube to form a CAAR, bending can be extended in the opposite directions. This would remove the need for turning the devices 180° during the procedures and could thus make the interventions less traumatic and reduce their duration.

Small scale continuum robots within confined spaces of the body

Different structural characteristics of continuum robots enable to scale them down, often far below the sizes that can be reached with traditional rigid-link robots. These millimeter to micrometer scale robots open opportunities for treatments in highly confined spaces that were previously not reachable. In the field of neurosurgery, telerobotic CTCRs and TACRs have been developed for access through the nose and assessed on phantoms [Burgner et al. 2014, Hu et al. 2019a]. Other devices plan to access directly through the skull, as the TACR developed in [Chitalia et al. 2021]. This last device dedicated to the treatment of pediatric hydrocephalus cases measures less than 2 mm in diameter. The authors conduct a robot control experiment evaluating their model and a reachability study of the device in simulation. Other fields where small scale continuum robots can outperform rigid-link robots include arthroscopy [Dario et al. 2000] and ophthalmic surgery [Iordachita et al. 2022]. Indeed, ophthalmic surgery is certainly a medical application that requires very

small scale robots. The multi-arm CTCR developed by the authors of [Mitros et al. 2020] and included in a study on high-fidelity phantoms features 3.5 mm diameter tubes to work around the eye for optic nerve sheath fenestration. The TACR developed in [Jinno and Iordachita 2022], designed for intraocular microsurgery and tested on an eye model measures less than 1 mm in diameter.

To fabricate such small robots (or wrists), some authors make use of notched tubes. In fact, it is the same technique, described in section 1.3.2, that is used for creating miniaturized tendon actuated wrists [York et al. 2015] that is also used to fabricate CAARs. Thus, CAARs have the potential to be fabricated at these scales while increasing the precision of the discussed devices.

Conforming to curvilinear paths for natural orifice transluminal endoscopic surgery

Natural orifice transluminal endoscopic surgery is yet another medical field that has attracted many continuum robot applications. The suitability is largely due to the ability of continuum robots to follow the tortuous paths within the human body, where rigid-link robots are less adequate. To access the lungs through the natural airways, researchers seek to fit TACR shapes to the branches of a bronchi anatomical phantom [Ai et al. 2021] and conduct simulation studies in order to optimize the reachable lung volume in [Fried et al. 2021]. Devices that allow endobronchial intervention have also been developed, as the electrospinning TACR evaluated on anatomical phantoms in [Wu et al. 2021] and the CTCR assessed on *ex vivo* ovine plucks in [Gafford et al. 2019]. Currently, two commercial bronchoscopy robots are food and drug administration (FDA) approved: The Ion system of Intuitive Surgical, Inc. and the Monarch platform of Auris Health, Inc.

Gastrointestinal applications include colonoscopy [Chen et al. 2007], where the challenge is to find a balance between the flexibility needed for insertion over long pathways and the rigidity required for tissue manipulation. The authors of [Ahmed and Gilbert 2022] investigate an original colonoscope that can anchor to the walls of the lumen. They conducted early stage experimental test in free-space. Further applications include gastric cancer screening [Campisano et al. 2017, Ma et al. 2021] and trans-vaginal diagnostic peritoneoscopy [Noonan et al. 2011]. While the devices proposed in [Campisano et al. 2017, Ma et al. 2021] are water jet continuum robots assessed on an experimental bench and a phantom, the TACR presented in [Noonan et al. 2011] is at the stage of porcine model studies.

Another area of great potential use is in ear, nose, and throat procedures. Such systems include the multi-arm TACR and multi-arm CTCR, respectively developed by the authors of [Berthet-Rayne et al. 2018a] and [Yu et al. 2016] for tumor resection in the nasopharyngeal cavity and evaluated in teleoperation on experimental benches. Another team developed a TACR for trans-nasal diagnosis of middle ear disease and conduct cadaver studies [Gafford et al. 2020]. The authors of [Nguyen et al. 2022b] design a hybrid CTCR TACR for cholesteatoma laser surgery. They study the behavior of the robot in a phantom and demonstrate the removal procedure with real cholesteatoma tissues. The TACR described in [Yoon et al. 2013] is devoted to maxillary sinus surgery. Several MBCRs have been developed for trans-oral surgery [Simaan et al. 2004, Simaan et al. 2009, Gu et al. 2019]. Simaan et al. evaluate their dual-arm MBCR through teleoperation experiments on a test bench, while Gu et al. have gone through cadaver studies. Noteworthy in this field of applications, is the Flex Robotic System of Medrobotics Corporation that gained FDA and European conformity (CE) approval for trans-oral procedures in 2014 (and colorectal procedures in 2016).

Urology procedures fall even well under the category of natural orifice transluminal endoscopic surgery, where miniaturized continuum robots have been implemented for applications as ureterorenoscopy [Schlenk et al. 2022] or trans-urethral laser prostate surgery [Hendrick et al. 2015].

Both systems are assessed with clinicians on a test bench with either a phantom or cadaver tissues.

Often, the insertion of robots over long pathways introduces some undesired kinematic coupling between the followed tortuous path and the position of the actuated tip. This is not the case for CTCRs, but the long pathways introduce extra friction and material to build up elastic energy, increasing the above discussed instabilities. One major advantage of CAARs is that they combine the advantage of CTCRs while not being subject to the same instabilities. Indeed, over their passive non-notched insertion part, the tube neutral lines of CAARs coincide. It is only in the active distal part that they are offset from the center. The authors of [Gafford et al. 2023] present a pre-clinical study with *ex vivo* porcine trials exploiting this property for interventional endoscopy applications. Moreover, as for CTCRs, the open lumen of CAARs can be used to insert tools [Oliver-Butler et al. 2017] or other CAARs to create multi-segment CAARs and increase the total number of DoF.

Enhanced dexterity and reachability

Due to their straight instruments, rigid-link robots as the *da Vinci* system are unable to provide the surgeon with intuitive DoF. Continuum robots that can bend inside the laparoscopic cavity are an answer to this limitation. The authors of [Ma et al. 2022] study a multi-segment TACR in an anatomical phantom. Moreover, with the additional DoF, continuum robots also enable the access of multiple instruments through a single port. The authors of [Ding et al. 2013, Xu et al. 2015] propose a single port access multi-arm MBCR and conduct free-space and loaded experiments, as well as dexterity evaluation through manipulation tasks on a surgical training bench. Even for single instrument procedures, curving manipulators are able to reach much larger workspaces while entering the surgical site through a single port. This enhanced reachability is particularly useful when not many ports are available, as in the removal of osteolysis formed behind the acetabular shell of primary total hip arthroplasties [Kutzer et al. 2011]. In [Sefati et al. 2022], a TACR is assessed on a printed osteolysis phantom based on segmented medical images and subsequently on cadaver studies. Enhanced reachability is also useful when the access needs to traverse delicate tissues, as in neurosurgery. As an example, the authors of [Leibrandt et al. 2017] present a workspace and dexterity analysis in simulation where a CTCR is constrained to pass through specified locations. Another potential use for such robots with improved dexterity, as compared to traditional rigid needles, is in navigating through tissue to reach abscesses for per-cutaneous abscess drainage, as explored in a laboratory environment in [Girerd and Morimoto 2021].

Clearly, there is promising potential for CAARs in single-port or multi-port laparoscopic procedures. Indeed, by varying the mechanical properties of the notched tubes along their length, the behavior of a CAAR can be modified. By changing the orientation of the notches along the tubes, they will bend in different directions corresponding to the notch orientations. This enables to create the typical 'S'-shapes that are useful for single-port access. By varying the notch depth along the length, it is possible to achieve variable curvature along the length of the robot. This last feature even allows designing patient specific robots that are able to reach a particular workspace from a particular access point and cavity constraints, as studied with CTCRs in [Lin et al. 2022b]. Examples of both of these alternatives can be seen in Figures 1.8a and 1.8b, respectively.

Another strategy for increasing the maximum reachable curvature of CAARs consists in precurving the robot, as proposed in [Remirez and Webster 2016] for MBCRs. The straight configuration of the tubes is then reached through actuation. In a setup where this precurved CAAR is used together with the axial rotation of the whole CAAR, the overall reachable workspace is increased. An example of a precurved CAAR is shown in Figure 1.8c.

Magnetic resonance imaging compatible robots

An additional advantage of continuum robots over rigid-link robots is the fact that their active effector can easily be made out of magnetic resonance compatible materials [Su et al. 2022]. Often, the actuation of magnetic resonance compatible robots is achieved through shape-memory alloy actuation [Ding et al. 2021]. In [Kim et al. 2018, Shao et al. 2020], a shape-memory alloy actuated continuum robot is successfully manipulated in a gelatin phantom during magnetic resonance imaging. Noteworthy is the fact that all extrinsically actuated structures also offer potential for magnetic resonance compatible manipulators, as long as the actuation unit is kept far enough from the active part of the robot.

As regards CAARs, notched tubes can be fabricated with additive manufacturing techniques. The tubes are printed as a single part directly with cutout notches. Beyond the low cost and short fabrication period, additive manufacturing techniques mostly employ materials that are electromagnetic and magnetic resonance imaging compatible.

To conclude this section on medical applications, it is worth noting that the mentioned studies are only a tip of an immense iceberg of applications. Several review papers treat specific areas of applications or types of robots. The review by the authors of [Alfalahi et al. 2020] zooms in on CTCRs for general medical applications, while the authors of [Cianchetti et al. 2018, Kwok et al. 2022] concentrate on soft robots. In the more general reviews [Troccaz et al. 2019, Taylor et al. 2022] on surgical robotics in the broader sense, continuum robots are put in perspective with their rigid counterpart. Finally, the review by the authors of [Dupont et al. 2022] proposes a point of view considering the slenderness ratio of continuum robots. Indeed, the length to diameter ratio of a surgical manipulator plays an important role with respect to the targeted application.

1.6 Conclusion

In this chapter, the differences between rigid-link robots and continuum robots were highlighted. Their inherent advantages make them very suited for medical applications. Categorizing around these specific characteristics, some medical applications are presented. Different types of continuum robots however offer different assets. In order to push the capabilities of continuum robots and to improve their integration in medical applications, hybrid structures have been developed. These structures thrive at combining the advantages of the standard continuum robots they are based on. CAARs are at the intersection between the three main types of standard, extrinsically actuated continuum robots. Some challenges that arise from the combination of structures for CAARs will be addressed through this manuscript. Moreover, while the literature on this topic is limited and the community has not had the opportunity to step back on the subject, other challenges will be identified and discussed in the 'Future Work' section page 142.

CAARs are a promising new type of continuum robots, but current studies only explored geometry based models, hampering the development of their full potential. This thesis analyzes, with a particular care, multiple aspects of CAARs down to the smallest details. It aims at providing the community with a better understanding of these up-and-coming systems. Ultimately, it derives a 2D general mechanical model for CAARs. Compared to the state-of-the-art models that are based on strong simplifying approximations, the proposed geometrically exact model can take external loads into account. Models with the same capabilities have been described for different types of PCRs. However, as will be discussed in sections 4.2.2 and 4.2.3, they are inadequate for CAARs and a whole new model needs to be derived.

The 2D CAAR model presented in chapter 4 is a strong foundation for future developments and advancements, as it is well suited for extension to 3D modeling. By expanding upon the 2D mechanical model, the community will be able to achieve greater capabilities with CAARs. In section 5.4, varying the angle of the notches along tubes or introducing rotation and torsion of the tubes/robot produces CAARs with 3D shapes. All these 3D features increase the dexterity and reachability of CAARs.

Before diving into modeling CAARs, the next chapter presents general modeling considerations for standard continuum robots. This first step, along with the case study on TACRs in chapter 3, will provide the necessary degree of understanding on the topic of continuum robot modeling for the derivation of a mechanical model of CAARs specifically.

Contributions of this chapter

1. CAARs are put in perspective with other types of continuum robots.
2. A literature review on CAARs is reported.
3. The potential for CAARs in medical applications is analyzed.

2

Methodology: General Modeling Framework for Continuum Robots

2.1 Foreword

As for all types of robots, the use of continuum robots requires modeling their kinematics and dynamics. Indeed, control [Renda et al. 2022, Rucker et al. 2022a], design optimization [Berthet-Rayne et al. 2018b, Hwang and Kwon 2019, Cheong et al. 2021], stability analysis [Till 2019], passivity analysis [Mochiyama 2005, Roozing et al. 2020] etc. are all robot related tasks that might require a model of the robot in the first place. The challenge is that modeling continuum robots is generally more complex than rigid-link robots where the robot pose can be geometrically defined by the joint angles and the link lengths with a good accuracy. Contrarily, the continuously curving shapes and the inherent compliance of continuum robots requires consideration of elasticity.

The first models that resemble the current continuum robot models are the ones that modeled hyper-redundant systems with a continuous approximation [Chirikjian 1994, Chirikjian and Burdick 1995]. Ever since, models for continuously curving robots have evolved [Chikhaoui and Rosa 2022]. The most precise models for continuum robot modeling are based on the Cosserat rod theory [Sadati et al. 2017, Chikhaoui et al. 2019]. As this thesis deals with such models, the purpose of this chapter is to explain didactically and methodically all aspects of Cosserat rod modeling.

Nevertheless, other interesting modeling strategies exist. Indeed, when Cosserat rod models become very complex and sometimes computationally ineffective, simpler types of models can be useful. To put Cosserat rod modeling in perspective with these other modeling strategies, section 2.2 briefly introduces continuum robot modeling means in general. Following this general foreword on continuum robot modeling, section 2.3 re-derives the Cosserat rod theory in a way that it is as general as possible. The chapter ends with section 2.4 presenting a brief analysis of Cosserat rod models of the literature, explaining how one can use such models for various types of continuum robots.

2.2 Different Continuum Robot Modeling Strategies

Today, the continuous models for continuum robots can be classified in two main categories: (i) the models that assume the robot can be approximated by general continuous curves in space, these models are called geometry based models or kinematic frameworks and (ii) the exact models that

see the robot as a nonlinear problem of elasticity with boundary conditions, these models are called mechanical models .

2.2.1 Geometry Based Models

Geometry based models have the advantage to lead to analytical formulations, which makes them suitable for easy real-time inverse kinematics and control [Gravagne et al. 2003, Neppalli et al. 2009, Kazemipour et al. 2022]. On the downside, these models are less precise, are subject to error propagation, and cannot take external efforts into account. Also, torsion is neglected while it often plays a significant role in continuum robots. Geometry based models can further be sub-categorized in constant curvature models and variable curvature models.

The constant curvature approach divides the robot in a finite number of curved links and approximates each link by a constant curvature arc [Gravagne and Walker 2000b, Jones and Walker 2006b, Webster et al. 2009b]. For each type of robot, the mapping from robot actuator variables to so-called "arc parameters"(curvature, angle of the bending plane, and arc length) is specific. But once the arc parameters are found, the pose of the robot can geometrically be derived, very much like rigid-link robots. The authors of [Webster and Jones 2010] present a very comprehensive review on constant curvature models for different types of continuum robots. This modeling approach is often applied to TACRs, computing the geometrical relationship between arc parameters and tendon displacements (and more recently tendon tensions [Gonthina et al. 2020]). Further, to achieve more complex shapes or model multi-segment manipulators, it is possible to divide the robot into multiple parts modeling each with a distinct constant curvature arc. This method is called the piecewise constant curvature approach [Mahl et al. 2013].

To even better fit models to tortuous robot shapes, the variable curvature approach describes the robot as a function that is integrated along the robot length. Functions that have been used to model continuum robots include clothoid curves [Webster and Jones 2010] and more recently polynomial curves [Santina and Rus 2020, Stella et al. 2022], Euler curves [Gonthina et al. 2019, Rao et al. 2021a, Rao et al. 2022], Bezier curves [Wang and Blumenschein 2022], or Pythagorean hodograph curves [Bezawada et al. 2022]. Instead of using a single function, another possibility is to use multiple functions (for example, Bessel functions or wavelets). In this case, the shape is approximated through a modal approach [Chirikjian and Burdick 1994, Gravagne and Walker 2000a]. The variable curvature approach was found to more precisely match the shape of robots than the constant curvature approach, while still maintaining analytical (though more complex) formulations. However, it requires more effort or even the use of sensors on the robots to map the robot actuator variables to the curve parameters.

2.2.2 Mechanical Models

Mechanical models take the elastic behavior of the constitutive materials of the robots into account and solve the problem over boundary conditions that can involve external loading of the structures.

Such models take their roots in the continuum mechanics community and full 3D mechanical models. In fact 3D mechanical models are very well suited to the modeling of soft robots [Bieze et al. 2018], where the cross-sections deform and often nonlinear constitutive relationships reign [Shiva et al. 2019, Marechal et al. 2021]. On the other hand, with continuum robots one can make a set of assumptions that simplify the problem. Generally, continuum manipulators, and especially medical ones, are used within a small strain regime (90-degree bending). This means that one stays within

the linear elastic regime and the cross-sections can be assumed to not undergo deformation. As a result, 1D beam theories are more popular, in the literature, for their modeling.

Linear mechanical beam models or non-geometrically exact beam models

Most linear mechanical models for continuum robots employ the Euler-Bernoulli [Camarillo et al. 2008, Webster et al. 2009a, Liu and Alambeigi 2021] or Timoshenko [Fattahi and Spinello 2013, Wenlong et al. 2013] beam theories that are geometrically linear and can model only small rotations of the beam cross-sections.

Multiple approaches for solving these models exist. As an example, one can mention the finite element modeling (FEM) approach, where all matrices and vectors are expressed in a common global basis and then assembled by identifying shared nodal coordinates [Gravagne and Walker 2002, Bosman et al. 2015, Gallardo et al. 2021, Vanneste et al. 2022]. A major difference between FEM and the other mechanical modeling approaches is that it uses absolute coordinates related to a global inertial reference frame (attached to space), in contrast to the deformation based parameterization that uses relative coordinates related to the material. A consequence of the absolute pose parameterization is that when kinematic constraints are introduced (in the form of Lagrange multipliers) between the different constituents of continuum robots, the numerical conditioning is deteriorated [Adagolodjo et al. 2021]. Furthermore, absolute coordinates can be an obstacle for control purposes [Boyer et al. 2021]. Nevertheless, the FEM approach has virtues of its own. Among others, it has the advantage to ease the interaction with other elements from the environment that would be modeled with FEM as well. Also the fact that it uses global coordinates can be an advantage for these interactions more generally and can ease the consideration of friction between the manipulator and its environment [Zhang et al. 2019b]. Furthermore, while the FEM mathematical formulation might seem a priori less suited to 1D media [Wiese et al. 2022], the authors of [Adagolodjo et al. 2021] have shown that it can be used efficiently by assembling finite beam elements in series, which in global coordinates yields a tridiagonal band matrix that is solved with linear complexity. With an efficient numerical implementation, such systems can be solved at high rates.

Besides the linear beam theories, other models are based on an equivalent spring-mass model [Yekutieli et al. 2005, Zheng et al. 2012, Schultz et al. 2022] that needs extensive tuning of parameters, cannot reproduce the majority of actuation principles, and is computationally expensive. The pseudo-rigid body representation [Rao et al. 2021b] is similar to the spring-mass model, but in this case the continuum robot is modeled as a series of rigid links as in the reduced order model approach of [Sadati et al. 2019, Sadati et al. 2020, Sadati et al. 2022]. One more possibility is to use an energy minimization criterion, as in the research activities of Simaan et al. [Simaan 2005, Xu and Simaan 2008].

Geometrically exact beam models

Most of the mechanical models for continuum robots model their rods or tubes as Cosserat rods [Trivedi et al. 2008, Dupont et al. 2010, Rucker et al. 2010a]. The geometrically exact theory was applied to various continuum manipulators as CTCRs [Lock et al. 2010, Rucker et al. 2010b], TACRs [Rucker and Webster 2011b, Oliver-Butler et al. 2019], and MBCRs [Orekhov et al. 2017, Wang et al. 2019]. Over the past years, Cosserat rod models have been studied extensively for modeling the statics and dynamics of continuum robot [Mahvash and Dupont 2011, Renda et al. 2014, Janabi-Sharifi et al. 2021, Briot and Boyer 2023].

To apply the Cosserat rod theory to continuum robots, multiple approaches have been used [Armanini et al. 2023]. The great majority of the research groups use a Newtonian approach to formulate an explicit boundary value problem (BVP). The BVP is set up by isolating subsystems, using Newton's second law to balance the interaction forces between them. Most of the time, the BVP is solved with a shooting method. This means that one need to find the unknown boundary conditions that, after 'shooting' to the other side of the problem, satisfy the other boundary condition. Typically, the 'shooting' (i.e. the integration of the ordinary differential equations (ODEs) of the BVPs) is achieved with iterative methods (for example the Runge–Kutta methods), spatially sweeping the rods or tubes.

Lately, another approach was proposed based on a Lagrangian viewpoint [Renda et al. 2020, Boyer et al. 2021, Renda et al. 2021]. In essence, the Lagrangian approach is based on two key ingredients: first the concept of configuration space, second a variational principle that allows the static or dynamic balance on this space to be derived [Goldstein et al. 2001]. It enables the application of efficient numerical approximation methods based on variational formulations, both in statics and in dynamics [Zienkiewicz et al. 2005].

Lastly, one can mention the FEM approach again, as it has recently been used to solve Cosserat rod models of continuum robots [Adagolodjo et al. 2021]. This is not a trivial problem. Indeed, taking a step back, the research communities using FEM generally use theories or linear geometric models in $\mathbb{R}^3$, while for modeling the geometrically exact Cosserat rod theory one needs $\mathbb{R}^6$ [Ibrahimbegović and Mikdad 1998, Boyer and Primault 2004]. To the extent of this thesis knowledge, Juan Carlo Simo is the father of this field of research [Simo and Vu-Quoc 1988] which is today continued by only few research teams as the the authors of [Cardona and Geradin 1988, Sonneville et al. 2014] in Belgium, and those of [Harsch et al. 2023] in Germany. While the potential of geometrically exact FEM is undoubtedly promising, it is important to acknowledge that the research on employing finite element Cosserat rod modeling for continuum robots is relatively new. Since this topic extends beyond the scope of the current manuscript, the remainder of this document will focus on the Newtonian and Lagrangian approaches.

2.2.3 Data-driven Modeling Strategies

A few less well known, yet recently blooming, modeling approaches cannot be categorized in the two preceding sections. With the advantage to remove the need for complex mathematical modeling, learning based approaches have proven to be able to account for the behavior of certain continuum robots. Different network architectures for mapping the position of the tip of continuum robots have been investigated as feed-forward neural networks [Giorelli et al. 2015a, Giorelli et al. 2015b, Grassmann et al. 2018, Grassmann and Burgner-Kahrs 2019], recurrent neural networks [Thuruthel et al. 2019], radial basis function neural network [Zhang et al. 2022], or combining a neural network with a constant curvature model [Jiang et al. 2017]. Building on these results, neural networks have also been used to model the entire shape of continuum robots [Kuntz et al. 2020, Liang et al. 2021] and to enable sensing [Ha et al. 2022]. A drawback of using neural networks is that the insight between the manipulator designs and dynamics is completely lost. As such, it becomes difficult to develop optimal design strategies or identify the sources of modeling errors.

Another drawback of deep learning based approaches is that they require great amounts of data [Grassmann et al. 2022] and often long and computationally heavy training or initialization phases [Chikhaoui and Burgner-Kahrs 2018]. This observation has lead to the development of learning methods that function with smaller amounts of data, as Gaussian Process Regression [Wang et al. 2022c] or locally weighted projection regression [Fagogenis et al. 2016]. The authors of [Yip

et al. 2017, Li et al. 2018] construct the Jacobian matrix by experimentally measuring the actuation space to task space relationships. An advantage of these computationally lighter methods is that they can also be trained online.

The main obstacle with data driven approaches in general is that it is challenging to acquire data that (i) are complete and representative of the considered workspace and (ii) unbiased [Ha et al. 2017]. Further, while learning based approaches can be precise in free-space, it is often more challenging to model robots in unstructured environments, which are the environments continuum robots are best suited to operate in. Also, for a given data approach, generalization to a new device may be challenging.

2.3 General Cosserat Rod Theory

The Cosserat rod theory is established by the brothers Eugène and François Cosserat in 1907 [Cosserat and Cosserat 1907, Cosserat and Cosserat 1909]. A modernized summary can be found in Stuart Antman's book on nonlinear problems of elasticity, published in 1995 [Antman 1995]. Cosserat rod theory is a one-dimensional theory of continuous media used to describe slender bodies subject to finite deformations. In contrast to vibration theory or strength of materials, Cosserat rod theory is geometrically exact in the sense that it is not based on any approximation of small displacements or slopes.

Since 2008, it has been used to model continuum robots with a Newtonian point of view. The majority of this research was carried out by research teams belonging to the robotics community. More recently, since 2019, the same theory has been used by researchers from the soft robots and bio-robotics communities to model continuum robots but from a Lagrangian point of view. These different viewpoints can offer certain advantages, depending on the problems to solve and to what end the models are used.

One of the motivations of this methodology chapter is to clearly expose all the ingredients coming from the Cosserat rod theory that are necessary for modeling continuum robots with either the Newtonian or the Lagrangian approaches. The major part of these ingredients are common to both approaches. Yet, as the approaches are coming from different communities and do not share a common set of notations or mathematical framework (see appendix A), the different communities fail to recognize the similarities between them. This section aims at re-deriving the Cosserat rod theory in a unique mathematical framework that will be used throughout the manuscript for both approaches. But also, at exhaustively integrating the different aspects of the theory that can be found in the literature [Simo 1985, Simo and Vu-Quoc 1986, Simo and Vu-Quoc 1988, Antman 1995, Cao and Tucker 2008]. The different constituent ingredients (corresponding to sections 2.3.1 to 2.3.5) are summarized in Figure 2.1. Section 2.3.6 discusses various useful formulation of the Cosserat BVPs.

2.3.1 Differential Geometry

The first building block in the Cosserat rod theory consists in describing a rod in space through parametric differential equations. Let us consider a single rod in space, of length l. The ambient space is equipped with a fixed inertial frame $\mathcal{F}_s = (O, e_x, e_y, e_z)$. The model of the rod is obtained by a continuous stacking of rigid cross-sections labeled by a continuous index. A convenient choice for this reference parameter is the arc length along the rod, noted $X \in [0, l]$. It is counted from

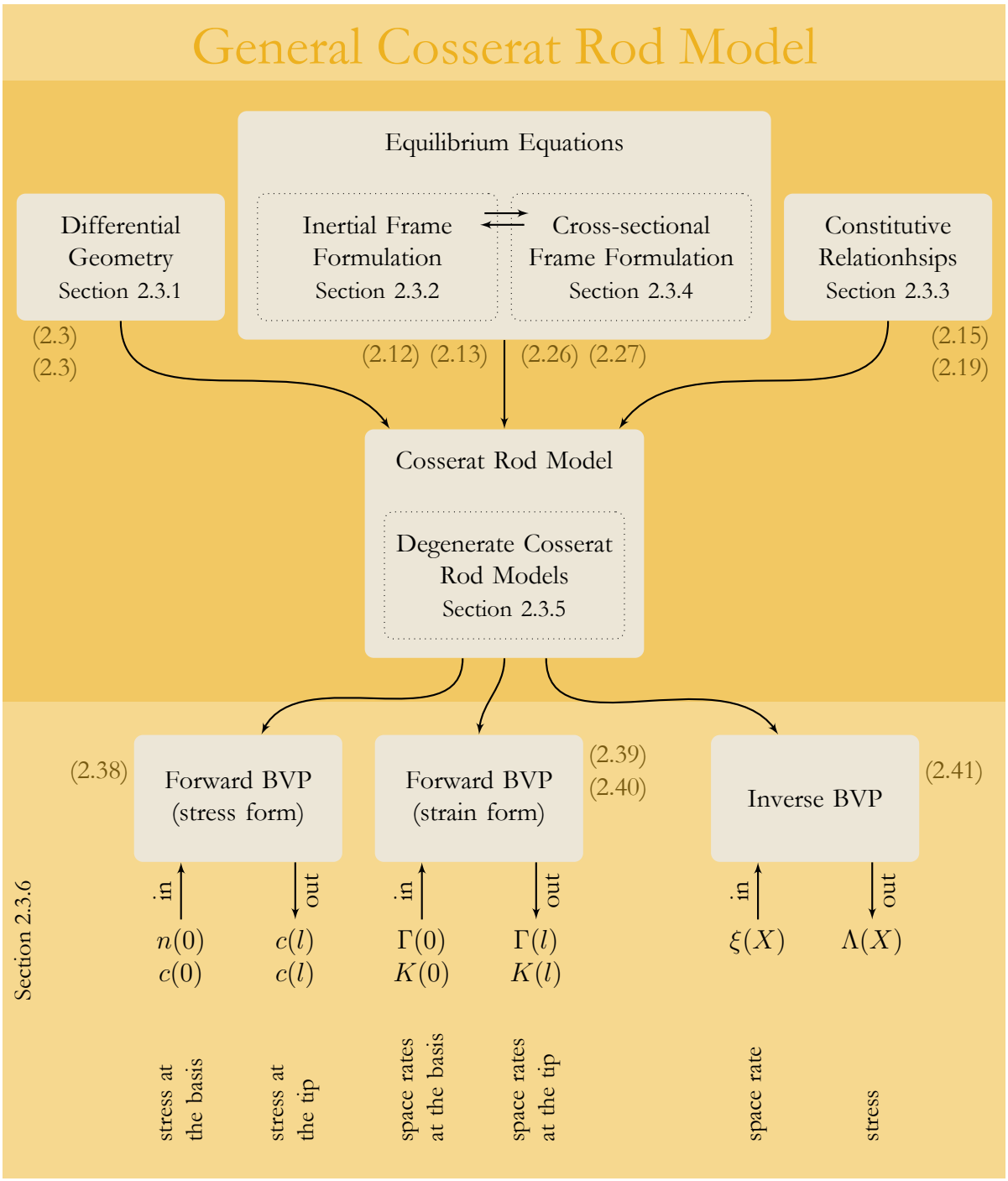

Figure 2.1: Synthesis of the ingredients constituting the Cosserat rod model and it various forms. The three main ingredients on the top row are assembled to formulate the Cosserat rod model, in the middle. The bottom rank schematizes the various forms of the boundary value problem (BVP) with their inputs and outputs. The corresponding section (Section 2.3.x) and equation ((2.xx)) numbers are provided.

one end of the rod to the other in a reference stress-less configuration. To each cross-section, a frame is attached whose origin coincides with the cross-section center of mass.

The position and orientation of rigid cross-sections are described, respectively, by an arc length parameterized curve in space $r : X \in [0, l] \mapsto r(X) \in \mathbb{R}^3$, and another in the Lie group of rotations $R : X \in [0, l] \mapsto R(X) \in \mathrm{SO}(3)$. $\mathrm{SO}(3)$ is the special orthogonal group in three dimensions,

$$\mathrm{SO}(3) = \{A \in \mathbb{R}_{3\times 3} | A^T A = I \text{ and } \det(A) = 1\}. \tag{2.1}$$

R and r are continuous functions along the arc-length parameter X thus, the rod is parameterized on an infinite-dimension configuration space.

Together, r and R define a field of homogeneous transformation that describes the entire rod

$$g : X \in [0, l] \mapsto g(X) = \begin{pmatrix} R(X) & r(X) \\ 0_{1\times 3} & 1 \end{pmatrix} \in \mathrm{SE}(3). \tag{2.2}$$

$\mathrm{SE}(3)$ is the special Euclidean group in three dimensions. The matrix $g(X)$ represents the position and orientation of the X-cross-section of the Cosserat rod or the pose of the $X-$'cross-sectional frame' in the inertial frame. The cross-sectional frame is also denoted $\mathcal{F}(X) = (r, b_X, b_Y, b_Z)(X)$ (see Figure 2.2).

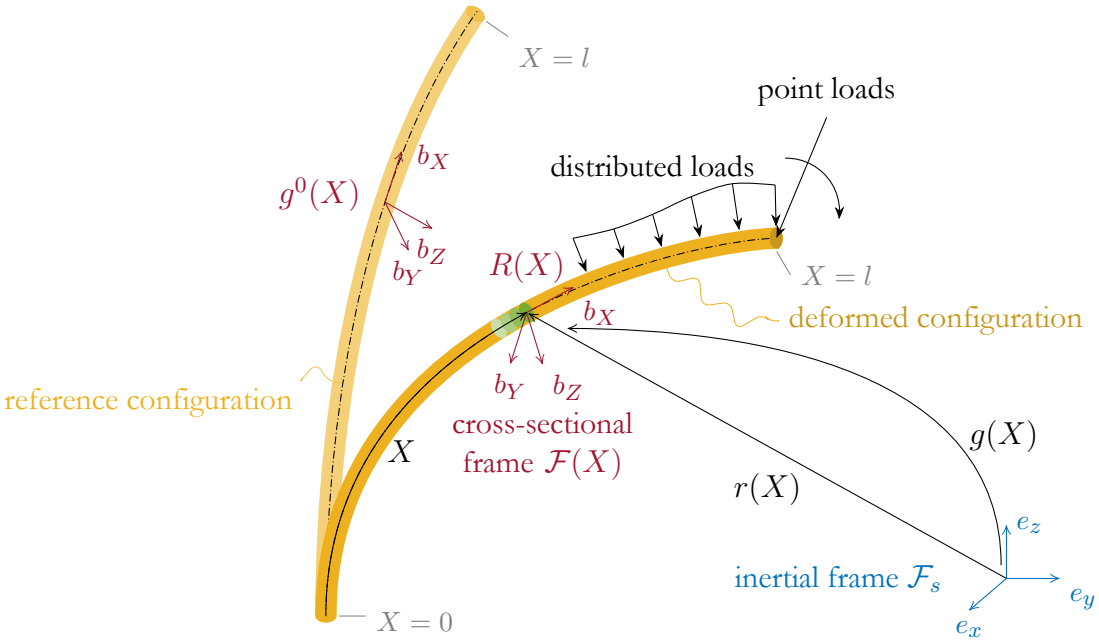

Figure 2.2: Definitions of the variables, frames, and transformations of a Cosserat rod. The light and dark yellow lines represent a rod from $X = 0$ to $X = l$ in its reference and deformed configurations respectively. All quantities related to the reference configuration are noted with a $\bullet^0$ superscript. The dash-dot lines represent the centerline of the rod along which the reference length parameter X evolves (solid line arrow). Some rod sections are represented (in green) to each of which a cross-sectional frame is attached (in red). The transformation $g(X) = (R, r)(X)$ shows the link between the inertial frame (in blue) and the cross-sectional frame.

The introduced terms 'cross-sectional frames' and 'inertial frame', will be used throughout this manuscript. The term 'cross-sectional frames' refers to the mobile frames attached to the cross-sections of a rod. Equivalent terms from the literature include 'body frame' (referring to rigid body-transformations) and 'material frame' (referring to the frame attached to the material of a continuous medium). Correspondingly, the reference frame is named the 'inertial frame' and is sometimes referred to as the 'fixed frame' or 'spatial frame'. The cross-sectional frames are oriented such that b_X is the unit normal vector to the cross-section, tangent to the curve of the rod $r(X)$and oriented towards increasing X (see Figure 2.2).

It is convenient for future developments to align b_Y and b_Z of each cross-sectional frame with the principal axes of the cross-sections to form an orthonormal basis. Other conventions are the Frenet-Serret convention [Bertails-Descoubes et al. 2018, Diezinger et al. 2022] or Bishop frames [Bishop 1975, Khadem et al. 2020]. Further, as this thesis primarily deals with manipulators, we assume the considered rods to be clamped with their proximal end coinciding with the inertial frame, i.e. $g(0) = 1_{4\times4}$.

A distinction is made between the reference or stress-less configuration of a rod noted with a $\bullet^0$ superscript, and the other possible configurations, without the subscript (see Figure 2.2).

The space-variations of position and orientation along the length of the rod are modeled by the linear and angular rates of change, respectively (see Figure 2.3). In the cross-sectional frame, these two rates are defined by the two fields Γ and K of $\mathbb{R}^3$ such that

$$r' = R\Gamma\,, \quad R' = R\widehat{K}\,, \tag{2.3}$$

where the $\bullet'$ symbol denotes differentiation[1] with respect to X, and the $\widehat{\bullet}$ symbol defines a bijective mapping from $\mathbb{R}^3$ to $so(3)$ as follows. If $W = (W_1, W_2, W_3)^T$ is a vector of $\mathbb{R}^3$, then $\widehat{W}$ denotes the skew-symmetric matrix of $\mathbb{R}^{3\times3}$ such that

$$\widehat{W} = \begin{pmatrix} 0 & -W_3 & W_2 \\ W_3 & 0 & -W_1 \\ -W_2 & W_1 & 0 \end{pmatrix}. \tag{2.4}$$

The reciprocal is denoted $\bullet^\vee$ such that $(\widehat{W})^\vee = W$. Similarly, if $W = (W_1, W_2, W_3)^T$ and $V = (V_1, V_2, V_3)^T$ are two vectors of $\mathbb{R}^3$, with $\omega = (W^T, V^T)^T$ a vector of $\mathbb{R}^6$, then $\widehat{\omega}$ denotes a bijective mapping from $\mathbb{R}^6$ to $se(3)$ defined by the matrix of $\mathbb{R}^{4\times4}$ as

$$\widehat{\omega} = \begin{pmatrix} \widehat{W} & V \\ 0_{1\times3} & 0 \end{pmatrix}, \tag{2.5}$$

where $\widehat{W}$ is the skew-symmetric matrix associated to $W \in \mathbb{R}^3$ [Murray 1994]. $so(3)$, respectively $se(3)$, are the Lie algebra of Lie groups $\mathrm{SO}(3)$ and $\mathrm{SE}(3)$. Interestingly, according to the definition in $\mathbb{R}^3$, one has the property

$$\widehat{W}V = W \times V\,. \tag{2.6}$$

[1] Special care is required when integrating the right expression of equation (2.3). Using a naïve discrete integration scheme

$$\begin{aligned} \frac{R(t+\Delta t) + R(t)}{\Delta t} &= R(t)\widehat{\Omega}(t) \\ R(t+\Delta t) &= R(t)\underbrace{[1_{3\times3} + \widehat{\Omega}(t)\Delta t]}_{>1}\,, \end{aligned}$$

one can see that the unity of the rotation matrix is not preserved [Rucker 2011]. One easy fix is to integrate over quaternions instead of rotation matrices but other solutions exist [Rucker 2018].

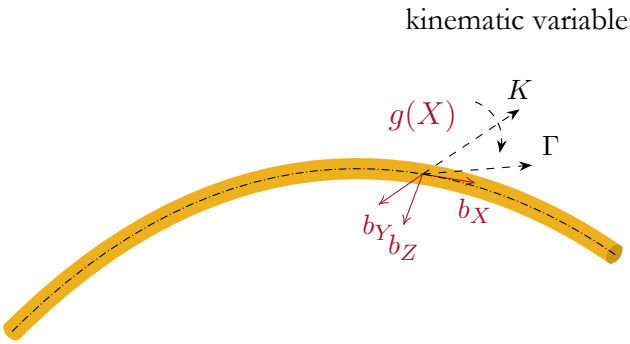

Figure 2.3: Differential geometry parameterization of the deformation of a Cosserat rod. The light and dark yellow lines represent a Cosserat rod. The dash-dot lines represent the centerline of the rod along which the reference length parameter X evolves (solid line arrow). The kinematic variables Γ and K define the space-variation of the cross-sectional frame.

Note that all vector fields in $\mathbb{R}^3$ can be expressed either in the inertial frame or in the cross-sectional frames, which can sometimes lead to confusion. To avoid ambiguity, this manuscript adopts the convention of Juan Carlos Simo: a vector of $\mathbb{R}^3$ is noted with a lowercase letter (preferably latin) when expressed in inertial frame, and uppercase, when expressed in cross-sectional frame. The only exception to this rule is the position vector field r, which is always expressed in the inertial frame, R being used for the orientation. Vector fields in $\mathbb{R}^6$ are not concerned by this rule, since they represent vectors in the Lie algebra $se(3)$, denoted with Greek letters as it is usually the case in geometric mechanics on $\mathrm{SE}(3)$ [Simo 1985, Marsden et al. 1999, Marsden and Ratiu 1999].

When combined, the fields of linear and angular space-rate Γ and K, define a unique field of twist ξ such that

$$g' = g\widehat{\xi} \tag{2.7}$$

is equivalent to the two relations of equation (2.3).

At this point, the configuration space of a rod clamped in a fixed basis can be defined in two possible ways, either directly through the knowledge of the pose field $g(X)\ \forall X \in [0,\ l]$, with $g(0) = 1_{4\times4}$,

$$\mathcal{C}(g) = \{g : X \in [0,\ l] \mapsto g(X) \in \mathrm{SE}(3)\}\ . \tag{2.8}$$

Alternatively, the configuration can be reconstructed when the field of stains $\xi(X)$ is given by integrating equation (2.7) from $X = 0$ to $X = l$, with $g(0) = 1_{4\times4}$,

$$\mathcal{C}(\xi, g(0)) = \left\{\xi : X \in [0,\ l] \mapsto \xi(X) \in \mathbb{R}^6\right\}\ . \tag{2.9}$$

In the second formulation, $\mathcal{C}$ is a (functional) linear space, since $\mathrm{SE}(3)$ in equation (2.8) is now replaced by the vector space $\mathbb{R}^6$. In other words, in equation (2.8), g exists in a non-commutative Lie group (i.e. a nonlinear manifold) where linear operations of interpolation or functional superimposition cannot directly be applied. Conversely, this alternate definition has the advantage to be linear with respect to the input ξ. The linearity enables to apply usual procedures of linear reduction as for example the Ritz reduction [Ritz 1909, MacDonald 1933]. Specifically, projecting the input of the configuration on a finite number of shape functions reduces the configuration from an infinite-dimensional space to a finite-dimensional one. The Lagrangian approach detailed in section 2.5.2 exploits this feature.

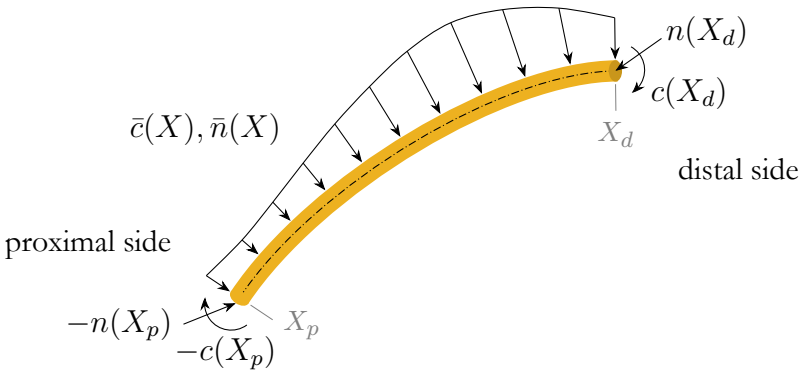

Figure 2.4: Free body diagram of a piece of rod. The yellow line represents an arbitrary finite piece of a rod from X_p to X_d. The dash-dot line represents the centerline of the rod along which the reference length parameter X evolves. The rod is at static equilibrium between the external forces $\bar{n}(X)$ and couples $\bar{c}(X)$, and its internal restoring forces $n(X)$ and couples $c(X)$.

2.3.2 Equilibrium Equations

At equilibrium, a rod as described in the previous section, is shaped by Newton's balance of forces between its internal forces $n(X)$ and couples $c(X)$, the effect of some external force $\bar{n}$ and couple $\bar{c}$ density fields defined over $]0, l[$, and some tip force n_+ and couple c_+. Let us consider an arbitrary section of a rod as pictured in Figure 2.4 to derive the equations expressing this equilibrium. Note that this manuscript adopts the conventions of continuum mechanics. When $n(X)$ and $c(X)$ are transmitted across the X-cross-section, if X is oriented positively from the proximal to the distal end of the rod, $n(X)$ and $c(X)$ are counted positively when exerted by the distal piece of rod (i.e. after arc-length X) onto the proximal piece (i.e. before arc-length X). This first convention is in contrast to the convention of rigid multi-body dynamics where the inter-body wrenches are counted positively when applied from the basis to the tip. In this derivation, all variables are expressed in the inertial frame.

The rod section between X_p and X_d, with $0 < X_p < X_d < l$, is subject to the following loads:

- at the distal side, the material of $(X_d, l]$ exerts a resultant contact force $n_{dist}(X_d)$ and a resultant contact couple $r(X_d) \times n_{dist}(X_d) + c_{dist}(X_d)$
- at the proximal side, the material of $[0, X_p)$ exerts a resultant contact force $-n_{prox}(X_p)$ and a resultant contact couple $-r(X_p) \times n_{prox}(X_p) - c_{prox}(X_p)$
- the resultant of all other forces is captured by $\displaystyle\int_{X_p}^{X_d} \bar{n}(X)\, dX$
- the resultant of all other couples is captured by $\displaystyle\int_{X_p}^{X_d} [r(X) \times \bar{n}(X) + \bar{c}(X)]\, dX$.

At equilibrium, the sum of all forces and the sum of all couples equal zero

$$n_{dist}(X_d) - n_{prox}(X_p) + \int_{X_p}^{X_d} \bar{n}(X)\, dX = 0_{3\times 1}\,, \tag{2.10}$$

$$c_{dist}(X_d) - c_{prox}(X_p) + r(X_d) \times n_{dist}(X_d) - r(X_p) \times n_{prox}(X_p) + \int_{X_p}^{X_d} [r(X) \times \bar{n}(X) + \bar{c}(X)]\, dX = 0_{3\times 1}\,. \tag{2.11}$$

Thanks to the continuity of the functions n and c, the subscripts $_{prox}$ and $_{dist}$ can be omitted [Antman 1995]. Differentiating equations (2.10) and (2.11) with respect to X yields the classical differential equations for a Cosserat rod defined over X$\in]0, l[$

$$n'(X) + \bar{n}(X) = 0_{3\times 1}\,, \tag{2.12}$$
$$c'(X) + r'(X) \times n(X) + \bar{c}(X) = 0_{3\times 1}\,. \tag{2.13}$$

Equation (2.13) is obtained by substituting equation (2.12) in equation (2.11) after differentiation.

Reminding that the rods considered in this thesis are assumed to be clamped at $X = 0$, these two sets of ODEs (equations (2.12) and (2.13)) need to be supplemented by the boundary conditions (BCs)

$$r(0) = 0_{3\times 1}\,, \quad R(0) = 1_{3\times 3}\,, \quad n(l) = n_+\,, \quad c(l) = c_+\,, \tag{2.14}$$

where n_+ and c_+ are the external tip force and couple respectively.

2.3.3 Constitutive Relationships

The relation that exists between deformation of an object and the internal forces and couples that this deformation generates is governed by constitutive relationships. More precisely, the kinematic variables, Γ and K, are related to material strain. Γ is related to shear (Γ_y and Γ_z) and extension (Γ_x), while K is related to bending (K_y and K_z) and torsion (K_x). Going yet one step further, the two strain fields of the rod, related to shear and extension, and bending and torsion, respectively, are defined, in the small strain regime, as $\Gamma - \Gamma^0$ and $K - K^0$. It is important to note that even small amounts of local strain can result in significant displacement when experienced over long spans.

Different possible linear or nonlinear constitutive relationships can be used to relate these strain fields to the internal forces and couples. In the scope of the present research and consistently with the small strain regime, continuum robots are used in the elastic range of their materials. In this case, a linear elastic relation holds:

$$n = R\mathcal{H}_{lin}\left(\Gamma - \Gamma^0\right)\,, \quad c = R\mathcal{H}_{ang}\left(K - K^0\right)\,, \tag{2.15}$$

where, $\forall X \in [0, l]$, $\mathcal{H}_{lin}(X)$ and $\mathcal{H}_{ang}(X)$ are the arc length parameterized stiffness matrices for shear and extension, and bending and torsion, respectively.

If the b_Y and b_Z of each cross-sectional frame are, in the reference configuration $g^0(X)$, aligned with the principal axis of the cross-sections, the stiffness matrices are defined as

$$\mathcal{H}_{lin}(X) = \begin{bmatrix} \mathcal{E}\mathcal{A}(X) & 0 & 0 \\ 0 & \mathcal{G}\mathcal{A}(X) & 0 \\ 0 & 0 & \mathcal{G}\mathcal{A}(X) \end{bmatrix} \tag{2.16}$$

and

$$\mathcal{H}_{ang}(X) = \begin{bmatrix} \mathcal{G}\mathcal{I}_X(X) & 0 & 0 \\ 0 & \mathcal{E}\mathcal{I}_Y(X) & 0 \\ 0 & 0 & \mathcal{E}\mathcal{I}_Z(X) \end{bmatrix}, \tag{2.17}$$

where $\mathcal{A}$ is the area of the cross section, $\mathcal{E}$ is Young's modulus, $\mathcal{G} = \mathcal{E}(1+\nu)/2$ is the shear modulus, $\mathcal{I}_Y$ and $\mathcal{I}_Z$ are, respectively, the second inertia moments along b_Y and b_Z, and $\mathcal{I}_X = \mathcal{I}_Y + \mathcal{I}_Z$ is the polar moment of inertia about b_X.

With such linear elastic relationships, the elastic energy U stored in the rod is given by

$$U = \int_0^l \frac{1}{2}(\Gamma - \Gamma^0)^T \mathcal{H}_{lin}(\Gamma - \Gamma^0) + \frac{1}{2}(K - K^0)^T \mathcal{H}_{ang}(K - K^0)\, dX \tag{2.18}$$

Similarly to the twist form of equation (2.7), equation (2.15) can be rewritten as

$$\Lambda = \mathcal{H}\epsilon = \mathcal{H}\left(\xi - \xi^0\right), \tag{2.19}$$

where $\epsilon = \xi - \xi^0 = \left(\left(K - K^0\right)^T, \left(\Gamma - \Gamma^0\right)^T\right)^T$ is the $\mathbb{R}^6$ field of strain, Λ is the $\mathbb{R}^6$ field of stress wrench, and $\mathcal{H} = \operatorname{diag}(\mathcal{H}_{ang}, \mathcal{H}_{lin})$ is the $\mathbb{R}^{6\times6}$ Hookean stiffness matrix. The corresponding expression for elastic energy is, concisely

$$U = \int_0^l \frac{1}{2}\epsilon^T \mathcal{H}\epsilon\, dX\,. \tag{2.20}$$

The elastic energy can further be used to solve rod problem by looking for the minimal energy configuration. This approach can be used to model CTCRs [Rucker et al. 2010a] or other types of continuum robots [Boyer et al. 2022b].

2.3.4 A Cross-Sectional Frame Formulation

While the above derivations hold in the inertial frame, a version of them that holds in the cross-sectional frame attached to the material can derived. Both formulations are equivalent but can be better suited to particular use cases. For example, in Newtonian approach the inertial frame formulation can be used to directly sum the efforts of different elements of a structure [Orekhov et al. 2017, Black et al. 2018] while Lagrangian approach mostly uses the more compact cross-sectional frame expressions because no interaction forces between system elements appear in the final model formulations [Boyer et al. 2021].

To derive the cross-sectional frame version of the equilibrium equations (2.12) and (2.13), all the vectors of the above formulation are shifted from the inertial frame to the mobile cross-sectional ones, using the notation conventions $r' = R\Gamma$, $n = RN$, $c = RC$, $\bar{n} = R\bar{N}$, and $\bar{c} = R\bar{C}$, as follows:

$$\begin{aligned} (RN)' + R\bar{N} &= 0_{3\times1}\,, \\ (RC)' + (R\Gamma)\times(RN) + R\bar{C} &= 0_{3\times1}\,. \end{aligned} \tag{2.21}$$

Then, via composition rules of derivatives along with the relation $R' = R\widehat{K}$

$$\begin{aligned} RN' + R\widehat{K}N + R\bar{N} &= 0_{3\times 1}\,, \\ RC' + R\widehat{K}C + (R\Gamma)\times(RN) + R\bar{C} &= 0_{3\times 1}\,. \end{aligned} \tag{2.22}$$

Owing to the definition of the hat operator (see equation (2.6))

$$\begin{aligned} R\left(N' + K\times N\right) + R\bar{N} &= 0_{3\times 1}\,, \\ R\left(C' + K\times C\right) + R\left(\Gamma\times N\right) + R\bar{C} &= 0_{3\times 1}\,, \end{aligned} \tag{2.23}$$

which, being true for any R, provides

$$\begin{aligned} N' + K\times N + \bar{N} &= 0_{3\times 1}\,, \\ C' + K\times C + \Gamma\times N + \bar{C} &= 0_{3\times 1}\,. \end{aligned} \tag{2.24}$$

Once supplemented with the BCs

$$\begin{aligned} r(0) = 0_{3\times 1}\,, \quad N(l) &= R(l)^T n_+\,, \\ R(0) = 1_{3\times 3}\,, \quad C(l) &= R(l)^T c_+\,, \end{aligned} \tag{2.25}$$

which are deduced from their inertial frame version of equation (2.14), equation (2.24) stands for the ODEs of a Cosserat rod in the cross-sectional frame.

Following the convention used in [Lynch and Park 2017], all pairs of angular and linear vectors gather in $\mathbb{R}^6$ vectors

$$\begin{pmatrix} C \\ N \end{pmatrix}' + \begin{pmatrix} K\times C + \Gamma\times N \\ K\times N \end{pmatrix} + \begin{pmatrix} \bar{C} \\ \bar{N} \end{pmatrix} = \begin{pmatrix} 0_{3\times 1} \\ 0_{3\times 1} \end{pmatrix}. \tag{2.26}$$

Let us introduce the notations $\bar{F} = \left(\bar{C}^T, \bar{N}^T\right)^T$ for the $\mathbb{R}^6$ field of external loads and $F_+ = \left(C_+^T, N_+^T\right)^T$, with $C_+ = R(l)^T c_+$ and $N_+ = R(l)^T n_+$ for the wrench of external tip loads. The $\mathbb{R}^6$ field of stress wrench can be detailed as $\Lambda = \left(C^T, N^T\right)^T$. These notations enable to rewrite the two ODEs of equation (2.26) in the more compact (geometric) form as a balance of wrenches expressed in the cross-sectional frame

$$\Lambda' - ad_\xi^T \Lambda + \bar{F} = 0_{6\times 1}\,, \tag{2.27}$$

where the adjoint map ad is a standard notation of geometric mechanics on the Lie group $\mathrm{SE}(3)$ defined as follows. For any field of twist

$$\omega = \begin{pmatrix} W \\ V \end{pmatrix} \tag{2.28}$$

ad_ω maps from $\mathbb{R}^6$ to $\mathbb{R}^{6\times 6}$ as the matrix

$$ad_\omega = \begin{pmatrix} \widehat{W} & 0_{3\times 3} \\ \widehat{V} & \widehat{W} \end{pmatrix}. \tag{2.29}$$

Throughout this dissertation, ad_ω will be used to take into account the contribution of derivative of the cross-sectional frame as it moves along a rod centerline with a twist ω when deriving a vector in the inertial frame.

Finally, the ODEs of equation (2.27) need to be complemented with the BCs

$$g(0) = 1_{4\times 4}\,, \quad \Lambda(l) = F_+\,. \tag{2.30}$$

2.3.5 Degenerate Cosserat Rod Models

In the above developments, all six fields of strain were assumed to be 'active'. In many circumstances, some of these internal DoF are negligible. In such circumstances, it may be interesting to remove the negligible strain fields to simplify the model and boost the computation speed at the implementation level. Removing undesirable internal DoF from the full internal kinematics is achieved by partitioning ξ as

$$\xi = B\xi_a + \bar{B}\xi_c \,, \tag{2.31}$$

where for any $n_a \leq 6$, ξ_a is the $n_a \times 1$ vector field of the strains allowed by the model and ξ_c is the $(6-n_a)\times 1$ vector field of restricted strains, while B and $\bar{B}$ are two complementary selection matrices of 1's and 0's such that $B^TB = 1_{n_a\times n_a}$, $B^T\bar{B} = 0_{n_a\times(6-n_a)}$ and $\bar{B}^T\bar{B} = 1_{(6-n_a)\times(6-n_a)}$. The subscript $\bullet_a$ stands for allowed and the subscript $\bullet_c$ stands for constrained.

It is easy to understand that the allowed strains are unknowns of the rod problem and are governed by the rod kinematics (equations (2.7) and (2.27)). Less straightforward is the comprehension of restricted strains. Choosing to restrict some fields means that, for these fields, the constitutive equations no longer hold in the model and the internal forces and couples are replaced by virtual internal forces and couples, in charge of imposing the internal constraints $\bar{B}^T\xi = \xi_c$.

To grasp a better understanding of this radical change, let us look at the counterpart of equation (2.31) on the stresses that writes

$$\Lambda = B\Lambda_a + \bar{B}\Lambda_c \,. \tag{2.32}$$

Here the fields of allowed stresses Λ_a is simply governed by the constitutive relationships (equation (2.19)) in their reduced form

$$\Lambda_a = \mathcal{H}_a\left(\xi_a - \xi_a^0\right) \,, \tag{2.33}$$

with $\mathcal{H}_a = B^T\mathcal{H}B$ the reduced matrix of Hooke coefficients and $\xi_a^0 = B^T\xi^0$ the value of ξ_a in the reference configuration. Contrarily, the fields of constrained stresses Λ_c no longer abide any constitutive relationships $\Lambda_c \neq \bar{B}^T\mathcal{H}\bar{B}\left(\xi_c - \xi_c^0\right)$ but rather equal any value that satisfies the corresponding equilibrium equations

$$\Lambda_c' - \bar{B}^T ad_\xi^T \Lambda_c + \bar{B}^T\bar{F} = 0_{(6-n_a)\times 1} \,. \tag{2.34}$$

From a Lagrangian point of view, Λ_c can be seen as a set of Lagrange multipliers that impose the internal constraints.

A popular choice of constrained fields is the case of Kirchhoff rods. In this theory, the shear and extension components are supposed to be negligible compared to the ones for bending and torsion [Kirchhoff 1859, O'Reilly 2017, Gazzola et al. 2018]. With this assumption, the selection matrices are

$$B = \begin{pmatrix} 1_{3\times 3} \\ 0_{3\times 3} \end{pmatrix} \,, \quad \bar{B} = \begin{pmatrix} 0_{3\times 3} \\ 1_{3\times 3} \end{pmatrix} \,, \tag{2.35}$$

and thus, for an initially straight rod, the fields of strain become

$$\xi_a = (K_X, K_Y, K_Z)^T \,, \quad \xi_c = (1,0,0)^T \,. \tag{2.36}$$

The popularity of this model simplification comes from the fact that continuum robots often have very stiff elastic properties for shear and extension, compared to bending and torsion. Multiple sources from the literature have shown to obtain satisfying results with Kirchhoff models [Dupont et al. 2010, Rucker et al. 2010a, Wu et al. 2022].

Apart from Kirchhoff rods, other examples of restrictions include a rod limited to in-plane bending (as in the model derived in chapter 4) or a rod with very high torsional stiffness as in [Azimian et al. 2014].

2.3.6 Reshaping the Cosserat Model as a BVP

Whether in the Newtonian approach or in the Lagrangian approach, the notion of BVP plays an essential role in the modeling of continuum robots. In short, a BVP is a system of ODEs whose solutions must satisfy BCs that partially determine the state variables at the boundaries. In the present context, such a system can be set in state space form

$$x' = f(x)\,, \quad h_-(x(0)) = 0\,, \quad h_+(x(l)) = 0\,, \tag{2.37}$$

where x is the vector of state variables, while the two functions $h_\pm$ of the state vector x, at $X = 0$ and l, fix the BCs at the two ends of the rod. Based on this definition, it is straightforward to show that inverting equation (2.15) to remove the space-rates from equation (2.3), gathering the resulting equations with equations (2.12) and (2.13) and the BCs equation (2.14) yields a closed formulation describing the statics of an elastic rod

$$\begin{pmatrix} r \\ R \\ n \\ c \end{pmatrix}' = \begin{pmatrix} R\left(\mathcal{H}_{lin}^{-1} R^T n + \Gamma^0\right) \\ R\left(\mathcal{H}_{ang}^{-1} R^T c + K^0\right)^\wedge \\ -\bar{n} \\ -r' \times n - \bar{c} \end{pmatrix}, \tag{2.38}$$

$$r(0) = 0_{3\times1}\,, \quad R(0) = 1_{3\times3}\,, \quad n(l) = n_+\,, \quad c(l) = c_+\,.$$

Equation (2.38) defines a BVP in the explicit state form as in equation (2.37), with $x = (r, R, c, n)$ being the state variables. Alternatively, using the constitutive relationships (equation (2.15)) to remove the internal forces and couples in equations (2.12) and (2.13), leads to the system

$$\begin{pmatrix} r \\ R \\ \Gamma \\ K \end{pmatrix}' = \begin{pmatrix} R\Gamma \\ R\widehat{K} \\ \Gamma^{0\prime} - \mathcal{H}_{lin}^{-1}\left[\left(\widehat{K}\mathcal{H}_{lin} + \mathcal{H}'_{lin}\right)\left(\Gamma - \Gamma^0\right) + R^T\bar{n}\right] \\ K^{0\prime} - \mathcal{H}_{ang}^{-1}\left[\left(\widehat{K}\mathcal{H}_{ang} + \mathcal{H}'_{ang}\right)\left(K - K^0\right) + \widehat{\Gamma}\mathcal{H}_{lin}\left(\Gamma - \Gamma^0\right) + R^T\bar{c}\right] \end{pmatrix},$$

$$\begin{aligned} r(0) &= 0_{3\times1}\,, \quad \Gamma(l) = \Gamma^0 + \mathcal{H}_{lin}^{-1} R(l)^T n_+\,, \\ R(0) &= 1_{3\times3}\,, \quad K(l) = K^0 + \mathcal{H}_{ang}^{-1} R(l)^T c_+\,, \end{aligned} \tag{2.39}$$

which is again in the form of equation (2.37), with $x = (r, R, \Gamma, K)$. Note that the closed formulations in equations (2.38) and (2.39) are equivalent and only differ by the choice of the state variables (stress or strain). For this reason, they are named, respectively, the stress-form and strain-form of the BVP. Alternative equivalent formulations of the same two forms can be obtained by changing the frames of expression (inertial or cross-sectional), or by gathering linear and angular components into poses, twists, and wrenches. For instance, the BVP equation (2.39) can be rewritten with (g, ξ) as state variables as

$$\begin{pmatrix} g \\ \xi \end{pmatrix}' = \begin{pmatrix} g\widehat{\xi} \\ \xi^{0\prime} + \mathcal{H}^{-1}\left(ad_\xi^T \mathcal{H}\left(\xi - \xi^0\right) - \bar{F} - \mathcal{H}'\left(\xi - \xi^0\right)\right) \end{pmatrix}, \tag{2.40}$$

$$g(0) = 1_{4\times4}\,, \quad \xi(l) = \xi^0 + \mathcal{H}^{-1} F_+\,.$$

The BVPs equations (2.38) to (2.40) are forward kineto-static BVPs, since they allow computing the motion variables, here the pose field g, from the knowledge of the force variables, here wrenches $\bar{F}$ and F_+. Reciprocally, one can define the inverse kineto-static BVP of a Cosserat rod as

$$\begin{pmatrix} g \\ \Lambda \end{pmatrix}' = \begin{pmatrix} g\widehat{\xi} \\ ad_{\xi}^{T}\Lambda - \bar{F} \end{pmatrix}, \qquad g(0) = 1_{4\times 4}\,, \quad \Lambda(l) = F_+\,, \tag{2.41}$$

which allows computing the stress Λ from the knowledge of the strain $\epsilon = \xi - \xi^0$. Note that in both cases, $(\bar{F}, F_+)$ are imposed (possibly g-dependent) external wrenches.

2.4 The Cosserat Rod Theory Applied to Continuum Robots

The single rod model described above is only a building block in continuum robot models. Usually, it needs to be extended or coupled to other models to account for the unique structural and actuation designs that continuum robots possess. This can lead to very sophisticated models, tailored to each specific case. The objective of this section is not to re-derive the full model for all types of robots. It is rather to provide insight by pointing to the particularities and assumptions of each case as keys to understand how to obtain the full robot model from the single rod case.

2.4.1 Modeling Tendon Actuated Continuum Robots

In a TACR model with m tendons, each tendon $i = 1\,..\,m$ is considered separately as a string but evolves alongside the backbone (see Figure 1.4 page 28). Their position r_i can thus directly be related to the backbone through the position of the routing holes in the cross-sectional frame $D_i(X)$ (assuming the routing holes have tight tolerances and the spacer disks are closely spaced):

$$r_i(X) = r(X) + R(X)D_i(X) \tag{2.42}$$

The backbone sees the efforts applied by the tendons as an added external force distribution or as added internal stresses, but in either case the final model of the robot is composed of only a single set of the Cosserat rod equations.

By neglecting friction, the tangent tension τ_i in the tendons is constant along their length. This is a key aspect of the TACR model derivation that allows writing the contribution of the tendons as function of only the tension.

Once the contribution of the tendons are integrated in the equations governing the backbone, the BVP of the backbone is solved like in the case of a single rod. This model was first derived through the Newtonian approach in [Rucker and Webster 2011b] and later, from a Lagrangian point of view, in [Renda et al. 2020, Boyer et al. 2021].

2.4.2 Modeling Concentric Tube Continuum Robots

Modeling CTCRs (see Figure 1.3 page 27) composed of m tubes will require one geometrical description $g_i(X) = (R_i, r_i)(X)$ and $K_i(X)$ for each tube $i = 1\,..\,m$ and corresponding constitutive relationships. As the tubes have one free end and only very little effort is exerted axially, the simplifying Kirchhoff rod assumption can be used (see section 2.3.5), thus, removing the need for individual shear and extension rates of change.

Let us first look at the geometric constraints. Because the tubes are arranged concentrically, their centerlines coincide with the centerline of the robot for every $X \in [0, l]$:

$$r_i(X) = r(X)\,, \quad \forall i = 1\,..\,m\,, \tag{2.43}$$

which drastically simplifies the derivation.

Regarding the rotation matrices however, only the b_X-axes coincide and the tubes can rotate relative to each other. Taking, arbitrarily, a first tube, $i = 1$, as reference, the angle of the other tubes $\theta_i(s)$ relative to this tube can be written such that:

$$R_i(X) = R_1(X)R_{X,\theta_i}(X)\,, \quad \forall i = 2\,..\,m\,, \tag{2.44}$$

where $R_{X,\theta_i}(X) = e^{\widehat{E_X\theta_i(X)}}$, with $E_X = (1,0,0)^T$, is a rotation about b_X. In this document, (E_X, E_Y, E_Z) will denote the canonical (numerical) base of $\mathbb{R}^3$, i.e. $E_X = (1,0,0)^T$, $E_Y = (0,1,0)^T$, and $E_Z = (0,0,1)^T$.

Using this relation, it is possible to further relate the angular rates of change $K_i(X)$. Finally, the equilibrium equations of the whole system need to be derived similarly to equations (2.12) and (2.13) but summing the internal forces and couples of all tubes. This model was derived simultaneously in [Dupont et al. 2010] and [Rucker et al. 2010a] in 2010. In 2021, The authors of [Renda et al. 2021] proposed a similar model derived through a Lagrangian point of view.

2.4.3 Modeling Parallel Continuum Robots

Modeling unconstrained parallel continuum robots

In the case of an (unconstrained) PCR (see Figure 1.5b page 29), the rods are completely independent and evolve according to their own set of governing equations. The rods are only linked at their basis through the holes of the baseplate and at their ends by what is called the endplate. The baseplate is clamped such that it defines the position and orientation of the rods at their intersection with it. The endplate needs to be at static equilibrium and thus additionally requires the sum of the forces and the sum of the couples applied by the rods and the backbone to equal zero.

The rods are integrated separately starting from initial conditions on one side of the robot, such that the constraints that link the rods as a system on the opposite boundary of the problem are satisfied.

These model equations are easier to derive from the single rod case but finding a solution to the problem requires more effort. The exact initial conditions for all rods need to be found such that all constraints are satisfied. This leads to problems with high dimension state vectors. An inverse kinematic approach solving the problem was published in [Bryson and Rucker 2014, Orekhov et al. 2016]. This approach was then further developed, enabling force sensing capabilities [Black 2017, Black et al. 2018].

Modeling constrained parallel continuum robots

Disks can be added to unconstrained PCRs limiting issues seen in section 1.3.2 (see Figure 1.5c page 29). These disks define routing holes for the individual rods called general intermediate constraints (GICs). 'Intermediate constraints' means they constrain the rods to pass through points between the baseplate and the endplate of the PCR. And 'general' means the defined routing paths can be any general curve in space. The disks that divide the robot in sections are fixed on an elastic

backbone. The backbone ensures the spacing between the disks but has a very low bending and torsional stiffness.

Adding GICs to the PCR model adds a lot of constraints to the problem. At each disk, the internal forces and couples of the entering and exiting rods contribute to the sum of forces and couples on the disks respectively and need to equal zero. As the rods are allowed to slide through the routing holes, this means they cannot transmit forces perpendicular to the disks. The same holds for couples around b_X (i.e. perpendicular to the disks). These efforts must thus not be added in the sums of efforts on the disks but transmitted to the next section of the corresponding rods to maintain the continuity (except for the backbone that is rigidly fixed to the disks). In the other directions (b_Y and b_Z) however, the internal forces and couples of the rods experience discontinuities as they pass the disks.

This complex problem can be solved with intricate BVPs as was proposed in [Orekhov et al. 2017]. While the authors report successful inverse kinematics computations, many unknowns need to be solved and this complexity makes the model less suited for real-time applications.

Modeling push-pull actuated continuum robots

Push-pull actuated robots (see Figure 1.5a page 29) can be seen as an even more constrained case of the constrained PCRs described in the previous section. They have mainly been explored by Simaan et al. [Xu and Simaan 2010].

Like PCR with GICs, push-pull robots consist of multiple rods. But, while the rods of PCRs could all run different paths, the rods of push-pull actuated robots run parallel and all follow the same path as the backbone with a constant offset. This is possible thanks to the reduced spacing of the routing disks and the constant position of the routing holes. A consequence of this design is that, unloaded, the bending will always occur in-plane. This is a fundamental consequence on which the whole model of this type of robots is based [Xu and Simaan 2006]. The drawback is that it does not allow modeling out-of-plane bending that could occur under external loads.

A notable result of the models of these robots is that, in this bending plane, the end effector angle λ_{end} depends only on the actuation and is independent of the shape of the robot. The robot presented in [Simaan et al. 2009] has three rods equally spaced around a backbone at a distance D of this backbone. The rods are of initial length l in the undeformed configuration. Each rod i can translate axially at its base by a quantity noted a_i which changes the length of the rod above the baseplate $(l - a_i)$ in the deformed configuration. The central backbone, however, remains of fixed length l even in the deformed configuration.

As the robot lies in a plane and that all rods are parallel to each other and to the backbone, the projection of each rod on this plane is a curve that is also parallel to the backbone. The offset of these projected curves with the backbone is noted Δ_i and relates the radius of curvature of the backbone $\mathfrak{r}(X)$ with the radius of curvature of the rods $\mathfrak{r}_i(X_i)$

$$\mathfrak{r}(X) = \mathfrak{r}_i(X_i) + \Delta_i \quad i = 1, 2, 3\,. \tag{2.45}$$

Using equation (2.45) yields the following result for the length l_i of the i^{th} rod above the baseplate

$$\begin{aligned} l - a_i &= \int dX_i = \int (dX_i - dX + dX) \\ l - a_i &= l + \int_0^{\lambda_{end}} (\mathfrak{r}_i(X) - \mathfrak{r}(X))\, d\lambda \\ l - a_i &= l - \Delta_i \lambda_{end}\,. \\ a_i &= \Delta_i \lambda_{end}\,. \end{aligned} \tag{2.46}$$

2.5 Formulating Cosserat Rod Models

Two main approaches exist for formulating the Cosserat rod models derived above, the Newtonian approach and the Lagrangian approach.

2.5.1 Newtonian Approach

In the Newtonian approach, a BVP is set up for each specific problem by isolating subsystems, using Newton's second law to balance the interaction forces between them. In some cases, algebraic manipulations are necessary to obtain a BVP in the explicit form. Solving the BVP then consists in finding the exact proximal BCs such that the distal BCs match. A residual is defined as the difference between the distal values of the state variables obtained for some guessed proximal BCs and the distal BCs imposed by the system. Most of the time, the task of finding the unknown proximal BCs is fulfilled with a shooting method [Press et al. 2007].

Obtaining the distal values of the state variables from the guessed initial conditions necessarily goes through an integration process of the ODEs of the BVP. This can be achieved by a variety of numerical methods but systematically requires the discretization of the spaces of the rods. Thus, the chosen numerical method or the discretization operation may have an impact on the calculated residual, but interestingly, it does not influence the state space of the problem. The drawback is that, through this spatial discretization, the robustness of the mechanical principles is lost. Indeed, while the balance of the intermediate ($X \in]0, l[$) interaction forces between the various elements of the considered system must be taken into account during the integration of the general BVP, such interactions are invisible at the distal BC at $X = l$ where the residual is defined.

Usually the more subsystems (rods) are involved in a robot architecture, the higher dimension the residual is. This is a beneficial correlation in the sense that no information is lost in the residual when system complexity increases. For systems involving many rods and/or links between the rods the high dimension residuals may however become an obstacle for numerical solvers.

2.5.2 Lagrangian Approach

In the Lagrangian approach, the starting point is always a basic mechanical principle (variational principle). In statics, the principle of virtual work holds. After having clearly defined the system, each contribution to the virtual work balance needs to be calculated.

Further, the problem goes through two successive reduction steps. In a first reduction step, the kinematics of the structure (or its constraints) define a minimal set of parameters or active strain fields to fully describe the problem. This can partially be achieved by referring to section 2.3.5.

Once the minimal set of active strain fields is defined, the second reduction step consists in projecting the continuous strain fields onto a finite set of shape functions, moving the considered problem from an infinite-dimensional space to a finite-dimensional one. The configuration of the system is now parameterized by a finite set of generalized coordinates.

In mechanics, the variational principles hold in any definition of the configuration space. Thus, applying the second reduction step to each contribution to the virtual work balance produces a static balance in the form of generalized force vectors Q. For a given input of generalized coordinates q, the static balance defines, through the generalized force vectors, a residual that has the same dimension as the input. The advantage is that the reduced form of the problem resembles that of classical rigid series manipulators [Walker and Orin 1982]. In a sense, generalized strain coordinates are analogous to joint coordinates, which is particularly useful for control purposes. In fact this is why the symbols q and Q are used for the generalized strain coordinates, and the corresponding generalized forces, respectively. This choice is inherited from the standards of Lagrangian mechanics [Goldstein et al. 2001]. In the context of continuum robotics, this choice reflects the fact that the strain coordinates of a continuum robot are the distributed counterpart of the localized joint coordinates of a rigid-link robot.

Another advantage of the Lagrangian approach is that it can be applied systematically to a wide variety of systems (closed loops, lumped joints etc.) without having to redefine the vector of residuals for each specific case. Defining residuals may be delicate as soon as one deviates from the single-stranded manipulators.

2.6 Conclusion

This chapter derived the kineto-static model of a Cosserat rod. It is the starting point of any continuum robot Cosserat rod model. While Cosserat rod models from the literature solved with the Newtonian or Lagrangian approaches can sometimes look completely different, they are, in fact, based on the same foundations presented here. This chapter continuously presented the correspondence between the notations making use of two $\mathbb{R}^3$ vectors popular in the Newtonian approach and the geometrical mechanics notations with $\mathbb{R}^6$ vectors, present in the literature on the Lagrangian approach (see appendix A for a side-by-side comparison of notation conventions).

More importantly, this chapter presented the two equivalent formulations of the configuration of a Cosserat rod in the chosen framework. While the formulation of equation (2.8) is used in the Newtonian approach that continuously integrates it, the linear formulation of equation (2.9) is used in the Lagrangian approach to enable a projection on a functional basis. Several BVP formulations are presented. Although these formulations are equivalent, they enable using considerably different algorithms that are useful in either the Newtonian or Lagrangian approaches.

The strategies for adequately manipulating and arranging the Cosserat rod theory for modeling standard continuum robots were exposed. At this point, one can observe that CAARs have points in common with almost all the continuum robots that were discussed. The expression for the routing paths of the tendons in a TACR resemble the relative position of the neutral lines of the tubes with respect to the center of the tubes. Also, the tubes are arranged concentrically as in CTCRs. In CAARs however, the sliding motion of the tubes forbid directly reusing the relations from these two models. Further, as discussed in section 2.4.3, the offset neutral lines of CAARs should be considered as separate rods but the GIC model for PCRs is inapplicable due to the continuity of the CAAR structure. Lastly, the result of equation (2.46), the foundation of the

models for push-pull actuated continuum robots does not hold for CAARs because the neutral lines are not constrained to run parallel to the centerline.

Hence, a whole new model for CAARs must be reinvented. This is a task that needs an in depth comprehension of the available modeling approaches. To grasp this deeper understanding of Cosserat rod modeling of continuum robots, the next chapter presents a side by side derivation of the Cosserat rod model for TACRs with both the Newtonian and Lagrangian approaches. It will allow to comfortably settle in with both approaches, giving the necessary keys for diving into the derivation of the CAAR model in chapter 4.

Contributions of this chapter

1. Cosserat rod modeling for continuum robots is put in perspective with the other state-of-the-art modeling approaches for continuum robots.
2. The various elements necessary for the implementation of both the Lagrangian and Newtonian approaches are, for the first time, derived in a common mathematical framework.
3. Many different aspects of Cosserat rod modeling required for modeling different types of continuum robots (see chapters 3 and 4) are brought together in a single structured picture, including the discussion of the Newtonian and Lagrangian formulations, the two main approaches in the community.
4. An analysis of Cosserat rod models of the literature, explaining how one can use such models for various types of continuum robots, is carried out.

The framework presented in this chapter has benefited from the input of Frédéric Boyer and Vincent Lebastard form the LS2N laboratory in Nantes, France. They helped in the quest of unwinding the Cosserat rod theory, especially regarding the Lagrangian mechanics viewpoint.

3

Modeling Tendon Actuated Continuum Robots from Different Perspectives: A Case Study

3.1 Foreword

The purpose of this chapter is to analyze the Newtonian and the Lagrangian approaches, applied to an example use-case, in order to clarify the similarities and differences between them and objectively compare the strengths and weaknesses of each.

While the modeling approaches developed in this chapter have been previously published, the effort of side-by-side derivation of the two approaches is a necessary step to grasp all the subtleties that link or separate them. It is this profound understanding that enabled the derivation of the new model for CAARs, presented in the next chapter.

The two approaches, coming from different communities, do not share a common set of notations or mathematical framework, which does not ease the comparison (see appendix A). This chapter provides an exhaustive derivation of both approaches using the mathematical framework proposed in chapter 2. While the two approaches were previously published, the present derivations provide new contributions to both. Further, a mathematical proof of equivalence between the two approaches is provided backed by an extensive set of simulations that allows the discussion of the approach performances.

While the contents have been revised for inclusion in this manuscript, a major part of this chapter was published in the following peer-reviewed journal article:

> Matthias Tummers, Vincent Lebastard, Frédéric Boyer, Jocelyne Troccaz, Benoît Rosa, and M. Taha Chikhaoui (Jun. 2023). "Cosserat Rod Modeling of Continuum Robots from Newtonian and Lagrangian Perspectives". In: *IEEE Transactions on Robotics*, 39.3, pp. 2360–2378, `https://hal.science/hal-03935561`.

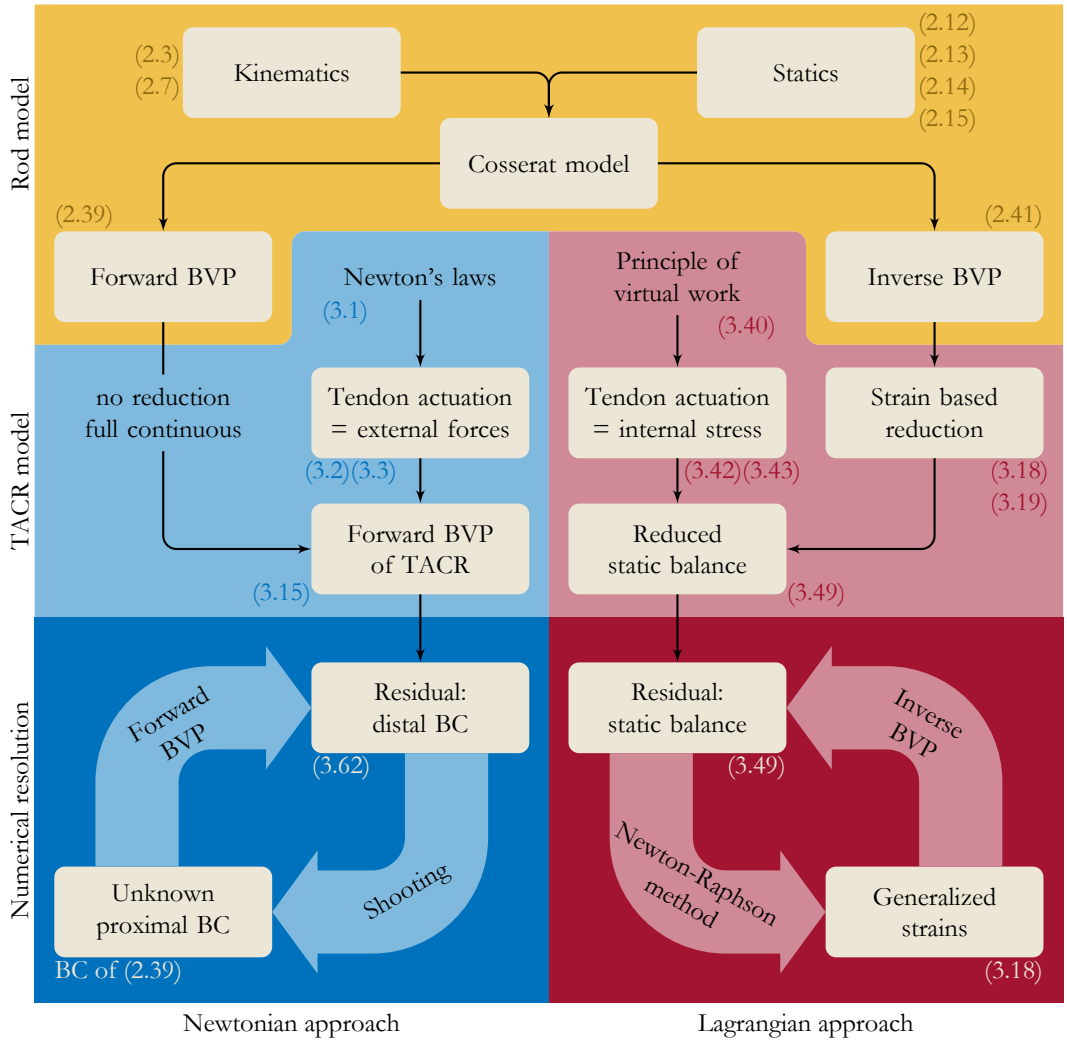

Figure 3.1: Synthesis of the steps in both approaches side by side. The corresponding steps meet horizontally across the columns. The blue and red areas are relative to the Newtonian and the Lagrangian approaches, respectively. The yellow area is common to both (see chapter 2). The corresponding equation numbers are provided for each step.

3.2 Common Considerations

The main steps of each of the approaches presented in sections 3.3 and 3.4 are synthesized in Figure 3.1 to help follow through the developments and highlight the correspondence of the steps between approaches.

Both approaches assume the same set of model simplifications. The tendons are inextensible, have negligible inertia, experience no friction, and are routed through continuous routing paths rather than through discrete disks. These are all reasonable assumptions for small curvatures and a large amount of routing disks, but may introduce significant discrepancies when this is not the case. Also, in addition to the assumption of material linear elasticity (see equation (2.15)), the considered robots have constant material properties along their length (i.e. $\mathcal{H}' = 0_{6\times6}$).

3.3 Newtonian Model of TACRs

In the Newtonian approach, the model is deduced from Newton's laws, i.e. by isolating the backbone and each of the tendons separately, and by using the action-reaction principle to remove the interaction forces between them. To detail this process, let us first remark that, in a TACR, the backbone of the robot can be modeled by the BVP of equation (2.39). Sections 3.3.1 and 3.3.2 describe how this BVP is complemented with a model of tendon actuation.

3.3.1 Model of Tendon Actuation

To introduce the model of tendon actuation in equation (2.39), the distributed loads are spelled out as

$$\bar{n} = \bar{n}_{ext} + \bar{n}_{act}\,, \quad \bar{c} = \bar{c}_{ext} + \bar{c}_{act}\,, \tag{3.1}$$

where $\bar{n}_{ext}$ and $\bar{c}_{ext}$ model the external loads applied by the environment such as gravity or contacts, while $\bar{n}_{act}$ and $\bar{c}_{act}$ stand for those applied by the tendons. Invoking the action-reaction principle, the distributed force exerted by each tendon i onto the backbone is equal to the opposite of the distributed force exerted by the backbone on this tendon, noted $\bar{n}_i$. Therefore, summing these contributions provides the distributed force of the m tendons on the backbone

$$\bar{n}_{act} = \sum_{i=1}^{m} -\bar{n}_i\,. \tag{3.2}$$

As a tendon cannot transmit any couples, the distributed moment of the tendons exerted on the backbone $\bar{c}_{act}$ is equal to only the sum of the cross products of each moment arm with each force

$$\bar{c}_{act} = \sum_{i=1}^{m} (r_i - r) \times (-\bar{n}_i) = -\sum_{i=1}^{m} d_i \times \bar{n}_i\,, \tag{3.3}$$

where $r_i = r + RD_i$ is the position of the i-th tendon expressed in the inertial frame, $D_i(X) = (0, D_{i,Y}, D_{i,Z})^T(X)$ the position of the i-th tendon expressed in the X-cross-sectional frame, and $d_i = RD_i$ (see Figure 3.2).

Modeling a tendon as an inextensible degenerate Cosserat rod, with no angular inertia, one can derive the expression for $\bar{n}_i$, by applying the linear static balance equations (2.12) and (2.13) with its internal forces n_i, to each tendon individually

$$\bar{n}_i + n_i' = 0_{3\times 1}\,. \tag{3.4}$$

Again, as a perfectly flexible string cannot support internal couples or shear forces but only a constant tension τ_i tangent to its path, the field of internal forces along each tendon i reads

$$n_i = \tau_i t_i\,, \tag{3.5}$$

with $t_i = r_i'/\|r_i'\|$ the unit tangent vector to the path of the tendon. Now, considering that the tension is constant ($\tau_i' = 0_{3\times 1}$), equation (3.4) provides the expression of the external forces of each tendon

$$\bar{n}_i = -n_i' = -\tau_i t_i'\,. \tag{3.6}$$

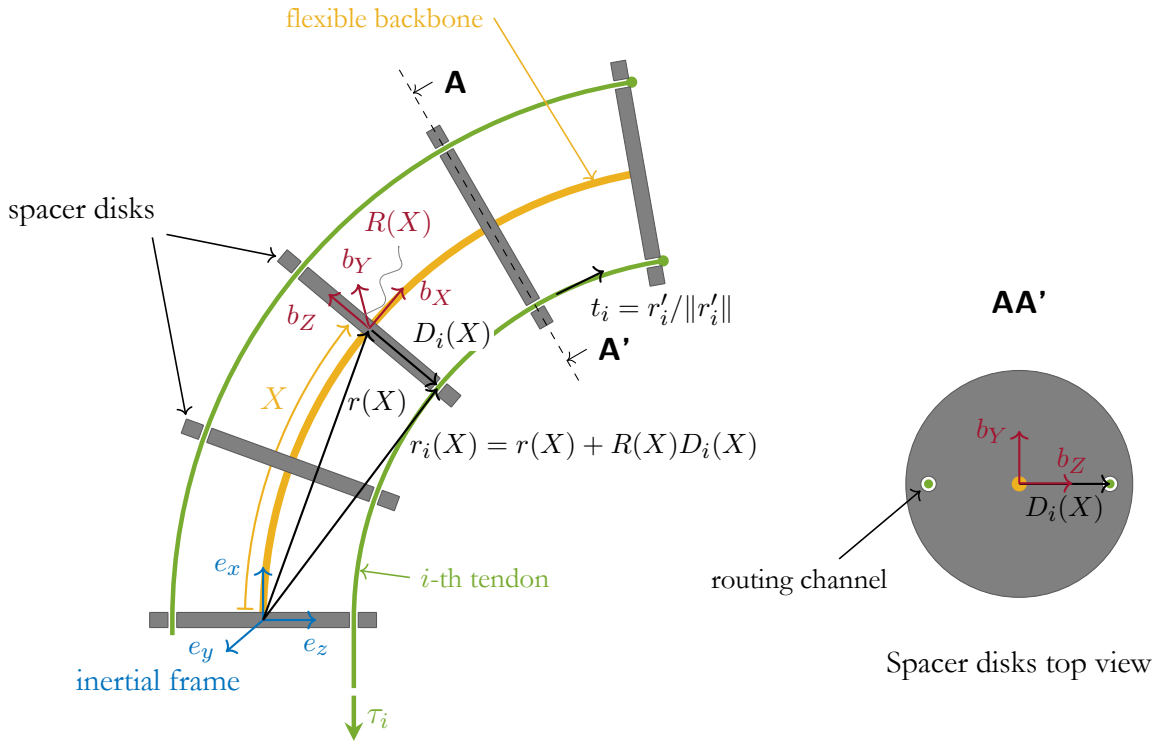

Figure 3.2: Side view of a TACR and top view of a spacer disk. The manipulator is embedded in the inertial frame at its base. The routing channels in the spacer disks (grey) define the routings of the tendons (green) around the backbone (yellow). The position of each tendon r_i is related to the position of the backbone r through the offset D_i in the cross-sectional frame. For any cross-section defined by a given arc length along the backbone X the slope of the routing of the i-th tendon at this cross-section is given by $t_i = r_i'/\|r_i'\|$. By applying a tension τ_i to a tendon, the manipulator deforms.

3.3.2 Forward Kineto-Static BVP of a TACR

Substituting equations (3.1) to (3.3) and (3.6) into equation (2.38), provides the static balance of a TACR actuated by a set of m tendons in stress-form

$$\begin{pmatrix} r \\ R \\ n \\ c \end{pmatrix}' = \begin{pmatrix} R\left(\mathcal{H}_{lin}^{-1} R^T n + \Gamma^0\right) \\ R\left(\mathcal{H}_{ang}^{-1} R^T c + K^0\right)^\wedge \\ -\sum_{i=1}^{m} \tau_i t_i' - \bar{n}_{ext} \\ -r' \times n - \sum_{i=1}^{m} d_i \times (\tau_i t_i') - \bar{c}_{ext} \end{pmatrix}, \tag{3.7}$$
$$(r, R)(0) = (0_{3\times1}, 1_{3\times3}), \quad (n, c)(l) = (n_+, c_+).$$

To get a BVP in the usual form of equation (2.37), the forces exerted by the tendons $\bar{n}_i = -\tau_i t_i'$ need to be expressed in terms of the state-variables $x = (r, R, n, c)$. To achieve this elimination, it is convenient to shift from the stress-form of equation (2.38) to the strain-form of equation (2.39). This requires first to express the internal elastic and external tendon forces and couples in terms of the backbone strains. While it was shown in section 2.3.6 that one can use the constitutive law to rewrite the internal elastic forces and couples, rewriting the external tendon forces and couples requires a few algebraic manipulations.

Following the methodology presented in [Rucker 2011], rearranging and subsequently deriving equation (3.5) provides the two relations

$$r_i' = \frac{1}{\tau_i} \|r_i'\| n_i, \quad r_i'' = \frac{1}{\tau_i} \left(\left(\|r_i'\|\right)' n_i + \|r_i'\| n_i' \right). \tag{3.8}$$

Taking the cross product of these two results one finds

$$r_i'' \times r_i' = \frac{\|r_i'\|^2}{\tau_i^2} (n_i' \times n_i) \tag{3.9}$$

and taking once more the cross product of r_i' and equation (3.9)

$$r_i' \times (r_i'' \times r_i') = \frac{\|r_i'\|^3}{\tau_i^3} (n_i \times (n_i' \times n_i)). \tag{3.10}$$

Considering the vector triple product identity $a \times (b \times c) = b\,(ac) - c\,(ab)$ and writing the cross products in skew-symmetric matrix notation (equation (2.6)) yields

$$\bar{n}_i = -\tau_i t_i' = -\tau_i \left(\frac{r_i'}{\|r_i'\|} \right)' = \tau_i \frac{\widehat{r_i'}^2}{\|r_i'\|^3} r_i''. \tag{3.11}$$

Next, one needs to expand the first and second derivatives of r_i. Expressing these quantities in cross-sectional frame coordinates allows a more concise writing, as follows:

$$\begin{aligned} r_i' &= R\Gamma_i = R\left(\widehat{K} D_i + D_i' + \Gamma\right), \\ r_i'' &= R\left(\Gamma_i' + \widehat{K}\Gamma_i\right), \end{aligned} \tag{3.12}$$

where $\Gamma_i = R^T r_i'$. Now, introducing equation (3.12) in equation (3.11) and the result in equations (3.2), (3.3), and (3.6) yields

$$\begin{aligned} \bar{n}_{act} &= R\left(a + A\Gamma' + GK'\right) , \\ \bar{c}_{act} &= R\left(b + B\Gamma' + HK'\right) , \end{aligned} \tag{3.13}$$

where

$$\begin{aligned} A_i &= -\tau_i \frac{\widehat{\Gamma}_i^{\,2}}{\|\Gamma_i\|^3} , & A &= \sum_{i=1}^{m} A_i , \\ B_i &= \widehat{D}_i A_i , & B &= \sum_{i=1}^{m} B_i , \\ G &= -\sum_{i=1}^{m} A_i \widehat{D}_i = B^T , & H &= -\sum_{i=1}^{m} B_i \widehat{D}_i , \\ a_i &= A_i \left(\widehat{K}\Gamma_i + \widehat{K} D_i' + D_i''\right) , & a &= \sum_{i=1}^{m} a_i , \\ b_i &= \widehat{D}_i a_i , & b &= \sum_{i=1}^{m} b_i . \end{aligned} \tag{3.14}$$

Finally, substituting equation (3.13) into equation (2.39) and rearranging the obtained expressions, yields the ODEs governing the statics of a TACR in the explicit strain-form

$$\begin{pmatrix} r \\ R \\ \Gamma \\ K \end{pmatrix}' = \begin{pmatrix} R\Gamma \\ R\widehat{K} \\ \begin{pmatrix} \mathcal{H}_{lin} + A & G \\ B & \mathcal{H}_{ang} + H \end{pmatrix}^{-1} \begin{pmatrix} c \\ d \end{pmatrix} \end{pmatrix} , \tag{3.15}$$

with

$$\begin{aligned} c &= \mathcal{H}_{lin}\Gamma^{0\prime} - \widehat{K}\mathcal{H}_{lin}\left(\Gamma - \Gamma^0\right) - R^T \bar{n}_{ext} - a , \\ d &= \mathcal{H}_{ang}K^{0\prime} - \widehat{K}\mathcal{H}_{ang}\left(K - K^0\right) - \widehat{\Gamma}\mathcal{H}_{lin}\left(\Gamma - \Gamma^0\right) - R^T \bar{c}_{ext} - b . \end{aligned} \tag{3.16}$$

Note that all the quantities A, B, G, H, a, and b depend on $\Gamma_i = R^T r_i' = \Gamma + K \times D_i + D_i'$.

This set of ODEs needs to be supplemented with the BCs of equation (2.39), where the values of n^+ and c^+ are the forces and moments generated by the attachment of each tendon at the boundary. These are equal to the opposite of the internal force of each tendon and the cross product of each moment arm with this force, respectively, yielding

$$\begin{aligned} n_+ &= \sum_{i=1}^{m} -n_i(l) = -\sum_{i=1}^{m} \tau_i t_i , \\ c_+ &= \sum_{i=1}^{m} d_i \times \left(-n_i(l)\right) = -\sum_{i=1}^{m} d_i \times \tau_i t_i . \end{aligned} \tag{3.17}$$

Finally, with these detailed BCs, equation (3.15) defines the same BVP as obtained in [Rucker and Webster 2011b]. This BVP is the forward kineto-static BVP of a TACR, "forward" because its resolution provides outputs in motion (here strains), from inputs in force (here tendon tensions).

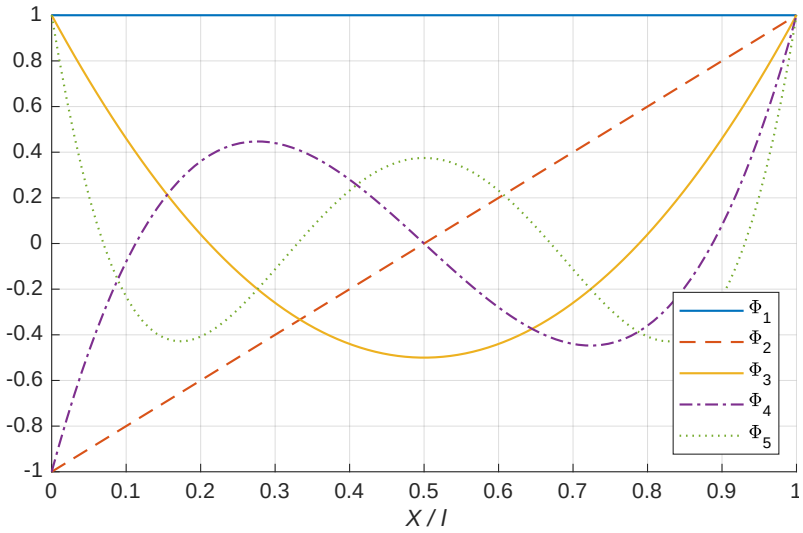

Figure 3.3: Example of a set of shape functions Φ for decomposing the strain field ϵ. Here, the first five Legendre Polynomials are shown.

3.4 Lagrangian Model of TACRs

In this section, the Lagrangian model of a TACR is derived from the principle of virtual work, starting from zero, i.e. calculating individually each contribution to the virtual work balance. In other words, to improve the intelligibility of the approach, TACR modeling is brought back to the canonical Lagrangian methodology. Note that this choice contrasts with recent publications on the topic, where the Lagrangian model is obtained either by projection of Cosserat partial differential equations (PDEs) with Jacobian matrices [Renda et al. 2020, Renda et al. 2021], or by feeding a continuous Newton-Euler inverse algorithm with specific inputs [Boyer et al. 2021].

Adopting this canonical viewpoint, Lagrangian modeling is achieved in two steps. In a first (kinematic) step (section 3.4.1), the Lagrangian approach consists of a reduction of the infinite-dimensional configuration space from section 2.3.1 into a finite-dimensional configuration space. In a second step (sections 3.4.2 and 3.4.3), this kinematic reduction is introduced in the principle of virtual work. As this principle holds in any definition of the configuration space, it allows shifting the static balance of section 2.3.2, from the infinite-dimensional configuration space equation (2.9), to the finite-dimensional configuration space. This two-step process finally produces the reduced kineto-static model of a TACR.

3.4.1 Strain Based Reduction

The purpose of the reduction is to shift the previously introduced continuous model to a finite-dimensional model in terms of a vector of generalized strain coordinates q, similar to the joint coordinates of a rigid manipulator [Spinelli and Katzschmann 2022]. According to the Ritz approach [Ritz 1909, MacDonald 1933], the strain field $\epsilon = \xi - \xi^0$ is decomposed on a functional basis of strain functions as

$$\epsilon = \Phi(X)q\,, \tag{3.18}$$

where q is a $\mathbb{R}^k$ vector of generalized strain coordinates and Φ is a $\mathbb{R}^{6\times k}$ matrix of shape functions whose choice is fixed by the user. A popular choice of shape functions are Legendre polynomials

(see Figure 3.3). As a result, any configuration of the rod can be reconstructed in the inertial frame by integrating the ODE

$$g' = g\left(\Phi q + \xi^0\right)^\wedge \tag{3.19}$$

from $X = 0$ where $g(0) = 1_{4\times4}$, to $X = l$. The purpose of the next two sections is to derive the static balance of a TACR in terms of the vector of generalized strain coordinates q of its backbone, i.e. on the finite-dimensional configuration (vector) space $\mathbb{R}^k$. Some necessary preliminary developments are detailed in section 3.4.2. In section 3.4.3, it is shown that the reduced model takes the usual matrix form of Lagrangian mechanics.

3.4.2 Principle of Virtual Work and Variations

Principle of virtual work

The variational principle of Lagrangian mechanics that holds in statics is the principle of virtual work. It considers the system in its static equilibrium where the external loads balance the internal restoring forces (stress)

$$\delta W_{ext} + \delta W_{int} = 0\,, \tag{3.20}$$

where δW_{ext} and δW_{int} stand, respectively, for the work of external and internal forces along any virtual displacement (or variation) of the configuration, compatible with the geometric BCs and the parameterization used to describe the system.

Variations on the system

In the case of TACRs, the system considered is the backbone and the part of the tendons contained inside the robot. Since the tendons have negligible inertia and elasticity, only the backbone needs to be considered in the configuration of the system. Thus, any field of kinematically compatible virtual displacement along the robot can be defined by a small perturbation of g noted δg, with $\delta g(0) = 0_{4\times4}$. As for equation (2.7), this field of transformation perturbations is entirely described by a field of twist noted $\delta\zeta$ and defined by

$$\delta g = g\delta\widehat{\zeta}\,,\ \text{with: } \delta\zeta(0) = 0_{6\times1}\,. \tag{3.21}$$

The condition at $X = 0$ is imposed by the compatibility of variations δg with the geometric BC $g(0) = 1_{4\times4}$. When applied to the backbone, such virtual displacements generate variations of its strain field $\delta\epsilon = \delta(\xi - \xi^0) = \delta\xi$.

Relation between $\delta\xi$ and $\delta\zeta$

These relative variations $\delta\xi$ are related to the absolute ones $\delta\zeta$ as follows. Since variations δ do not affect the label (i.e. arc-length parameter) X, the variation and X-derivation are exchangeable, i.e.

$$\delta(g') = (\delta g)'\,. \tag{3.22}$$

Introducing in equation (3.22) the definitions $g' = g\widehat{\xi}$ and $\delta g = g\delta\widehat{\zeta}$ of equations (2.7) and (3.21), respectively, yields

$$\delta\left(g\widehat{\xi}\right) = \left(g\delta\widehat{\zeta}\right)' \Leftrightarrow \delta g\widehat{\xi} + g\delta\widehat{\xi} = g'\delta\widehat{\zeta} + g\left(\delta\widehat{\zeta}\right)'\,. \tag{3.23}$$

Using the same definitions, once more, leads to

$$g\left(\delta\widehat{\zeta}\,\widehat{\xi}+\delta\widehat{\xi}\right)=g\left(\widehat{\xi}\delta\widehat{\zeta}+\left(\delta\widehat{\zeta}\right)'\right)\,, \tag{3.24}$$

which, holding for any g, yields

$$\delta\widehat{\xi}=\left(\delta\widehat{\zeta}\right)'+\widehat{\xi}\delta\widehat{\zeta}-\delta\widehat{\zeta}\,\widehat{\xi}=\left(\delta\widehat{\zeta}\right)'+[\widehat{\xi},\delta\widehat{\zeta}]\,, \tag{3.25}$$

where $[\bullet,\bullet]$ denotes the usual commutator of matrices. Finally, using the anti-hat ($\bullet^\vee$) operation, one can show that $[\widehat{\xi},\delta\widehat{\zeta}]^\vee=ad_\xi\delta\zeta$ which provides the commutation relation

$$\delta\zeta'=\delta\xi-ad_\xi\delta\zeta \tag{3.26}$$

that relates the relative variations $\delta\xi$ to the absolute variations $\delta\zeta$.

Second version of the relation between $\delta\xi$ and $\delta\zeta$

For subsequent developments, it is useful to rewrite equation (3.26) in an alternate form with another standard notation of geometric mechanics, namely the adjoint map Ad. In general, Ad_g is used to pass a twist from one frame to another, the two being separated by a pose g. For any homogeneous transformation g,

$$g=\begin{pmatrix}R & r\\ 0_{1\times3} & 1\end{pmatrix}, \tag{3.27}$$

Ad_g maps from $\mathrm{SE}(3)$ to $\mathbb{R}^{6\times6}$ as the matrix

$$Ad_g=\begin{pmatrix}R & 0_{3\times3}\\ \widehat{r}R & R\end{pmatrix}. \tag{3.28}$$

Now injecting $ad_\xi=Ad_g^{-1}Ad_g'$ in the equation (3.26), the alternate form of the commutation relation reads

$$Ad_g\delta\zeta'+Ad_g'\delta\zeta=Ad_g'\delta\xi\,. \tag{3.29}$$

Relation between $\delta\epsilon$ and δq

The expression of the strain variations $\delta\epsilon$ in terms of variations on the generalized coordinates δq is obtained by applying the variation to equation (3.18)

$$\delta\xi=\delta\epsilon=\Phi\delta q\,. \tag{3.30}$$

Relation between $\delta\zeta$ and δq

Finally, using equation (3.30), the expression of any virtual displacements $\delta\zeta$ in terms of variations on the generalized coordinates δq arises from the integration of equation (3.29) over $[0,\,X]$ with the initial condition $\delta\zeta(0)=0_{6\times6}$ (consequence of $g(0)=1_{4\times4}$)

$$\delta\zeta(X)=Ad_{g(X)}^{-1}\int_0^X Ad_{g(Y)}\delta\xi(Y)\,dY=\left[Ad_{g(X)}^{-1}\int_0^X Ad_{g(Y)}\Phi\,dY\right]\delta q=J_\zeta(X)\delta q\,, \tag{3.31}$$

where $J_\zeta(X)$ defines the Jacobian matrix, which maps any variation δq to $\delta\zeta(X)$. In other words, equation (3.31) is the expression of any virtual displacement $\delta\zeta$ that is compatible with the internal kinematics and the geometric BCs.

Variation of the length of the tendons

Similarly to the strain variations $\delta\epsilon$ that act on the backbone, the tendons experience variations on their length δl_i. Rigorously, δl_i is the variation of length of the part of tendon i contained in the robot. Applying the variation on the expression of the length of a tendon

$$l_i = \int_0^l \|r_i'\| \, dX = \int_0^l (r_i'^T r_i')^{1/2} \, dX \tag{3.32}$$

leads to

$$\delta l_i = \int_0^l \delta \|r_i'\| \, dX = \int_0^l \frac{\delta r_i'^T r_i'}{\|r_i'\|} \, dX \, . \tag{3.33}$$

In order to rewrite the last term of equation (3.33), the definitions $r_i' = R\Gamma_i$ and $\delta r_i' = \delta(R\Gamma_i)$ are inserted in the product $\delta r_i'^T r_i'$

$$\delta r_i'^T r_i' = (\delta R\Gamma_i + R\delta\Gamma_i)^T (R\Gamma_i) = (R^T \delta R\Gamma_i)^T \Gamma_i + \delta\Gamma_i^T \Gamma_i \, . \tag{3.34}$$

Further, since $R \in \mathrm{SO}(3)$, there always exists a vector $\delta\psi \in \mathbb{R}^3$ such that $R^T\delta R = \delta\widehat{\psi}$. As a result

$$\frac{\delta r_i'^T r_i'}{\|r_i'\|} = \frac{(\delta\psi \times \Gamma_i)^T \Gamma_i + \delta\Gamma_i^T \Gamma_i}{\|\Gamma_i\|} = \frac{\delta\Gamma_i^T \Gamma_i}{\|\Gamma_i\|} \, . \tag{3.35}$$

Finally, introducing the expression $\Gamma_i = \Gamma + K \times D_i + D_i'$ into equation (3.35) and the result of this substitution into equation (3.33) provides, after factorization of $\delta\epsilon = (\delta K^T, \delta\Gamma^T)^T$, the relation

$$\delta l_i = \int_0^l \frac{1}{\|\Gamma_i\|} \left(\Gamma_i^T, \Gamma_i^T\right) \begin{pmatrix} \widehat{D}_i^T & 0_{3\times3} \\ 0_{3\times3} & 1_{3\times3} \end{pmatrix} \delta\epsilon \, dX = \int_0^l \bar{J}_{l_i} \delta\epsilon \, dX \, , \tag{3.36}$$

where the Jacobian (continuum) operator $\bar{J}_{l_i}$ is introduced, with $\Gamma_i = R^T r_i' = \Gamma + K \times D_i + D_i'$, and $D_i = R^T d_i$, the vector of the components of the radial position of the tendon i in the cross-sectional frame of the backbone.

3.4.3 Reduced Static Balance

Based on the developments of the previous section, one can now develop the balance of virtual works (equation (3.20)) and apply the kinematic reduction in order to obtain the reduced static balance. The virtual work of internal elastic stress reads

$$\delta W_{int} = -\int_0^l \delta\epsilon^T \mathcal{H}\epsilon \, dX \, . \tag{3.37}$$

Using equation (3.30) allows writing equation (3.37) as

$$\delta W_{int} = \int_0^l \delta q^T \Phi^T \mathcal{H}\epsilon \, dX = \delta q^T Q_{rod} = \delta q^T \mathcal{K}_{\epsilon\epsilon} q \, , \tag{3.38}$$

with the $\mathbb{R}^k$ vector of generalized restoring forces

$$Q_{rod} = \int_0^l \Phi^T \mathcal{H}\epsilon \, dX = \left(\int_0^l \Phi^T \mathcal{H}\Phi \, dX \right) q = \mathcal{K}_{\epsilon\epsilon} q \, , \tag{3.39}$$

and $\mathcal{K}_{\epsilon\epsilon}$ the $\mathbb{R}^{k\times k}$ matrix of generalized stiffness.

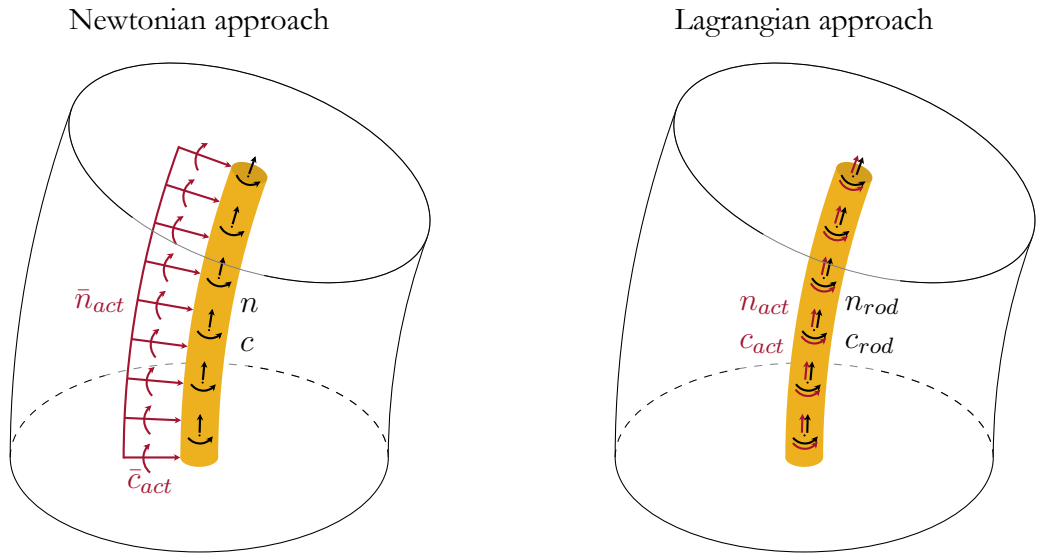

Figure 3.4: Models of tendon actuation for the Newtonian and Lagrangian approaches.

As regards the work of external forces, it can be detailed as the sum

$$\delta W_{ext} = \delta \tilde{W}_{ext} + \delta W_{act} = \left(\int_0^l \delta\zeta^T \bar{F}\, dX + \delta\zeta(l)^T F_+ \right) + \left(\sum_{i=1}^{m} \delta l_i\, \tau_i \right) , \tag{3.40}$$

where $\delta\tilde{W}_{ext}$ stands for the virtual work of external gravity and contact forces, while δW_{act} is the virtual work of tensions exerted on the tendons. Introducing equation (3.36) in the second term of equation (3.40), and exploiting the fact that $\tau_i' = 0_{3\times1}$, allows rewriting the virtual work of actuation in the form

$$\delta W_{act} = \sum_{i=1}^{m} \int_0^l \delta\epsilon^T \bar{J}_{l_i}^T \tau_i\, dX = \int_0^l \delta\epsilon^T \left(\sum_{i=1}^{m} \bar{J}_{l_i}^T \tau_i \right) dX\,. \tag{3.41}$$

This last equation shows that the effect of tendons naturally appears as stress (and not forces in contrast to the Newtonian approach) since they work along strain variations $\delta\epsilon$ (and not along configuration variations, i.e. virtual displacements $\delta\zeta$) (see Figure 3.4). Based on this remark, the field of actuation stress Λ_{act} is defined as

$$\delta W_{act} = \int_0^l \delta\epsilon^T \Lambda_{act}\, dX \quad \Rightarrow \quad \Lambda_{act} = \left(\sum_{i=1}^{m} \tau_i \bar{J}_{l_i}^T \right) = \sum_{i=1}^{m} \frac{1}{\|\Gamma_i\|} \begin{pmatrix} D_i \times \Gamma_i \\ \Gamma_i \end{pmatrix} \tau_i\,, \tag{3.42}$$

which can be integrated to the constitutive law equation (2.19) yielding the more general active-passive law

$$\Lambda = \Lambda_{act} + \mathcal{H}\epsilon\,. \tag{3.43}$$

Again, using equation (3.30) in equation (3.41) allows writing

$$\delta W_{act} = -\int_0^l \delta q^T \Phi^T \Lambda_{act}\, dX = \delta q^T Q_{act}\,, \tag{3.44}$$

with the $\mathbb{R}^k$ vector of generalized forces of actuation

$$Q_{act} = -\int_0^l \Phi^T \Lambda_{act}\, dX = -\sum_{i=1}^{m} \left[\int_0^l \frac{\Phi^T}{\|\Gamma_i\|} \begin{pmatrix} D_i \times \Gamma_i \\ \Gamma_i \end{pmatrix} dX\right] \tau_i = L(q)\tau\,. \tag{3.45}$$

Applying the reduction to the first term $\delta\tilde{W}_{ext}$ of equation (3.40) yields

$$\delta\tilde{W}_{ext} = -\int_0^l \delta q^T J_\zeta^T \bar{F}\, dX - \delta q^T J_\zeta(l)^T F_+\,, = \delta q^T Q_{ext}\,, \tag{3.46}$$

where one recognizes the mapping J_ζ between the variations δq and $\delta\zeta(X)$ defined in equation (3.31), with the $\mathbb{R}^k$ vector of generalized external forces

$$Q_{ext} = -\int_0^l J_\zeta^T \bar{F}\, dX - J_\zeta(l)^T F_+\,. \tag{3.47}$$

Looking back at the balance of virtual works of equation (3.20), it now reads

$$\delta q^T Q_{ext} + \delta q^T \mathcal{K}_{\epsilon\epsilon} q = \delta q^T Q_{act}\,. \tag{3.48}$$

Equation (3.48), being true for any δq, provides the static balance of generalized forces

$$Q_{ext} + \mathcal{K}_{\epsilon\epsilon} q = Q_{act}\,. \tag{3.49}$$

In equation (3.49), the generalized external forces Q_{ext} (equation (3.47)) are computed with Jacobian matrices, as in [Renda et al. 2020, Renda et al. 2021], according to a matrix projective process, often called Kane's method in the mechanical literature [Kane and Levinson 1985]. There is however, a more convenient method, as in [Boyer et al. 2021], where the generalized external forces are computed through the field of internal stress Λ that balances the imposed external wrenches $\bar{F}$ and F_+ when the backbone is in the configuration $\mathcal{C}(\xi, g(0))$. With this field of internal stress, the vector of generalized external forces takes the form

$$Q_{ext} = -\int_0^l \Phi^T \Lambda\, dX\,. \tag{3.50}$$

In equation (3.50), Λ is simply the solution of the inverse kineto-static BVP of a TACR introduced in equation (2.41)

$$\begin{pmatrix} g \\ \Lambda \end{pmatrix}' = \begin{pmatrix} g\widehat{\xi} \\ ad_\xi^T \Lambda - \bar{F} \end{pmatrix}, \qquad \text{(remember: (2.41))}$$
$$g(0) = 1_{4\times 4}\,, \quad \Lambda(l) = F_+\,.$$

The equivalence between the external forces in equation (3.47) and internal stress in equation (3.50) is obtained by starting with the relation $Ad_g' = Ad_g\, ad_\xi$. Rearranging this equation leads to

$$ad_\xi^T = -Ad_g^T Ad_g^{-T\prime}\,. \tag{3.51}$$

Then, introducing this relation in equation (2.27), one can integrate it, and obtain the balance of wrenches

$$\Lambda(X) = Ad_{g(X)}^T \int_X^l Ad_{g(Y)}^{-T} \bar{F}(Y)\, dY + Ad_{g(X)}^T Ad_{g(l)}^{-T} F_+\,. \tag{3.52}$$

Projecting this balance on the strain basis (pre-multiplying by Φ^T and integrating the products over $[0,\ l]$), and using by-part integrations, yields the desired equality between equations (3.47) and (3.50)

$$-\int_0^l \Phi^T \Lambda \, dX = -\int_0^l J_\zeta^T \bar{F} \, dX - J_\zeta(l)^T F_+ \,. \tag{3.53}$$

Although the two expressions for Q_{ext} in equation (3.53) are equivalent, choosing one or the other to calculate the generalized external forces, leads to fundamentally different algorithms. In section 3.6.2, this second approach will be addressed, yet with new numerical methods (compared to [Boyer et al. 2021]).

3.5 Equivalence of the Two Models of Tendon Actuation

Before Lagrangian reduction, the two approaches only differ by the model of tendon actuation (see Figure 3.1). Indeed, in the Newtonian approach, the model of tendon actuation arises from the action-reaction principle and the tendon loads are modeled as external wrenches. Conversely, the Lagrangian approach naturally deduces its model of tendon actuation (equation (3.42)) through the principle of virtual works including them as internal wrenches (see Figure 3.4).

The objectives of this section are twofold. First, in order to establish more direct relations between the Newtonian and the Lagrangian approaches, this section shows how the Lagrangian model of tendon actuation can be alternatively deduced from the continuous formulation on which the Newtonian approach is based (and deduced from Newtonian mechanics). The second objective is to demonstrate the equivalence between including the tendon loads as external wrenches, as in equation (3.1), and including them as internal wrenches (i.e. stress), as they appear in equation (3.43).

Let us first reconsider equation (3.1)

$$\bar{n} = \bar{n}_{ext} + \bar{n}_{act} \,, \quad \bar{c} = \bar{c}_{ext} + \bar{c}_{act} \,, \qquad \text{(remember: (3.1))}$$

and recall that, in the Newtonian approach (see section 3.3), the action of the tendons is modeled as external forces $\bar{n}_{act}$ and couples $\bar{c}_{act}$. Both are integrated in the wrench of external distributed loads $\bar{F}$ applied along the backbone as follows:

$$\begin{aligned} \bar{F} = \begin{pmatrix} \bar{C} \\ \bar{N} \end{pmatrix} &= \begin{pmatrix} \bar{C}_{ext} \\ \bar{N}_{ext} \end{pmatrix} + \begin{pmatrix} \bar{C}_{act} \\ \bar{N}_{act} \end{pmatrix} \\ &= \begin{pmatrix} R^T \bar{c}_{ext} \\ R^T \bar{n}_{ext} \end{pmatrix} + \begin{pmatrix} R^T \bar{c}_{act} \\ R^T \bar{n}_{act} \end{pmatrix} \\ &= \begin{pmatrix} R^T \bar{c}_{ext} \\ R^T \bar{n}_{ext} \end{pmatrix} + \sum_{i=1}^{m} \begin{pmatrix} D_i \times (R^T t_i') \\ R^T t_i' \end{pmatrix} \tau_i \,. \end{aligned} \tag{3.54}$$

Whereas in the Lagrangian approach (see section 3.4), the same actions are modeled by the wrench of stress Λ_{act} across the backbone whose expression is defined by equation (3.42),

$$\Lambda_{act} = \left(\sum_{i=1}^{m} \tau_i \bar{J}_{l_i}^T \right) = \sum_{i=1}^{m} \frac{1}{\|\Gamma_i\|} \begin{pmatrix} D_i \times \Gamma_i \\ \Gamma_i \end{pmatrix} \tau_i \,. \qquad \text{(remember: (3.42))}$$

Using $R\Gamma_i = r_i'$, $t_i = r_i'/\|r_i'\|$, and $d_i = RD_i$, the stresses Λ_{act} can be expressed in the inertial frame as

$$\begin{pmatrix} c_{act} \\ n_{act} \end{pmatrix} = \begin{pmatrix} RC_{act} \\ RN_{act} \end{pmatrix} = \sum_{i=1}^{m} \begin{pmatrix} d_i \times t_i \\ t_i \end{pmatrix} \tau_i \,. \tag{3.55}$$

To demonstrate the equivalence of both approaches, the first step is to reconsider the BVP of equation (2.38)

$$\begin{pmatrix} r \\ R \\ n \\ c \end{pmatrix}' = \begin{pmatrix} R\left(\mathcal{H}_{lin}^{-1} R^T n + \Gamma^0\right) \\ R\left(\mathcal{H}_{ang}^{-1} R^T c + K^0\right)^\wedge \\ -\bar{n} \\ -r' \times n - \bar{c} \end{pmatrix}, \qquad \text{(remember: (2.38))}$$

$$r(0) = 0_{3\times 1}\,, \quad R(0) = 1_{3\times 3}\,, \quad n(l) = n_+\,, \quad c(l) = c_+\,.$$

on which the Newtonian approach is based. But, in contrast to section 3.3.2, the action of tendons is no more modeled as a field of external forces and couples defined by equations (3.2), (3.3), and (3.6),

$$\bar{n}_{act} = \sum_{i=1}^{m} -\bar{n}_i\,, \quad \bar{c}_{act} = \sum_{i=1}^{m} (r_i - r) \times (-\bar{n}_i) = -\sum_{i=1}^{m} d_i \times \bar{n}_i\,, \quad \bar{n}_i = -n_i' = -\tau_i t_i'\,.$$

(remember: (3.2), (3.3), and (3.6))

but as the field of stress wrench across the backbone (equation (3.55)). This change of view point means that, in equation (2.38), $\bar{c}_{act}$ and $\bar{n}_{act}$ are removed from the model of external loads (equation (3.1)), to be replaced by internal forces and couples across the backbone n_{act} and c_{act}. These internal forces superimpose to its usual elastic forces and couples, now noted n_{rod} and c_{rod}, to form the full field of internal couples and forces along the robot considered as a stress-actuated backbone

$$c = c_{rod} + c_{act}\,, \quad n = n_{rod} + n_{act}\,. \tag{3.56}$$

c_{rod} and n_{rod} are still governed by the constitutive law (2.15), while n_{act} and c_{act} are given by (3.55), that are rewritten as

$$n_{act} = \sum_{i=1}^{m} n_i = \sum_{i=1}^{m} \tau_i t_i\,, \quad c_{act} = \sum_{i=1}^{m} d_i \times n_i = \sum_{i=1}^{m} d_i \times (\tau_i t_i). \tag{3.57}$$

Note that once expressed in the cross-sectional frames, these two relations do define the active constitutive law of equation (3.43), which takes the detailed form

$$\Lambda = \Lambda_{act} + \mathcal{H}\epsilon = \begin{pmatrix} R^T c_{act} \\ R^T n_{act} \end{pmatrix} + \begin{pmatrix} \mathcal{H}_{ang}\left(K - K^0\right) \\ \mathcal{H}_{lin}\left(\Gamma - \Gamma^0\right) \end{pmatrix}, \tag{3.58}$$

where, in this case, the loads of the tendons are directly the sum of the internal loads of the tendons. Instead, in the Newtonian approach the loads of the tendons were equal to the sum of the opposite (action-reaction) of the external loads as seen by the tendons as in equations (3.2) and (3.3).

As announced, substituting equations (3.56) and (3.57) in the stress balance of equation (2.38), produces

$$\begin{aligned} \left(n_{rod} + \sum_{i=1}^{m} \tau_i t_i\right)' + \bar{n}_{ext} &= 0_{3\times 1}\,, \\ \left(c_{rod} + \sum_{i=1}^{m} d_i \times (\tau_i t_i)\right)' + r' \times \left(n_{rod} + \sum_{i=1}^{m} \tau_i t_i\right) + \bar{c}_{ext} &= 0_{3\times 1}\,. \end{aligned} \tag{3.59}$$

Which, once rearranged with the usual composition rules of derivatives and using $d_i = r_i - r$ and $\tau_i' = 0_{3\times1}$, yields

$$\begin{aligned} n_{rod}' + \sum_{i=1}^{m} \tau_i t_i' + \bar{n}_{ext} &= 0_{3\times1}\,, \\ c_{rod}' + r' \times n_{rod} + \sum_{i=1}^{m} d_i \times (\tau_i t_i') + \sum_{i=1}^{m} (r' + d_i') \times (\tau_i t_i) + \bar{c}_{ext} &= 0_{3\times1}\,. \end{aligned} \tag{3.60}$$

Finally, using the relations $r' + d_i' = r_i' = \|r_i'\|\, t_i$ and $t_i \times t_i = 0_{3\times1}$, leads to

$$\begin{aligned} n_{rod}' + \sum_{i=1}^{m} \tau_i t_i' + \bar{n}_{ext} &= 0_{3\times1}\,, \\ c_{rod}' + r' \times n_{rod} + \sum_{i=1}^{m} d_i \times (\tau_i t_i') + \bar{c}_{ext} &= 0_{3\times1} \end{aligned} \tag{3.61}$$

that are the two stress balances of equation (3.7)

$$\begin{pmatrix} r \\ R \\ n \\ c \end{pmatrix}' = \begin{pmatrix} R\left(\mathcal{H}_{lin}^{-1} R^T n + \Gamma^0\right) \\ R\left(\mathcal{H}_{ang}^{-1} R^T c + K^0\right)^{\wedge} \\ -\sum_{i=1}^{m} \tau_i t_i' - \bar{n}_{ext} \\ -r' \times n - \sum_{i=1}^{m} d_i \times (\tau_i t_i') - \bar{c}_{ext} \end{pmatrix}, \qquad \text{(remember: (3.7))}$$

$$(r, R)(0) = (0_{3\times1}, 1_{3\times3})\,, \quad (n, c)(l) = (n_+, c_+)\,,$$

which lead to the static balance in strain-form equation (3.15) of the Newtonian approach. Therefore, modeling the effect of tendons as external loads as in the Newtonian approach or as internal stress as in the Lagrangian approach leads to equivalent continuous models[1].

3.6 Numerical Implementation

Sections 3.6.1 and 3.6.2 deal with the numerical implementation of the Newtonian and Lagrangian approaches, respectively. They both start with the case of a single-segment TACR and then extend the resolution to the multi-segment case.

3.6.1 Numerical Implementation of the Newtonian Approach

In the Newtonian approach, the simulation of a TACR is achieved by solving the forward kineto-static BVP of equation (3.15). Although this can be done by different numerical methods (finite differences, shooting, spectral methods ...), this chapter adopts the shooting method, since it is largely dominant in the community.

[1] In more details, the BVP equation (3.15) with the BCs of equation (2.39) of the Newtonian approach is equivalent to the closed continuous formulation equations (2.41), (3.42), and (3.43) exploited by the Lagrangian approach.

Newtonian resolution of a single-segment TACR

Solving the forward statics BVP equation (3.15) with the shooting method consists in finding the unknown proximal BCs on the space rates $\Gamma(0)$ and $K(0)$ such that the known distal BCs $\Gamma(l)$ and $K(l)$, defined by equation (2.39), are fulfilled, for any imposed vector of tendon tensions $\tau = (\tau_1 \,..\, \tau_m)^T$ (see bottom left area of Figure 3.1). This search is achieved iteratively by applying a root finding algorithm to the residual vector

$$\mathfrak{Res}(\Gamma^\star(0), K^\star(0)) = \begin{pmatrix} \Gamma(l) - \Gamma^\star(l) \\ K(l) - K^\star(l) \end{pmatrix}, \tag{3.62}$$

where $\Gamma^\star(l)$ and $K^\star(l)$ are the distal values of Γ and K obtained by forward integrating the ODEs of equation (3.15) with the guessed values $(\Gamma^\star, K^\star)(0)$ from $X = 0$ to $X = l$.

This process proposes to iterate over the values of $\Gamma(0)$ and $K(0)$ but the relations of equation (2.15) allow to equivalently iterate over $N(0)$ and $C(0)$ or any combination of these variables. Changing the state variables can be of interest, for instance, when the rod is very stiff for shear and extension, which may cause convergence issues. When computing the residual vector at each iteration, the kinematic ODE $R' = R\widehat{K}$ is integrated using quaternions, which ensures that R remains in $\mathrm{SO}(3)$. Note also that other methods based on Magnus expansions in $\mathrm{SO}(3) \times \mathbb{R}^3$ or $\mathrm{SE}(3)$ can be used [Orekhov and Simaan 2020, Renda et al. 2020].

Choosing the initial guess is a crucial step that may determine the outcome of the implemented algorithm. When the initial guess is too far from the solution, the root finding algorithm may converge to a local minimum or fail to converge due to gradients that lead to infeasible points. Nonetheless, finding a good initial guess may be a tricky task. A solution to address this issue is to start from a vector of zeros. If the TACR is subject to small loads, the solution will be close to zero and the solver will likely converge. If, on the contrary, the TACR is subject to higher loads, the strategy consists in dividing the total load of the problem in a number of increasing loading steps such that the first step can be solved starting with the zero vector (see Figure 3.5). Then, the subsequent steps are solved for, using the previous solution as input for the following guess. Another advantage of specifying the loading history is that the final solution can be controlled in the case of multiple possible solutions for a given load [Bretl and McCarthy 2013, Bretl and McCarthy 2014].

Newtonian resolution of a multi-segment TACR

In a multi-segment robot, the poses as well as the internal forces and couples propagate from one segment to the next. Consequently, their values at the distal end of the first segment are used as inputs for the ODEs of the second segment and so on, until the most distal segment, where the BCs are evaluated. The implementation of multi-segment robots is thus straightforward based on the single-segment case and does not increase the size of the state vector of the problem.

One particular case that has not previously been reported in the literature, deserves a special focus: when a tendon undergoes a slope discontinuity. The tension applied to such a tendon will create a force, acting at the location of the discontinuity, which needs to be taken into account in the implementation. This happens for instance in a multi-segment TACR where a tendon is routed following a convergent routing path in the distal segment but runs parallel to the backbone in the proximal segments (see Figure 3.6 and Figure 3.7 – Scenario 3.7.5.). Practically, for a tendon i undergoing a slope discontinuity between the segments j and $j+1$, the shift in routing orientation is equal to

$$[\![t_i]\!]_j = \lim_{\varepsilon \to 0} \left(t_i(X_j^+) - t_i(X_j^-) \right), \tag{3.63}$$

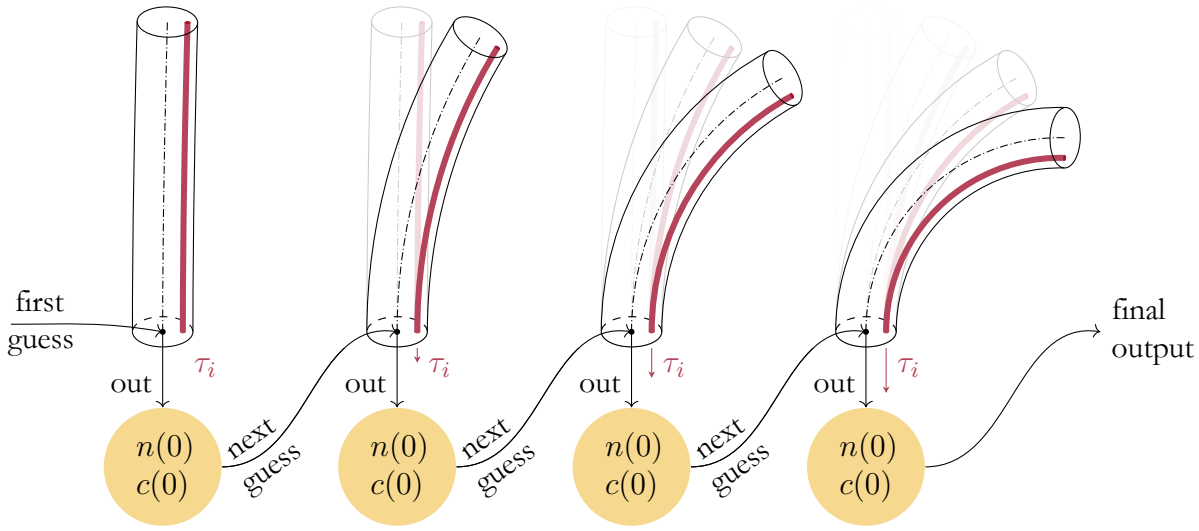

Figure 3.5: Proceeding in steps towards the final solution, reusing the output (proximal BCs) of the previous step as input for the next step and gradually increasing the actuation tension.

where $X_j^{\pm} = X_j \pm \varepsilon$, X_j is the arc length abscissa of the backbone cross-section to which is attached the disk connecting segments j and $j+1$, and $[\![f]\!]_j$ denotes the jump of any field f when crossing the junction between segments j and $j+1$. $t_i = r_i'/\|r_i'\|$ denotes the unit tangent vector to the i-th tendon (see Figure 3.6). Applying Newton's laws to the tendon at the junction point, provides the jump of force and couple transmitted to the backbone by a tendon i subject to a slope discontinuity at junction j

$$[\![n]\!]_j = \tau_i \, [\![t_i]\!]_j \ , \quad [\![c]\!]_j = d_i \times [\![n]\!]_j \ . \tag{3.64}$$

Note that equation (3.64) is no more than a discrete version of equation (3.6). Equation (3.64) will need to be added to the static balance equation (3.17) while forward integrating the BVP equation (3.15), each time a tendon slope discontinuity is encountered. The slope discontinuity $[\![t_i]\!]_j$ can be obtained with the relation $[\![\Gamma_i/\,\|\Gamma_i\|]\!]_j = R^T \, [\![t_i]\!]_j$. Hence, equation (3.64) is rewritten in its cross-sectional frame version

$$[\![N]\!]_j = \tau_i \left[\!\!\left[\frac{\Gamma_i}{\|\Gamma_i\|} \right]\!\!\right]_j \ , \quad [\![C]\!]_j = D_i \times [\![N]\!]_j \ , \tag{3.65}$$

where $\Gamma_i^{\pm}$ is computed similarly to equation (3.12), with

$$\Gamma_i(X_j^{\pm}) = \Gamma(X_j^{\pm}) + \widehat{K}(X_j^{\pm}) D_i(X_j) + D_i'(X_j^{\pm}) \, . \tag{3.66}$$

In practice, this calculation is achieved by using the following jump relations on the space-rates:

$$\begin{pmatrix} \Gamma \\ K \end{pmatrix}_+ = \begin{pmatrix} \Gamma \\ K \end{pmatrix}_- + \begin{pmatrix} \mathcal{H}_{lin} + A & G \\ B & \mathcal{H}_{ang} + H \end{pmatrix}_-^{-1} \left[\!\!\left[\begin{pmatrix} c \\ d \end{pmatrix} \right]\!\!\right]_j \ , \tag{3.67}$$

where the expressions of A, G, B, H, c, and d are again given by equations (3.14) and (3.16), except that the continuous X-derivatives D_i' and D_i'' are replaced by their jumps $[\![D_i]\!]_j = 0_{3\times1}$ and $[\![D_i']\!]_j \neq 0_{3\times1}$, respectively. Owing to the continuity of poses, all other quantities are evaluated equivalently at $X = X_j^-$ or $X = X_j^+$. The necessary contribution of this term can be observed

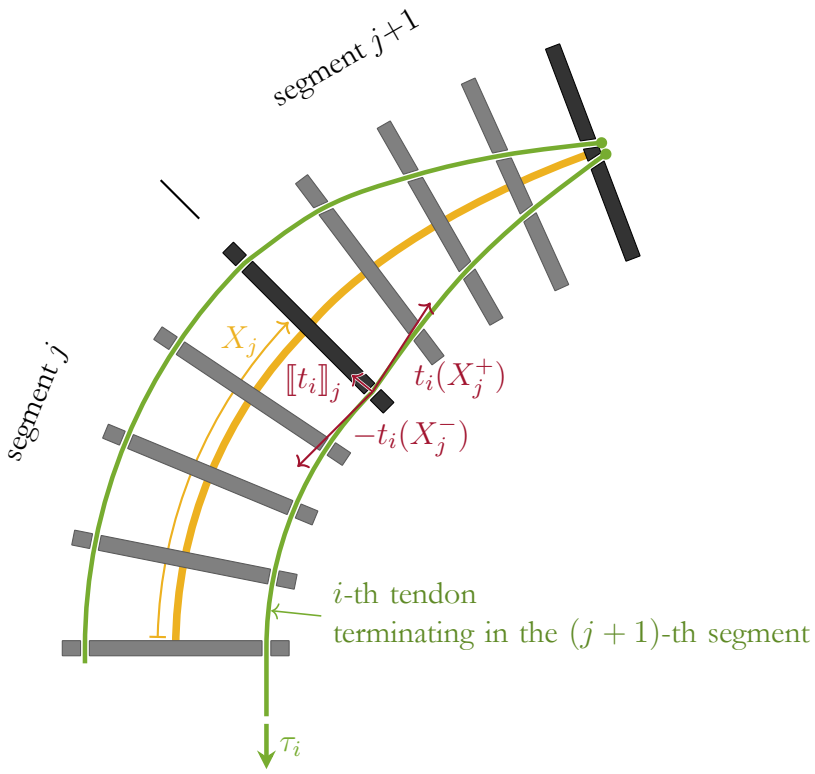

Figure 3.6: Side view of a multi-segment TACR featuring a tendon slope discontinuity. The tendons are routed parallel in the j-th segment and convergently in the (j+1)-th segment introducing a discontinuity at the tendon routing between segments (at arc length X_j).

in an example simulation in Figure 3.10 and in an online available video[2] where the Newtonian approach is shown to fail without the slope discontinuity compensation term.

Finally, using equation (3.67) from segment to segment while piece-wise integrating the ODEs of equation (3.15) from $X = 0$ to l, allows calculating the residual vector of equation (3.62) in the general case with possible tendon slope discontinuities between segments.

3.6.2 Numerical Implementation of the Lagrangian Approach

Following the standard numerical techniques of the Lagrangian approach, the quasi-static simulation of a TACR is performed here by solving the implicit system of non-linear algebraic equations defined in equation (3.49). Note that this is more straightforward than the approach in [Boyer et al. 2021], where the resolution is performed by the explicit time integration of an overdamped equivalent system.

Lagrangian resolution of a single-segment TACR

In the Lagrangian approach, the numerical resolution of the static problem consists in calculating the vector of generalized strain coordinates $q = (q_1 \,..\, q_k)^T$ that fulfills the reduced static balance equation (3.49), for any imposed vector of tendon tensions $\tau = (\tau_1 \,..\, \tau_m)^T$ (see bottom right area of Figure 3.1). Since this balance defines a set of algebraic nonlinear equations, one can apply any root finding algorithm to solve for the vector of residuals $\mathfrak{Res}$ that takes the generic form

$$\mathfrak{Res}(q, \tau) = 0_{k\times 1}\,, \text{ with: } \mathfrak{Res}(q, \tau) = Q_{ext} + \mathcal{K}_{\epsilon\epsilon} q - Q_{act}\,. \tag{3.68}$$

[2]Video available at: https://youtu.be/W1E-oA42OOM.

It is of common use in nonlinear structural statics (and dynamics) to use Newton-Raphson's method, which allows updating the q-vector at each step of a loop, iteratively reducing the residual, according to the linear relation

$$q^+ = q - J^{-1}(q)\mathfrak{Res}(q,\tau)\,, \tag{3.69}$$

where $J(q) = \frac{\partial \mathfrak{Res}}{\partial q}$ denotes the $\mathbb{R}^{k\times k}$ Jacobian matrix of the residual vector, and q^+ is the updated value of q. Therefore, applying this method requires to calculate the vector of residuals $\mathfrak{Res}$ and its Jacobian matrix J.

To numerically compute the residual vector $\mathfrak{Res}$ from any q-vector, the expressions of equations (3.39), (3.45), and (3.47) are added to the inverse BVP equation (2.41) through the state variable

$$y(X) = -\int_X^l \Phi^T\left(\Lambda_{act} - \Lambda + \mathcal{H}\Phi q\right) dY \tag{3.70}$$

such that $y(0) = \mathfrak{Res}$. The state variables (g, Λ, y) are then governed by the augmented inverse BVP, which is fed with $\xi = \xi^0 + \Phi q$, and reads

$$\begin{gathered}\begin{pmatrix} g \\ \Lambda \\ y \end{pmatrix}' = \begin{pmatrix} g\left(\xi^0 + \Phi q\right)^\wedge \\ ad^T_{(\xi^0+\Phi q)}\Lambda - \bar{F} \\ \Phi^T\left(\Lambda_{act} - \Lambda + \mathcal{H}\Phi q\right) \end{pmatrix}, \\ g(0) = 1_{4\times 4}\,, \quad \Lambda(l) = F_+\,, \quad y(l) = 0_{k\times 1}\,,\end{gathered} \tag{3.71}$$

where Λ_{act} is a function of q and τ, given by equation (3.42), while $\bar{F}$ depends on the context. For instance, if the robot is only subject to gravity, $\bar{F} = \left(0_{1\times 3}, R^T a_g^T \mathcal{A}\mu\right)^T$, with a_g the acceleration gravity field expressed in the inertial frame, $\mathcal{A}$ the area of the robot section, and μ its density.

Note that, similarly to the inverse kineto-static BVP of equation (2.41), equation (3.71) possesses interesting properties that make its resolution straightforward compared to that of the forward BVP equation (3.15). In particular, it can be solved with two decoupled passes (i.e. without resorting to the shooting algorithm), with standard explicit space integrators. One can first integrate forward (from $X = 0$ to l), the ODE in g, and then integrate backward (from $X = l$ to 0) the two other ODEs in Λ and y producing $\mathfrak{Res}(q) = y(0)$. This method has been proposed and interpreted as a Newton-Euler computed torque algorithm in [Boyer et al. 2021], similar to those developed for rigid multi-body systems [Featherstone 2007]. In this chapter, a further property of the inverse BVP is exploited. Since the q-vector is an imposed input, equation (3.71) is linear with respect to the state variables (g, Λ, y). As a result, one can apply a spectral collocation method [Hussaini et al. 1989] and replace the previous explicit ODE integrations by the resolution of some linear algebraic systems with respect to the vector of the state variables on a Chebyshev grid [Trefethen 2000].

In the continuum robotics community, Jacobian matrices are often calculated numerically. This chapter proposes a more accurate calculation of J, based on the exact linearization of the residual vector. To this end, the BVP of equation (3.71) is linearized with respect to its input q by propagating the differential consequences of a variation Δq as

$$\begin{gathered}\begin{pmatrix} \Delta\zeta \\ \Delta\Lambda \\ \Delta y \end{pmatrix}' = \begin{pmatrix} -ad_{(\xi^0+\Phi q)}\Delta\zeta + \Phi\Delta q \\ ad^T_{\Phi\Delta q}\Lambda + ad^T_{(\xi^0+\Phi q)}\Delta\Lambda - \Delta\bar{F} \\ \Phi^T\left(\Delta\Lambda_{act} - \Delta\Lambda + \mathcal{H}\Phi\Delta q\right) \end{pmatrix}, \\ \Delta\zeta(0) = 0_{6\times 1}\,, \quad \Delta\Lambda(l) = \Delta F_+\,, \quad \Delta y(l) = 0_{k\times 1}\,,\end{gathered} \tag{3.72}$$

where $\Delta\zeta$ is the differential of g in $se(3)$ defined by $\Delta\zeta = \left(g^{-1}g\right)^\vee$, while $\Delta\Lambda_{act}$, $\Delta\bar{F}$, and ΔF_+ are the differentials of the model of actuation stress and external forces, respectively. Note here

that, the variation Δ being only generated by the variation of the configuration Δq, the variation of the actuation $\Delta\tau = 0_{m\times 1}$ in $\Delta\Lambda_{act}$. Moreover, the dependence of Λ_{act} on q is very weak[3] and may be neglected in the calculation of the Jacobian. Thus, $\Delta\Lambda_{act}$ is set to $0_{6\times 1}$ when solving equation (3.72).

The BVP of equation (3.72) defines the augmented inverse tangent boundary value problem (TBVP) of the robot. The full BVP obtained by gathering equations (3.71) and (3.72) is linear, and can, once again, be solved with a spectral method applied forward and backward, as for the BVP. Now, by virtue of the linear identity $\Delta y(0) = \Delta\mathfrak{Res} = J(q)\Delta q$, applying the unit input vector $\Delta q = \delta_\alpha$ to equation (3.72), where δ_α is a $\mathbb{R}^k$ vector of zeros, except the entry α, which is equal to 1, equation (3.72) yields the column α of J. Hence, repeating the process for $\alpha = 1\,..\,k$ allows the Jacobian to be filled column by column.

Lagrangian resolution of a multi-segment TACR

The Lagrangian model of a multi-segment TACR is simply obtained by applying the principle of virtual work to the system defined by the serial connection of the χ segments. All segments are subject to the external forces applied by the environment (e.g. gravity), those exerted by the tendons across the basis, as well as the restoring internal forces. Such a virtual work balance takes the generic form

$$\sum_{j=1}^{\chi} \delta\tilde{W}_{ext,j} + \delta W_{act,j} + \delta W_{int,j} = 0\,, \tag{3.73}$$

with j the index of segments and where each of the three contributions can be defined and detailed as in the single-segment case of equation (3.40). In particular, applying the same strain reduction segment by segment provides the vector of generalized strain coordinates of the entire robot $q = (q_{(1)}\,..\,q_{(\chi)})^T$. The subscript $\bullet_{(j)}$ denotes a generalized vector or matrix, related to the segment j. Introducing these reduced virtual works in equation (3.73) allows writing, for any δq,

$$\delta q^T(Q_{ext} + \mathcal{K}_{\epsilon\epsilon} q - Q_{act}) = 0_{k\times 1}\,, \tag{3.74}$$

where $\mathcal{K}_{\epsilon\epsilon} = \text{diag}(K_{\epsilon\epsilon,(1)}\,..\,K_{\epsilon\epsilon,(\chi)})$, $Q_{ext} = (Q_{ext,(1)}\,..\,Q_{ext,(\chi)})^T$, and $Q_{act} = (Q_{act,(1)}\,..\,Q_{act,(\chi)})^T$. In other words, the multi-segment TACR model is simply obtained by appending the matrices and vectors of each segment one after another.

To numerically solve this multi-segment model, the above single-segment method can be extended by considering a BVP of the form of equation (3.71) for each of the segments, and its associated TBVP equation (3.72). Using normalized arc-length variables along each segment, these χ BVPs and TBVPs, are now connected through their BCs (or connectivity conditions) as follows:

$$g_j(1) = g_{j+1}(0)\,, \qquad \Lambda_j(1) = \Lambda_{j+1}(0)\,, \tag{3.75}$$

$$\Delta\zeta_j(1) = \Delta\zeta_{j+1}(0)\,, \quad \Delta\Lambda_j(1) = \Delta\Lambda_{j+1}(0)\,. \tag{3.76}$$

Note that, as it is usually the case in Lagrangian mechanics, the above relations introduce no jumps on the stress. Indeed, the inter-segment forces of equation (3.64) are considered as internal forces of the multi-segment system that do not work in any virtual displacement field compatible with the inter-segment connections. Finally, the multi-segment solution is obtained by solving equation (3.69) applied to the whole structure. The Jacobian and the residual are computed, as in the single-segment case, by forward and backward integrations of equations (3.71) and (3.72), and starting from $g_1(0) = 1_{4\times 4}$ and $\Lambda_\chi(1) = F_+$, respectively.

[3]The dependence of Λ_{act} has been observed in preliminary simulations to be negligible for the convergence of the algorithm.

Table 3.1: Geometry and Material parameters of the simulated robot.

Parameter Name	Parameter Symbol	Value
Backbone radius	R_b	0.4 mm
Backbone length (3.7.1 to 3.7.3)	l	242 mm
Backbone length (3.7.4 and 3.7.5)	$l = l_j \times 3$	300 mm
Tendon offset	R_t	8 mm
Gravity constant	$\|a_g\|$	9.81 N/kg
Robot equivalent density[5]	$\mu = \frac{0.47\,\mathrm{N/m}}{\|a_g\|\pi(\mathbb{R}_b)^2}$	$95 \cdot 10^3 \mathrm{kg/m^3}$
Young's modulus	$\mathcal{E}$	210 GPa
Poisson's ratio	ν	0.3125

3.7 Performance Comparison

The objective of this section is to compare the behavior of both approaches when modeling various TACRs. This section proceeds through the comparison of five example scenarios of increasing complexity and that are representative of the TACRs studied in the literature and numerous other configuration possibilities. The robots and their routings are represented in Figure 3.7 and 3D views are shown in an online available video[4]. To confront our simulations with results from the literature, the modeled TACR corresponds to the one presented in [Rucker and Webster 2011b], but with various tendon routings. Its geometry and material parameters are given in Table 3.1. In all scenarios, the robot is oriented with its base pointing upwards, opposite to the action of gravity. The associated code can be found at: https://github.com/TIMClab-CAMI/Cosserat-Rod-Modeling-of-Tendon-Actuated-Continuum-Robots.

Both approaches also involve some numerical parameters. For the Newtonian approach, all the ODEs are integrated using the Runge-Kutta Dormand–Prince method with Matlab 2022a `ode45` function. The relative error tolerance parameter, `'ResTol'`, and absolute error tolerance parameter, `'AbsTol'`, are both specified to 10^{-8}. The global BVP equation (3.15) is solved using Matlab 2022a `fsolve` function with the Levenberg-Marquardt algorithm with all parameters set to default values. For the Lagrangian approach, the ODEs are integrated using a spectral method over a Chebyshev grid of 10 nodes. The strain distributions are projected on Legendre polynomials of orders 5 for torsion; 7 for bending in both directions; and 3 for extension and shearing in both directions. Summing all polynomial orders results in a total of 28 shape functions. Finally, the residual of the BVP equation (3.71) is brought to $< 10^{-8}$ with Newton-Raphson's method[6].

When running simulations, particularly in the case of high loads, the algorithms may fail to converge if the actuation load is applied as a single step. Progressively increasing the tension in the tendons and iteratively building upon the previous solutions may solve this problem (see Figure 3.5). This method will be used when required for some of the simulated cases and will be referred to as the number of needed loading steps.

[4]Video available at: https://youtu.be/W1E-oA42OOM.

[5]The equivalent density is the density applied to the backbone capturing the weight of the backbone itself, disks, and tendons. The value of the robot self-weight is from [Rucker and Webster 2011b].

[6]The algorithm parameters were chosen empirically during preliminary simulations such that the simulation results had converged for each approach.

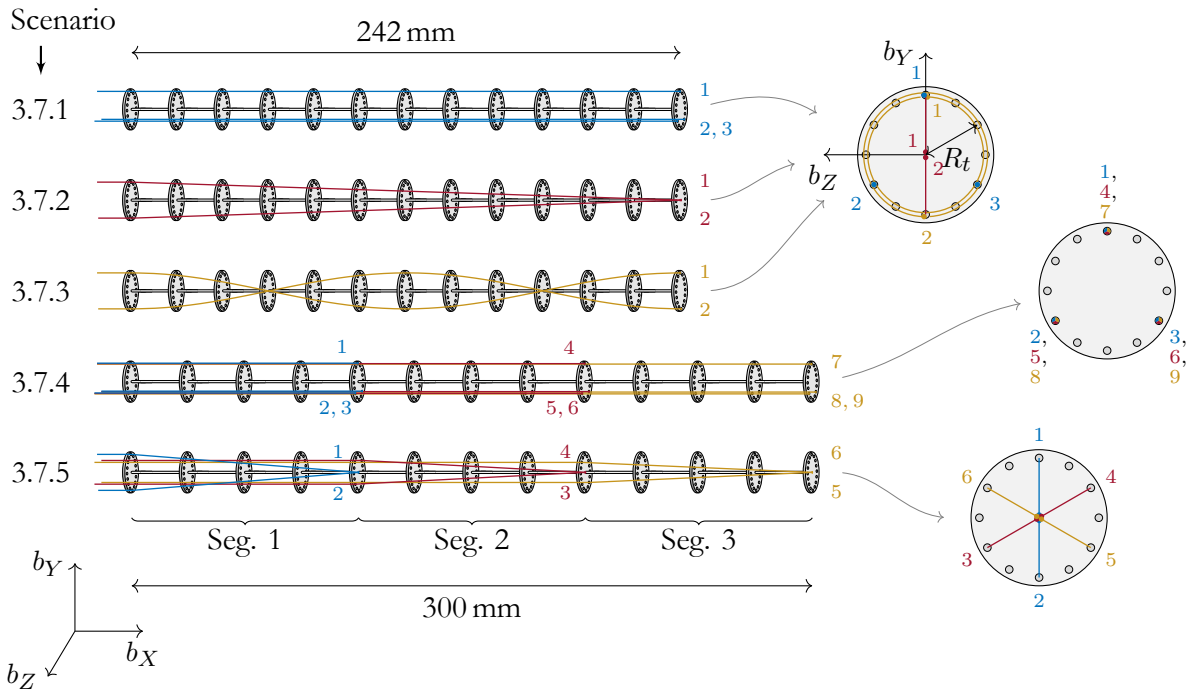

Figure 3.7: Left, front view (b_Y pointing upwards) of the different routings corresponding to the investigated scenarios. Right, top view of the robot routing disks, with the tendon offset R_t. The top views of the first three scenarios are superimposed. The numbers next to the tendons correspond to their index in each scenario. For details on each specific routing, please refer to the corresponding section.

For each scenario, the simulations are analyzed by pair (Newtonian and Lagrangian approaches) and the position and orientation of the tip are compared in Table 3.2. This table also displays the main characteristics of the simulated robots. As none of the codes for either approach were fully optimized, the computation times of the simulations are not provided. Information regarding which approach is more efficient for which case is discussed in section 3.8. Sections 3.7.1 to 3.7.5 give detailed information on the scenarios and analyze the results.

3.7.1 Single-Segment Parallel Routing

The first scenario starts with a simple case: a single-segment TACR with 3 tendons routed parallel around the backbone at 120° ($R_t = 8$ mm, see Figure 3.7 – Scenario 3.7.1). 216 simulations are run with each approach corresponding to the possible combinations of the integer values of tension between 0 and 5 N for each tendon. Figure 3.8a shows a sample of 20 pairs of the 432 simulations. One can see how both approaches render the same robot shape.

For this scenario, depending on the load combination in the tendons, all cases in both methods could be solved with only 1 loading step, except 3 cases (1.39%) with the Newtonian approach that required 2 loading steps.

3.7.2 Single-Segment Convergent Routing

In this scenario, the parallel routing from the TACR above is changed to a convergent routing. Examples of existing physical robots with this kind of routing can be found in [Laschi et al. 2012,

Table 3.2: Synthesis of results for the five simulated scenarios.

Scenario*	3.7.1	3.7.2	3.7.3	3.7.4	3.7.5
Robot characteristics					
Type of routing	Parallel	Convergent	Helical	Parallel	Convergent
Number of segments	1	1	1	3	3
Robot length [mm]	242	242	242	300	300
Tip position difference [mm]**					
Median value	$5.43 \cdot 10^{-4}$	$9.40 \cdot 10^{-3}$	$1.42 \cdot 10^{-1}$	$3.42 \cdot 10^{-1}$	$6.93 \cdot 10^{-2}$
Lower bound 95% confidence interval	$2.41 \cdot 10^{-9}$	$8.77 \cdot 10^{-15}$	$4.48 \cdot 10^{-3}$	$1.00 \cdot 10^{-5}$	$1.11 \cdot 10^{-2}$
Upper bound 95% confidence interval	$3.13 \cdot 10^{-3}$	$2.32 \cdot 10^{-2}$	$7.21 \cdot 10^{-1}$	1.29	$2.76 \cdot 10^{-1}$
Tip orientation difference [°]**					
Median value	$3.26 \cdot 10^{-4}$	$1.10 \cdot 10^{-3}$	$1.99 \cdot 10^{-1}$	$5.56 \cdot 10^{-2}$	$1.32 \cdot 10^{-2}$
Lower bound 95% confidence interval	$1.03 \cdot 10^{-7}$	$5.42 \cdot 10^{-8}$	$8.09 \cdot 10^{-3}$	$3.39 \cdot 10^{-7}$	$2.78 \cdot 10^{-3}$
Upper bound 95% confidence interval	$1.65 \cdot 10^{-3}$	$3.20 \cdot 10^{-3}$	$5.74 \cdot 10^{-1}$	$2.14 \cdot 10^{-1}$	$4.74 \cdot 10^{-2}$

* The labels of the scenarios correspond to the subsections in section 3.7.
** Differences between the results that are obtained with both approaches.

Oliver-Butler et al. 2019]. In this case, 2 tendons are routed at opposite positions of the robot, linearly convergent towards its end, starting at offset $R_t = 8\,\text{mm}$ at the proximal end of the robot and ending coincident with the backbone at its tip (see Figure 3.7 – Scenario 3.7.2). The cross-sectional frame position of the tendons now depends on the reference length parameter X as follows:

$$D_i(X) = (0, \pm R_t(1 - X/l), 0)^T \ . \tag{3.77}$$

Simulations are run for all combinations of tendon tensions over the integer values between 0 and 8 N. The maximum tension is higher than in section 3.7.1 in order to operate the robot over a comparable workspace. With the two-tendon robot described, these combinations yield 162 simulations. Figure 3.8b displays a sample of 20 pairs of these simulations. As in the previous case, one can see how both approaches render the same robot shapes. The values for the differences between tip positions and orientations between the two approaches are similar to those for the previous scenario (see Table 3.2). As for the previous scenario, a majority of cases of this scenario could be solved with 1 loading step. 6.17% of the cases with the Newtonian approach required 2 loading steps.

3.7.3 Single-Segment Helical Routing

In this scenario, the routing is set to 2 helically routed tendons in a full turn around the length of the backbone, lying opposite to each other (see Figure 3.7 – Scenario 3.7.3). As such, the cross-sectional frame position of the tendon i is equal to

$$D_i(X) = R_t \left(0, \cos\left(\frac{2\pi}{l}X + i\pi\right), \sin\left(\frac{2\pi}{l}X + i\pi\right)\right)^T , \tag{3.78}$$

with $R_t = 8\,\text{mm}$.

The simulation results for tendon tensions varying over the integer values between 1 and 10 N for each tendon independently for both approaches are shown in Figure 3.8c. The tension range

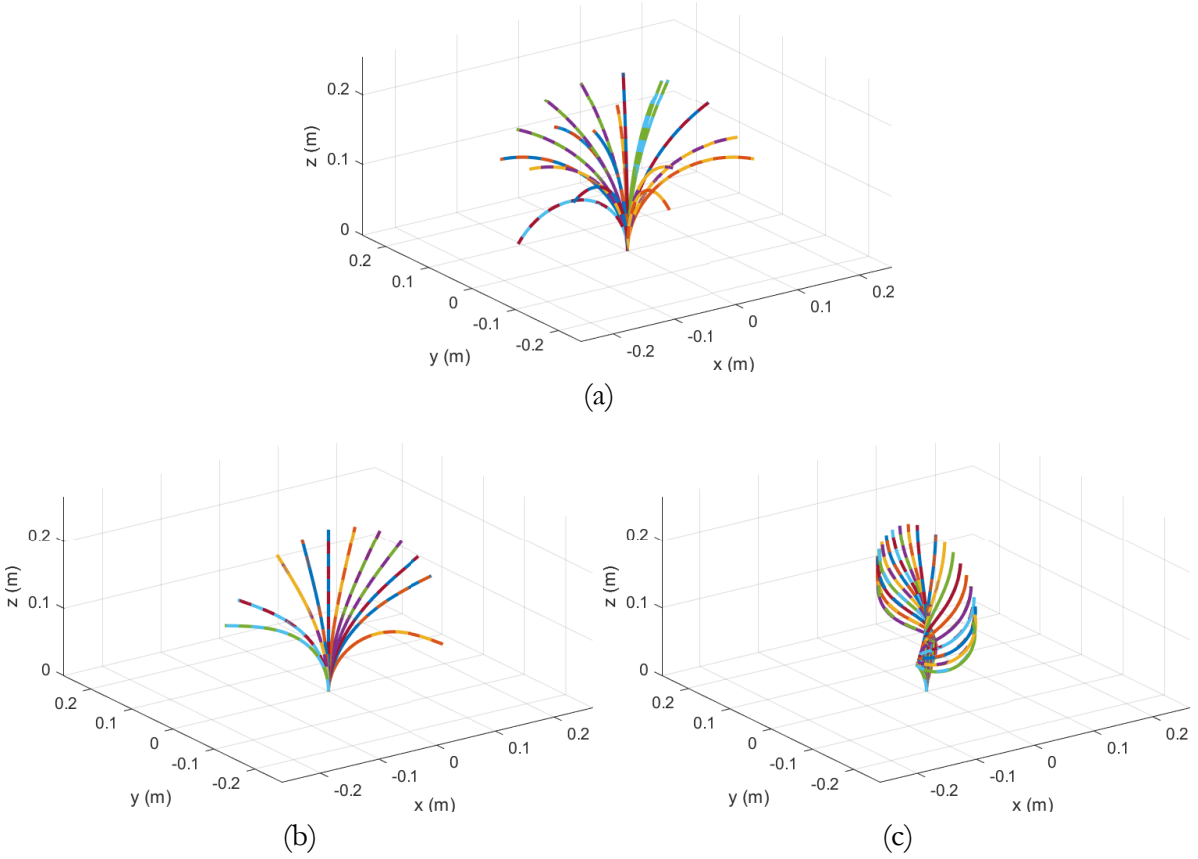

Figure 3.8: A sample of 20 random pairs of the simulation results for single-segment TACRs with (a) parallel routing, (b) convergent routing, and (c) helical routing. The geometry and material parameters of the simulated robot are given in Table 3.1. Full and dashed lines represent simulations obtained using the Newtonian approach and the Lagrangian approach, respectively.

is increased compared to the previous scenarios in order to cover a comparable workspace with the studied routing. Similar existing physical robots of the literature can be found in [Rucker and Webster 2011b, Starke et al. 2017]. The differences in position and orientation between the two approaches are still several orders of magnitudes lower than the length of the robot (see Table 3.2). For this batch of simulations, all cases of both approaches were solved with a single loading step.

3.7.4 Multi-Segment Parallel Routing

As the implementation of multi-segment TACRs considerably varies from one approach to the other (see sections 3.6.1 and 3.6.2), it is interesting to compare simulation results with multi-segment TACRs as well. This section starts with a multi-segment TACR scenario involving no routing path discontinuities. The next section follows up with a scenario that does involve routing path discontinuities defined in equation (3.63).

The multi-segment TACR studied is a three-segment robot with 3 parallel routed tendons per segment at 120° around the backbone. Tendons (1,2,3) terminate in the first segment, tendons (4,5,6) in the second segment, and tendons (7,8,9) in the third segment (see Figure 3.7 – Scenario 3.7.4). The robot geometry and material parameters are the same as for the previous robots, except for the length of the segments, shortening them to $l_j = 100\,\text{mm}$ for a total robot length of $l = 3l_j = 300\,\text{mm}$. Indeed, a too slender robot [Dupont et al. 2022] is subject to instabilities [Li and Rahn 2002] and for some tendon load combinations, multiple solutions (i.e. configurations)

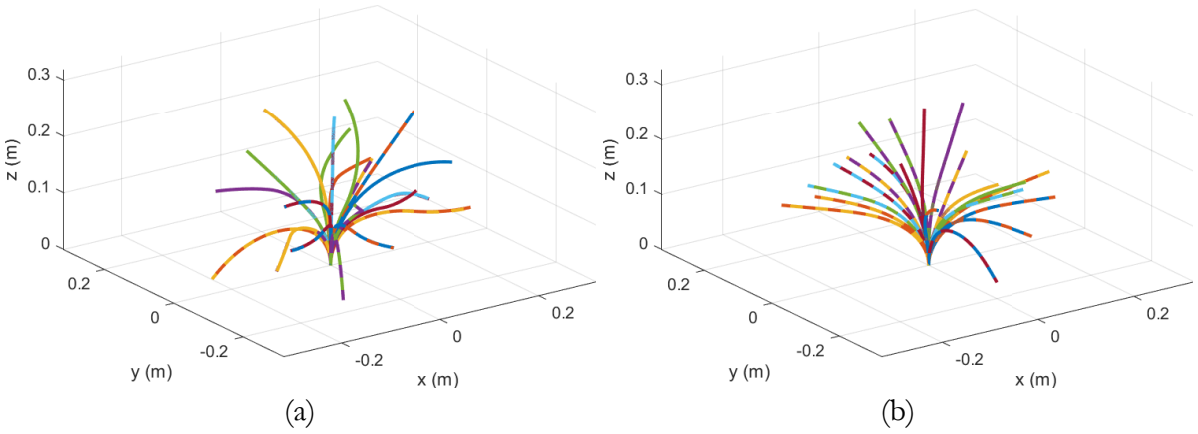

Figure 3.9: A Sample of 20 random pairs of the simulation results for the three-segment TACRs with (a) parallel routing and (b) convergent routing. The geometry and material parameters of the simulated robot are given in Table 3.1. Full and dashed lines represent simulations obtained using the Newtonian approach and the Lagrangian approach, respectively.

would be possible [Bretl and McCarthy 2014]. This simulation scenario can be compared to the physical multi-segment TACR examples of the literature [Jones and Walker 2006a, Gonthina et al. 2020, Amanov et al. 2021].

505 tendon tension combinations that cover the workspace are simulated with integer values of tendon tensions varying from 0 to 5 N. Figure 3.9a displays a sample of 20 pairs of these total 1010 simulations. The robot shapes with both approaches superimpose and the differences between the two approaches in position and orientation of the tip remain very small (0.43% of the robot length) (see Table 3.2). In this scenario, 1.58% of the cases required 2 loading steps with the Newtonian approach. All other cases were solved with 1 loading step.

3.7.5 Multi-Segment Convergent Routing

Here, the same robot as in the previous scenario is simulated, but with 2 convergent tendons per segment. The tendons are only routed convergent in their terminating segment and are routed parallel to the backbone elsewhere. With the same value for $R_t = 8\,\text{mm}$ as for the other cases, the routing paths are defined by

$$D_{i,j}(X) = (-1)^i \, R_t \, \varphi_j(X) \, (0, \cos(\vartheta_j), \sin(\vartheta_j))^T \,, \tag{3.79}$$

with

$$\varphi_j(X) = \begin{cases} 1 & \text{for } X < (j-1)\, l_j \\ 1 - \frac{X-(j-1)l_j}{l_j} & \text{for } (j-1)\, l_j \leq X \leq j\, l_j \\ 0 & \text{for } X > j\, l_j \,, \end{cases} \tag{3.80}$$

where $D_{i,j}(X)$, stands for the routing path of tendon $i = 1..6$ that ends in segment $j = 1..3$ and $\vartheta_j = (j-1)\, 2\pi/3$. As such, the pair of tendons of each segment run on opposite sides of the backbone. The tendons of the first segment are aligned with the $b_X b_Y$-plane. For the following segments, the tendons are shifted 120° counterclockwise with respect to the previous segment (see Figure 3.7 – Scenario 3.7.5).

Figure 3.9b displays a sample of the 686 simulations, corresponding to 343 actuation combinations covering the workspace with integer values of tendon tensions ranging from 0 to 4 N.

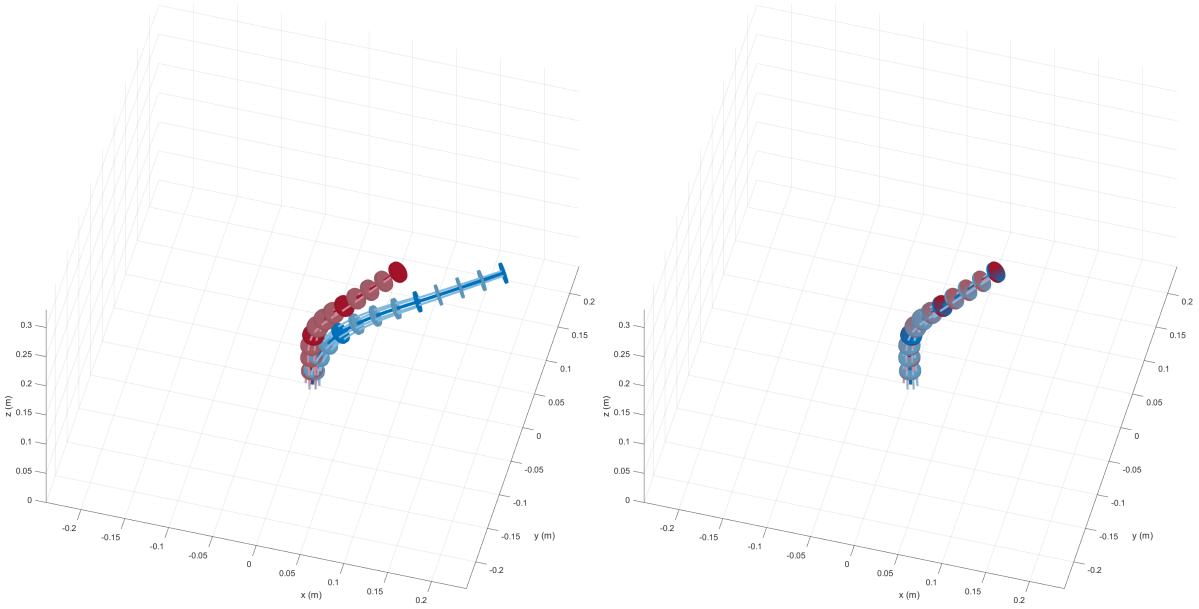

(a) (b)

Figure 3.10: Demonstration of necessity of the tendon slope discontinuity compensation term. The blue and red representations of the TACR correspond to the Newtonian and Lagrangian approaches respectively. The displayed configuration is a randomly sampled configuration from the set of simulations described in section 3.7.5. Left the state-of-the-art Newtonian models (without compensation term) fail to match the real robot shape that is correctly modeled by the Lagrangian approach. Right, including the tendon slope discontinuity compensation term restores proper behavior for the Newtonian approach.

The differences in position and orientation of the tip are reported in the last column of Table 3.2. For this batch of simulations, all cases of both approaches were solved with a single loading step. Building upon a design featuring convergent routings, as presented in [Oliver-Butler et al. 2019], this scenario, with multiple such segments, involves tendon slope discontinuities between the segments. Still, the values are similar to those of other scenarios. In Figure 3.10 and in an online available video[7] an example in shown which the Newtonian approach fails without the slope discontinuity compensation term introduced in section 3.6.1. In some cases, the discrepancies can go up to 50% of the length of the robots.

3.8 Discussion on the Two Mechanical Modeling Approaches for the TACR Case

In terms of mathematical modeling, the Newtonian approach makes use of Newton's action-reaction principle and gathers ad hoc equations to form the global BVP of the problem. The main challenge consists in reshaping the BVP, in order to find an explicit form suited for solving with a shooting method. This challenge is addressed through complex algebraic manipulations [Rucker and Webster 2011b]. On the other hand, the philosophy of Lagrangian mechanics is to consider the system as a whole, removing the need for isolating subsystems and making them interact. The difficulty here resides in reducing the infinite-dimensional problem to a finite-dimensional problem

[7] Video available at: https://youtu.be/W1E-oA42OOM.

in both the spaces of kinematics and statics, the latter involving evolved calculus [Boyer et al. 2021].

Numerically, the results from section 3.7 show that both approaches produce almost identical results. All tip position differences are comprised between 0 and 1.29 mm, which is 8.00% of the robot diameters and stays within 0.43% of the robot lengths. These discrepancies are negligible compared to the modeling errors that are reported in studies that involve experimental setups, which go over 7% of the robot lengths [Starke et al. 2017].

The Lagrangian approach proposes a reduction of the problem that can be adapted for each particular system. Shape functions that determine the size of the residual must be specified to represent the strains in the various segments of the modeled robot. A great variety of choices are available, and it may be challenging to find the strain basis that is best suited to a particular problem while keeping the computational cost low. Including the routing schemes of the tendons as shape functions was proven to be an efficient choice [Renda et al. 2020], but complex interactions between the robot and its environment will however require including higher dimension generic shape functions. Moreover, when modeling multi-segment robots, a number of shape functions must be added for every new segment. Thus, the combination of high dimension shape functions and multiple segments may lead to excessively long residual vectors. The benefit of this reduction is that the variational principles are transferred to the numerical implementation, which are proven to be numerically robust. As such, for virtually any given number of DoF, the problem remains well conditioned and can be solved with Newton-Raphson's method, even for very high actuation and external loads. In our simulations, the benefit of preserving the variational principles through the reduction is demonstrated by the fact that all simulations could be solved with a single loading step.

The Newtonian approach is the easiest to implement, particularly for those not familiar with Lagrangian mechanics. Its infinite configuration space removes the need for determining shape functions. The consequence is that the robustness of the mechanical principles is lost at the implementation. Therefore, the approach is particularly dependent on the initial guess that is fed to the solver. This approach is thus well suited for problems where an approximation of the solution is known (which is seldom the case) or for problems whose solution is close to zero. In other words, the method is efficient for solving non-complex cases with small deformations, but increasing the problem complexity or modeling high strains requires proceeding in steps, which is computationally costly. In the Newtonian approach, multi-segment robots require more complex action-reaction considerations (see section 3.6.1). Moreover, increasing the number of segments entangles the problem without providing more DoF to the state vector or the residual, and therefore makes the convergence less certain for this kind of robots. On the other hand, the constant residual size goes together with an approximately linear relation between the number of segments and the computational cost. Besides, in this approach, computing the Jacobian matrix of the residual vector is complicated and using finite differences to estimate the gradient is less efficient and may lead to inaccuracies.

The above discussed reduction, influencing the size of the residual of the problem in the Lagrangian approach, must not be confused with the spatial discretization. Both approaches require to numerically integrate the PDEs along the backbones, requiring to discretize the backbones over a number of nodes or integration points. Increasing the number of these integration points contributes to the accuracy of the simulations but also increases the computational cost, meaning an equilibrium must be found. On this point, note that the spectral integration benefits from an exponential convergence, compared to the polynomial convergence of the conventional Runge-Kutta integrators [Trefethen 2000]. This enhanced convergence enables to integrate over a reduced number of integration points with the Lagrangian approach (typically 10 to 20).

3.9 Conclusion

The following conclusions result from the whole processes used to model and simulate the presented scenarios and more generally from the acquired experience with these processes. Apart from the numerical implementations presented in this chapter, other numerical methods can be used. For instance, the BVP of the Newtonian approach can be solved with finite differences or spectral methods, while the authors of [Renda et al. 2020, Boyer et al. 2021, Renda et al. 2021] present different numerical methods for the Lagrangian approach. In what follows, the derivation of the Newtonian approach solved with a shooting method is compared to the derivation of the Lagrangian approach solved with Newton-Raphson's method.

Overall, the Newtonian approach is more efficient for two types of problems: (i) problems that include one or only a few segments and involving low tendon tensions, and (ii) problems solved iteratively with a known close solution, as can be the case in robot control. Indeed, starting from a close solution favors the convergence, especially for complex structures. These more complex structures with many segments and tendons, and problems involving large deformations for which the solution is completely unknown have a better chance of convergence with the Lagrangian approach.

As for the Newtonian approach, the Lagrangian approach is more efficient when solving problems iteratively. And even more so, considering the fact that establishing the generalized stiffness matrix $\mathcal{K}_{\epsilon\epsilon}$, the most costly operation, is a constant function of the shape functions Φ and, therefore, is computed only once.

This chapter allowed to highlight the similarities between the Newtonian and Lagrangian approaches, which was previously a strenuous task due to their different frameworks and community backgrounds [Rucker and Webster 2011b, Boyer et al. 2021]. In comparison with the derivations from the literature, substantial additional material was formulated in the present derivation of the Lagrangian approach, improving its intelligibility. Also, a missing piece in the literature related to the implementation of tendon slope discontinuities with the Newtonian approach is added [Rucker and Webster 2011b, Neumann and Burgner-Kahrs 2016, Starke et al. 2017].

With the gained insight on Cosserat rod modeling for continuum robots, and in particular the deep understanding of the Newtonian and Lagrangian approaches, the next chapter dives into the derivation of a whole new model, namely, a Cosserat rod model for CAARs.

Contributions of this chapter

1. The Newtonian and Lagrangian approaches that are currently dominant in the robotics community are presented in a single structured picture. The approaches that did not previously share a common set of notations are here derived using the unified framework of chapter 2.

2. In the case of the Newtonian approach, beyond the works of the literature, the case of a multi-segment TACR with slope discontinuities in the tendon routings between segments is addressed.

3. The derivation of the Lagrangian approach is renewed by a more in-depth derivation of the model through a canonical application of the principle of virtual work.

4. A mathematical proof of equivalence between the two approaches is provided, this mathematical proof is backed by an extensive set of simulations.

5. In the numerical implementation of the Lagrangian approach, the latest work of the literature performs the numerical resolution through explicit time integration of an overdamped equivalent system. In contrast, here, the dedicated section introduces a linearization of the nonlinear static balance equations, which enables using computationally efficient methods (e.g. Newton-Raphson's method).

6. In the numerical implementation of the Lagrangian approach, efficient spectral methods are used to calculate the residual vector and the Jacobian matrix thanks to the use of the inverse kineto-static BVP, and its tangent BVP.

The extensive discussions and confrontations of viewpoints during Matthias Tummers' (MT) thesis have led to the insight that is reflected in the presented derivations. The draft of the Newtonian and Lagrangian approaches (sections 3.3 and 3.4) were respectively written by MT and Frédéric Boyer (FB). Both sections have then gone through numerous iterations of all collaborators. The mathematical equivalence was written jointly by FB and MT. Vincent Lebastard produced the first building blocks of the numerical implementation of the Lagrangian approach. MT completed the implementation with missing elements and implemented the Newtonian approach. The results of section 3.6.1 were initially proposed and implemented by MT, FB helped for the mathematical formalization. The interpretation of the results and the discussion comparing both approaches was first drafted by MT.

4

Modeling Concentric Agonist-Antagonist Robots

4.1 Foreword

From chapter 1 it became clear that a mechanical model for CAARs is a major missing piece in the continuum robotics community. Such a model will allow to deploy CAARs for numerous applications (discussed in section 1.5) by enabling taking into account interactions with the environment and optimizing designs for specific applications or even patients. This chapter derives such a mechanical model. To further put the presented model in perspective, this chapter starts with section 4.2 that presents and discusses the existing CAAR models and other related models from the literature. Sections 4.3 to 4.6 present the new mechanical model for CAARs. Section 4.3 introduces the adopted mechanical modeling approach. Section 4.4 develops the necessary preliminaries regarding the geometrical and mechanical properties of CAARs. Then, section 4.5 derives a kineto-static model for CAARs based on the Cosserat rod theory. At last, section 4.6 implements a Lagrangian mechanics reduction of the system, leading to a generalized static balance formulation, and describes an efficient algorithm for numerically solving it. Finally, section 4.7 discusses the prospects and limitations of the proposed model and concludes the chapter.

While the contents have been revised for inclusion in this manuscript, a major part of this chapter and the corresponding part of the following chapter was submitted to a peer-reviewed journal in the following article (currently in review):

> Matthias Tummers, Frédéric Boyer, Vincent Lebastard, Alexis Offermann, Jocelyne Troccaz, Benoît Rosa, and M. Taha Chikhaoui (2023). "Planar Continuum Concentric Agonist-Antagonist Robots: A Cosserat Rod Model". In review.

4.2 State of the Art Models

Two CAARs models are currently to be found in the literature. Both of these CAAR models are 2D geometry based models, (as opposed to the mechanical model that is derived in this chapter). They are presented in section 4.2.1. Besides, as the structure of CAARs closely resembles PCRs, another natural first step consists in analyzing those models to verify their potential applicability to CAARs. This analysis is carried out in section 4.2.2.

4.2.1 Constant Curvature CAAR Models

The constant curvature model for CAARs is the first model proposed in [Oliver-Butler et al. 2017], when CAARs were initially introduced. It functions as follows. When a CAAR is actuated, the length of the offset neutral lines (i.e. neutral axes[1]) of the tubes above the baseplate changes (see Figure 1.7d page 32). The constant curvature model uses arc geometry while looking at a notch of the system to resolve the difference in length of the neutral lines at this notch. Multiplying this result with the number of notches yields the model for the whole robot. Indeed, the model relates axial displacement at the base of the tubes to the angle of the tip of the tubes while assuming the robot shape to be an in-plane constant curvature arc between its base and its tip.

Due to the constant curvature assumption, this model is limited to regularly notched CAARs (i.e. with parallel neutral lines). Using simple beam mechanics, the actuation push or pull force is approximated for a given configuration of the robot. The underling model being purely geometrical, it can however not take external forces into account.

Subsequently, based on the first model, a piecewise constant curvature model was developed. It models each notch with a constant curvature arc but considers each notch individually [Oliver-Butler et al. 2022]. Computing the moment generated by the bending in each notch and stating that the tension in the robot is constant yields the model of the whole robot. In this model again, the tension is the result of beam mechanics with very strong simplifying approximations (see section II.A of [Oliver-Butler et al. 2022]).

This second model captures the variable curvature shape of variably notched CAARs in 2D for a given input tension or axial displacement at the base of the robot. Although this model has to make use of the tension to link the curvature of the multiple different notches, the underlying model is, again, purely geometrical. Modeling external forces is thus not possible with this second model either. Moreover these models can not be extended to further include friction, to model the dynamics of CAARs, or to consider nonlinear material behaviors.

4.2.2 Related Cosserat Rod Models of Other Continuum Robots

Sections 2.4.1 to 2.4.3 show that the modeling of CAARs is closest to the modeling of MBCRs and especially the kind of MBCRs where the rods are constrained relatively to each other (i.e. PCRs with GICs). Indeed, the offset neutral lines of CAARs can be seen as individual backbones, but constrained around the center of the tubes that are arranged concentrically. As in MBCRs, the consequence of this constraint is the transmission of efforts from one rod to the others and vice versa.

Two such PCRs have been modeled with mechanical models over the recent years. Both elaborate a Cosserat rod model taking into account the interaction of the rods at constraint points that are the disks of the robots.

The PCR with GIC studied in [Orekhov et al. 2017] consists of a number of rods embedded together at their distal extremity and constrained at intermediate constraint points by disks, carried on a central backbone (see Figure 4.1a). In each section, between two successive disks, the individual rods evolve freely in space. To model this robot, the strategy is to model each section individually. The sections are linked by the static balance between them. The internal efforts and

[1]The neutral axis is an axis in the cross section of a beam along which there are no longitudinal stresses or strains when the beam deforms.

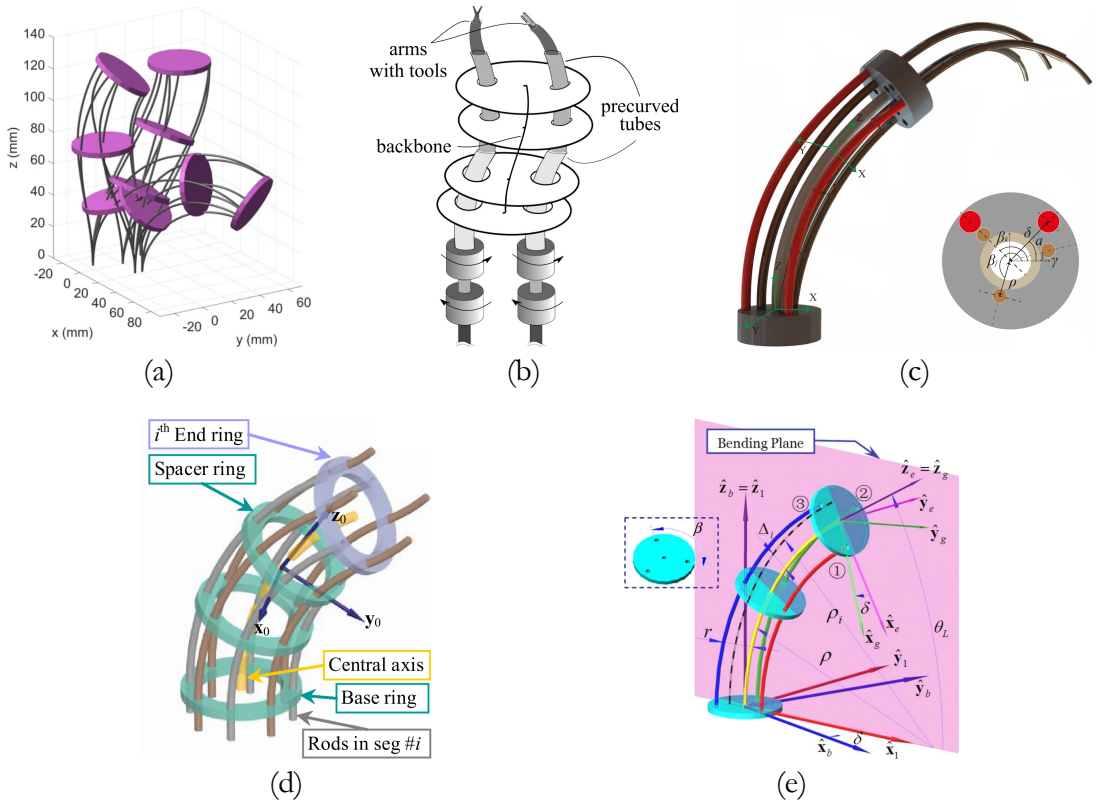

Figure 4.1: (a) The PCR with GICs studied in [Orekhov et al. 2017]. (b) The eccentric tube robot presented in [Wang et al. 2022b]. (c) The eccentric tube robot developed in [Mitros et al. 2022b]. (d) The PCR with GICs featuring many disks and parallel backbones in [Chen et al. 2021]. (e) The Push-pull robot developed in [Xu and Simaan 2008]

pose of the rods propagate to the next section. Two problems arise in such approach. The interaction of the rods at the disks induces discontinuities in their internal efforts. Thus, the internal efforts of each rod exiting each disk is a priori unknown. Also, as the rods can evolve freely in space between the disks, the length of each rod in each section is unknown. To address these problems, the authors formulate a general BVP to solve for all internal efforts. The BVP is solved using a shooting method to iterate over a guess for all these unknowns. Simultaneously, for each rod at each section of each of these iterations, secondary BVPs are solved to find the lengths of the rods in the sections. This method introduces $6n_r + 6 + n_d(4n_r + 6)$ unknowns for the internal efforts, where n_r is the number of rods and n_d the number of disks. For a robot with six rods and four disks this goes up to 162 unknowns to guess for only the outer shooting algorithm, i.e. without counting the unknown lengths of each rod in each section ($n_d\, n_r = 24$).

The eccentric tube robot, first presented in [Wang et al. 2019], consists of only two tubes that are also constrained by intermediate disks, carried on a central backbone (see Figure 4.1b). Here, however, the rods are not fixed at their extremity. More recently, an evolution of the robot was presented in [Wang et al. 2022b] where the rods are replaced by CTCRs. The model derived in this work is similar to the one described above, except for the free ends of the rods and for the fact that the interactions of the tubes with the disks are considered to be point forces. In the initial publication [Wang et al. 2019], the authors describe their implementation as follows. A global BVP solves for the sliding of the rods (the length of the rod sections) and the interaction forces. And three individual BVPs solve for the two tubes and the backbone at each iteration of the global BVP. In these iterations it is noted that the BVPs of the tubes should be solved before solving the backbone as the latter needs tube orientations as inputs. In this model implementation also, the nested BVPs and the high dimension parameter spaces lead to complex numerical issues. Two years later, the authors describe a slightly different implementation [Wang et al. 2022b]. Here they guess for all unknowns at once and integrate the two tubes and the backbone simultaneously but independently. As the used numerical methods are very sensitive to the initial guess, the authors suggest to iteratively solve close configurations by taking small steps, starting from a known solution (see Figure 3.5 page 77). They divide the residual of the shooting function into three parts and affect weights to the different parts. The weights are hand selected and subsequently tuned empirically. They solve the problem over an additional, constrained parameter space for the variables representing the sliding of the rods such that the disks are not allowed to make contact.

A similar model for a robot with multiple eccentric CTCRs constrained by disks (see Figure 4.1c) is the model derived in [Mitros et al. 2022b]. Unfortunately, the presented model does not propose solutions to simplify the problem and the numerical resolution is mentionned in a rather concise manner.

Another recent work of interest, modeling a PCR with the Cosserat theory of rods, is the study conducted by the authors of [Chen et al. 2021] (see Figure 4.1d). Two major assumptions make this model quite different, however. First, the rods are assumed to run parallel to the backbone at all times. This is possible by using a theoretically infinite number of spacer disks and parallel routing paths. Of course, in the physical robot, the actual number of disks used, introduces discrepancies to some extent. Secondly, the rods are assumed to not undergo torsion. This is possible by actuating the robot in a sole push-pull manner, by only permitting external efforts that lie in the robot bending plane, and by considering that, with the previous assumption, the rods run parallel to the backbone. These two assumptions allow to derive relations between the arc lengths of the different rods at a given section of the robot. Further, this considerably reduces the size of the parameter spaces of the problem. With all these assumptions however, this PCR model tends to be closer to the model of the push-pull robot developed in [Xu and Simaan 2006, Xu and Simaan 2010] (see Figure 4.1e).

4.2.3 Discussion

Currently the models from the literature devoted to CAARs are 2D geometry based models. While one of the models is capable of capturing CAARs with in-plane variable curvature shapes, the models are incapable of modeling CAARs in interaction with their environment.

Regarding the discussed PCR models, despite their intricacy and the numerical complications, auspicious results were reported. The major difference with CAARs however, is that the interaction constraints of the multiple rods operate at distinct locations instead of continuously, as it is the case with the concentricity constraint of CAARs.

From these two statements, it is clear that the continuum robotics community would greatly benefit from a mechanical model for CAARs and that a whole new model needs to be derived from square one.

4.3 CAAR Mechanical Modeling Approach

The three following sections derive a mechanical model for CAARs through the Lagrangian approach. Based on the previous analysis, the choice for the Lagrangian approach over the Newtonian approach can be explained as follows.

Each of the presented state of the art PCR models is derived through a Newtonian approach. In each of the models, this choice brings in numerous interaction forces to consider between the rods at the GIC points. Depending on the model assumptions and the resolution method, each or part of these interaction forces translates into unknowns of the problem to solve for. The consequence of high dimension parameter spaces is that the numerical resolution of the problem becomes a challenging task. Moreover, with such tangled problems with complex numerical resolution methods, it becomes difficult to unwind the intricacy and to capture insight on the behavior of the robot.

In the case of CAARs, because the constraints are continuous (concentricity constraints) and should be verified at each integration step, following a similar approach leads to infinitely high parameter spaces. Adopting the Lagrangian approach removes the need for isolating the subsystems and hence, does not require considering the interaction forces.

The first step to derive the model is to express the geometrical parameters and mechanical properties of notched tubes as continuous functions along their length. Subsequently, a redundant Cosserat model is formulated based on the classical ingredients of the Cosserat rod theory and additional elements specific to CAARs. Then, following the Lagrangian methodology, the kinematics of the CAAR system is parameterized to a minimal set of parameters compatible with the constraints. A Rayleigh-Ritz reduction is operated, projecting the internal and external loads to vectors of generalized forces. Finally, the generalized forces are used to express the static balance of the system, providing the residual of the problem. This final formulation is called the reduced model. Figure 4.2 presents a flowchart synthesizing the different steps leading to the reduced model, to help follow through the developments.

4.4 Geometrical Parameters and Mechanical Properties

CAARs consist of concentric tubes attached at their distal ends, hereafter called the tip. The tubes have an asymmetric geometry that offsets their neutral bending axis form the tube centerlines (see Figure 4.3a to Figure 4.3c). The tubes can be translated axially at their base to induce a movement

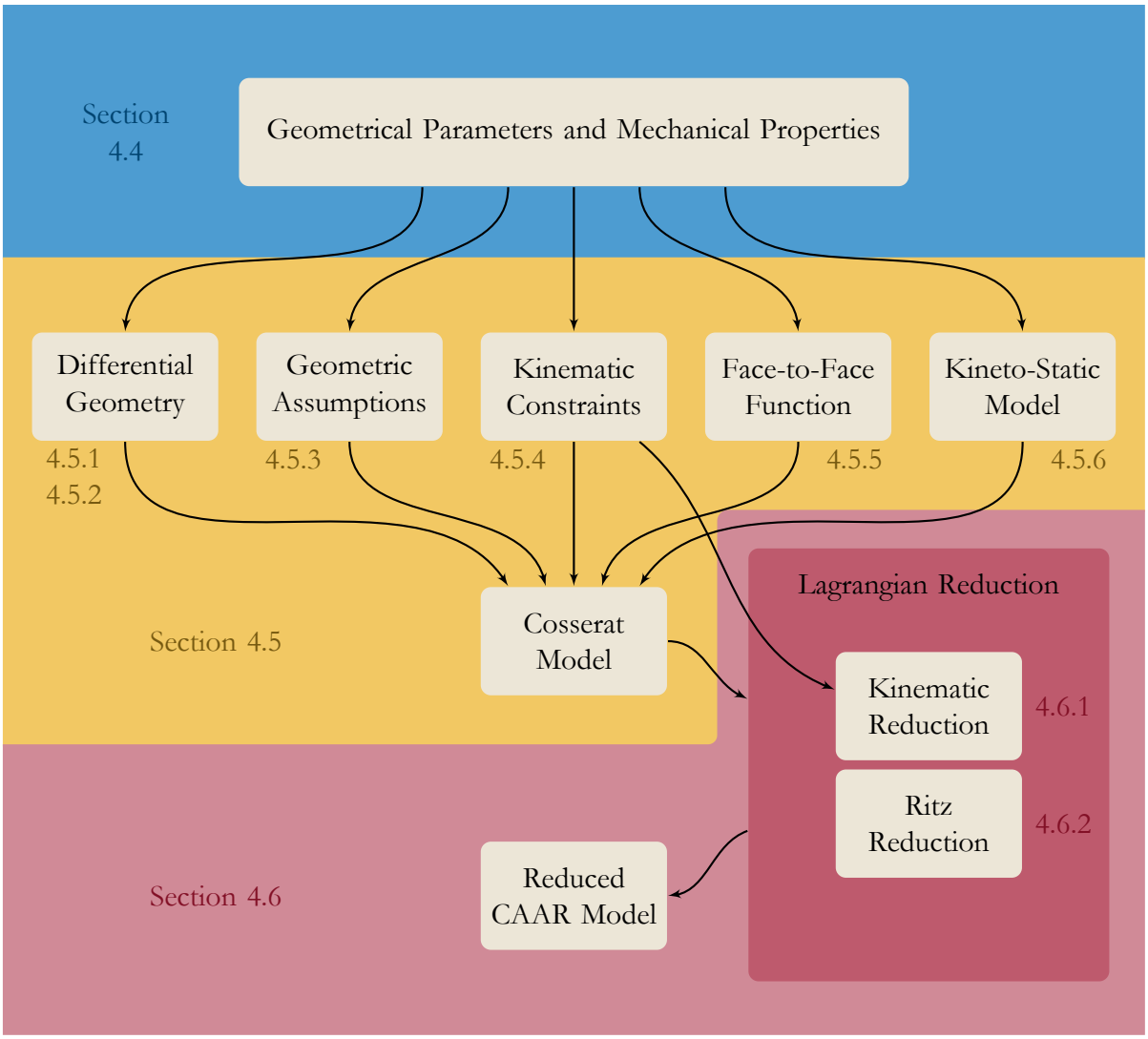

Figure 4.2: . Synthesis of the steps producing the reduced Cosserat rod model for CAARs. The colored areas correspond to the three sections of this chapter devoted to the derivation of the model (corresponding section numbers are provided).

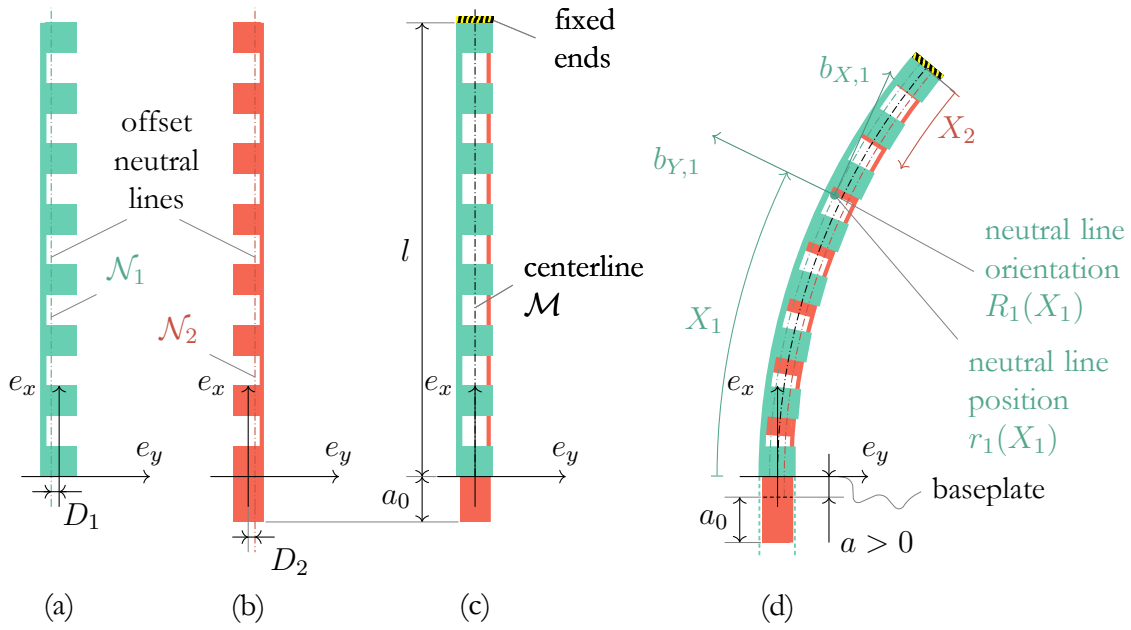

Figure 4.3: Composition and working principle of a CAAR. (a) The outer tube 1 in its reference configuration (b) The inner tube 2 in its reference configuration. (c) The tubes assembled forming the CAAR in its reference configuration. (d) Example of an actuated configuration of the CAAR where $a > 0$.

by the difference in length and position of the offset neutral lines (see Figure 4.3d). In the following, the index of the outer tube is 1 and index of the inner tube is 2. Quantities that are related to tube 1 are labeled with a subscript $\bullet_1$ and those related to tube 2 with a subscript $\bullet_2$. The subscript $\bullet_i$ will be used for generic expressions[2]. As for the previous chapters, the symbols and notations are summarized in the 'Notations' preamble page 13. Due to limitations in the representation of mathematical symbols, there is a slight overlap in notation between this chapter and the previous one. Wherever this occurs, it is clearly specified in the 'Notations' preamble.

The next section derives a kineto-static model for CAARs. This model approximates the two tubes as Cosserat rods whose cross-sectional parameters vary continuously along their axis. As is the case in the theory of rods, these design parameters consist of the area $\mathcal{A}$, the centroids, and the moments of inertia $I_{X,Y,Z}$ of the non-symmetric cross-sections of each of the tubes. The remainder of this section is devoted to the expression of all these parameters. Whenever derivations apply to both the inner and the outer tubes, the tube subscripts $i = 1, 2$ will be omitted for clarity.

4.4.1 Neutral Line and Cross-Sectional Area of Notched Tubes

Asymmetrically cutting notches out of plain tubes offsets the neutral line of each tube towards the thin remaining backbone. The geometrical parameters of such notches are displayed in Figure 4.4. By cutting regular notches, the neutral lines are parallel to the centerline of the tubes and the robot shape approximates a constant curvature when actuated in free-space. By varying the geometry of the notches along a tube, it is possible to obtain neutral lines with varying offset from the tube centerline. Figure 4.5 schematizes such tubes with convergent and divergent neutral lines.

[2]In chapter 3, the subscript $\bullet_i$ is related to the i-th tendon instead of to the i-th tube. This should however not bring in any confusion as CAARs do not feature tendons and TACRs are not composed of multiple tubes.

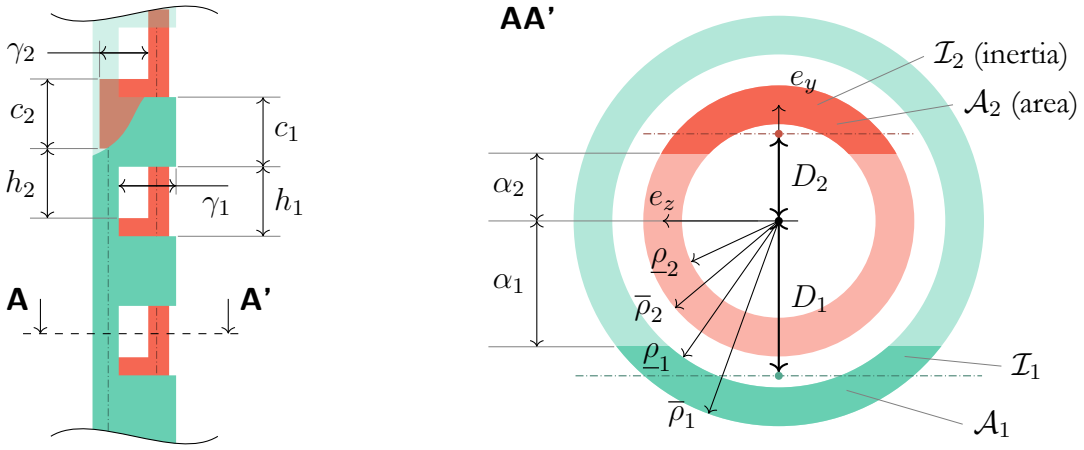

Figure 4.4: Partial front view and sectional view of a CAAR. Left, the front view displays the geometrical parameters of the notches of tubes 1 and 2. Right, the sectional view corresponds to the AA' cross-section of the front view. The clearer parts show where the notches are cut out of the tubes, offsetting the neutral line (dash-dot lines).

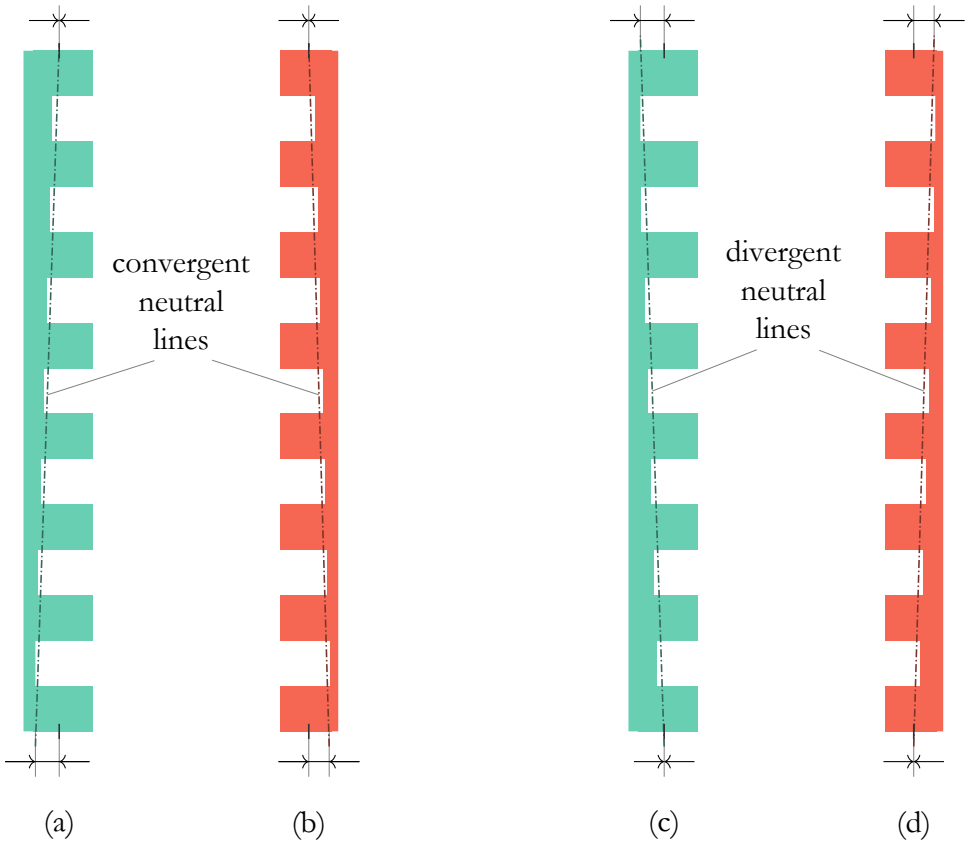

Figure 4.5: Varying the notch depth along the tubes varies the position of the offset neutral line. (a) and (b) tubes with convergent neutral lines. The notch depth decreases towards the tip of the tubes. (c) and (d) tubes with divergent neutral lines. The notch depth increases towards the tip of the tubes.

Prototypes with such variable neutral lines are capable of achieving variable curvature shapes such as the CAAR presented in Figure 1.8b page 33.

Let $\overline{\rho}$ and $\underline{\rho}$ denote the outer and inner radius of a tube. Following the methodology presented in [York et al. 2015, Swaney et al. 2016], the first step is to compute the areas $\overline{\mathcal{A}}$ and $\underline{\mathcal{A}}$ of the pieces of full disk of radius $\overline{\rho}$ and $\underline{\rho}$ above $Y = \alpha$ (see Figure 4.4), as well as the offsets of their centroids $\overline{D}$ and $\underline{D}$, with respect to the CAAR centerline

$$\overline{\mathcal{A}} = \frac{\overline{\rho}^2(\overline{\phi} - \sin(\overline{\phi}))}{2}\,, \quad \underline{\mathcal{A}} = \frac{\underline{\rho}^2(\underline{\phi} - \sin(\underline{\phi}))}{2}\,, \tag{4.1}$$

$$\overline{D} = \frac{4\overline{\rho}\sin^3(\frac{1}{2}\overline{\phi})}{3(\overline{\phi} - \sin(\overline{\phi}))}\,, \quad \underline{D} = \frac{4\underline{\rho}\sin^3(\frac{1}{2}\underline{\phi})}{3(\underline{\phi} - \sin(\underline{\phi}))}\,, \tag{4.2}$$

where the notations

$$\overline{\phi} = 2\cos^{-1}(\alpha/\overline{\rho})\,, \quad \underline{\phi} = 2\cos^{-1}(\alpha/\underline{\rho}) \tag{4.3}$$

were introduced, with $\alpha = \gamma - \overline{\rho}$ and γ the depth of the notches as shown in Figure 4.4. Then, using two such pieces of full disk, one of positive, the other with negative area, the cross-sectional area of the notched tube is

$$\mathcal{A} = \iint dY\,dZ = \overline{\mathcal{A}} - \underline{\mathcal{A}}\,, \tag{4.4}$$

while the offset of its centroid is

$$D = \frac{1}{\mathcal{A}}\iint Y\; dY dZ = \frac{\overline{D\mathcal{A}} - \underline{D\mathcal{A}}}{\overline{\mathcal{A}} - \underline{\mathcal{A}}}\,. \tag{4.5}$$

In this implementation, extra attention must be paid to check whether the notches reach deeper than the opposing inner wall of the tube ($\gamma > \underline{\rho} + \overline{\rho}$). In this case $\underline{\mathcal{A}} = 0$ and the offset is simply $D = \overline{D}$.

4.4.2 Cross-Sectional Inertia and Stiffness of Notched Tubes

The stiffness of the tubes depends on the second area moments of their cross-sections. Assuming that the deformation essentially operates in the notched parts of the tubes, these moments are computed at these locations only. Indeed, for a set of springs linked in series, the compliance (i.e. the inverse of the stiffness) is additive. This means that the parts of the tubes between the notches which are virtually infinitely rigid do not contribute to the general stiffness of the whole notched tube. Following algebraic manipulations, the cross-sectional second area moments about b_X, b_Y, and b_Z read

$$\mathcal{I}_X = \mathcal{I}_Y + \mathcal{I}_Z\,, \tag{4.6}$$

$$\mathcal{I}_Y = \iint Z^2\; dY dZ = \frac{\overline{\rho}^4}{48}\Psi_Y(\overline{\rho}) - \frac{\underline{\rho}^4}{48}\Psi_Y(\underline{\rho})\,, \tag{4.7}$$

$$\mathcal{I}_Z = \iint Y^2\; dY dZ = \frac{\overline{\rho}^4}{16}\Psi_Z(\overline{\rho}) - \frac{\underline{\rho}^4}{16}\Psi_Z(\underline{\rho}) - \mathcal{A}D^2\,, \tag{4.8}$$

with

$$\Psi_Y(\rho) = 6\pi - 12\sin^{-1}\left(\frac{\alpha}{\rho}\right) - 8\sin\left(2\sin^{-1}\left(\frac{\alpha}{\rho}\right)\right) - \sin\left(4\sin^{-1}\left(\frac{\alpha}{\rho}\right)\right)\,, \tag{4.9}$$

$$\Psi_Z(\rho) = 2\pi - 4\sin^{-1}\left(\frac{\alpha}{\rho}\right) + \sin\left(4\sin^{-1}\left(\frac{\alpha}{\rho}\right)\right)\,. \tag{4.10}$$

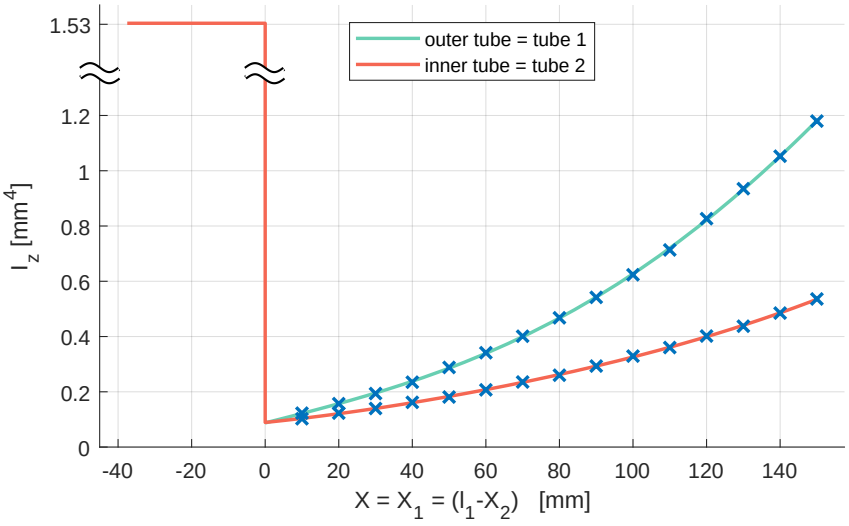

Figure 4.6: Varying bending inertia along the length of tubes with a convergent neutral line (see Figure 4.5a and Figure 4.5b). The blue marks indicate the inertia as calculated by equation (4.8) at each of the notches for the tubes of a robot with the following parameters (all units are mm): $\overline{\rho}_1 = 4.5$; $\underline{\rho}_1 = 3.7$; $\overline{\rho}_2 = 3.2$; $\underline{\rho}_2 = 2.4$; $h = 5$; $c = 5$; $l = 150$; $\gamma_1(0) = 8.20$; $\gamma_1(l) = 7.20$; $\gamma_2(0) = 5.60$; and $\gamma_2(l) = 4.95$. $\gamma_i(0)$ and $\gamma_i(l)$ are respectively, the initial and final depth of the notches varying linearly from the bottom to the tip of the tubes. The green and red lines are the interpolations of the calculated inertia for any X-cross-section of the tubes. The inertia for the inner tube $\mathcal{I}_2(X_2)$ is also defined for $X < 0$ (or equivalently $X_2 > l_1$) in the reference (straight) configuration because this non-notched part can be slid inside the outer tube. The colors correspond to the colors of the tubes across Figures 4.3 to 4.8.

Referring to section 2.3.3 and assuming that the material is homogeneous, the calculated inertias allow to model the stiffness of a tube with the reduced Hooke matrix

$$\mathcal{H} = \text{diag}\left(\mathcal{G}\mathcal{I}_X, \mathcal{E}\mathcal{I}_Y, \mathcal{E}\mathcal{I}_Z, \mathcal{E}\mathcal{A}, \mathcal{G}\mathcal{A}, \mathcal{G}\mathcal{A}\right) , \tag{4.11}$$

with $\mathcal{E}$ Young's modulus, $\mathcal{G} = \mathcal{E}(1+\nu)/2$ the shear modulus, and ν Poisson's ratio.

4.4.3 From Notched Tubes to Continuous Material Properties

Reintroducing the tube indices ($i = 1$ for the outer tube and $i = 2$ for the inner tube) into the notations, let us note that the above expressions of cross-sectional parameters $\mathcal{A}_i$, D_i and $\mathcal{I}_{X,i}, \mathcal{I}_{Y,i}, \mathcal{I}_{Z,i}$ depend on the considered notch along the i-th tube through the design parameters γ_i, h_i, and c_i. In the rest of this chapter, the tubes are modeled as continuous one-dimensional media of (non-symmetric) cross-sections labeled by a material abscissa X_i. Defining X_i as the arc-length of the neutral line of tube i in its reference configuration, the discrete values of $\mathcal{A}_i$, D_i and $\mathcal{I}_{X,i}, \mathcal{I}_{Y,i}, \mathcal{I}_{Z,i}$ computed at each notch with the above formulas, need to be changed into continuous functions of $X_i \in [0, l_i]$. This is achieved by polynomial interpolation and illustrated by Figure 4.6, in the case of $\mathcal{I}_{Z,i}$, and for tubes with convergent neutral lines (see Figure 4.5a and Figure 4.5b). In the next section, a kineto-static model of a CAAR able to deform in the $e_x e_y$-plane is proposed. This model will depend on the neutral line offset functions D_1 and D_2 of the two tubes 1 and 2, their cross-section area functions $\mathcal{A}_1, \mathcal{A}_2$ (gravity is a-priori not neglected), and their second inertia moments about b_Z only. For the sake of concision, these inertias will be noted $\mathcal{I}_{Z,1} = \mathcal{I}_1$ and $\mathcal{I}_{Z,2} = \mathcal{I}_2$.

4.5 Cosserat Rod Modeling Applied to CAARs

The present model considers a CAAR subject to planar deformations. The tubes define two material bodies denoted $\mathcal{B}_1$ and $\mathcal{B}_2$. The ambient space is equipped with a fixed reference frame $\mathcal{F}_s = (O, e_x, e_y, e_z)$ called the inertial frame, located at the base of $\mathcal{B}_1$ that is clamped in the baseplate. The baseplate is defined as the $e_y e_z$-plane. Each of the tubes is modeled as a single Cosserat rod thanks to the above approximation process of its cross-sectional parameters. Let us first recall that in Cosserat's theory, a beam is considered as a continuous stack of rigid material cross-sections, along a reference material line drawn along the largest dimension of its reference (unstressed) configuration. By adjusting the definitions of this reference line and the cross-sections, it is possible to accommodate Cosserat's theory for modeling CAARs.

4.5.1 Material Parameterization of the Rods

In this section, the CAAR is considered only in its reference (straight) configuration (or material space), in which its centerline noted $\mathcal{M}$ is assumed to be rectilinear[3] (see Figure 4.7). The reference material line of each tube i is defined as the line of its cross-section centroids, or "neutral line", noted $\mathcal{N}_i$. Each of the cross-sections of $\mathcal{B}_i$ is labeled by a Lagrangian continuous index $X_i \in [0, l_i]$ that is naturally defined as the arc length along $\mathcal{N}_i$ of total length l_i oriented from the base to the tip for tube 1, and from the tip to the base for tube 2, as indicated in Figures 4.3 and 4.7. It is important to note here that, although the geometry of the bodies $\mathcal{B}_i$ appears to be straight at rest, $\mathcal{N}_i$ is in general not parallel to $\mathcal{M}$ and may even be curved. To easily grasp the consequences of the concentricity of the two tubes, it is convenient to choose the material cross-sections of the tubes as orthogonal to $\mathcal{M}$ (in the reference configuration). Note that this choice differs from common practice in rod theory where, in general, the geometric centerline and the neutral line of a rod coincide. In the next section, the Cosserat model will naturally accommodate for this choice, by declaring a shear offset field (consequence of design) along each tube.

4.5.2 Parameterization of the Deformation of the Tubes

Once the material reference lines and cross-sections are defined, the procedure of section 2.3.1 is applied but, in this case, once for each neutral line. Thus, the equations are rewritten with a subscript $\bullet_i$.

A moving cross-sectional frame $\mathcal{F}_i(X_i) = (r_i, b_{X,i}, b_{Y,i}, b_{Z,i})(X_i)$ is attached to each cross-section, whose origin $r_i(X_i)$ is located along $\mathcal{N}_i$, while $b_{X,i}(X_i)$ is the unit normal vector to the cross-section, oriented towards increasing X_i, and $(b_{Y,i}, b_{Z,i})(X_i)$ completes $b_{X,i}$ to form an orthonormal basis according to the schematic of Figure 4.7. For all $X_i \in [0, l_i]$, the pose of $\mathcal{F}_i(X_i)$ with respect to $\mathcal{F}_s$ is parameterized by a homogeneous transformation $g_i(X_i) \in SE(2) \subset SE(3)$ as

$$g_i = \begin{pmatrix} R_i(X_i) & r_i(X_i) \\ 0_{1\times 4} & 1 \end{pmatrix}, \quad r_i = \begin{pmatrix} r_{X,i}(X_i) \\ r_{Y,i}(X_i) \\ r_{Z,i}(X_i) \end{pmatrix}. \tag{4.12}$$

[3]The extension of the model to CAARs that have precurved reference configuration is straightforward but not presented here for better readability. In the case of precurved CAARs, the precurvature is captured by a reference twist component ξ_a^0 (cf. computation of $\epsilon_i = \xi_{a,i} - \xi_{a,i}^0$ in equation (4.44)).

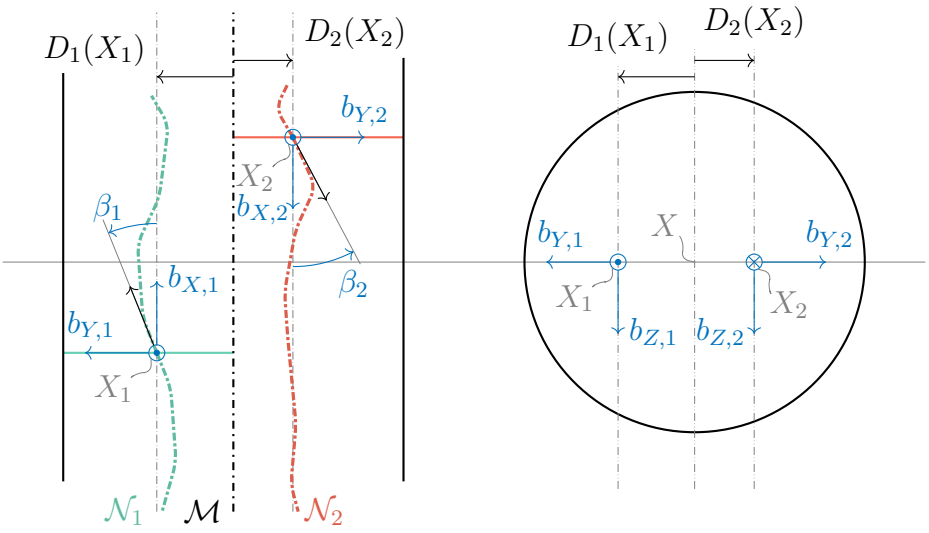

Figure 4.7: Parameterization of the reference (straight) configuration of a CAAR with non-parallel neutral (centroid) lines. Left, lateral view. Right, top view.

The internal deformation of each tube is defined by the field of twists in $se(2) \subset se(3) \cong \mathbb{R}^6$

$$\xi_i = \left(g_i^{-1} \frac{\partial g_i}{\partial X_i} \right)^\vee , \tag{4.13}$$

where $\xi_i = (K_i^T, \Gamma_i^T)^T$, with $K_i = (K_{X,i}, K_{Y,i}, K_{Z,i})^T$ and $\Gamma_i = (\Gamma_{X,i}, \Gamma_{Y,i}, \Gamma_{Z,i})^T$, respectively the angular and linear rates of change.

According to section 2.3.5, ξ_i is partitioned as

$$\xi_i = \bar{B}_i \xi_{c,i} + B_i \xi_{a,i} , \tag{4.14}$$

where B_i and $\bar{B}_i$ are two selection matrices associated to tube i. In all the following developments, the tubes of the CAAR are modeled as two Kirchhoff rods moving in the $e_x e_y$-plane. The selection matrices are therefore

$$B_1 = B_2 = (0,0,1,0,0,0)^T , \quad \bar{B}_1 = \bar{B}_2 = \begin{pmatrix} 1 & 0 & 0 & 0 & 0 & 0 \\ 0 & 1 & 0 & 0 & 0 & 0 \\ 0 & 0 & 0 & 1 & 0 & 0 \\ 0 & 0 & 0 & 0 & 1 & 0 \\ 0 & 0 & 0 & 0 & 0 & 1 \end{pmatrix}^T , \tag{4.15}$$

that ensure that the allowed components of the spatial twists are

$$\xi_{a,1}(X_1) = K_{Z,1}(X_1) , \quad \xi_{a,2}(X_2) = K_{Z,2}(X_2) . \tag{4.16}$$

Once the selection matrices are established, the next step is to determine the value of ξ_{c_i} in equation (4.14). With $\bar{B}_i$ defined by equation (4.15), ξ_{c_i} is composed of five components $\xi_{c_i} = \xi_{c_i}^0 = (K_{X,i}^0, K_{Y,i}^0, \Gamma_{X,i}^0, \Gamma_{Y,i}^0, \Gamma_{Z,i}^0)$, $(i = 1, 2)$. To determine the values of these components, the first step is to note that, since the deformation holds in a plane normal to b_Z, $\Gamma_{Z,i}^0 = K_{X,i}^0 = K_{Y,i}^0 = 0$. Second, as Kirchhoff rods are inextensible, $\Gamma_{X,i}^0 = 1$. Finally, with the definition of the material cross-sections and neutral lines (see section 4.5.1), $\Gamma_{Y,i}^0$ measures the angle between the unit tangent to $\mathcal{N}_i$ at X_i, and the unit normal to the X_i cross-section, respectively defined by dr_i/dX_i and $b_{X,i}$.

In the terms of Cosserat rod theory, $\Gamma^0_{Y,i}$ stands for an independent shear component that can be identified by a small angle $\beta_i(X_i)$ measuring the slope of the profile of $\mathcal{N}_i$ along the CAAR centerline $\mathcal{M}$ (as sketched in Figure 4.7). In accordance with Kirchhoff's theory, these shear offsets are not DoF of the CAAR and do not store any internal energy, but instead, are fixed by design through the relationships

$$\beta_i(X_i) = \frac{dD_i}{dX_i}(X_i)\,, \tag{4.17}$$

which are deduced from simple geometric considerations applied to Figure 4.7, with $X_i \in [0, l_i] \mapsto D_i(X_i) \in \mathbb{R}^+$, the function defining the oriented distance from $\mathcal{M}$ to $\mathcal{N}_i$ along the second unit vector $b_{Y,i}$ of $\mathcal{F}_i(X_i)$. Gathering all the ingredients, the expression of ξ_{c_i}, in the partition of equation (4.14) writes

$$\xi_{c,i}(X_i) = \xi^0_{c,i}(X_i) = (0, 0, 1, \beta_i(X_i), 0)^T = (0, 0, \Gamma_i^{0T})^T\,, \tag{4.18}$$

with β_i ($i = 1, 2$) defined by equation (4.17).

4.5.3 Geometric Assumptions of the Model

The tubes are slender bodies, i.e. $|d/l| \simeq \varepsilon$ where $d = 2\overline{\rho}_1$ is the diameter and $l = l_1$ the length of the outer tube, both being typical characteristic values of the CAAR, and ε is a small positive number. Moreover, the Cosserat rod model assumes finite deformations and small strains. First, this means that $|K_{Z,i}d|$ is a small quantity compared to unity. Second, since the tilt $\beta_i(X_i)$ of the neutral lines along the CAAR is captured by the shear component of the model, these tilts must be small as well. Third, the translation of the portion of tube 2 below the baseplate, noted a in Figure 4.3, characterizes the retraction of tube 2 and is also a small quantity compared to l (typically the displacement actuation a is of the order of the diameter d of the CAAR). All these assumptions that are compatible with the operating principle of a CAAR, can be summarized as follows:

$$|K_{Z,i}d| \simeq \varepsilon\,, \quad \left|\frac{dD_i}{dX_i}\right| = |\beta_i| \simeq \varepsilon\,, \quad \left|\frac{a}{l}\right| \simeq \varepsilon\,. \tag{4.19}$$

According to Cosserat's model, the next section derives a model for CAARs consistent to first order approximation with respect to ε. In practice, this means that any quantity of the order of ε^2 and higher orders is ignored in the developments. A more general summary of the assumptions of the present model is given in Table 4.1.

As a first illustration of the use of these assumptions, let us consider the CAAR in its reference (straight) configuration. If $X \in [0, l]$ denotes the length along its rectilinear central line $\mathcal{M}$, measured from its base to its tip (see Figure 4.7), then $dX = \pm\cos(\beta_i)dX_i \simeq \pm(1 - \beta_i^2/2)dX_i$ (positive if $i = 1$, negative if $i = 2$) and thus, when considering only the first order of ε,

$$X \simeq X_1 \simeq l_1 - X_2\,, \quad \forall (X_1, X_2) \in [0, l_1] \times [0, l_2 - a_0]\,, \tag{4.20}$$

where a_0 is the length of the portion of the inner tube below the baseplate when the CAAR is at rest. As will be made clear in the next section, this correspondence between the two tube labels no longer holds once the CAAR deforms. To address this challenge, section 4.5.5 derives a so-called face-to-face function that relates the labels of the tubes in any configuration.

Table 4.1: Summary of the assumptions of the CAAR model.

1.	The considered CAARs are slender robots, i.e. $\|d/l\| \ll 1$.
2.	The robots deform in the small strain regime. As a consequence $\|K_{Z,i}D\| \ll 1$.
3.	The model considers ideal sliding of the tubes (concentricity and guiding constraints), i.e. without friction.
4.	The bending of notched tubes is assumed to operate essentially in the notched parts.
5.	The neutral lines of the notched tubes are assumed to be continuous material lines and the mechanical properties of the tubes are continuous functions along the length of the tubes.
6.	The tubes are made out of homogeneous material.
7.	The tubes are modeled as in-plane bending Kirchhoff rods. Thus, in the model, the tubes undergo no shearing, torsion, or extension/compression and the bending occurs in-plane through a single component $K_{Z,i}$.
8.	The tilt of the neutral lines is supposed to be small, i.e. $\|dD_i/dX_i\| = \|\beta_i\| \ll 1$.
9.	The maximum translation actuation of the tubes is of the order of the diameter of the robot, thus $\|a/l\| \ll 1$.
10.	There is sufficient clearance between the tubes such that the notched outer tube parts can bend unhampered around plain inner tube parts and vice-versa.

4.5.4 Kinematic Constraints

When tube 2 is pulled ($a > 0$) or pushed ($a < 0$) through the baseplate (i.e. the $e_y e_z$-plane) defined in Figures 4.3 and 4.4, it slides into tube 1. Thus, the CAAR is subject to internal and external sliding contacts. These contacts are all considered ideal, i.e. friction-less, and can therefore be fully modeled by kinematic constraints. To capture these constraints, it is convenient to define a function $\tilde{X}_2(\,\cdot\,) : X_1 \in [0, l_1] \to [0, \tilde{X}_2(0)]$, named face-to-face function since it gives the label $\tilde{X}_2(X_1)$ of the cross-section of tube 2 co-planar with that of the X_1-cross-section of tube 1. Denoting $\tilde{X}_2^0(\,\cdot\,)$ the particular value of this function in the reference (straight) configuration of Figure 4.7, one can see from equation (4.20) that $\tilde{X}_2^0(X_1) = l_1 - X_1$ along $[0, l_1]$. However, as soon as the CAAR bends, the two tubes slide relative to each other, and a deformation-dependent shift appears between the initially coincident sections X_1 and $X_2 = l_1 - X_1$ on the reference configuration (see Figure 4.8). As will be detailed hereafter, this axial displacement brings first order terms with respect to ε in the kinematic model of the CAAR, and consistently with the order of approximation of the model, one must consider $\tilde{X}_2(X_1) \neq \tilde{X}_2^0(X_1) = l_1 - X_1$ in any deformed CAAR configuration. Throughout this chapter, any function $f_2(\,\cdot\,)$ related to tube 2, and defined on $[0, l_2]$, is associated to its pull-back function $\tilde{f}_2(\,\cdot\,) = f_2 \circ \tilde{X}_2(\,\cdot\,)$ defined on $[0, l_1]$ by

$$f_2(\tilde{X}_2(X_1)) = \tilde{f}_2(X_1)\,. \tag{4.21}$$

With this relabeling operation and the definition of the material cross-sections along the two tubes, it is henceforth possible to model the concentricity of the two tubes above the baseplate, i.e. $\forall (X_1, X_2) \in [0, l_1] \times [0, \tilde{X}_2(0)]$. The two cross-sections facing each other on each of the two tubes are forced to evolve in the same plane, i.e. forced by the (ideal) point geometric constraints. Introducing the notation $D(X_1) = D_1(X_1) + \tilde{D}_2(X_1)$, the positions of the two cross-sections

are related by the constraint

$$\forall X_1 \in [0, l_1] : \tilde{r}_2(X_1) = r_1(X_1) - D(X_1)R_1(X_1)E_Y \,, \tag{4.22}$$

while the coplanarity of the two coincident cross-sections X_1 of tube 1 and $\tilde{X}_2(X_1)$ of tube 2 constrains their orientations as

$$\forall X_1 \in [0, l_1] : \tilde{R}_2(X_1) = R_1(X_1)R_{Z,\pi} \,, \tag{4.23}$$

where $R_{Z,\pi} = \exp(\widehat{E_Z \pi})$ stands for a rotation of $+\pi$ in the plane of the deformation, and reflects the opposite orientation of the neutral lines $\mathcal{N}_i$ of the two tubes. Gathering equations (4.22) and (4.23) yields the concentricity constraints

$$\forall X_1 \in [0, l_1] : g_2(\tilde{X}_2(X_1)) = g_1(X_1)g_{1,2}(X_1) \,, \tag{4.24}$$

where $g_{1,2}(X_1)$ is the relative transformation between the X_1-cross-sectional frame of tube 1 and the $\tilde{X}_2(X_1)$-cross-sectional frame of tube 2, which, referring to Figure 4.7, takes the detailed form

$$g_{1,2}(X_1) = \begin{pmatrix} R_{Z,\pi} & -D(X_1)E_Y \\ 0_{1\times 3} & 1 \end{pmatrix} . \tag{4.25}$$

Similarly, the effect of the rigid tubular guide (see Figure 4.3d) on the part of tube 2 below the baseplate can be modeled by another set of (ideal) point-wise geometric guiding constraints defined $\forall X_2 \in [\tilde{X}_2(0), l_2]$, by

$$r_{Y,2}(X_2) = r_{Z,2}(X_2) = 0 \,, \quad R_2(X_2) = 1_{3\times 3} \,. \tag{4.26}$$

4.5.5 Derivation of the Face-to-Face Function $\tilde{X}_2(\,\cdot\,)$

To derive the expression of the face-to-face function $\tilde{X}_2(\,\cdot\,)$, it is necessary to introduce the following key relationship, tangent to the pull-back function of equation (4.21),

$$h(X_1)\left(\frac{df_2}{dX_2}\right)^{\sim} = \frac{d\tilde{f}_2}{dX_1} \,, \text{ with: } h = \left(\frac{d\tilde{X}_2}{dX_1}\right)(X_1) \,, \tag{4.27}$$

which allows transforming the X_2-derivative of any function $f_2(\,\cdot\,)$ originally defined on $[0, \tilde{X}_2(0)]$, into a X_1-derivative on $[0, l_1]$. The detailed expression of this tangent pull-back function is obtained as follows. Differentiating equation (4.22) with respect to X_1 and using equation (4.27) with $f_2 = r_2$ gives

$$h\left(\frac{dr_2}{dX_2}\right)^{\sim} = \frac{dr_1}{dX_1} - R_1\left(\frac{dD}{dX_1}E_Y + DK_1 \times E_Y\right) . \tag{4.28}$$

Further, using equation (4.23) in equation (4.28) and rearranging yields

$$hR_{Z,\pi}\tilde{R}_2^T\left(\frac{dr_2}{dX_2}\right)^{\sim} = R_1^T\frac{dr_1}{dX_1} - \left(\frac{dD}{dX_1}E_Y - DK_{Z,1}E_X\right) , \tag{4.29}$$

in which Γ_i, the translational component of equation (4.13), is given by

$$\Gamma_i = R_i^T\left(\frac{dr_i}{dX_i}\right) . \tag{4.30}$$

Hence, one can rewrite equation (4.29) as

$$hR_{Z,\pi}\tilde{\Gamma}_2 = \Gamma_1 - \left(\frac{dD}{dX_1}E_Y - DK_{Z,1}E_X\right) . \tag{4.31}$$

From equation (4.18), Γ_1 and Γ_2 can be decomposed as

$$\Gamma_i = \Gamma_i^0 = (1, \beta_i(X_i), 0)^T = E_X + \beta_i(X_i)E_Y . \tag{4.32}$$

Introducing the detailed expressions of equation (4.32) into equation (4.31) and projecting the result onto E_X gives

$$h = -(1 + D(X_1)K_{Z,1}) , \tag{4.33}$$

where the minus sign comes from $R_{Z,\pi}$ in equation (4.31).

Observing that in this expression, $D(X_1) = D_1(X_1)+\tilde{D}_2(X_1)$, with $\tilde{D}_2(X_1) = D_2(\tilde{X}_2(X_1))$, the relation is a priori implicit[4]. However, consistently with the assumptions of section 4.5.3, its leading order approximation is explicit. Indeed, $\tilde{D}_2(X_1) = D_2(\tilde{X}_2(X_1))$ can be expanded as

$$D_2(\tilde{X}_2^0(X_1)) + \left(\frac{dD_2}{dX_2}\right)(\tilde{X}_2^0(X_1))\Delta\tilde{X}_2 + O((\Delta\tilde{X}_2)^2) , \tag{4.34}$$

where $\Delta\tilde{X}_2 = \tilde{X}_2(X_1) - \tilde{X}_2^0(X_1)$ stands for the variation of X_2 seen by the X_1-cross-section of tube 1, when tube 2 slides inside tube 1 in a deformed configuration of the CAAR (see Figure 4.8). Consistently with the assumptions of section 4.5.3, $\left|K_{Z,1}\Delta\tilde{X}_2\right| \simeq |K_{Z,1}a| \simeq \varepsilon$, and the linear term in $\Delta\tilde{X}_2$ is of order ε^2 and is thus negligible in equation (4.33). Therefore, reminding that $\tilde{X}_2^0(X_1) = l_1 - X_1 \; \forall X_1 \in [0, l_1]$, one can replace equation (4.33) by

$$h = -(1 + K_{Z,1}(D_1(X_1) + D_2(l_1 - X_1))) , \tag{4.35}$$

which is consistent with the first order approximation. For the sake of concision, the remainder of this chapter maintains the notation of equation (4.33) in which $D(X_1)$ is computed as $D(X_1) = D_1(X_1) + D_2(l_1 - X_1)$.

Finally, by integrating equation (4.33) along tube 1 starting from $X_1 = l_1$ where $\tilde{X}_2(l_1) = 0$, the face-to-face function $\tilde{X}_2(\,\cdot\,)$ is defined by the path integral

$$\tilde{X}_2(X_1) = -\int_{X_1}^{l_1} h(Y)\, dY = \int_{X_1}^{l_1} (1 + K_{Z,1}D)\, dY , \tag{4.36}$$

which in the general case, must be calculated numerically.

4.5.6 Kineto-Static Model of a CAAR

This section presents a model for CAARs that reflects the static balance between internal restoring forces and external forces that are assumed to be comprised of gravity, the actuation push-pull force applied at the base ($X_2 = l_2$) of tube 2, and a possible external wrench, applied at the tip of the CAAR. Based on the above parameterization, in the (quasi)static regime, the deformations of

[4] In details, $\tilde{X}_2(\,\cdot\,)$ is solution of an ODE.

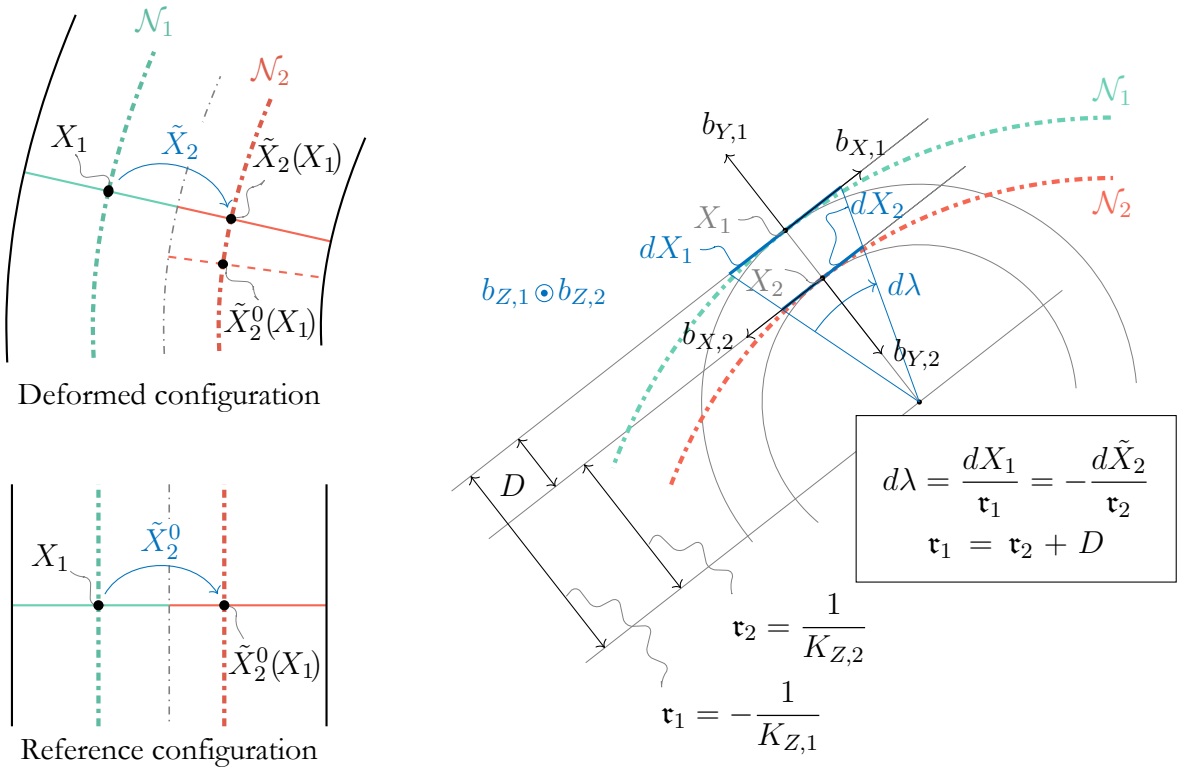

Figure 4.8: Left, visualization of the cross-section label shift due to the sliding between tubes. Bottom left, reference (straight) configuration. Top left, deformed configuration. Right, geometric picture for regular notches. In this example, the distance D between the neutral lines of the two tubes is constant along the robot. Simple geometrical considerations on the osculating circles of radii $\mathfrak{r}_1$ and $\mathfrak{r}_2$ tangent to, respectively, the neutral lines $\mathcal{N}_1$ and $\mathcal{N}_2$ allow to intuitively find the two key relations of equations (4.33) and (4.51).

the material bodies of the tubes $\mathcal{B}_1$ and $\mathcal{B}_2$ are governed by their kineto-static model defined by the set of Cosserat's ODEs which hold for $i = 1, 2$

$$\begin{aligned} \frac{dg_i}{dX_i} &= g_i \widehat{\xi_i}\,, \\ \frac{d\Lambda_i}{dX_i} &= ad^T_{\xi_i}\Lambda_i - \bar{F}_i\,, \end{aligned} \tag{4.37}$$

The first ODEs of equation (4.37) stand for a continuous geometric model of the tubes, while second ODEs of equation (4.37) represent their static wrench balances (all expressed in the cross-sectional frames), with $\Lambda_i \in se(2)^\star \subset se(3)^\star \cong \mathbb{R}^6$ the wrench of stress transmitted across the X_i-cross-section, and $\bar{F}_i \in se(2)^\star \subset se(3)^\star \cong \mathbb{R}^6$, the density of external wrench exerted by the environment along $\mathcal{B}_i$. These ODEs are supplemented with the boundary and connectivity conditions. For $\mathcal{B}_1$, the BC at its base $X_1 = 0$ is

$$g_1(0) = 1_{4\times 4}\,. \tag{4.38}$$

For $\mathcal{B}_2$, the BC at $X_2 = l_2$ is

$$\Lambda_2(l_2) = F_{+,2} = (0, 0, 0, T_+, 0, 0)^T\,, \tag{4.39}$$

where T_+ represents the vertical actuation push-pull force applied to the end of tube 2 (i.e. $X_2 = l_2$). At $X_1 = l_1$ and $X_2 = 0$ the tubes are clamped, which translates into the connectivity condition on transformations

$$g_2(0) = g_1(l_1)g_{1,2}(l_1)\,, \tag{4.40}$$

where $g_{1,2}(l_1)$ is given by equation (4.25) in which $D(l_1) = (D_1 + \tilde{D}_2)(l_1) = D_1(l_1) + D_2(0)$. And similarly, the connectivity condition on wrenches reads

$$\Lambda_1(l_1) = Ad^{-T}_{g_{1,2}(l_1)}\Lambda_2(0) + Ad^{-T}_{g_{1,s}}F_+\,, \tag{4.41}$$

where $F_+ = (0_{1\times 3}, (R_1^T(l_1)f_+)^T)^T$ is the wrench of a possible external concentrated force f_+, expressed in the inertial frame and imposed at the tip of the CAAR, while $g_{1,s}^{-1}$ is the pose of the tip cross-sectional frame of tube 1 with respect to a frame (defined in the inertial frame) located at the application point of the force. In the case of CAARs, the external wrench density $\bar{F}_i$ can be detailed as follows:

$$\bar{F}_i = \bar{F}_{ext,i} + \bar{F}_{c,i}\,. \tag{4.42}$$

$\bar{F}_{ext,i}$ models the effect of all distributed external forces applied to the CAAR except those due to contacts. In the present model, the distributed external forces are restricted to gravitational forces which take the detailed form

$$\bar{F}_{ext,i}(X_i) = (0_{1\times 3}, (\mu_i\mathcal{A}_i)(X_i)(R_i^T(X_i)a_g)^T)^T\,, \tag{4.43}$$

where $(\mu_i\mathcal{A}_i)(\,\cdot\,)$ is the mass density per unit of length of tube i, while a_g is the uniform gravitational acceleration field expressed in the inertial frame $\mathcal{F}_s$. The second component $\bar{F}_{c,i}$ of equation (4.42) stands for a field of contact wrenches whose components play the role of Lagrange multipliers in charge of forcing the concentricity constraints of equation (4.24) and the guiding of $\mathcal{B}_2$ below the baseplate of equation (4.26). Considering an ideal system without friction, the two tubes are subject to reaction wrenches obeying the action-reaction principle (i.e. $\bar{F}_{c,1} = -\bar{F}_{c,2}$).

To fully close the formulation defined by equations (4.24), (4.26), and (4.37) to (4.43), it needs to be supplemented by the constitutive relation (see sections 2.3.3 and 2.3.5)

$$B_i^T\Lambda_i = \mathcal{H}_{a,i}\epsilon_i\,, \tag{4.44}$$

where $\epsilon_i = \xi_{a,i} - \xi^0_{a,i}$ defines the strain field along $\mathcal{B}_i$, with $\xi^0_{a,i}$ the value of equation (4.13) in the reference configuration of $\mathcal{B}_i$, and $\mathcal{H}_{a,i} = B_i^T \mathcal{H}_i B_i$ its reduced Hooke's tensor, with $\mathcal{H}_i$ defined for each tube by equation (4.11). In the case of Kirchhoff rods, straight at rest and subject to planar deformations, the strain along tube i $\epsilon_i = \xi_{a,i} = K_{Z,i}$ and the bending stiffness $\mathcal{H}_{a,i}(X_i) = (E_i I_i)(X_i)$. Finally, the inertia along tube i $I_i = I_{Z,i}$ is defined by equation (4.8).

4.6 Lagrangian Reduction and Implementation

Because the pose fields $g_i(\,\cdot\,)$ can be entirely reconstructed[5] from the knowledge of $\xi_{a,i}(\,\cdot\,)$, the set of equations (4.37) to (4.44) with the constraints of equations (4.24) and (4.26) define a closed formulation of a CAAR kineto-static model on the configuration space $\mathcal{C} = \mathcal{C}_1 \times \mathcal{C}_2$, with: $\mathcal{C}_i = \{\xi_{a,i}(\,\cdot\,) : X_1 \in [0, l_i] \mapsto \xi_{a,i}(X_i) \in \mathbb{R}^{n_a}\}$, i.e. on a non-minimal configuration space (with more dimensions than DoF). This parametric redundancy is a consequence of the presence of constraints of equations (4.24) and (4.26) and their associated Lagrange multipliers (4.42) in the formulation. This redundant formulation is called the constrained formulation.

The idea of the reduction is to re-parameterize the fields $\xi_{a,i}(\,\cdot\,)$ by a reduced (finite) set of generalized coordinates $q \in \mathbb{R}^n$. Using a standard Lagrangian process, the expected static model will take the conventional matrix form

$$Q_{int}(q) + Q_{ext}(q) = 0\,, \tag{4.45}$$

where Q_{int} and Q_{ext} denote generalized internal and external force vectors, respectively. The balance of equation (4.45), that is called the reduced model, will be derived by applying the principle of virtual work. Since all constraints are assumed to be ideal, the reaction forces they generate do not work in any virtual displacement field compatible with them, and Q_{int} (respectively Q_{ext}) will consist only of the elastic restoring forces (respectively of the generalized forces imposed by the environment, i.e. the gravity, push-pull, and tip forces along with a potential wrench imposed at the tip of the CAAR).

Technically, this reduction process is performed in two stages. The first stage is completed at a continuous level. It consists in removing the concentricity and guiding constraints of equations (4.24) and (4.26) from the above formulation, as well as the associated internal reaction wrenches $\bar{F}_{c,i}$. This first stage produces a minimal continuous unconstrained formulation. In the second stage, the strain based reduction process discussed in section 2.3.1 is applied to the unconstrained formulation, producing the expected reduced model defined by equation (4.45).

4.6.1 First Reduction Stage

Starting from the constrained formulation above, the first stage is performed in two steps. The first step consists in removing the guiding constraints of equation (4.26). The second step consists in removing the concentricity constraints of equation (4.24).

First step: removing the guiding constraints

This can be simply achieved by considering the part of tube 2 above the baseplate only. In other words, the CAAR is modeled by isolating the material system contained in a control volume above

[5] Indeed, introducing $\xi_{a,i}(\,\cdot\,)$ into equation (4.14) allows to integrate forward equation (4.37) from $X_i = 0$ to $X_i = l_i$.

the baseplate. Hence, tube 2 is subject to the BCs

$$\Lambda_2(\tilde{X}_2(0)) = \tilde{\Lambda}_2(0) = F_{+,2} = (0,0,0,T_+,0,0)^T\,. \tag{4.46}$$

Such simplification which is entirely justified in the present quasi-static conditions. This has been recently shown in the wider context of the dynamics of sliding Kirchhoff rods [Boyer et al. 2022a]. This simplification changes the configuration space $\mathcal{C}_2$ into $\tilde{\mathcal{C}}_2 = \{\tilde{\xi}_{a,2}(\,\cdot\,) : X_1 \in [0,l_1] \mapsto \tilde{\xi}_{a,2}(X_1) = \xi_{a,2}(\tilde{X}_2(X_1)) \in \mathbb{R}^{n_a}\}$, i.e. the deformation of tube 2 is now parameterized by the field $\tilde{\xi}_2(\,\cdot\,)$ function of X_1 which is a non-material (sliding) variable for tube 2. In summary, this first step consists in re-expressing all the relations of equations (4.13) to (4.18) and (4.22) to (4.26) related to tube 2, in terms of X_1 instead of X_2 and to restrict them to the part of the tube that is above the baseplate. Technically, this relabeling process is achieved with the pull-back functions of equations (4.21) and (4.27).

Second step: removing the concentricity constraints

Once through the first relabeling step, the concentricity constraints of equation (4.24) can be removed. This is done by explicitly parameterizing $\tilde{\xi}_{a,2}$ in terms of $\xi_{a,1}$ thanks to the differential consequences of the concentricity constraints of equation (4.24). At the end of this second step, the deformation of the CAAR is entirely parameterized by $\xi_{a,1}(\,\cdot\,)$ and its configuration space is defined by the configuration space $\mathcal{C}_1$ only. In other words, the configuration space of the CAAR is reduced to the configuration space of tube 1, which thus plays the role of the reference tube.

Application of the first reduction stage: reduced continuous model

The first equation that needs to be considered is the continuous kinematic model of equation (4.37) for $i = 2$. In order to satisfy the concentricity constraints of the tubes, it is replaced by the X_1-derivative of equation (4.24), in which X_2 is replaced by X_1. Following algebraic manipulations, one finds

$$\frac{d\tilde{g}_2}{dX_1} = \tilde{g}_2\left(Ad_{g_{2,1}}\xi_1 + \xi_{2/1}\right)^\wedge \tag{4.47}$$

that introduces the relative twists between the two tubes

$$\xi_{2/1} = \left(g_{1,2}^{-1}\frac{dg_{1,2}}{dX_1}\right)^\vee = \begin{pmatrix} 0_{3\times 1} \\ (dD/dX_1)E_Y \end{pmatrix}. \tag{4.48}$$

Based on this first result, one can calculate the pull-back function $\tilde{\xi}_2(\,\cdot\,)$. To that end, equation (4.27) is used with $f_2(\,\cdot\,) = g_2(\,\cdot\,)$ in the definition (4.13) of ξ_2. Then, using equation (4.47) gives

$$\tilde{\xi}_2 = h^{-1}(Ad_{g_{2,1}}\xi_1 + \xi_{2/1})\,. \tag{4.49}$$

Going into further details, using equation (4.48) and

$$Ad_{g_{2,1}} = \begin{pmatrix} R_{Z,\pi} & 0_{3\times 3} \\ -D\widehat{E}_Y R_{Z,\pi} & R_{Z,\pi} \end{pmatrix}, \tag{4.50}$$

in equation (4.49) and pre-multiplying (projecting) with $B_2 = (0,0,1,0,0,0)^T$ provides the relation between the curvature fields of the two planar neutral lines

$$\tilde{\xi}_{a,2} = h^{-1}\xi_{a,1} \quad \Rightarrow \quad \tilde{K}_{Z,2} = \frac{-K_{Z,1}}{1 + K_{Z,1}D}\,. \tag{4.51}$$

Note that when the two neutral lines are parallel, i.e. $(dD/dX_1) = 0$, this relation can be directly deduced from the simple geometric consideration $\mathfrak{r}_1 = \mathfrak{r}_2 + D$, with $\mathfrak{r}_1$ and $\mathfrak{r}_2$ the radii of the osculating circles tangent to, respectively, the neutral lines $\mathcal{N}_1$ and $\mathcal{N}_2$, as sketched in Figure 4.8. Concerning the balance of stress, let us first recall that the reaction wrenches $\bar{F}_{c,i}$ in equation (4.42), associated to the concentricity and guiding constraints of equations (4.24) and (4.26), can now be ignored since they will not contribute to the virtual work balance. Thus, it is sufficient to replace ξ_2 by $\tilde{\xi}_2$ given by equation (4.49), and apply equation (4.27) to $f_2(\,\cdot\,) = \Lambda_2(\,\cdot\,)$, to change the stress balance of tube 2 into

$$\frac{d\tilde{\Lambda}_2}{dX_1} - ad^T_{(Ad_{g_{2,1}}\xi_1 + \xi_{2/1})}\tilde{\Lambda}_2 + h\tilde{\bar{F}}_{ext,2} = 0_{6\times 1}\,, \tag{4.52}$$

where $\tilde{\bar{F}}_{ext,2}(X_1)$ now denotes the density of external (gravitational) wrenches applied on tube 2 per unit of X_2, at X_1 along tube 1. Reconsidering equation (4.43) yields

$$\tilde{\bar{F}}_{ext,2} = (0_{1\times 3}, \mu_2 \tilde{\mathcal{A}}_2 (\tilde{R}_2^T a_g)^T)^T\,. \tag{4.53}$$

The constitutive relation of equation (4.44) remains unchanged for tube 1, while for tube 2, equation (4.44) turns into

$$B_2^T \tilde{\Lambda}_2 = \tilde{\mathcal{H}}_{a,2}\tilde{\epsilon}_2 = E_2 \tilde{I}_2 \tilde{\epsilon}_2\,. \tag{4.54}$$

Finally, note that for tube 1, it is sufficient to remove $\bar{F}_{c,1}$ in its stress balance, while in the connectivity conditions of equations (4.40) and (4.41), only $\Lambda_2(0)$ changes into $\tilde{\Lambda}_2(l_1)$.

At the end of this first reduction stage, the constrained (redundant) formulation defined by equations (4.24), (4.26), and (4.37) to (4.44) is replaced by a minimal (continuous) unconstrained formulation defined for tube 2 by equations (4.47) and (4.52) to (4.54) with the BCs of equations (4.40) and (4.46), while for tube 1, nothing has changed, except that the concentricity constraints and their associated Lagrange multipliers $\bar{F}_{c,1}$ have been removed. This continuous unconstrained formulation represents the CAAR model on the $\mathcal{C}_1$ configuration space of its reference tube.

4.6.2 Second Reduction Stage

The second reduction stage consists in parameterizing $\mathcal{C}_1$ on a functional truncated basis of strain functions of tube 1. This is similar to the process described in section 3.4.1 for TACRs, but in this case, the reduction is applied to tube 1. And since the present model is a reduced Kirchhoff model, only the allowed strains are considered.

Thus, the allowed strain fields $\xi_{a,1}(\,\cdot\,)$ are decomposed on a truncated basis of k Ritz functions $\Phi = (\Phi_1, \Phi_2, \ldots, \Phi_k)$ as

$$\xi_{a,1}(X_1) = K_{Z,1}(X_1) = \Phi(X_1) q\,, \tag{4.55}$$

where $q = (q_1, q_2, \ldots, q_k)^T$ stands for the set of generalized coordinates of the expected final model defined by equation (4.45).

As for the TACR model, the final form of the model is obtained through a canonical application of the principle of virtual work, which takes the form of the following equilibrium, valid for any variation of the configuration (virtual displacement field) compatible with the kinematics of the CAAR,

$$\delta W_{int} + \delta W_{ext} = 0\,. \tag{4.56}$$

In this balance, δW_{int} and δW_{ext}, denote the virtual work of internal and external forces, respectively, which both take the generic form

$$\delta W = \int_0^{l_1} \delta\epsilon_1^T \Lambda_{a,1}\, dX_1 + \int_0^{\tilde{X}_2(0)} \delta\epsilon_2^T \Lambda_{a,2}\, dX_2\,, \tag{4.57}$$

where $\Lambda_{a,i} = B_i^T \Lambda_i$ stands for $-\mathcal{H}_{a,i}\epsilon_i$ in the case of δW_{int}, and for the allowed stress that balance the external gravitational, actuation push-pull, and tip forces, in the case of δW_{ext}. When applying equation (4.56), the variations $\delta\epsilon_1 = \delta\xi_{a,1} = \delta K_{Z,1}$ and $\delta\epsilon_2 = \delta\xi_{a,2} = \delta K_{Z,2}$ are compatible with the concentricity constraints of equation (4.51), i.e. they are related by

$$\delta\tilde{K}_{Z,2} = \frac{-\delta K_{Z,1}}{(1 + K_{Z,1}D)^2}\,. \tag{4.58}$$

Finally, the virtual work principle being invariant with respect to any kinematic transformation and the balance of equation (4.56) holding for any variation, the generalized force vector Q generated by a given stress state of the CAAR, can be deduced from equation (4.57). Equations (4.51) and (4.58), as well as the relabeling of equation (4.27), and the Ritz reduction of equation (4.55) of $K_{Z,1}$ need to be injected in equation (4.57) that is identified with

$$\delta W = \delta q^T Q(q)\,. \tag{4.59}$$

Applying this process and rearranging yields

$$Q = \int_0^{l_1} \Phi^T \left(C_{Z,1} - \frac{\tilde{C}_{Z,2}}{(1 + D\Phi q)} \right) dX_1\,, \tag{4.60}$$

which allows converting any pair of stress fields $(\Lambda_{a,1},\, \tilde{\Lambda}_{a,2})(\,\cdot\,) = (C_{Z,1}, \tilde{C}_{Z,2})(\,\cdot\,)$ transmitted across the two tubes, into the corresponding generalized force vector Q applied to the CAAR. For the generalized vector of internal forces, using equations (4.51) and (4.55) and the fact that $\epsilon_i = K_{Z,i}$ yields

$$\begin{aligned} C_{Z,1} &= -\mathcal{H}_{a,1}\epsilon_1 = -E_1\mathcal{I}_1\Phi q \\ \tilde{C}_{Z,2} &= -\tilde{\mathcal{H}}_{a,2}\tilde{\epsilon}_2 = \frac{E_2\tilde{I}_2\Phi q}{(1 + D\Phi q)}\,, \end{aligned} \tag{4.61}$$

which, once introduced in equation (4.60), provides the detailed expression for Q_{int}

$$Q_{int}(q) = -\int_0^{l_1} \Phi^T \left(E_1\mathcal{I}_1 + \frac{E_2\tilde{I}_2}{(1 + D\Phi q)^2} \right) \Phi q\, dX_1\,. \tag{4.62}$$

Finally, to practically compute Q_{int} and Q_{ext}, a computed torque style algorithm is applied. This algorithm is detailed in the next section.

4.6.3 Algorithm for Computing Q_{int} and Q_{ext}

While $Q_{int}(q)$ can be directly calculated for any q with the explicit expression of equation (4.62), as long as $\tilde{I}_2$ is known, the calculation of $Q_{ext}(q)$ requires more attention. This essential difference is explained by the fact that Q_{int} is directly generated by a field of stress wrench (governed by the constitutive relation of equation (4.44)), while in contrast, the external gravity, push-pull, and tip

forces are primarily defined as wrenches of forces $\bar{F}_{ext,i}$, $F_{+,2}$, and F_+. A natural way to calculate $Q_{ext}(q)$ is to first convert $\bar{F}_{ext,i}$, $F_{+,2}$ and F_+ into stress fields $\Lambda_{a,1} = C_{Z,1}$ and $\tilde{\Lambda}_{a,2} = \tilde{C}_{Z,2}$, and then to introduce these torque fields into equation (4.60). This conversion is achieved with an inverse (computed torque) algorithm, proposed in [Boyer et al. 2006, Boyer et al. 2021], adapted to the statics of CAARs. This inverse static algorithm is structured in two passes. The first one is a forward kinematic pass that computes, for a given q, the pose field of the two tubes from the base $X_1 = 0$ of tube 1, to the intersection of tube 2 with the baseplate $\tilde{X}_2(0)$. The second pass is a backward pass that calculates the stress generated by the external forces along the structure, starting from the intersection of tube 2 with the baseplate, and ending at the base of tube 1. In a last step, these two stress fields are used in equation (4.60) to compute Q_{ext}. Finally, this algorithm also produces Q_{int} through equation (4.62), which needs the numerical integration of the face-to-face function of equation (4.36). It is summarized as follows.

■ Inputs of the algorithm:

$$\xi_1 = B_1\Phi(X_1)q + \bar{B}_1\xi_{c,1}\,. \tag{4.63}$$

■ Forward kinematics (1st pass):

$$\text{Initial conditions: } g_1(0) = 1_{4\times4}\,. \tag{4.64}$$

Integrate from $X_1 = 0$ to l_1

$$\frac{dg_1}{dX_1} = g_1\widehat{\xi_1}\,. \tag{4.65}$$

Initial conditions:

$$\tilde{X}_2(l_1) = 0\,, \quad \tilde{g}_2(l_1) = g_1(l_1)g_{1,2}(l_1)\,. \tag{4.66}$$

Integrate from $X_1 = l_1$ to 0

$$\frac{d\tilde{X}_2}{dX_1} = h = -(1 + D\Phi q)\,, \tag{4.67}$$

$$\frac{d\tilde{g}_2}{dX_1} = \tilde{g}_2\left(Ad_{g_{2,1}}\xi_1 + \xi_{2/1}\right)^\wedge\,. \tag{4.68}$$

$$\text{Store } (g_1, \tilde{X}_2, \tilde{g}_2)(\,\cdot\,)\,. \tag{4.69}$$

■ Backward statics (2nd pass):

Initial conditions:

$$\tilde{\Lambda}_2(0) = (0_{1\times3}, T_+E_1^T)^T. \tag{4.70}$$

Integrate from $X_1 = 0$ to $X_1 = l_1$

$$\frac{d\tilde{\Lambda}_2}{dX_1} = ad^T_{(Ad_{g_{2,1}}\xi_1+\xi_{2/1})}\tilde{\Lambda}_2 - h\tilde{\bar{F}}_{ext,2}\,. \tag{4.71}$$

Initial conditions:

$$\Lambda_1(l_1) = Ad^{-T}_{g_{1,2}(l_1)}\tilde{\Lambda}_2(l_1) + Ad^{-T}_{g_{1,s}}F_+ \tag{4.72}$$

Integrate from $X_1 = l_1$ to 0

$$\frac{d\Lambda_1}{dX_1} = ad^T_{\xi_1}\Lambda_1 - \bar{F}_{ext,1}\,. \tag{4.73}$$

$$\text{Store } (\tilde{\Lambda}_2, \Lambda_1)(\,\cdot\,)\,. \tag{4.74}$$

■ Calculation of the outputs of the algorithm:

Compute:

$$Q_{ext} = \int_0^{l_1} \Phi^T \left(B_1^T \Lambda_1 - \frac{B_2^T \tilde{\Lambda}_2}{(1 + D\Phi q)} \right) dX_1 \tag{4.75}$$

$$Q_{int} = - \int_0^{l_1} \Phi^T \left(E_1 \mathcal{I}_1 + \frac{E_2 \tilde{I}_2}{(1 + D\Phi q)^2} \right) \Phi \; dX_1 \, q \, . \tag{4.76}$$

The spectral integration [Hussaini et al. 1989] of Q_{int} is performed by first computing $\tilde{X}_2$ in each X_1 of the Chebyshev grid [Trefethen 2000] from equation (4.67), and then by computing the corresponding values of I_2, i.e. $\tilde{I}_2(X_1)$, through the interpolation process of section 4.4. This algorithm is summarized in Figure 4.9 where the equation numbers of the corresponding definitions are given. Ultimately, this algorithm defines a numerical input-output map that produces $Q_{ext}(q)$ and $Q_{int}(q)$ from q, T_+, and F_+.

4.6.4 Quasi-Static Simulation of a CAAR

The simulation of the quasi-static evolution of a CAAR is based on the reduced Lagrangian model defined by equation (4.45), where $Q_{int}(q)$ and $Q_{ext}(q)$ are computed by the above algorithm. This model consists of a set of nonlinear algebraic equations (static equilibrium in the generalized coordinate space q), which can be set into the standard conventional form

$$\mathfrak{Res}(q) = Q_{int}(q) + Q_{ext}(q) = 0 \, , \tag{4.77}$$

with $\mathfrak{Res}(q)$, the residual vector of the system. This system can be solved with respect to q at each step of load (T_+, F_+) with standard root-finding algorithms (e.g. Newton-Raphson, Levenberg-Marquardt). In the next chapter, this approach is applied to different robot designs. The iterative search for the roots of equation (4.77) is performed with Matlab 2022a `fsolve` function with the Levenberg-Marquardt algorithm, all parameters being set to defaults. The Jacobian matrices of the residual vector $(\partial \mathfrak{Res}/\partial q)(q)$ are numerically approximated by finite differences. The spatial integrations of the above computed torque algorithm are performed with a spectral method [Trefethen 2000]. To conclude this section, remind that this algorithm needs to be fed with the design parameters of the CAAR, which are defined $\forall X_1 \in [0, l_1]$, $\forall X_2 \in [0, l_2]$, by

$$\begin{aligned} &D(X_1) = D_1(X_1) + D_2(l_1 - X_1) \, , \\ &\mathcal{A}_1(X_1) \, , \quad \mathcal{A}_2(X_2) \, , \quad \mathcal{I}_1(X_1) \, , \quad \mathcal{I}_2(X_2) \, , \end{aligned} \tag{4.78}$$

i.e. from top to bottom and from left to right, the lateral offset field between the neutral lines, the fields of area and inertia, all being interpolated along the two tubes by the process described in section 4.4.

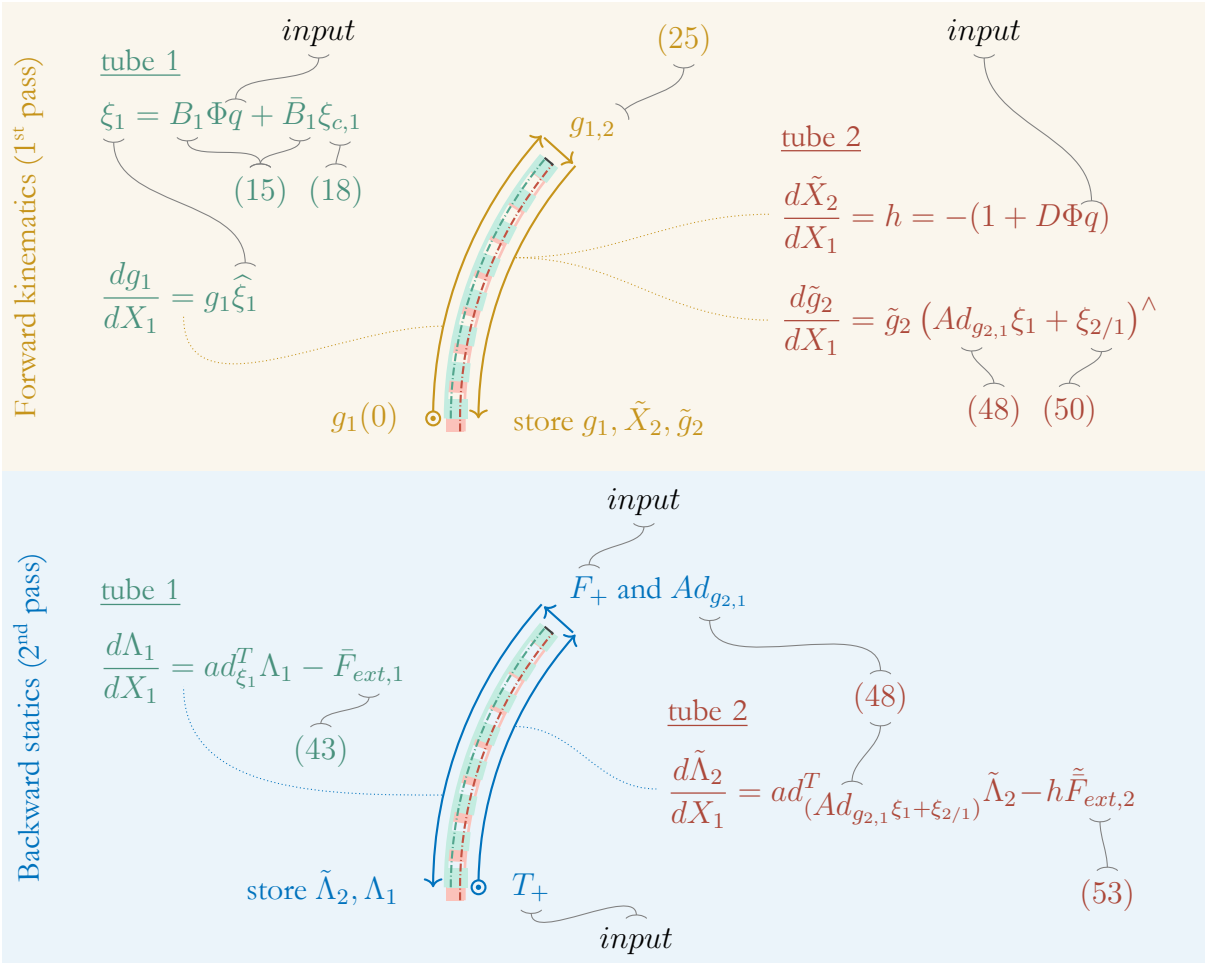

Figure 4.9: Schematic of the two passes of the inverse static algorithm. For both passes, the integration starts at the circled bullet with the corresponding initial condition and follows through the arrows from one tube to the other. The dotted lines show the associated differential equations. The light grey lines link the quantities that are necessary for the implementation of the algorithm to the corresponding equation numbers of this chapter.

4.7 Conclusion

In this chapter, the need for a novel mechanical model for CAARs was highlighted. Such a model based on Cosserat rod theory was introduced. Contrarily to state-of-the-art models, the present mechanical model allows taking external wrenches into consideration, as well as variable notch designs. The model should, in the course of time, enable the use of CAARs in various applications, especially in medical and surgical contexts (see section 1.5).

A few physical phenomenons remain unmodeled in the proposed approach. Examples include the clearance between tubes, the effect of static friction between tubes that may introduce a hysteresis effect, and the effects of transverse shear deformation and extension.

Further, it is worth noting that the model proposed in this chapter is, as a first step and as the first CAAR mechanical model in the literature, restricted to planar robots and to the (quasi) static case. The formulation of the model is however generic enough to allow its extension to full 3D shapes and to dynamic behavior, with the aim of using such models for 3D design optimization, sensing, or control applications.

Of course, before any further use of the model, it should be validated experimentally. In the next chapter, experiments are carried out with various CAAR designs in order to validate the developed model. The prototypes are used in various configurations and under external loading.

Contributions of this chapter

1. The potential of state-of-the-art models of continuum robots that are closely related to CAARs is evaluated. This interpretation is followed by a discussion concluding with the need for a novel CAARs mechanical model.

2. A first in-plane mechanical model for CAARs is formulated. The model is capable of taking external forces from the environment into account and to model CAARs with 'general' variable neutral lines.

3. This contribution includes the production of an algorithm for numerically solving the proposed model.

4. Beyond the main contribution (2.), an in depth analysis of the kinematics of CAARs is carried out, providing the community with deeper knowledge and new tools to understand and investigate CAARs.

Regarding the last three contributions, the input for the external collaborators was the following: the know-how regarding the Lagrangian approach was mainly provided by Frédéric Boyer and Vincent Lebastard. The knowledge of the CAAR system was mainly provided by Matthias Tummers' thesis. The present model was established through numerous iterations with continuous inputs from all contributors.

5

Experimental Validation of the 2D CAAR Model and Analysis of 3D CAARs

5.1 Foreword

This chapter is devoted to experiments carried out with CAARs. The objectives of these experiments are twofold. The first one is to validate the model developed in chapter 4 through experiments. The second one is to investigate new ways of constructing and actuating CAARs leading to CAARs in 3D.

Prior to the exposition of the results, section 5.2 describes the materials of the experimental setup. The description includes the design and references of the materials, as well as the data acquisition apparatus and processing. Then, for the first objective, in order to validate the different capabilities of the model, section 5.3 presents an extensive set of experiments that can be divided in three groups. The first group, the most basic tests, concerns regularly notched CAARs in free-space. The second group includes tests with external tip forces applied to the prototypes in various actuated configurations and is intended for validating the model capabilities of taking into account external forces. The third group concerns CAARs with variable notches and thus variable neutral lines, for validating the 'general neutral lines' aspect of the model.

For the second objective, section 5.4.1 describes possible ways to bring the neutral lines of CAARs out of the plane they were previously restricted to. Section 5.4.1 also details the design of the experimentally tested prototypes. Then, section 5.4.2 presents experiments demonstrating the capabilities of such 3D CAARs. Section 5.4.3 concludes on CAARs in 3D by discussing the results and their perspectives for future (medical) applications.

5.2 Experimental Setup

This section is devoted to the designed robot with all its apparatus. It covers the design and materials of the actuation unit as well as the data acquisition devices and the software that controls the system.

5.2.1 Actuation Unit

The actuation unit displayed in Figure 5.1 was designed for the actuation of continuum robots that are made out of concentric tubes (up to four tubes). It is thus capable of actuating CAARs, but also CTCRs. It is composed of a fixed frame and four actuation carriages or stages. The carriages are translated with EC-max22 brushless 12W Maxon motors via a PTGSG-10X2-01-R IGUS 2 mm pitch lead screw. To ensure position and orientation precision, the carriages are guided with two µm precision linear guides. Each stage carries an additional EC-max22 brushless 12W Maxon motor linked to a hollow shaft through precision timing belts. Cable chains securely convey the cables from the moving carriages to the fixed frame. The hollow shafts are guided on the carriages with two angular bearings to enable precise rotation while transmitting axial forces. The shafts are provided with a hexagonal imprint for the fixture of the tubes such that precise axial and angular positioning is ensured. The through-holes of the shafts allow to pass tubes concentrically through one another. Aside from the off-the-shelf parts, the 3D printed parts of the actuation unit were printed with polylactic acid (PLA) using a Raise3D Pro2 printer which has a 10 µm precision.

All motors are equipped with MR 2048 CPT Maxon encoders and controlled with a DMC-4040 Galil control board, which enable an actuation precision below 1 µm for translation and below 0.1° for rotation. The software of the robot was implemented with MatLab 2022a. It consists of a Matlab application that allows to translate or to rotate individually each of the shafts, but also to launch batches of specific workspace sweeping with data acquisition. All data acquisition apparatus (see section 5.2.2) are integrated in the application to ease the experimental workflow. Besides the display of all motor translation and rotation values, this integration also allows a graphical preview of an approximated robot shape based on the sensor positions in the workspace.

In the case of the present dissertation, the basis of the two tubes of the CAARs are attached to the upper two carriages of the actuation unit (see Figure 5.1). The outer tube remained clamped in the baseplate at all times and only one stage was used to actuate the inner tube with respect to the fixed outer tube.

All the CAAR tubes are 3D printed with PLA using the same Raise3D Pro2 printer in exactly the same position and orientation on the printing bed to limit printing variability. For an in-depth discussion on 3D printing CAAR tubes, please refer to appendix B.

5.2.2 Data Acquisition

End-effector pose feedback, as well as visual feedback was used to assess the performance of the studied CAARs.

Electromagnetic sensors

The setup is equipped with two 6 DoF electromagnetic sensors (Aurora, NDI). One reference 6 DoF sensor is attached to the baseplate of the actuation unit in a purpose-designed slot at a known position and orientation with respect to the inertial frame $\mathcal{F}_s$ (as defined in Figures 4.3 and 4.4). The transformation between the inertial frame $\mathcal{F}_s$ and the reference sensor fame $\mathcal{F}_{RS}$ is noted g_{RS}.

The other miniaturized 6 DoF sensor is attached to the tip of the prototypes, or more precisely, in a purposely designed slot on a rigid extension of the tip (see Figure 5.2). As the tip sensor is fixed manually for each series of tests, it first requires a calibration step to find the transformation $g_{TS,tip}$ between the pose of the sensor and the pose of the physical tip of the robot $g(l)$ as defined

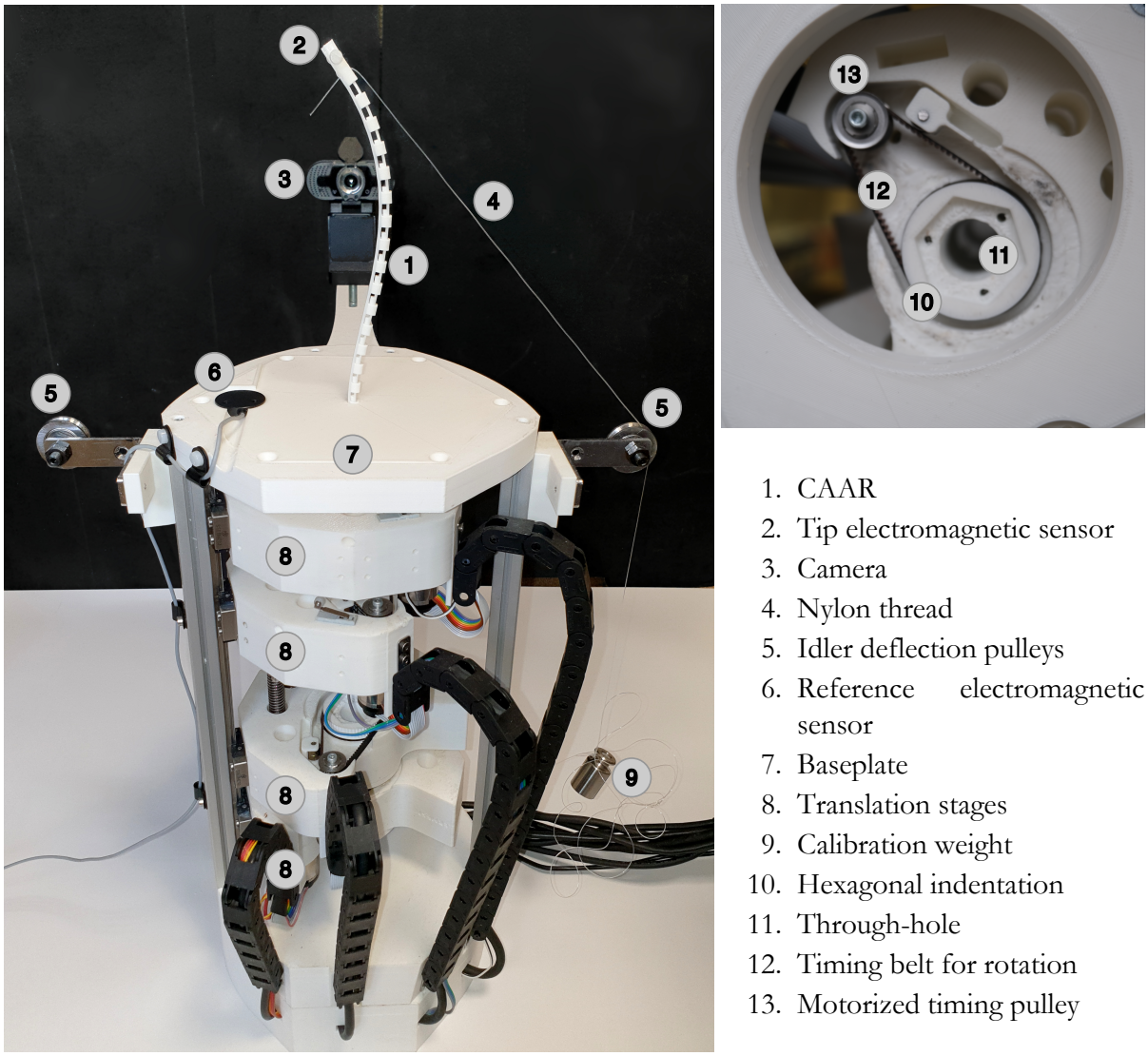

1. CAAR
2. Tip electromagnetic sensor
3. Camera
4. Nylon thread
5. Idler deflection pulleys
6. Reference electromagnetic sensor
7. Baseplate
8. Translation stages
9. Calibration weight
10. Hexagonal indentation
11. Through-hole
12. Timing belt for rotation
13. Motorized timing pulley

Figure 5.1: The multi-stage actuation unit with a mounted 6 mm diameter CAAR prototype used for experimental validation. For the experiments presented in this dissertation, only one stage was used to actuate the inner tube with respect to the fixed outer tube. A nylon thread is attached at the tip of the robot and routed around the right idler pulley to a calibrated weight, applying a tip force to the robot. The hexagonal indentation allows fixing the tubes in translation and rotation. The carriages are provisioned with a through-hole for the tubes of the other carriages. Rotation of the tubes is achieved thanks to the visible timing belt and motorized timing pulley.

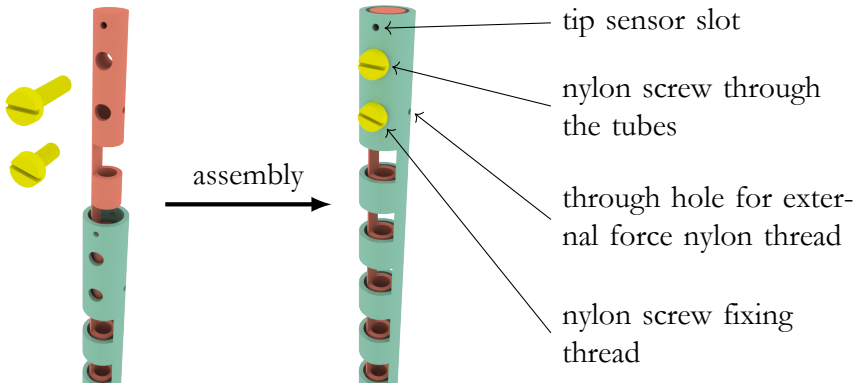

Figure 5.2: Exploded and assembled views of the tip of the prototypes.

in the model (see Figure 5.3). In the reference configuration

$$g(l) = g^0(l) = \begin{pmatrix} 1_{3\times3} & lE_X \\ 0_{1\times3} & 1 \end{pmatrix}, \tag{5.1}$$

with l the length of the robot. The calibration procedure was the following. After the CAAR is fixed in its straight undeformed configuration on the actuation unit and the tip sensor is fastened manually on the robot, a measure of the reference sensor pose $g_{AU,\,RS}$ and tip sensor pose $g_{AU,\,TS}$ in the aurora reference frame $\mathcal{F}_{AU}$ is recorded. Then, rearranging transformations yields the desired calibrated transformation

$$g_{TS,tip} = g_{AU,\,TS}^{-1}\ g_{AU,\,RS}\ g_{RS}^{-1}\ g^0(l)\,. \tag{5.2}$$

$g_{TS,tip}$ is stored for the tests that follow, until the tube pair is changed for another one.

Now that $g_{TS,tip}$ is known, the measures of the pose of the tip of the robot in the inertial frame for any configuration $g(l) \neq g^0(l)$ are obtained with

$$g(l) = g_{RS}\ g_{AU,\,RS}^{-1}\ g_{AU,\,TS}\ g_{TS,tip}\,. \tag{5.3}$$

Data from the Aurora electromagnetic sensors tend to be relatively noisy, especially when the sensors are fixed on an actuation unit featuring many metallic parts and motors driven by electric current. To palliate to the signal variability, the following measures were applied.

1. The tip of the robot was designed to be clear from metallic parts. Nylon screws were used to fasten the tip sensor or nylon thread for applying external tip forces (see Figure 5.2).

2. The reference sensor, mounted on the baseplate, was moved away from the actuation unit with a strut to limit the possible interference with the metallic parts and electronics.

3. Preliminary investigations showed that the exact position and orientation of Aurora electromagnetic sensors can play a significant role in the precision of the acquired data. The reference sensor was placed in a specific position that was found to yield best results (the lowest possible estimated error as estimated by the NDI Tool Tracker software from the NDI ToolBox) while staying within a 'mountable' distance of the baseplate.

4. Each acquired data point is an averaged value of 20 sensor signal samples. The orientations were averaged taking the mean of unit quaternions after ensuring that all quaternions were consistent with each other (i.e. no inverted quaternions were found).

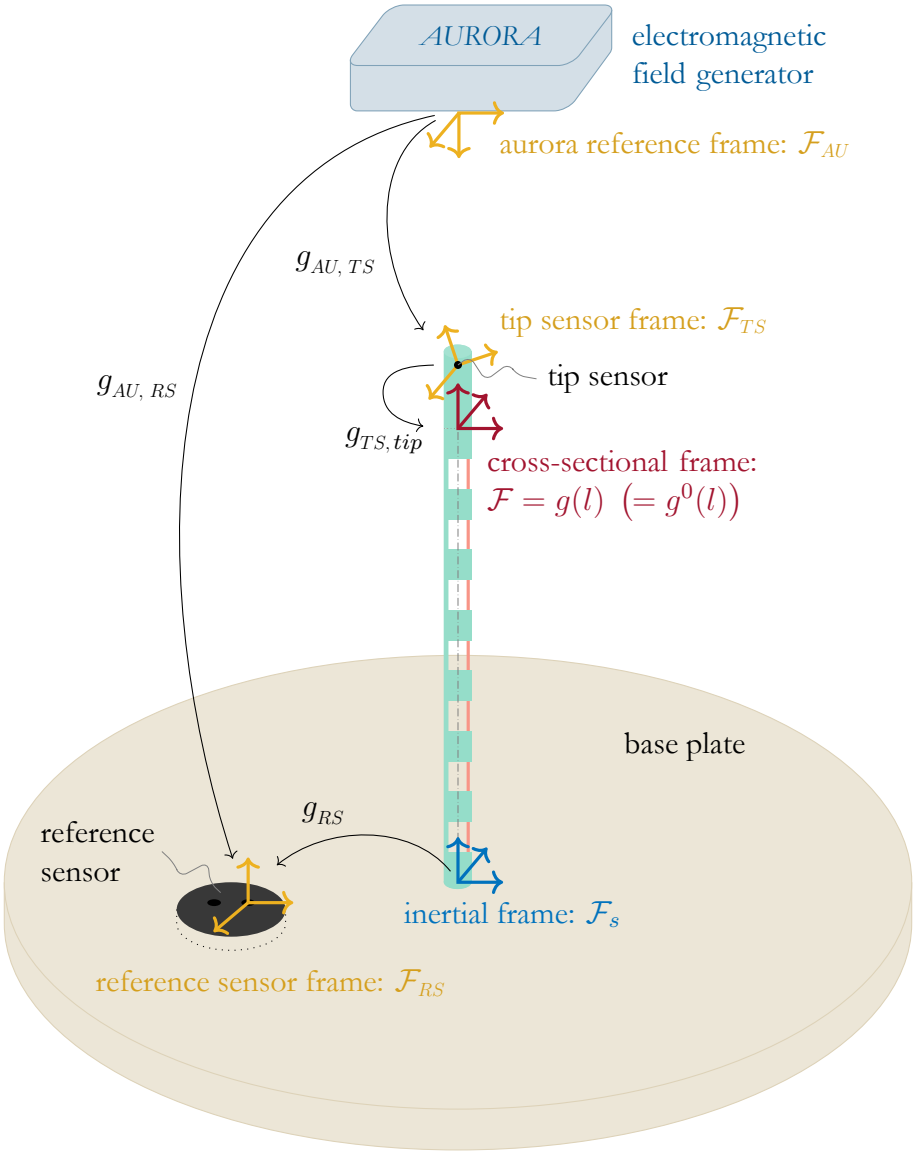

Figure 5.3: Representation of the frames involved in the sensor calibration and data acquisition procedures. The homogeneous transformations $g_{x,\,y}$ allow to pass from one frame $\mathcal{F}_x$ to another $\mathcal{F}_y$. When moving from the inertial frame $\mathcal{F}_s$, the subscript $\bullet_s$ is omitted.

The result of this process was assessed visually to be satisfying by comparing with the computer vision data (see next section). Moreover, the repeatability could be assessed thanks to a set of 248 measures of robot poses with 4 different prototypes and external loading covering the workspace that were repeated three times (each robot design, actuation value, and loading condition) for a total of 744 measurements. The 95% confidence interval for the repeatability is found in the range $[0, 2.53]$ mm, with a median at 0.6 mm, suggesting an excellent repeatability between experiments with the same conditions. The 95% confidence interval for accuracy of the Aurora measurement apparatus is specified by the manufacturer to be $[0, 0.88]$ mm.

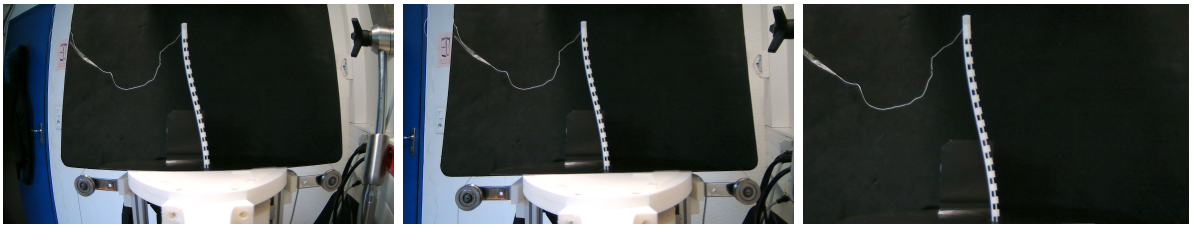

(a) (b) (c)

Figure 5.4: Example of the computer vision data processing with a camera snapshot of a CAAR. (a) The initial image where straight object lines are distorted by the camera lens. (b) The undistorted image where straight object lines appear straight but in perspective. (c) Image of the robot workspace warped on the bending plane.

Computer vision

The setup also includes a Renkforce RF-WC-150 Full HD camera used to qualitatively verify the shapes of the robots. No quantitative measures were performed on the images. All the images that appear in section 5.3 are reprojected onto the robot bending plane. To achieve such reprojection, the first step is to calibrate the intrinsic parameters of the camera. A series of 150 images of a checkerboard in a variety of positions were recorded in the field of view. The OpenCV library implementation of the calibration algorithm presented in [Zhang 2000] was used to compute the intrinsic parameters of the camera.

Next, to compute the extrinsic parameters of the camera, a series of object points from a camera image must be linked to their 3D positions in the experiment. To this end, a dedicated part with numerous 3D features in the workspace was printed and fixed to the baseplate of the actuation unit. On these features, a series of 44 object points were identified in both a camera snapshot and the 3D space of the experiment. In the image, the points were clicked manually by zooming in to pixel level. The 3D positions in the inertial frame $\mathcal{F}_s$ are known by design of the dedicated part. In order to cover a larger portion of the field of view of the camera, some easily identifiable features (e.g. the centers of the idler deflection pulleys) from the actuation unit were also included. Feeding the list of 2D and corresponding 3D points to the algorithm presented in [Gao et al. 2003] enables to solve the perspective-three-point problem and yields the extrinsic parameters of the camera. As for the intrinsic calibration, the OpenCV library implementation of this algorithm was used.

With these parameters set, the OpenCV library was used once more to compute warping parameters for warping the camera images on the plane of robot deformation ($e_x e_y$-plane). Finally, the warping parameters are used to warp all the acquired images of the experiment test. By reprojecting points with the calculated intrinsic and extrinsic parameters, the maximum error of this procedure was estimated to be less than 1 mm in the workspace. Of course, only the images of section 5.3 with 2D CAARs are considered. Indeed, such warping procedure is not valid for the robots treated in section 5.4 that curve out-of-plane.

Table 5.1: Geometrical and mechanical parameters of the 2D prototypes.

Robot design		$\overline{\rho}_1$ [mm]	$\underline{\rho}_1$ [mm]	$\overline{\rho}_2$ [mm]	$\underline{\rho}_2$ [mm]	γ_1 [mm]	γ_2 [mm]	a_{max} [mm]
$\mathcal{R}_1$	(regular)	3.0	2.0	1.5	0.5	5.0	2.0	7
$\mathcal{R}_2$	(regular)	5.5	4.5	4.0	3.0	10.0	7.0	7
$\mathcal{R}_3$	(convergent)	4.5	3.7	3.2	2.4	8.20 — 7.20*	5.60 — 4.95*	11
$\mathcal{R}_4$	(divergent)	4.5	3.7	3.2	2.4	7.20 — 8.20*	4.95 — 5.60*	11

* Values of the initial (γ_0) and final (γ_l) depth of the notches varying linearly (cf. section 5.3.5).

5.3 2D CAARs

This section and section 5.4 are devoted to the CAAR prototypes that were experimentally tested during this thesis. This first section only treats the in-plane-bending CAARs (or 2D CAARs), while section 5.4 generalizes to CAARs in 3D. Both sections detail the design of the corresponding manipulators and the experimental results. Each of the tested prototypes is identified with a symbol $\mathcal{R}_k$, with $k = 1 \,..\, 4$ for section 5.3 and $k = 5 \,..\, 6$ for section 5.4. This section then uses the experimental results to validate the model presented in chapter 4, while the purpose of the experimental results of section 5.4 is to demonstrate the capabilities of the designed robots.

Two different regularly notched CAAR designs, $\mathcal{R}_1$ and $\mathcal{R}_2$, with outer diameters of respectively 6 and 11 mm, and two variably notched prototypes, $\mathcal{R}_3$ and $\mathcal{R}_4$, respectively, with convergent and divergent neutral lines, are studied. All prototypes are 150 mm long. The height h of all notches and the distance c between all notches is 5 mm. A summary of all the geometrical parameters of the robots is provided in Table 5.1 (see Figure 4.4 page 98 for the graphical definition of the parameters). The prototypes are used in various configurations and under external loading.

5.3.1 Experimental Protocol

In the free-space experiments, all prototypes defined in Table 5.1 (cf. sections 5.3.3 and 5.3.5 for more details) were actuated by alternating 1 mm steps $a \in \{0, \pm 1\,\text{mm}, \pm 2\,\text{mm}, \ldots, \pm a_{max}\}$. a_{max} was determined once for, respectively, the regularly and the variably notched CAARs such as to cover a representative workspace, i.e. bending angle of approximately 90°. In the case of the regularly notched CAARs ($\mathcal{R}_1$ and $\mathcal{R}_2$ detailed in section 5.3.3), this value was determined by the CAAR with smallest diameter and is $a_{max,reg} = 7$ mm. In the case of the variably notched CAARs ($\mathcal{R}_3$ and $\mathcal{R}_4$ detailed in section 5.3.5), $a_{max,var} = 14$ mm. While alternating positive and negative actuation, the home position ($a = 0$) is systematically measured and compared to the initial position in order to detect potential plastic deformations that might occur during bending.

The loaded experiments were carried out over 5 fixed actuation values ($a \in \{0, \pm 3, \pm 6\}$ mm). Calibration weights of 20 g were attached to the tip and routed through idler deflection pulleys located symmetrically in the bending plane at both sides of the robot, yielding two possible external loads to be applied to each configuration (thread and weight visible on the right side of the actuation unit in Figure 5.1).

All the experiments (each robot design, actuation value, and loading condition) were repeated three times. In the following results, for each test, the mean tip position across repetitions is used. The mean across repetitions is an additional step based on the mean of 20 signal samples (see

Table 5.2: Calibrated model parameters.

Robot design		f_D [−]	$\mathcal{E}$ [GPa]
$\mathcal{R}_1$	(regular)	1.27	5.39
$\mathcal{R}_2$	(regular)	1.27	5.39
$\mathcal{R}_3$	(convergent)	1.32	5.39
$\mathcal{R}_4$	(divergent)	1.06	5.39

measure 4. in electromagnetic sensors data collection procedure detailed in section 5.2.2). Two outliers were found in one set of experiments compared to the two other repetitions of the same case (design $\mathcal{R}_1$ in free-space at $a = \{-7, -6\}$ mm). After analysis, it was found that a motor stall of the actuation was the source of the problem, and those two data points were removed from the subsequent data analysis (i.e. only two repetitions were considered for these two configurations).

Further, as discussed in section 5.3.6, the highest actuation values of the experiments were found to translate to an internal load in simulations that goes beyond the model critical load τ_{crit}. Therefore, the subsequent model validation restricts the more exhaustive experiment set to actuation values up to $a_{max} = 11$ mm.

5.3.2 Model Calibration

3D printing allows designing a variety of CAAR designs. There is, however, inherent variability due to the printing process used, which may impact the tube diameters, notch depth, etc. It is therefore necessary to calibrate the model. Two model parameters were calibrated: the distance between the neutral lines and the Young modulus. The distance between the neutral lines $D_{simulation} = f_D \times D_{theoretical}$ was calibrated once for the two regularly notched prototypes ($\mathcal{R}_1$ and $\mathcal{R}_2$) and then once for each of the two designs with variable notches ($\mathcal{R}_3$ and $\mathcal{R}_4$). The minimization criterion was the sum of squares of the tip error for all free-space configurations in the actuation spaces a_j described in section 5.3.1

$$f_D = \arg\min_{f_D} \sum_{k,j} \left\| r_{l,sim}(f_D, \mathcal{R}_k, a_j) - r_{l,exp}(\mathcal{R}_k, a_j) \right\|^2 . \tag{5.4}$$

Other quantities in the model, such as the bending stiffness, depend on the distance between the neutral lines. In the present simulations, the distance between the neutral lines was calibrated after the computation of these other quantities such that all other quantities remained unaffected. Also, the abrupt step in the inertia of the inner tube at $\tilde{X}_2^0(0)$ (see Figure 4.6 page 100) was found to slow down the convergence of the root-finding algorithms. Preliminary simulations allowed to identify a smaller value for $I_2(X_2 > l_1)$ that is yet sufficiently large for the reduction to have a negligible impact on the results.

Once the calibrated value for distance between the neutral lines was determined, Young's modulus $\mathcal{E}$ was calibrated in a similar way with the loaded experiments. The value of f_D remained unchanged.

$$\mathcal{E} = \arg\min_{\mathcal{E}} \sum_{k,j,f_+} \left\| r_{l,sim}(\mathcal{E}, \mathcal{R}_k, a_j, f_+) - r_{l,exp}(\mathcal{R}_k, a_j, f_+) \right\|^2 , \tag{5.5}$$

where f_+ stands for the tip external loading conditions. Both calibrated values are given in Table 5.2.

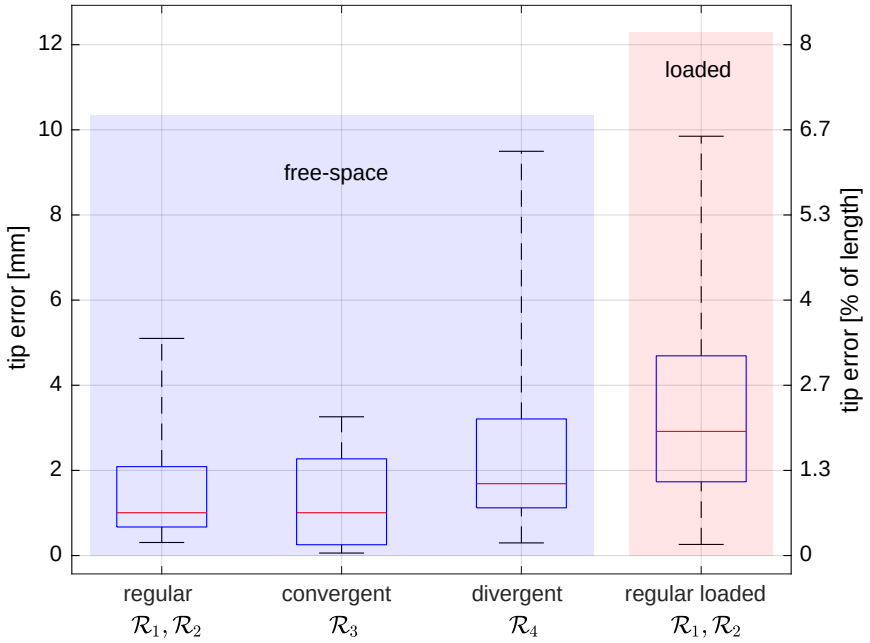

Figure 5.5: Boxplots of the tip position error between experimental results and simulations for all tests. The first three groups are cases in free-space.

5.3.3 Regularly Notched CAARs

Two different regularly notched CAAR designs ($\mathcal{R}_1$ and $\mathcal{R}_2$) with outer diameters of respectively 6 and 11 mm were studied. The geometrical parameters are given in Table 5.1, referring to Figure 4.4 page 98 for the notations. The two robots exhibit different workspaces when actuated over the same range of actuation values in free-space which is intended for validating the model on robots with different mechanical properties. Actuating the two robot designs over the 14 actuation values $\{0, \pm 1, \pm 2, \ldots, \pm 7\}$ mm yields 28 simulation to experiment comparisons. Figure 5.6 shows sample experiment to simulation comparisons for one of the two robots over the whole workspace (the one with the larger workspace). The tip errors between the simulation and experimental results for both regularly notched robots are reported in Figures 5.5 and 5.6. This error captures both the error of the model and the error of the electromagnetic sensors data.

5.3.4 Externally Loaded CAARs

External tip forces are applied both to the right and to the left to each configuration obtained at the actuation values $\{0, \pm 3, \pm 6\}$ mm for both robots from the previous section ($\mathcal{R}_1$ and $\mathcal{R}_2$). With the exact location of the idler deflection pulleys r_{ply} known, the experimentally applied tip loads are calculated as follows. The position of the application of the tip force on the robot is located at the nylon thread attachment point. In the inertial frame, this position is calculated as

$$r_{f_+} = r_1(l_1) - R_1(l_1) E_Y \left(D_1(l_1) \pm \overline{\rho}_1 \right) , \tag{5.6}$$

plus or minus sign for tip forces respectively to the right or left. Further, from the geometry of the system (see Figure 5.7) and again with plus or minus sign for tip forces respectively to the right or left, the applied tip force is computed as

$$f_+ = \pm a_g m \left(\sin(\varsigma), \cos(\varsigma), 0 \right)^T , \tag{5.7}$$

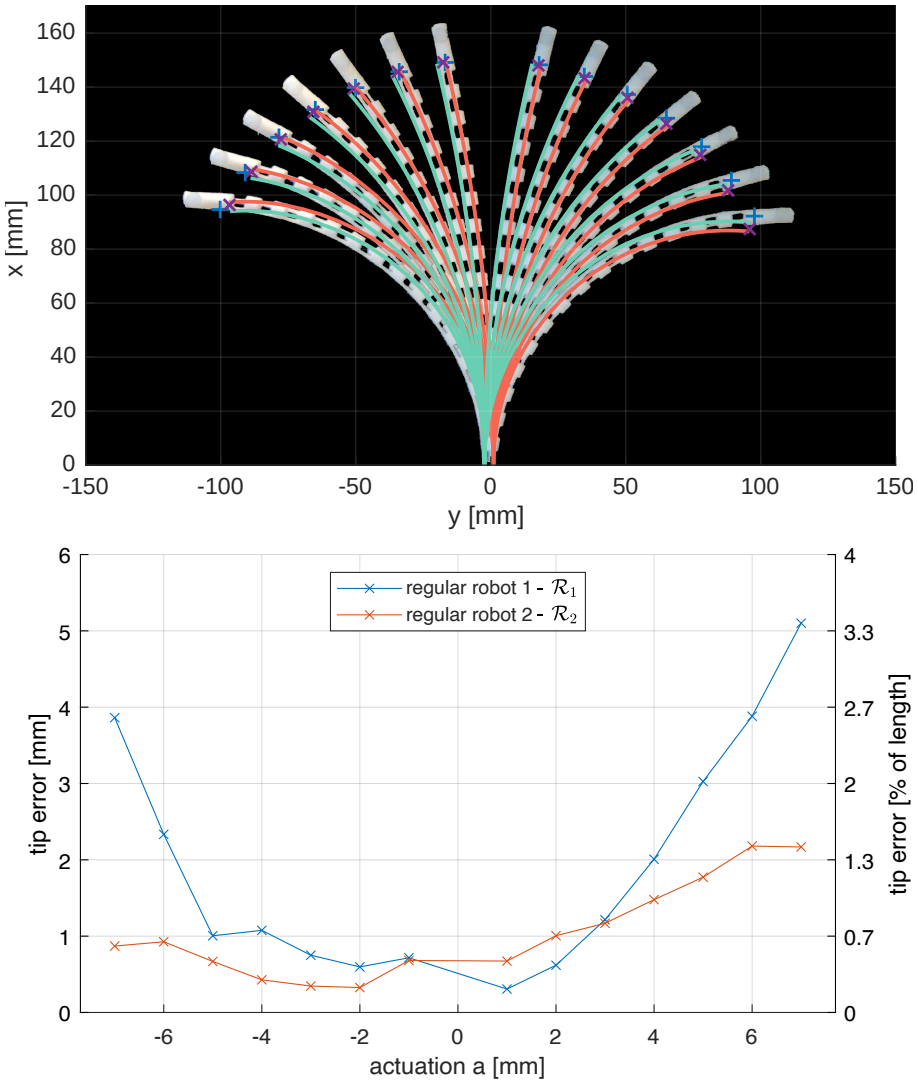

Figure 5.6: Top, snapshots of the experiments and simulation results for the regularly notched prototypes, here with prototype $\mathcal{R}_1$. The colored lines represent for each case the neutral line of tube 1 and 2, respectively, with corresponding colors. The blue marks are the tip electromagnetic sensor data. The purple marks are the simulated robot tips. Bottom, tip error as function of the actuation for both regularly notched prototypes.

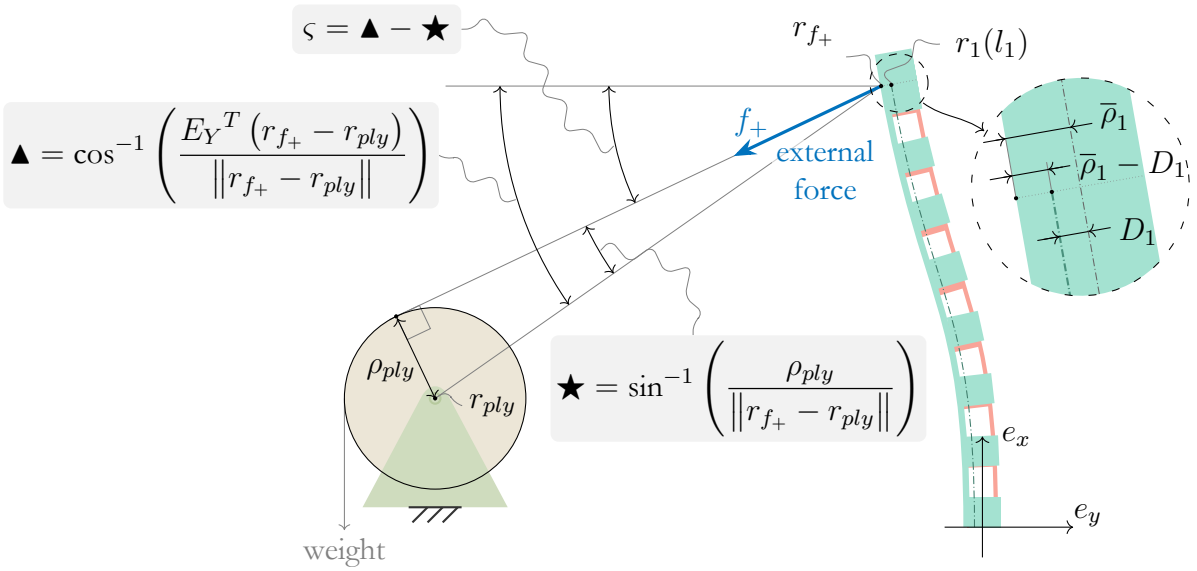

Figure 5.7: Schematic of an external force applied to the left at the tip of a CAAR prototype that is directed towards a pulley at a known position r_{ply} and radius ρ_{ply}. The force vector anchors at r_{f_+} located on the outer diameter of the robot in the same cross-section as the end of the neutral line of the outer tube $r_1(l_1)$.

where m is the mass of the calibrated weight and ς is the result of

$$\varsigma = \cos^{-1}\left(\frac{E_Y{}^T\left(r_{f_+} - r_{ply}\right)}{\left\|r_{f_+} - r_{ply}\right\|}\right) \pm \sin^{-1}\left(\frac{\rho_{ply}}{\left\|r_{f_+} - r_{ply}\right\|}\right), \tag{5.8}$$

with ρ_{ply} the radius of the pulleys and the output of inverse trigonometric functions restricted between $-\pi/2$ and $\pi/2$. As detailed in section 4.6.3, $F_+ = (0_{1\times3}, (R_1^T(l_1)f_+)^T)^T$ is input in the model during the backward integration of the wrenches from tube 2 to tube 1.

Comparing, by pairs from left to right, the shaded shapes on the background with the ones on the foreground in Figure 5.8, one can see how the prototypes are deflected when applying forces in comparison to the tests in free-space. The deflection imposed tip displacements between $[9.36, 31.20]$ mm across all loaded tests compared to free-space tests with same robots and actuation values. The mean deflections for robots $\mathcal{R}_1$ and $\mathcal{R}_2$ were respectively 22.19 mm (14.79%) and 10.93 mm (7.29% of robot length).

For both robots, a total 20 simulation to experiment comparisons are carried out. Examples of comparisons between the experimental and simulation results are presented in the snapshots of Figure 5.8 for robot $\mathcal{R}_1$. The tip errors between the simulation and experimental results for all loaded experiments are reported in Figures 5.5 and 5.8.

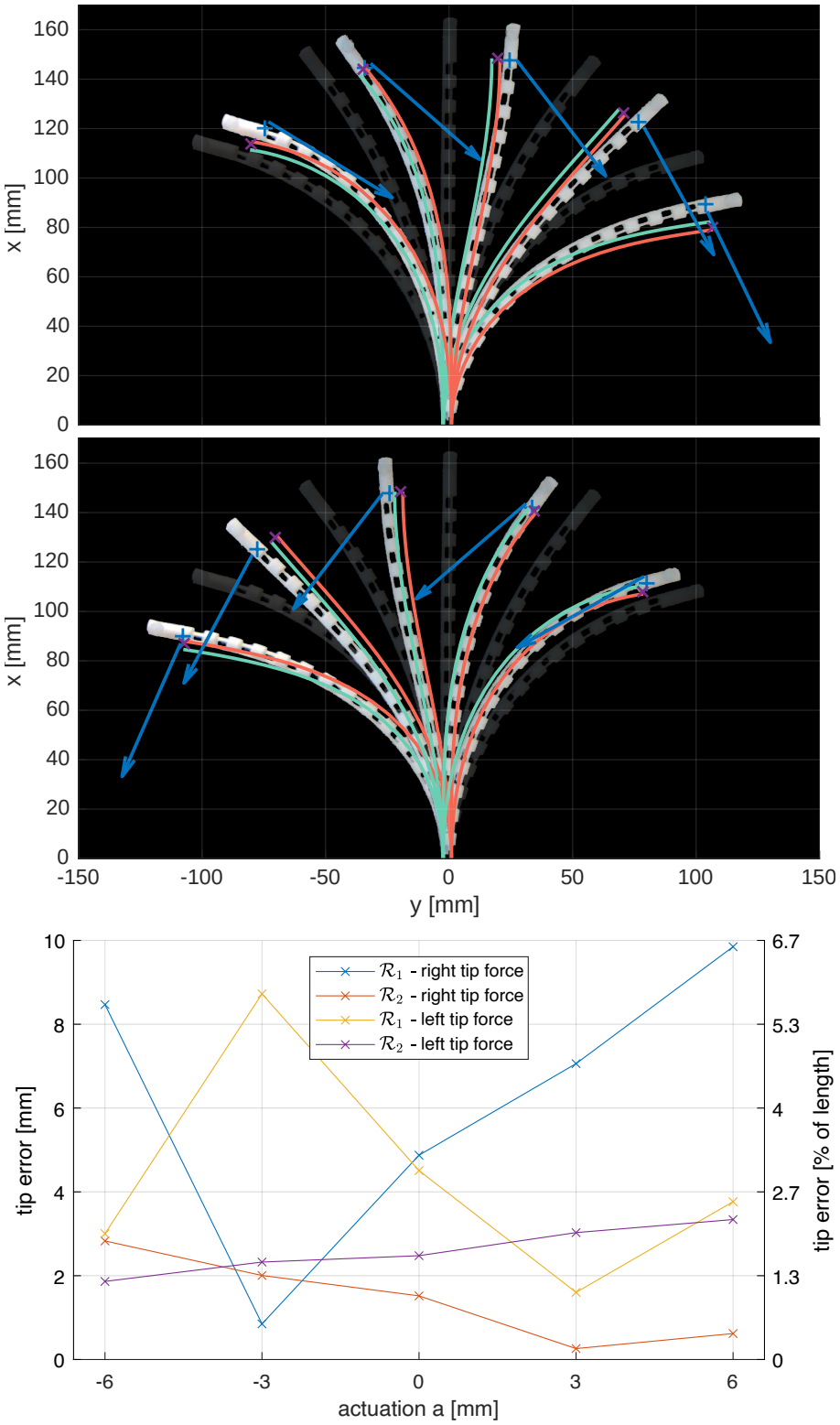

Figure 5.8: Top, snapshots of the experiments and simulation results for loaded tests with the regularly notched prototypes, here with prototype $\mathcal{R}_1$. The snapshots are split (right/left tip forces, identified by the blue arrow) over two plots to prevent overlapping. The shaded shapes on the background correspond to the free-space shapes at identical actuation (match left to right by pairs). The colored lines represent for each case the neutral line of tube 1 and 2, respectively, with corresponding colors. The blue marks are the tip electromagnetic sensor data. The purple marks are the simulated robot tips. Bottom, tip error as function of the actuation for all loaded tests with both regularly notched prototypes.

5.3.5 CAARs with Variable Neutral Lines

To validate the model with CAARs that have variable neutral lines, two additional prototypes, $\mathcal{R}_3$ and $\mathcal{R}_4$, respectively, with convergent and divergent neutral lines are assessed. To obtain convergent or divergent neutral lines, the depth of the notches decreases, respectively increases, from the bottom to the tip of the robot

$$\gamma(X) = \gamma_0 + \left(\frac{\gamma_l - \gamma_0}{l}\right) X\,, \tag{5.9}$$

where γ_0 and γ_l are, respectively, the initial and final notch depths given as the first and second values for γ in Table 5.1. The comparisons between the experimental and simulation results are presented in Figures 5.9 and 5.10 for prototypes with convergent and divergent neutral lines respectively. The tip errors for the comparison between the simulations and the experimental data for both designs are reported in Figures 5.5, 5.9, and 5.10.

5.3.6 Discussion on the Model Validation

An extensive experimental validation was carried out on four different 3D-printed CAAR designs (different dimensions and notch geometries), with and without external forces applied on the tip of the robot. Results show that the CAAR model derived in chapter 4 has a good performance, with mean and median tip errors of 1.47% and 1.06% of the robot length, respectively, over all experiments. It is capable of capturing general CAARs subject to external loads while the tip errors stay below 6.33% of the robots' length in free-space and 6.57% for the loaded cases. Figure 5.5 provides a graphical summary of the tip error statistics. Overall, in 94.6% of the experiments, the tip error was below 5% of the robot length, including experiments under external loading. In the experimental procedure, the CAARs were actuated with alternative positive and negative displacements of tube 2, followed by a measurement in the unactuated reference configuration. Only limited plastic deformation of the prototypes was observed ($< 2\,$mm tip displacement in all cases), which confirms that the basic hypothesis on the use of the materials in their elastic range was not violated.

High actuation cases were discarded from the results as mentioned in section 5.3.1. Indeed, the application of a pushing force at the base of the inner tube is countered by a reaction force at its opposite end, from the outer tube. This force is opposed to the former and charges the inner tube into compression. Conversely, the application of a pulling force on the inner tube exerts a pair of opposing compressing forces at the ends of the outer tube. Therefore, due to its operating principle, the CAAR can buckle beyond a certain critical load which can be approximated by calculating Euler's critical load for a pin ended rod

$$\tau_{crit} \simeq \frac{\mathcal{E}\mathcal{I}\pi^2}{l^2}, \tag{5.10}$$

where $\mathcal{I} = \max\left(\mathcal{I}_1 + \mathcal{I}_2\right)$.

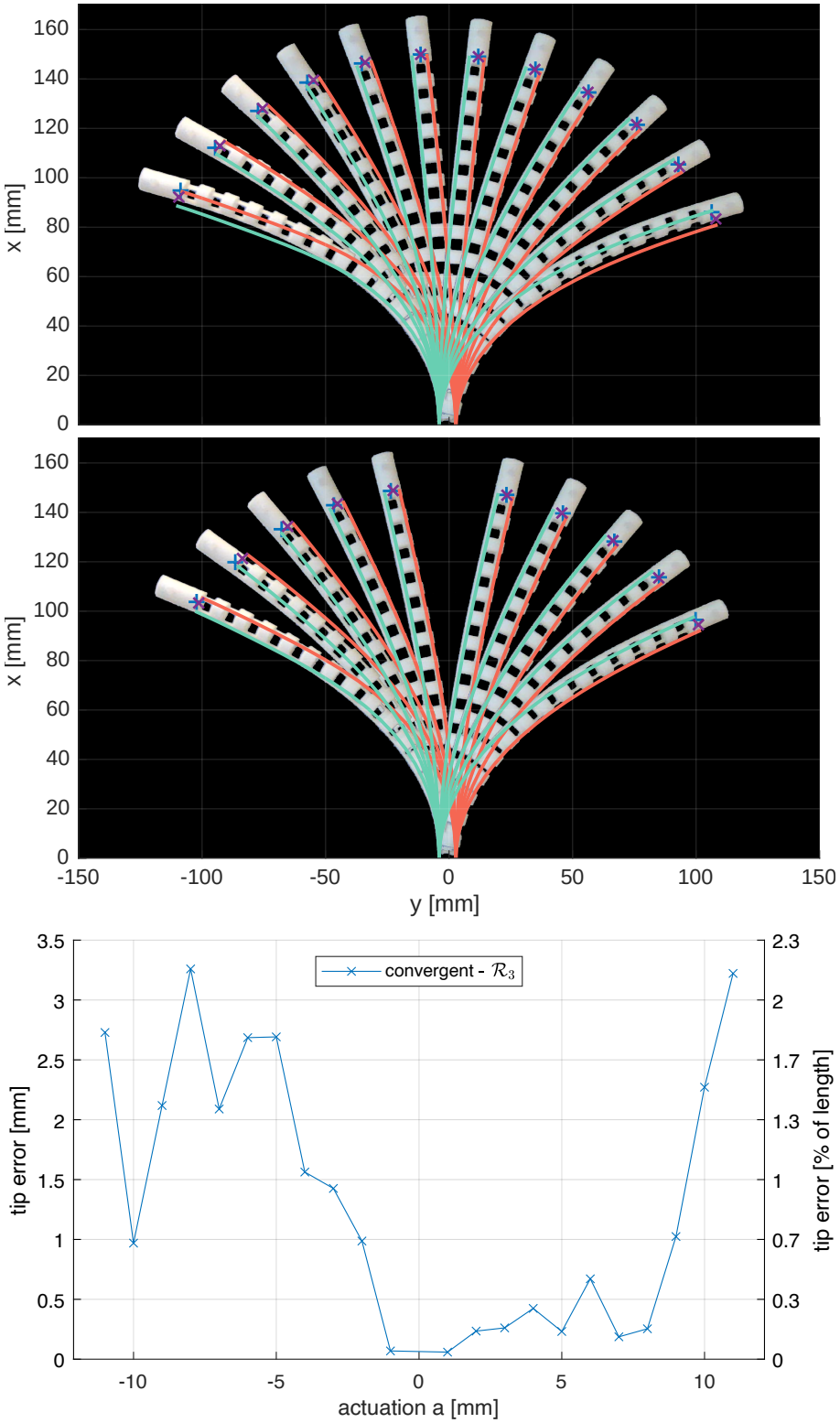

Figure 5.9: Top, snapshots of the experiments and simulation results for the convergent neutral line prototypes ($\mathcal{R}_3$). The snapshots are split (odd/even translation actuation values) over two plots to prevent overlapping. The colored lines represent for each case the neutral line of tube 1 and 2, respectively, with corresponding colors. The blue marks are the tip electromagnetic sensor data. The purple marks are the simulated robot tips. Bottom, tip error as function of the actuation.

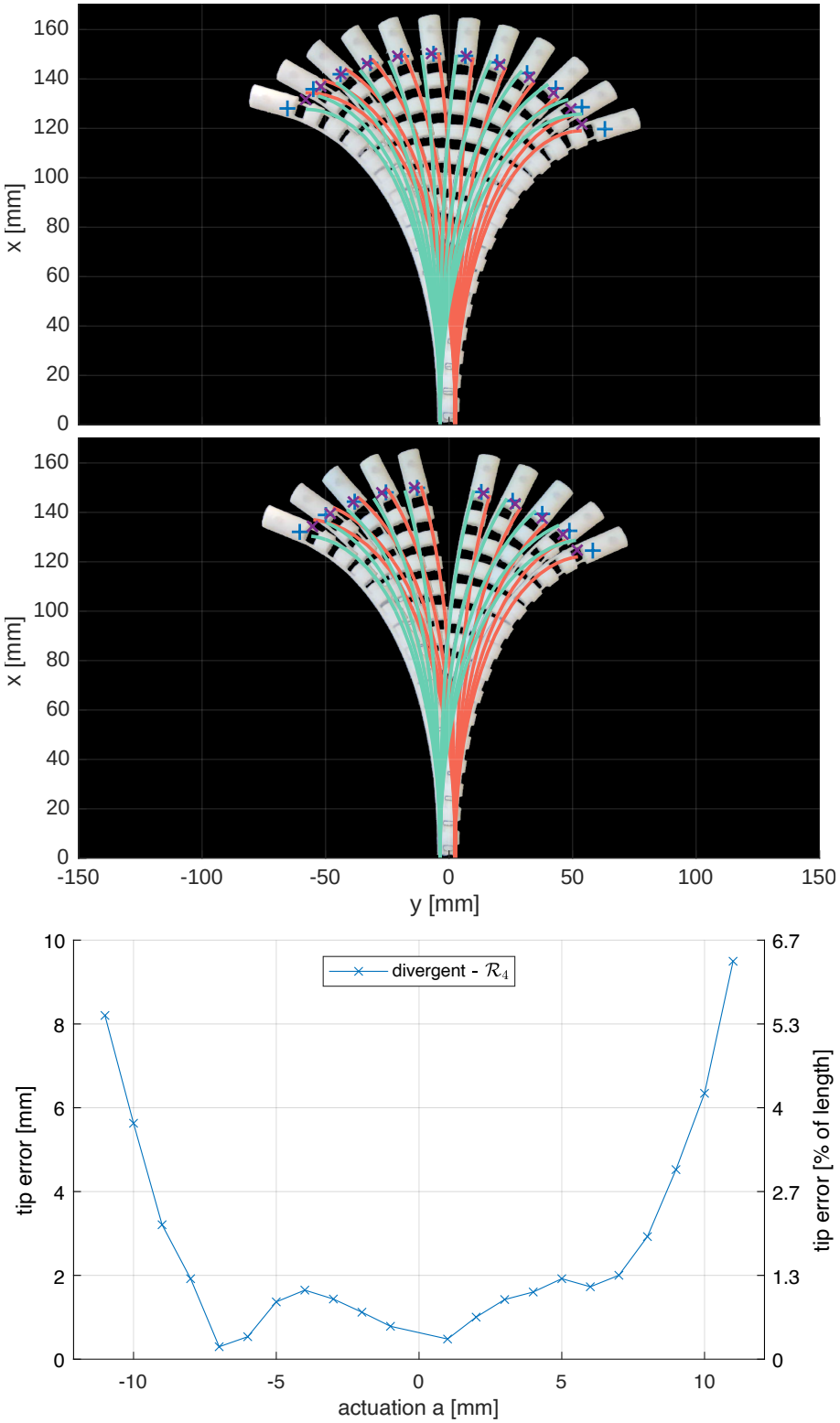

Figure 5.10: Top, snapshots of the experiments and simulation results for the divergent neutral line prototypes ($\mathcal{R}_4$). The snapshots are split (odd/even translation actuation values) over two plots to prevent overlapping. The colored lines represent for each case the neutral line of tube 1 and 2, respectively, with corresponding colors. The blue marks are the tip electromagnetic sensor data. The purple marks are the simulated robot tips. Bottom, tip error as function of the actuation.

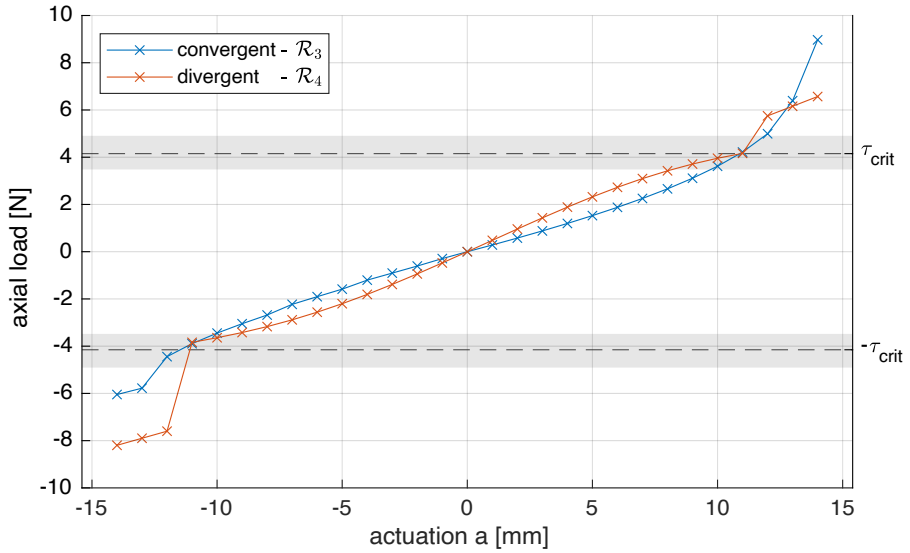

Figure 5.11: Axial load in the variable neutral line prototypes. The absolute value of the load increases with increasing actuation translation. Beyond $|a| > 11$ mm the axial load was found to exceed Euler's critical load of the rods composing the CAAR. The shaded area around the critical load value indicate uncertainty regarding the computed value, considering the uncertainty on the geometry due to printing imperfections.

Applying this approximation to the studied robots, the critical load is as indicated in Figure 5.11 (dashed line). First, note that the model accuracy decreases when approaching the theoretical critical load, i.e. when approaching an actuation of approximately ± 9 mm for the convergent $\mathcal{R}_3$ and divergent $\mathcal{R}_4$ designs. Indeed, in the experiments, several factors may impact the exact value of the critical load. For example, considering printing imperfections, varying the notch depth by 100 µm for the two designs $\mathcal{R}_3$ and $\mathcal{R}_4$, the theoretical value of the critical load varies as indicated by the shaded areas in Figure 5.11. Second, above this critical value, the equilibrium configurations calculated with the model were found to jump abruptly to another family of solutions. Furthermore, in some cases, the algorithm may not converge or converge very slowly. This explains why these pathological cases cannot be included in the simulation analysis.

One interesting observation is that the model correctly models the characteristic asymmetry of the bending of CAARs that is due to the difference between pushing and pulling the inner tube. When pushing (actuated to the left in our experiments) the inner tube of a CAAR inside the outer tube, the inserted rigid tube part virtually translates the active basis of the robot by preventing motion in the rigidified portion. Thus, for symmetrical actuation values, the configurations to the left side are translated towards positive e_x compared to the configurations on the right side. In the model this asymmetry is captured when computing $\mathcal{I}_2$ for $X_2 > l_1$ (see Figure 4.6 page 100).

The CAAR model proposed in this thesis also provides the full shape of the robots, in the present experimental validation however, only the tip errors were quantified. The robot shapes were qualitatively (i.e. visually) analyzed using the camera embedded in the setup, revealing that the maximum error along the robot is generally at the tip — which is coherent with previously validated models based on Cosserat rod theory. Nevertheless, full analysis of the obtained shapes will need to be carried out in future work, especially for designs capable of out-of-plane motion. Indeed, the configurations of the 3D CAARs presented in the next section can clearly not be assessed through their tip positions only. The tortuous, helical or 'S'-shaped, curves of 3D CAARs are ever more complex.

Table 5.3: Geometrical parameters of the helically notched prototypes.

Robot design		$\overline{\rho}_1$	$\underline{\rho}_1$	$\overline{\rho}_2$	$\underline{\rho}_2$	γ_1	γ_2	a_{max}
		[mm]	[mm]	[mm]	[mm]	[mm]	[mm]	[mm]
$\mathcal{R}_5$	(regular - 0° rev.)	3.6	2.8	2.3	1.5	6.4	3.8	7
$\mathcal{R}_6$	(helical - 180° rev.)	3.6	2.8	2.3	1.5	6.4	3.8	7
$\mathcal{R}_7$	(helical - 360° rev.)	3.6	2.8	2.3	1.5	6.4	3.8	7

5.4 3D CAARs

This section treats CAARs that can deform in 3D. First the design of such CAARs will be detailed. In this dissertation, two ways for deforming CAARs in 3D were explored and are presented in section 5.4.1. Then section 5.4.2 presents experimental results obtained with the constructed 3D prototypes. The results are discussed in section 5.4.3 where the potential of such 3D CAARs is analyzed.

5.4.1 Design of 3D CAARs

The main idea for deforming CAARs in 3D is to bring the neutral lines of the CAARs, that were previously assumed to evolve in the $e_x e_y$-plane (see Figure 4.3 page 97), out of this plane.

CAARs with 3D neutral lines

A first strategy that was investigated to bring the neutral lines of CAARs out of the $e_x e_y$-plane is by orienting the notches of the tubes with angles that are not aligned with the $e_x e_y$-plane. To avoid brisk discontinuities in the position of the neutral lines, a natural first choice is to continuously vary the angle of the notches along the length of the tubes. Evidently, these helically notched tubes yield neutral lines in the from of helices. Figures 5.12a and 5.12b (respectively Figures 5.12d and 5.12e) show notched tubes with continuously varying notch angles with a 180° (respectively 360°) counterclockwise turn along the length of the tubes when looking from the tip to the base of the robots. Of course, a broad range of other design possibilities can be imagined.

These possibilities become even more diverse when assembling two notched tubes to form a CAAR. Some ideas among others are to combine tubes with different notch revolution angles, tubes with counterclockwise and clockwise notch revolution angles, a helically notched tube with a regularly notched tube, and tubes that simultaneously vary depth and angle of the notches. The only preliminary design guideline that can be formulated is to avoid to create CAARs with superimposed neutral lines as this would prevent any translation motion of the tubes.

Because this thesis takes place in a world where the counterclockwise notch turns do not make the clock tick backwards, only two of the infinite imaginable designs were further investigated. In order to start with a simple case study, the two investigated designs are a CAAR composed of two 180° counterclockwise notch revolution angles ($\mathcal{R}_6$) and a CAAR composed of two 360° counterclockwise notch revolution angles ($\mathcal{R}_7$) (see Figures 5.12c and 5.12f, respectively). In both designs, the helices of the neutral lines lie on opposite sides of the center of the tubes. The other geometrical parameters of the helically notched CAARs are identical to those of an additional regularly notched

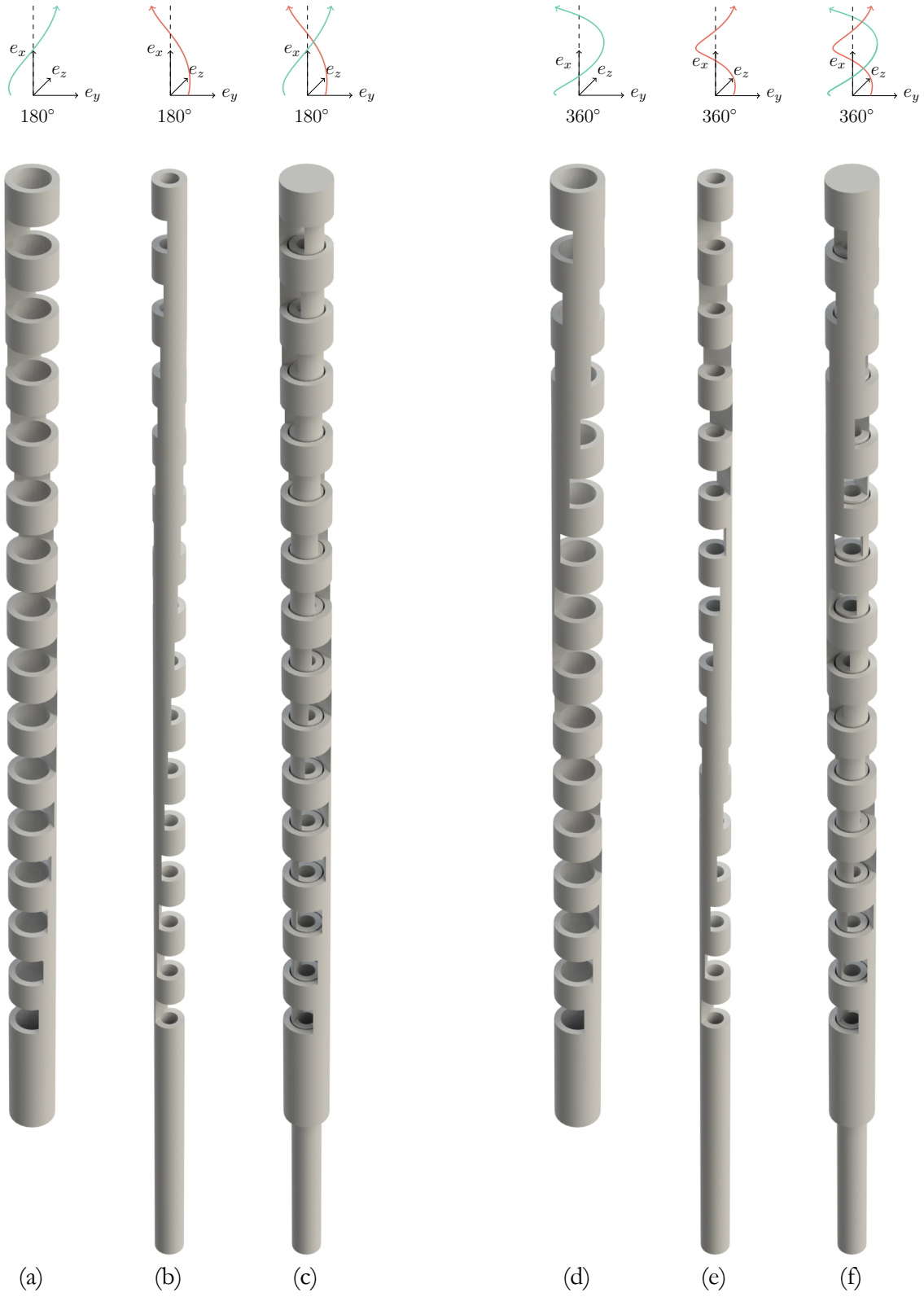

Figure 5.12: Helically notched CAAR prototypes, the dimensions are summarized in Table 5.3. (a) to (c), prototype $\mathcal{R}_6$ with notches in a half turn (180°) counter-clockwise around the axis. (d) to (f), prototype $\mathcal{R}_7$ with notches in a full turn (360°) counter-clockwise around the axis. (a) and (d) are the outer tubes. (b) and (e) are the inner tubes. (c) and (f) are the assembled robots. The paths of the neutral lines of the tubes are represented in the inertial frame with the colors from chapter 4 (the axial orientation of the renderings and plots does not correspond for better visualization).

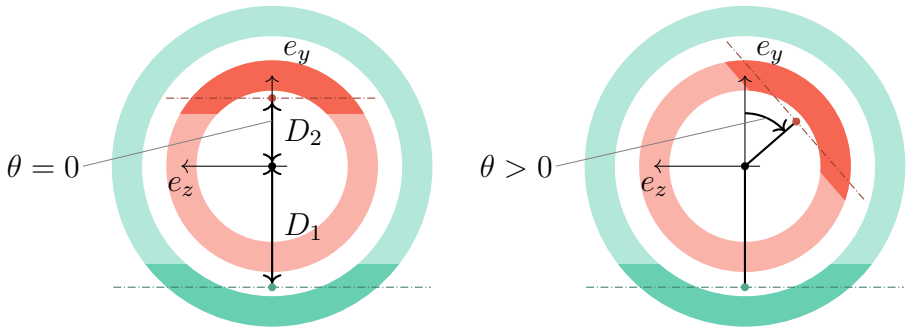

Figure 5.13: Sectional view of a CAAR at the baseplate (fixed $e_z e_y$-plane) as represented in Figure 4.3. The clearer parts show where the notches are cut out of the tubes, offsetting the neutral line (dash-dot lines). Left, with no rotation actuation ($\theta = 0$), the neutral lines lie opposite to each other, corresponding to in-plane bending. Right, introducing rotation actuation brings the neutral lines out-of-plane. θ is defined positively as rotating the inner tube clockwise with respect to the outer tube when looking from the tip of the robot to the baseplate.

prototype ($\mathcal{R}_5$) that will be used as reference for comparison. The geometrical parameters of all three prototypes are summarized in Table 5.3.

CAARs with rotation actuation

A second investigated strategy for bringing the neutral lines out of the $e_x e_y$-plane is to rotate one of the tubes at its base, relative to the other tube. In Figure 5.13, one can see how the neutral line of the inner tube moves out of the $e_x e_y$-plane thanks to the actuation in rotation θ. Along with the translation a, defined in Figure 4.3 page 97, the angle θ is a second actuation variable, defined as the relative rotation of the inner tube with respect to the outer tube, positive when turning clockwise looking from the tip of the robot to the baseplate. Recently, a similar actuation strategy has been studied in [Uppalapati and Krishnan 2020] where pneumatic chambers can be rotated, yielding helical robot shapes.

This actuation strategy can be applied to any CAAR design, it only requires to provide the base of the tubes with a fastening system that allows secure transmission of an axial actuation couple. While one could imagine actuating in rotation tubes with variable neutral line positions, this dissertation investigates rotation actuation with regularly notched CAARs. Indeed, as a first step, in order to evaluate the contribution of the rotation actuation without the influence of other parameters. The tested prototypes correspond to robot $\mathcal{R}_5$ in Table 5.3.

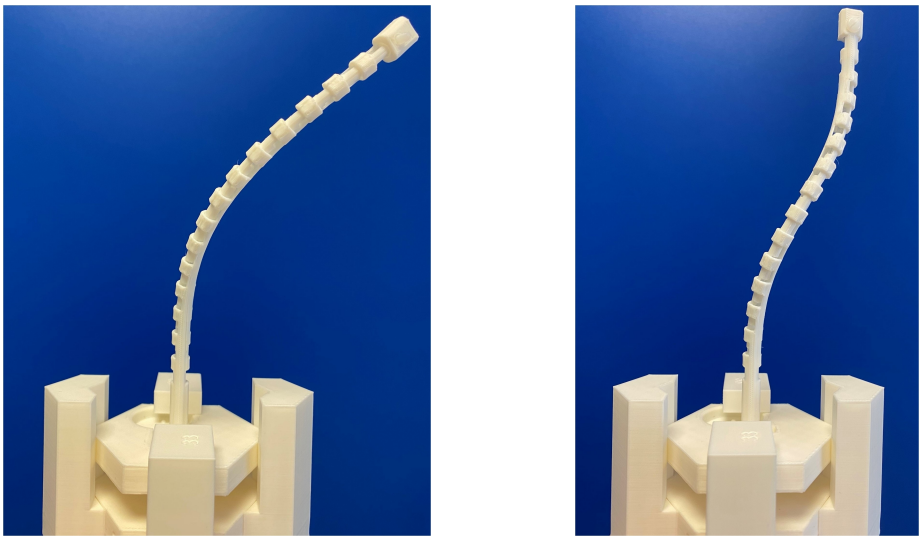

(a) (b)

Figure 5.14: Photos of helically notched robots of 7.2 mm in diameter, actuated in translation. Left, the 180° helically notched prototype $\mathcal{R}_6$ actuated at $a = -7$ mm exhibiting a twisting shape. Right, the 360° helically notched prototype $\mathcal{R}_7$ actuated at $a = -7$ mm exhibiting pure translation of the tip.

5.4.2 Experimental Results

CAARs with 3D neutral lines

The regularly notched prototype $\mathcal{R}_5$ and the two helically notched prototypes $\mathcal{R}_6$ and $\mathcal{R}_7$ are actuated in translation by alternating incremental 1 mm steps $a \in \{0, \pm 1\,\text{mm}, \pm 2\,\text{mm}, \ldots, \pm a_{max}\}$. Consistently with regularly notched prototype experiments of section 5.3.3, a_{max} was set to $a_{max,reg} = 7$ mm. As for the 2D experiments, while alternating positive and negative actuation, the reference configuration (home position, $a = 0$) is systematically measured and compared to the initial position in order to detect potential plastic deformations that might occur during bending. One example configurations for both helically notched prototypes is pictured in Figure 5.14.

Figure 5.15 shows the workspace of the two helically notched prototypes $\mathcal{R}_6$ and $\mathcal{R}_7$ compared to the workspace of the regularly notched prototype $\mathcal{R}_5$. One can see that the 180° helically notched prototype $\mathcal{R}_6$ bends out of the plane. During bending, the tip orientation pivots towards the bending direction (see Figure 5.15d), which is a similar behavior as for $\mathcal{R}_5$. Also, an axial rotation (torsion) of the tip is introduced (especially visible in Figure 5.15b). In fact, this torsion, measured at the tip, is propagated through the whole CAAR body, creating a novel twisting shape (see Figure 5.14a).

The workspace of the 360° helically notched prototype $\mathcal{R}_7$ indicates yet a different behavior. In this case, the tip moves in a plane that is perpendicular to the bending plane ($e_x e_y$-plane) of the regularly notched prototype $\mathcal{R}_5$. Interestingly, the orientation of the tip of $\mathcal{R}_7$ does not change during the sweeping of the workspace. In other words, the tip translates almost parallel to e_z, with a slight drop towards the boundaries of the workspace. In Figure 5.14b, displaying an example of an actuated robot shape, one can see how the robot conforms to an 'S'-shape during such tip translation.

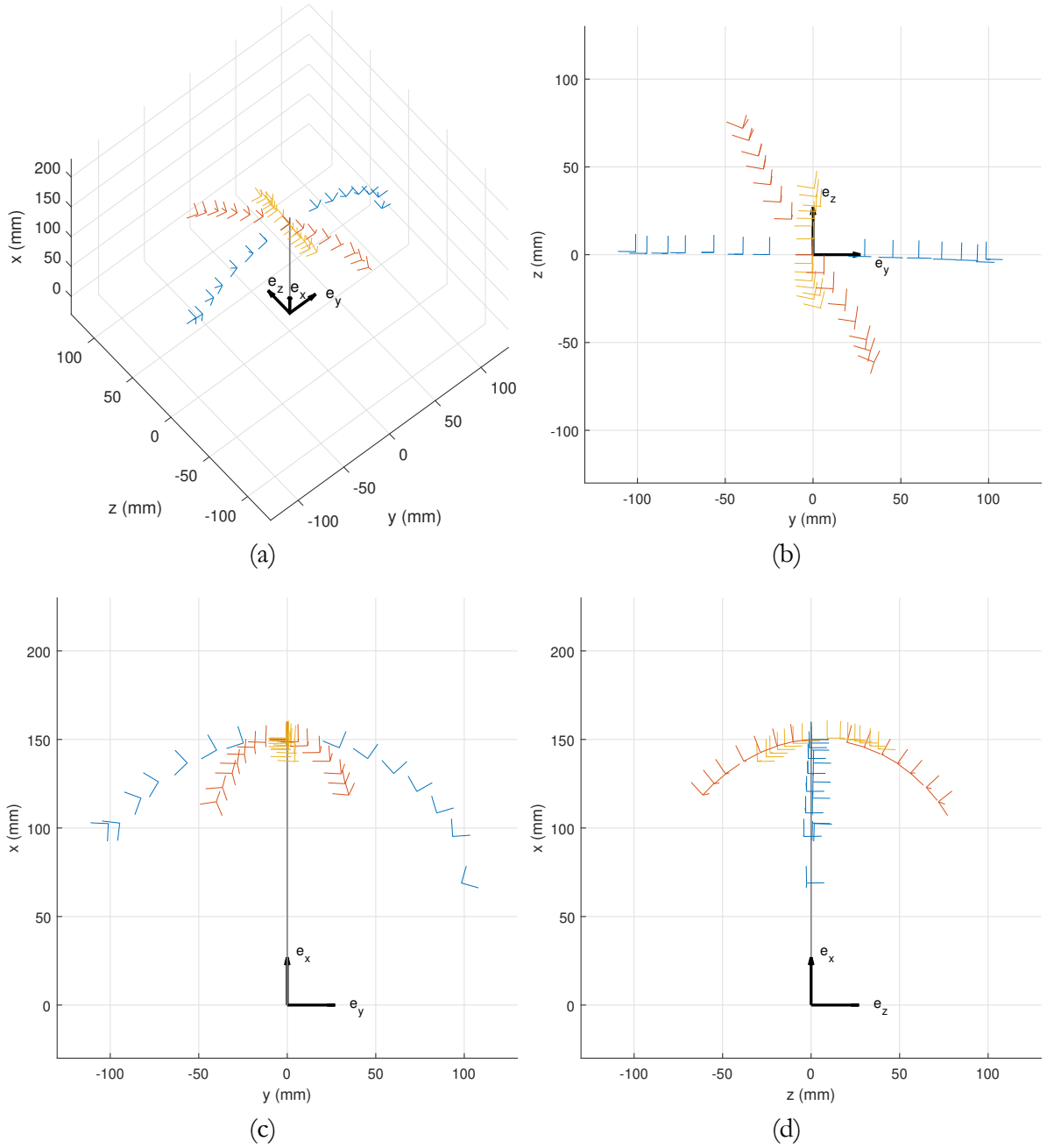

Figure 5.15: Workspace of helically notched CAARs actuated in translation, compared to the workspace of a regularly notched prototype $\mathcal{R}_5$ (blue). For each plotted data point, three lines are drawn from the measured tip position, representing the measured tip frame orientation. Red, the 180° helically notched prototype $\mathcal{R}_6$. Yellow, the 180° helically notched prototype $\mathcal{R}_7$. (a), (b), (c), and (d) are respectively perspective, top, front, and side views of the robots workspace, the inertial frame is provided in each. The grey vertical line in the plots represents the robot in undeformed (straight) configuration.

CAARs with rotation actuation

Introducing rotation as a second actuation variable changes the possible tip trajectories of CAARs from curves to surfaces. The workspace that is obtained by actuating the regularly notched prototype $\mathcal{R}_5$ both in translation and rotation is shown in Figure 5.16. The translation actuation range and stepping is the same as for the other experiments, i.e. $a \in \{0, \pm 1\,\text{mm}, \pm 2\,\text{mm}, \ldots, \pm a_{max}\}$ with $a_{max} = 7\,\text{mm}$. The rotation actuation space was set to $\theta \in \{0, \pm 30°, \pm 60°, \ldots, \pm \theta_{max}\}$ with $\theta_{max} = 180°$ such as not to break the prototypes. The maximum rotation angle was determined experimentally after breaking multiple prototypes with a rotation angle beyond 180°. The fracture limit of the prototypes is function of the printing material (PLA) but also of the 3D printing procedure which makes the prototypes relatively fragile. The workspace is characterized by two opposite quadrants of a dome surface. With increasing rotation actuation, the CAAR deforms in a twisting helical shape, also reducing the reach of the bending.

5.4.3 Discussion of 3D CAARs Experimental Results

The experiments of section 5.4.2 show that the investigated 3D CAARs can move out of the $e_x e_y$-plane of 2D CAARs reported in the literature. While a 3D workspace could also be achieved by rotating the whole CAAR (i.e. the two tubes at once) three interesting characteristics of the 3D CAARs approach can be noted.

1. By introducing rotation actuation or arranging notches helically along the tubes, complex 3D shapes can be achieved. These new shapes enable to reach new possible tip orientations and to reach specific points or a workspace through new robot paths. Conversely, when rotating the whole CAAR, the bending plane rotates, but the bending in this plane does not change.

2. Second, by orienting notches with a varying angle along the robot length, such complex 3D shapes can be achieved with only translation actuation which is a major advantage for the simplicity of fabrication and control of actuation units and for making such actuation units less bulky.

3. Translation of the tip can be achieved while maintaining its orientation constant.

From these observations, real added value of 3D CAARs for medical applications can be identified. Indeed, to better match the dexterity of a real surgeons' hand with a robot that can navigate to a surgical site through minimally invasive pathways, the medical robotics community is continuously thriving at improving the dexterity of developed devices. In the present case, 3D CAARs demonstrated an increased dexterity compared to 2D CAARs (see number 1. above). Also avoiding obstacles is an active field of research in medical robotics to be able to reach targets while avoiding bones or delicate tissues. The new complex shapes to which 3D CAARs can conform open up new perspectives regarding obstacle avoidance and path-planning. Finally, the translation with constant orientation of the tip of 3D CAARs is a promising feature for single port surgical procedures where it is necessary to deport the tool tips from the access port axis.

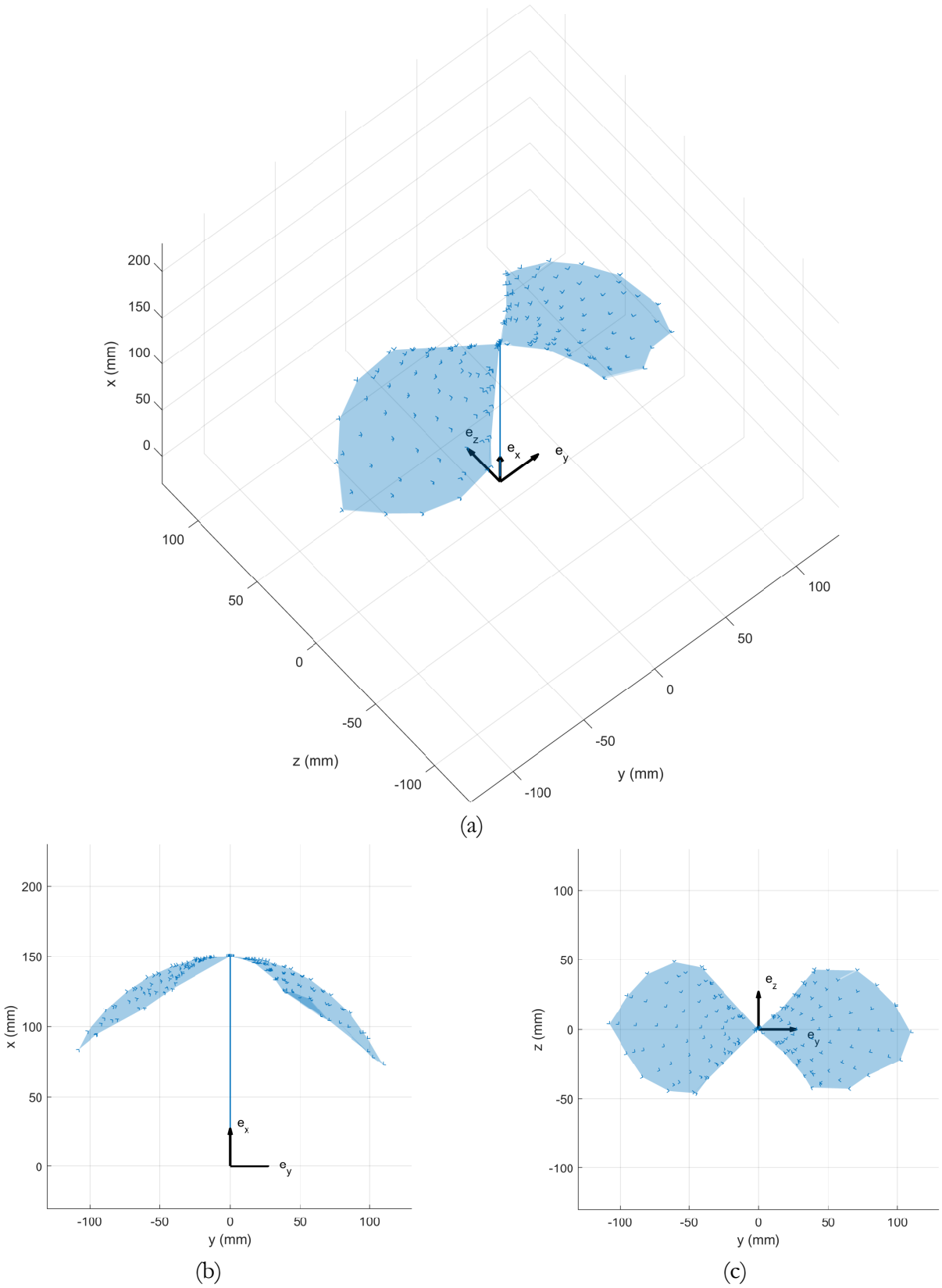

Figure 5.16: Workspace of a regularly notched CAAR ($\mathcal{R}_5$) when actuating both in translation and rotation. For each plotted data point, three lines are drawn from the measured tip position, representing the measured tip frame orientation. (a), (b), and (c) are respectively perspective, front, and top views of the robots workspace, the inertial frame is provided in each. The blue vertical line in the plots represents the robot in undeformed (straight) configuration.

5.5 Conclusion

This chapter presented the development of a versatile actuation unit with integrated tip position and orientation electromagnetic sensors and computer vision. Also, precise application of external punctual forces is possible. The actuation unit can accommodate CAAR or CTCR prototypes with up to four tubes and precisely actuate each tube in both rotation and translation. For example, it can serve as an actuation unit for actuating a two-segment CAARs similar to the one studied in [Oliver-Butler et al. 2022]. The presented setup is subsequently used to validate the multiple aspects of the CAARs mechanical model presented in chapter 4.

To this end, various CAAR prototypes were designed, including CAARs with variable neutral lines. The experimental validation on four different robot designs shows very satisfactory accuracy with a tip error of 1.47% of the robot length and testify that the model accurately captures the studied CAAR motion. Yet, including the unmodeled phenomenons discussed in section 4.7 might further improve the model accuracy.

Beyond the planar model validation, CAARs were also designed with out-of-plane neutral lines. While the literature on CAARs only reports in-plane-bending CAARs, the new type of CAARs introduced in section 5.4.1 are able to deform in 3D. Pushing the concept of 3D CAARs even further, adding rotation of the tubes as a new actuation variable is investigated. Again, auspicious experimental results were reported with interesting 3D shapes. Through reasoning and evaluation of the reported shapes, real potential for 3D CAARs in various medical applications is identified. Future work regarding the maturity of the prototypes and the extension of the CAARs mechanical model to the 3D case is discussed hereafter, in the Conclusions and Perspectives.

Contributions of this chapter

1. The model presented in chapter 4 is validated through an extensive set of experiments with various CAAR designs with and without external loading.
2. It is shown through experiments that various strategies allow to extend the CAAR concept to 3D.
3. The capabilities of 3D CAAR prototypes are analyzed.

While the CAAR model presented in the previous chapter was derived in collaboration with the LS2N Laboratory in Nantes, France, the experiments were carried out in whole at the TIMC Laboratory as part of Matthias Tummers' (MT) thesis. The actuation unit presented in section 5.2.1 was designed by MT and assembled by Alexis Offermann, a research engineer of the CAMI team, with the help of MT. Concerning CAARs in 3D, the results of section 5.4 have benefited of the input of Lèna De Thomasis who was a second year engineer student at GrenobleINP, Industrial Engineering, during her three-month project in the CAMI team. All experiments up to section 5.4 were carried out by MT. In section 5.4, the original idea of extending the workspace and dexterity of CAARs to 3D came from MT. Lèna De Thomasis carried out the experimental results presented in section 5.4.2. Her internship was co-supervised by M. Taha Chikhaoui and MT.

Summary, Perspectives, and Conclusion

Summary of the Contributions

In this dissertation, the design and modeling of a novel continuum robot structure has been investigated. First, in chapter 1, CAARs have been identified as a promising new type of continuum robot and their potential for medical applications has been analyzed. In order to deploy CAARs and control their shape or tip position, a precise mechanical model was yet to be derived.

Past years in the continuum robotics community have seen the development of geometrically exact models for standard types of continuum robots in 2010 for CTCRs, in 2011 for TACRs, in 2014 for PCRs, and in 2017 for PCRs with GICs. For the recent hybrid continuum robot structures are more complex than the standard types, it has been six years since the community has not witnessed the development of new such models. In this dissertation, a new geometrically exact model for CAARs is derived based on Cosserat rod theory.

To accomplish this challenging objective, it was necessary to unwind the many tangled aspects of the Cosserat rod theory. Two major modeling approaches for modeling continuum robots with such theory were identified: the Newtonian approach and the Lagrangian approach. The first step was to flatten out the two approaches in order to gain a deep understanding of Cosserat rod modeling from these different view points. In chapter 2 all features necessary for modeling continuum robots through one or the other approach were exposed in a single structured picture. Chapter 3 presents a side-by-side derivation of Cosserat rod modeling applied to the use-case of TACRs. While Cosserat rod models of this type of continuum robots were previously published, the dedicated analysis in this thesis allowed to provide additional contributions to both (see end of chapter 3 page 89).

Based on these strong foundations, chapter 4 derives a mechanical model for CAARs. Compared to existing state-of-the-art models, the proposed model is capable of taking into account interactions between CAARs and their environment. Moreover, the new geometrically exact model is not based on geometrical simplifications as the constant curvature assumption for the state of the art models.

The model is validated in chapter 5 through a thorough and extensive set of experiments using various 3D-printed CAAR designs, in free-space and with external forces applied at the robot tip (see Figure C.1). Results show that the model has a good performance with mean and median tip errors of 1.47% and 1.06% of the robot length, respectively, over all experiments. Overall, in 94.6%

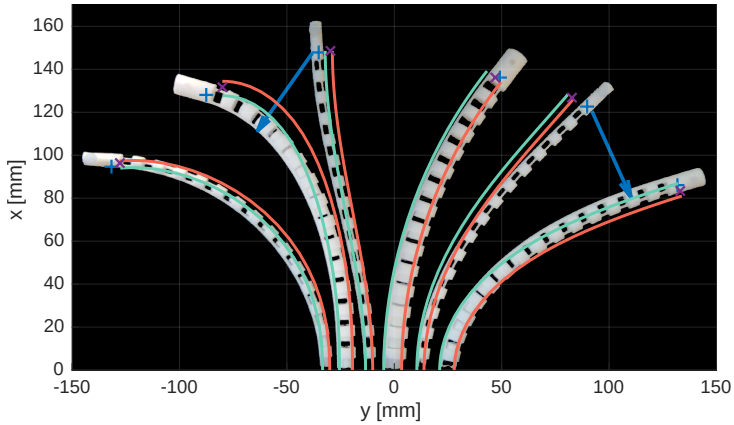

Figure C.1: Geometrically exact modeling of various CAAR designs with possibly varying notches and possibly under external loads. From left to right: (1) a 6 mm diameter regularly notched CAAR; (2) a 9 mm diameter CAAR with increasing notch depth towards the tip; (3) a 6 mm diameter regularly notched CAAR under external tip force to the left (blue arrow); (4) a 11 mm diameter regularly notched CAAR; (5) a 6 mm diameter regularly notched CAAR under external tip force to the right (blue arrow); and (6) a 9 mm diameter CAAR with decreasing notch depth towards the tip. The blue marks are the experimental data, the purple marks are the simulated robot tips. The colored lines represent the neutral lines of the tubes.

of the experiments, the tip error was below 5% of the robot length, including experiments under external loading. These results compare well with prior Cosserat rod models for continuum robots (CTCR: 1.5% to 3%; TACR: 1.7%; PCR: 2.83%; PCR with GIC: 8%[1]). Moreover, a mean tip error of 1.47% in open-loop control is an acceptable error for many clinical applications. For applications in fields like neurology or ophthalmology that requiring even more precision, the control loop will need to be closed, but the benefits of a model that takes into account external loads remains.

Chapter 5 was also the occasion to present promising perspectives for CAARs able to deform in 3D. The increased dexterity and complex shapes offer undeniable advantages for future medical applications. Ultimately, all the contributions of this dissertation fall within the general long-term objective of improving therapeutic yields and clinicians' comfort in the healthcare sector.

Future Work

Considering notched tubes and CAAR locking

While this thesis has focused on the advantages and potential of CAARs, there are still some open questions related to these structures that need to be further investigated. Using notched tubes as elements to construct continuum robots is not an inconsequential alternative. In the present dissertation, the experimental validation evinced that 3D printing enables easy manufacturing of notched tubes with various designs. 3D printing is however subject to imperfections, which can lead to large errors in key dimensions. For example, in simulation, increasing the notch depth by 100 µm for design $\mathcal{R}_1$ in chapter 5 leads to a tip error up to 4.1 mm in the workspace with respect to the nominal model results. In order to compensate for such effects, a calibration of

[1]These values correspond the mean tip error with respect to the nominal manipulator length for all (free-space/loaded) experiments of the corresponding communications, except for PCRs where only free-space experiments are reported and for PCRs with GICs, where only an estimated maximum tip error is reported.

the parameter D (see section 5.3.2), was performed. This calibration procedure, albeit relatively simple, adds a layer of complexity to the model and may be questionable in clinical applications. The use of precision manufacturing and measurement devices in future work, potentially using laser manufacturing for notching Nitinol tubes following a process similar to the one described in [York et al. 2015], may remove the need for such a calibration.

Nitinol is indeed a popular material for the fabrication of continuum robots for its biomedical compatibility, its super-elastic properties and the fact that they can be easily purchased off-the-shelf in the form of thin walled tubes. It is however necessary to pay special attention to the mechanical properties of such tubes. Nitinol can be subject to phase shifting between its austenite and martensite states, which both exhibit different mechanical properties [Šittner et al. 2014]. Laser cutting notches out of stock tubes may locally change the mechanical properties due to heating of the material. This undesirable effect can be limited with the use of femtosecond lasers [Chitalia et al. 2020], but it is not a trivial issue, regardless.

Some recent studies started looking into on the complex mechanics of notched Nitinol tubes [Wenlong et al. 2013, Yu et al. 2018]. The most advanced model, considering individual notch deflection and friction in a notched tube continuum robot (NTCR), is the model described in [Pacheco et al. 2021]. It takes into account the individual geometry of the notches and friction that operates along the robot length. Also, the authors carry out a study of the impact of phase transformations of Nitinol on the robot behavior. A similar analysis is carried out in [Chitalia et al. 2021]. In this case, a NTCR is proposed for pediatric neurosurgery and a specific strategy is included in the control algorithm to compensate for the hysteresis that arises due to the phase transformations of Nitinol when actuating the robot. The authors of [Legrand et al. 2021] explore the large deformation case of NTCRs and feed their model with an equivalent Young's modulus that accounts for the super-elastic behavior. These results were obtained for NTCRs that are made out of a single notched tube and are actuated by a tendon instead of push-pull motion of multiple tubes. Nevertheless, such results are of interest for CAARs as well.

Clearly, the mechanical properties of notches are not the only challenge. It is difficult to imagine a clinical robot prototype with apparent cutout notches. First, this could harm tissues during operation, but also, it introduces great amounts of friction. Even worse, introducing rotation actuation, CAARs can be subject to locking of the tubes due to notches of the inner tube getting stuck with the notches of the outer tube. One solution to improve surface quality and reduce friction and locking is to provide the tubes with silicon coating as in [Amanov et al. 2017]. As a side remark, the buckling phenomenons discussed in section 5.3.6 are, in the experiments, partially captured by the clearances and the dry friction between the two tubes, which delays buckling (virtually increases the critical load value). Reducing the clearances, smoothening the printing surface quality, and lubricating the tubes could narrow down the observed discrepancies between model and experiments.

Another interesting research path to circumvent all these notched tubes considerations is the design of tubes with offset neutral lines that do not feature notches. This could be achieved by printing tubes with multi-material printers. Loaded with materials of different stiffnesses and specifying a material gradient in the tubes to be printed, the obtained parts would be plain tubes at first sight, but with effective offset neutral lines. The same could be achieved by printing tubes with recently developed anisotropic pattering techniques [Vanneste et al. 2020]. Another idea is to print tubes whose inner and outer cylindrical surface are not concentric, yielding a thin tube wall on one side and a thicker tube wall on the other. With these specific meso-structured tubes, one can even imagine, for a longer-term perspective, to print tubes out of other materials as Nitinol or glass. The latter is currently being used by research teams to print miniaturized needles [Zanaty et al. 2019].

Countless possibilities with 3D CAARs

As exposed in section 5.4.1, the design space of 3D CAARs has barely been explored. This thesis assessed the combination of two helically notched tubes with 180 or 360° counterclockwise notch revolution. It might be interesting to invert the revolution angle of the notches for one of the tubes or to combine tubes with different notch revolution angles.

Constructing CAARs with multiple tubes could also add a third dimension to the workspace. The neutral lines of CAARs actually behaving as the multiple rods of PCRs, there is no theoretical limitation in restricting their number to two. Adding a third notched tube with its neutral line out-of-plane could naturally add a DoF to the system.

These perspectives on 3D shapes also open up new possibilities regarding design optimization for (patient) specific anatomical constraints. Algorithms could be used similar to those developed in previous work on design optimization for CTCRs [Anor et al. 2011, Mitros et al. 2022a] and TACRs [Rox et al. 2022] . Yet, a 3D CAAR mechanical model is required in the first place.

3D CAAR mechanical model

Indeed, to further deploy 3D CAARs, the next step is to extend the model presented in chapter 4 to the 3D case. While this extension is not per se straightforward, the planar model was derived in a generic way, specifically for this purpose. The general derivation flow of the 2D model can be taken over. The kinematic constraints need to be extended to the 3D case. For the concentricity constraint (equation (4.24)) this means that the link between the two neutral lines is no more merely a translation of a neutral line offset, but must include the rotation of the neutral lines around the centerline of the tubes. The face-to-face functions (equation (4.21)) and the kinematic reduction (equations (4.47) and (4.51)) must be revised accordingly. Additional strain fields will have to be 'activated' in the partition of equation (4.14) to take into account the new deformations. From there, starting over from the principle of virtual work should enable to derive the reduced static balance for 3D CAARs.

Besides, adding stretch and transverse shear fields to the model could contribute to capturing buckling phenomenons described in section 5.3.6. Indeed, the hyperstatic stresses observed in the pathological cases would be transferred to the new modes.

Recently, the authors of [Adagolodjo et al. 2021] achieved to solve a coupled Discrete Cosserat Model and FEM through the use of global and reduced coordinates. This approach that uses Lagrange multipliers might be an interesting alternative to the Cosserat model derived in this dissertation. Concerning the 3D case of the model, it would enable a short-cut to the above described extension procedure in the way that the expressions of the kinematic reduction would not have to be derived. Indeed, in this approach, only the constraints of the structure need to be considered.

Other CAAR mechanical model extensions

Using the open lumen of a first CAAR to pass another CAAR segment of smaller diameter allows creating multi-segment CAARs [Oliver-Butler et al. 2022]. If one considers the possibility of translating one CAAR segment with respect to the other, the outer CAAR segment is traversed either by plain tubes or portions of the inner CAAR segment. In either case, some coupling between the mechanics of the two tubes occurs. The presented mechanical model being capable of taking external loads into account is suited for modeling these interactions but clearly defining the interactions as functions of the actuation parameters of the robots is subject to future work.

Another valuable model extension is to consider what happens below the baseplate. In the presented experiments, the tubes were attached to the actuation unit with the basis of their active parts close to the actuation unit. In clinical applications, it is however likely that the actuation of the tubes will be transferred over longer portions of plain tubes and the mechanical deformation in these actuation linkages may become significant. Including these developments in the CAAR model would help close the gap with future the medical applications. As this challenge is a shared one between CAARs, CTCRs [Peyron et al. 2019] and other continuum robots that are actuated over considerable transmission lengths, one should also investigate how to transfer research contributions from one type to the others.

In continuum robots consisting of concentric tubes as CTCRs and CAARs, there is a necessary clearance between tubes. As for many concentric tube robot models [Rucker and Webster 2008, Dupont et al. 2010], our model assumes that the clearance between tubes is just enough to permit their relative movement while keeping their tangents coincident. As shown in [Ha et al. 2019] for CTCRs, modeling the clearance allows incorporating friction between tubes, which can be considered to improve the model accuracy. It remains however an open problem to incorporate such phenomenons in a Lagrangian Cosserat rod formulation in the context of CAARs.

While the herein derived model is limited to statics, consistent with the nominal regime of continuum robots in the context of medical applications, the use of CAARs in other fields as the industry may benefit from a model taking dynamics into account. The formulation presented in this thesis can be extended to include the dynamics of the system in a similar way as in [Boyer et al. 2021, Boyer et al. 2022a]. Moreover, a dynamic model would enable to study the elastic stability.

During this thesis, no stability issues were observed with CAAR prototypes, nevertheless exhaustivity cannot be claimed. Elastic instability is a known phenomenon for certain continuum robots as TACRs [Li and Rahn 2002], PCRs [Briot and Goldsztejn 2022, Zaccaria et al. 2022], or CTCRs [Peyron et al. 2019]. While fixing the ends of the tubes of CAARs should avoid the particular instabilities know for CTCRs, other yet undiscovered instabilities may be lurking in the dark. Instabilities can be predicted with modeling and avoided through design, by restraining the workspace or the actuation history. In fact, this is directly in link with the simulation observations where the equilibrium configurations jump to another family of solutions (see section 5.5). Indeed, bifurcation analysis [Gilbert et al. 2016a] might enable to characterize this other family of solutions. Future work, which can use the mechanical model presented in this thesis as computational tools, should include an elastic stability analysis for CAARs to ensure their safe use.

Finally, during this dissertation, the numerical implementation was not optimized for the sake of time. Regarding standard types of continuum robots, the community has seen the development of efficient real time implementations of their corresponding mechanical models [Till et al. 2015, Till et al. 2019]. In the current state of the model, the simulation of an actuated configuration of a CAAR is typically of the order of 1 s which is similar to the computation times that were observed before optimization for the other types of continuum robots. This is why it is reasonable to expect that translating the previously implemented strategies to the present CAAR mechanical model should enable to run the model at real-time speeds required for control. One point of attention however, is that the computation times were found to increase when the internal load approached the critical load value. This will have to be taken into account, for example by defining multi-objective control laws that avoid high loads or by implementing other above-discussed solutions/extensions. Finally, once implemented in a control loop, further optimizing the computational speed can be achieved with specific methods for computing Jacobians as described in [Rucker and Webster 2011a].

General Conclusion

Minimally invasive or endoluminal surgery is preferred over open surgery for its benefits of reducing infection risks and adverse effects, faster recovery (thus shorter hospital stays), and reducing costs. The current surgical robots are mainly rigid-link robots and are not able to reproduce the dexterity and reach of open procedures within a minimally invasive system. To overcome these limitations, the medical robotics community developed continuum robots characterized by infinite degrees of freedom, allowing them to navigate complex paths into the anatomy and provide the required dexterity. Currently, challenges inherent to the structure of standard continuum robots remain unanswered.

By implementing the discussed propositions for fabricating CAARs with a higher maturity, such robots have the potential to outperform standard types of continuum robots for medical applications. Of course, it is still a long way from the experiment bench presented in this thesis to the operating room. Modeling CAARs and their interactions in their environment with precision is certainly an essential brick for further controlling them in applications. Further, prototypes will also have to be assessed on phantoms and subsequently cadaver or animal studies prior to evaluating a high-fidelity prototype through clinical trials. Putting clinicians in the loop at early stages of the development is critical for efficiently integrating the operating workflow [Patesson et al. 2018].

The contributions presented in this thesis bring us one step closer to the goal of deploying continuum robots for medical applications for which they are well suited: vascular applications, heart surgery, neurosurgery, ophthalmology, ear-nose-and-throat surgery, arthroscopy, bronchoscopy, gastrointestinal surgery, and urology. A recent example where CAARs are pre-clinically assessed in *ex vivo* porcine trials for the minimally-invasive removal of early-stage gastrointestinal neoplasia manifestly testifies of the exposed potential [Gafford et al. 2023]. At the end of the day, the same goal remains: to improve patient outcomes in technically challenging interventional procedures.

Appendix

A

Comparison of the Notation Conventions of the Literature for TACRs

When the Newtonian approach and the Lagrangian approach first occurred in the literature, two different systems of notations were recognizable. This appendix aims at bringing some insight between the two systems and provides a dictionary between the approaches for the case of TACRs. The symbols in the Newtonian approach were chosen to match as closely as possible both the notation proposed by S. S. Antman [Antman 1995] and the existing literature on the modeling of continuum robots [Rucker et al. 2010a]. On the other hand, the Lagrangian approach privileged notations from geometric mechanics [Marsden and Ratiu 1999] and its applications to rigid multi-body systems and continuous media, including fluid mechanics [Boyer et al. 2010]. This choice also eases the application of developments on manipulators to other contexts as eel-like robots. A dictionary of the two systems of notations is presented in Table A.1.

Table A.1 highlights some key differences that can be summarized as follows. In the Newtonian approach, vector fields are mostly expressed in $\mathbb{R}^3$ whereas the Lagrangian approach makes extensive use of wrenches and twists, expressed in $\mathbb{R}^6$. In the literature on the Newtonian approach, these $\mathbb{R}^3$ vectors are represented by bold symbols to differentiate them from scalars and matrices. As many developments of the Lagrangian approach are conducted in other (vector) spaces than $\mathbb{R}^3$, this practice is not applicable in this context. In both approaches, all vector fields in $\mathbb{R}^3$ can be expressed either in the inertial frame or in the cross-sectional frames, which can sometimes lead to confusion.

Another difference concerns the partial derivation with respect to the rod arc length variable in its reference (stress-less) configuration. It is denoted $\dot{\bullet}$ in the Newtonian approach and $\bullet'$ in the Lagrangian approach. In the Lagrangian approach, densities of external forces, couples, and wrenches per unit arc length are distinguished from the ordinary forces, couples, and wrenches by an overbar (e.g. $\bar{n}$ or $\bar{F}$ in Table A.1).

Table A.1: Comparison of the notation conventions of the literature for TACRs.

	Newtonian approach	Lagrangian approach	Dimensions	Units
Reference length parameter	$s \in [0,\, l]$	$X \in [0,\, l]$	$\mathbb{R}$	m
Position	$\boldsymbol{p}(s)$	$r(X)$	$\mathbb{R}^3$	m
Orientation	$R(s)$, (z-axis aligned)	$R(X)$, (X-axis aligned)	$\mathbb{R}^{3\times3}$	
Cross-sectional frame	$g(s) = (\boldsymbol{p}, R)(s)$	$g(X) = (R, r)(X)$	$\mathbb{R}^{4\times4}$	
Linear rate of change (shear & extension)	$\boldsymbol{v}(s)$	$\Gamma(X)$	$\mathbb{R}^3$	
Angular rate of change (bending & torsion)	$\boldsymbol{u}(s)$	$K(X)$	$\mathbb{R}^3$	m^{-1}
Space-rate twist	-	$\xi = (K^T, \Gamma^T)^T$	$\mathbb{R}^6$	$(\mathrm{m}^{-1}, -)$
Initial value or prior to deformation*	$\bullet^*$	$\bullet_0$		
Total length of the robot	l	l	$\mathbb{R}$	m
Strain	-	$\epsilon = \xi - \xi^0$	$\mathbb{R}^6$	$(\mathrm{m}^{-1}, -)$
Related to the i^{th} tendon	$\bullet_i$	$\bullet_i$		
Number of tendons	n	m	$\mathbb{R}$	
Length of the i^{th} tendon	l_i	l_i	$\mathbb{R}$	m
Related to the j^{th} segment	$\bullet_j$	$\bullet_j$		
Number of segments	m	χ	$\mathbb{R}$	
Length of the j^{th} segment	l_j	l_j	$\mathbb{R}$	m
Cross-sectional frame position of the i^{th} tendon	$\boldsymbol{r}_i(s) = [x_i(s)\, y_i(s)\, 0]^T$	$D_i(X) = (0, D_{i,Y}, D_{i,Z})(X)$	$\mathbb{R}^3$	m
Inertial frame tendon position	$\boldsymbol{p}_i(s) = \boldsymbol{p} + R\boldsymbol{r}_i$	$r_i(X) = r + RD_i$	$\mathbb{R}^3$	m
Tangent to the path of the i^{th} tendon	$\dot{\boldsymbol{p}}_i / \lVert\dot{\boldsymbol{p}}_i\rVert$	$t_i = r_i' / \lVert r_i'\rVert$	$\mathbb{R}$	
Tension in the i^{th} tendon	τ_i	τ_i	$\mathbb{R}$	N
Vector of tensions	-	$\tau = (\tau_1 \,..\, \tau_m)^T$	$\mathbb{R}^m$	N
Stress (bending & torsion)	$\boldsymbol{m}(s)$	$C(X)$	$\mathbb{R}^3$	Nm
Stress (shear & extension)	$\boldsymbol{n}(s)$	$N(X)$	$\mathbb{R}^3$	N
Stress (wrench)	-	$\Lambda(X) = \left(C(X)^T, N(X)^T\right)^T$	$\mathbb{R}^6$	(Nm, N)
Angular and linear stiffness matrices	$K_{bt}(s), K_{se}(s)$	$\mathcal{H}_{ang}(X), \mathcal{H}_{lin}(X)$	$\mathbb{R}^{3\times3}$	N, Nm^2
Hookean stiffness matrix		or $\mathcal{H}(X) = \mathrm{diag}(\mathcal{H}_{ang}(X), \mathcal{H}_{lin}(X))$	$\mathbb{R}^{6\times6}$	(N, Nm^2)
Generalized stiffness	-	$\mathcal{K}_{\epsilon\epsilon}$	$\mathbb{R}^{k\times k}$	**
Total external distributed couples	$\boldsymbol{l}(s)$	$\bar{c}(X),\ \bar{C}(X)$	$\mathbb{R}^3$	Nm/m
Total external distributed forces	$\boldsymbol{f}(s)$	$\bar{n}(X),\ \bar{N}(X)$	$\mathbb{R}^3$	N/m
Total external distributed wrench	-	$\bar{F}(X) = \left(\bar{C}(X)^T, \bar{N}(X)^T\right)^T$	$\mathbb{R}^6$	(Nm/m, N/m)
External tip couples	-	$c_+,\ C_+$	$\mathbb{R}^3$	Nm
External tip forces	-	$n_+,\ N_+$	$\mathbb{R}^3$	N
External tip wrench	-	$F_+ = \left(C_+^T, N_+^T\right)^T$	$\mathbb{R}^6$	(Nm, N)
Relative to external loads (not tendons)	-	$\bullet_{ext}$		
External distributed forces (not tendons)	$\boldsymbol{f}_e(s)$	$\bar{n}_{ext}(X)$	$\mathbb{R}^3$	N/m
External distributed couples (not tendons)	$\boldsymbol{l}_e(s)$	$\bar{c}_{ext}(X)$	$\mathbb{R}^3$	Nm/m
Relative to rod elastics	-	$\bullet_{rod}$		
Relative to actuation by the tendons	-	$\bullet_{act}$		
Distributed forces applied by the tendons	$\boldsymbol{f}_t(s)$	$\bar{n}_{act}(X)$	$\mathbb{R}^3$	N/m
Distributed couples applied by the tendons	$\boldsymbol{l}_t(s)$	$\bar{c}_{act}(X)$	$\mathbb{R}^3$	Nm/m
Distributed forces applied to the i^{th} tendon	$\boldsymbol{f}_i(s)$	$\bar{n}_i(X)$	$\mathbb{R}^3$	N/m
Stress of actuation	-	$\Lambda_{act}(X)$	$\mathbb{R}^6$	(Nm, N)
Generalized external forces	-	Q_{ext}	$\mathbb{R}^k$	**
Generalized restoring forces	-	Q_{rod}	$\mathbb{R}^k$	**
Generalized forces of actuation	-	Q_{act}	$\mathbb{R}^k$	**
Matrix of actuation	-	L	$\mathbb{R}^{k\times m}$	**
Number of shape functions	-	k	$\mathbb{R}$	
Shape functions	-	$\Phi(X) = (\Phi_1 \,..\, \Phi_k)^T$	$\mathbb{R}^{6\times k}$	**
Generalized strain coordinates	-	$q = (q_1 \,..\, q_k)^T$	$\mathbb{R}^k$	**
First and second derivative wrt. s or X	$\dot{\bullet}, \ddot{\bullet}$	$\bullet', \bullet''$		
Residual vector	-	$\mathfrak{Res}$		

* The subscript $\bullet_o$ sometimes encountered in the literature on the Lagrangian approach is here replaced with a subscript $\bullet_0$ to prevent confusion.

** The units of these quantities depend on the choice of the shape functions.

B

3D Printing CAARs

While Nitinol stock tubes are a popular choice for the fabrication of continuum robots [Gilbert and Webster 2016] and have been used for fabricating CAARs [Oliver-Butler et al. 2022], CAARs are more often fabricated through additive manufacturing also known as 3D printing techniques. 3D printing offers numerous advantages as

- enabling fast production of specific prototypes;
- being cost-effective;
- the possibility to design patient specific manipulators;
- getting along stringent electromagnetic and magnetic resonance compatibility constraints;
- allowing to achieve designs that are not 'machinable' with standard techniques.

Additive manufacturing can even be used to directly produce sterile devices on-site with FDA/CE approved materials, matching the demand in the course of the workflow.

3D printing CAAR prototypes is however not straightforward. During this thesis, many parts and prototypes were printed. The aim of this appendix is to drop a note on the gained insight. Among the various 3D printing techniques that exist, the one that was used for the CAARs presented in chapter 5 is called fused deposition modeling (FDM). It fuses material that is fed through the heated printing nozzle and deposits the material on a calculated path, layer by layer. The contours of the parts to be printed should be laid out through continuous paths, but the interior of the volumes can be filled with any pattern and density. Standard FDM printers typically allow to print tubes with smallest wall thickness of approximately 0.6 mm. Due to the effects of gravity, printing overhanging material is generally not possible without 'supporting' material, to be removed once the parts are printed. 'Supports' can only be omitted when the overhanging angle is small (generally $<45°$) or the overhanging material is bridging two closely placed features, but this will inevitably affect the nominal dimensions of the part. For example, a cylinder with a sufficiently small diameter (typically <15 mm) could be printed horizontally, but, the bigger this cylinder, the more its upper part will sag. Printing the cylinder vertically enhances the trueness of the part. In addition to precision and dimensional trueness, the printing orientation of a part has a significant impact on its mechanical properties [Chacón et al. 2017]. Hence, printing orientation is a major concern and will influence the printing strategies detailed below.

To print CAARs with FDM, different alternatives must be considered. The two tubes of the CAAR can be printed as a single part with the ends directly fixed or as two separate tubes that will need to be subsequently attached. For the former option, it was found that the best printing orientation is vertical. Indeed, the notches of the two tubes facing each other, laying the CAAR

horizontally would require to support the remaining backbone of at least one of the tubes which conflicts with the fact that the tubes are assembled concentrically and the clearances between them should remain free of any material. Printing CAARs vertically also requires adding support in the notches, but this material can be removed post printing as it can be accessed with forceps from both sides of the tubes. The main concern with printing CAARs vertically is that the plastic fibers are laid out in on paths in the cross-sections, but that the continuity between cross-sections is lost between printing layers. This considerably weakens the resistance of the prototypes to traction and bending because the layers can be pulled apart.

To circumvent this issue, the two tubes of a CAAR can also be printed as separate parts horizontally. This is the option that was for all prototypes presented in chapter 5. In this case, the plastic fibers are laid out axially, thus increasing the axial and bending resistance while preserving similar rigidity. Prototypes with in-plane neutral lines should be printed with their remaining backbone facing down, such that no support is needed between the notches. The tubes must be provided with a slot or attachment system in order to securely fix their tips together. On the downside, printing the tubes (i.e. cylinders) horizontally affects the circularity of the plain tube parts. Because the inner tube needs to slide unhampered through the outer tube, it is important to ensure sufficient clearance to compensate for the slight sagging of the cylinders, especially for larger diameters. When printing helically notched tubes, some portions of the tubes may require supporting the remaining backbone. The support material must then be carefully removed, paying attention to the quality of the inner surface of the tube, prior to the assembly of the tubes.

An interesting option with FDM is the use of soluble support material. Once the part is printed and removed from the print bed it is immersed in water or more aggressive liquid, depending on the type of soluble material, such that only the desired features remain. The drawback is that extra equipment is needed. First, to obtain proper cleaning results, it is recommended to use a dedicated immersion tank, preferably with integrated heating and liquid flow. Second, soluble support materials being very sensitive to ambient humidity, the material spools should be stored in boxes with controlled atmosphere and should be changed every few weeks. This makes the technology less applicable to small scale laboratory prototyping.

In this thesis, Poly-jet printing has been tested as an alternative to FDM for producing CAARs. In this technology, a liquid resin material is laid out in thin layers and selectively cured with an ultraviolet lamp. Incurable liquid is laid out in the void as support and needs to be removed in a tank. This printing technique offers the possibility to mix resins of different rigidity and hence to fine-tune the output rigidity of the part. Additionally, it offers higher resolution than standard FDM and could allow to print tubes with thinner walls. Tubes should however not feature narrow lumens over long plain tube sections, hindering the removal of the support liquid. Indeed, extended cleaning times eventually corrode the part itself, leading to bad precision and increased risk of failure. While the tested prototypes showed good mechanical properties and smoother surface finish, the tests with Poly-jet printing were not pursued for being not as easily accessible as FDM at the TIMC laboratory.

Regardless of the chosen printing technique, every additive manufacturing method involves process parameters. The precise tuning of these parameters is beyond the scope of the present manuscript, but is surely of interest for future work. For example, with FDM, the nozzle temperature is known to impact Young's modulus of the printed material. Also, the feeding rate or print-head speed can determine the surface quality. On the one hand, better mastering these parameters should limit the necessity to fall back on model parameter calibration procedures as described in section 5.3.2. On the other hand, rigorously studying the impact of printer parameters on the behavior of CAARs may enable to purposely tweak them for specific needs. In the same sense, it

should be noted that, printing such delicate parts as notched tubes, requires a thorough calibration of the printer.

Future work should also include the investigation of post-processing of the surface of the tubes in order to reduce friction and analyze the possibility to directly embed sensors with a method similar to the one reported in [Meisel et al. 2014]. Additive manufacturing is a vast field of research with far-reaching possibilities, where many open questions remain. For further reading on 3D printing of continuum robots for medical applications, refer to [Amanov et al. 2015, Morimoto and Okamura 2016, Desai et al. 2019].

Bibliography

Abrar, T., F. Putzu, Ahmad Ataka, H. Godaba, and Kaspar Althoefer (May 2021). "Highly Manoeuvrable Eversion Robot Based on Fusion of Function with Structure". In: *Proceedings of the IEEE International Conference on Robotics and Automation (ICRA)*, pp. 12089–12096.

Adagolodjo, Yinoussa, Federico Renda, and Christian Duriez (Apr. 2021). "Coupling Numerical Deformable Models in Global and Reduced Coordinates for the Simulation of the Direct and the Inverse Kinematics of Soft Robots". In: *IEEE Robotics and Automation Letters* 6.2, pp. 3910–3917.

Ahmed, Shahrior and Hunter B. Gilbert (Apr. 2022). "Kinestatic Modeling of a Spatial Screw-Driven Continuum Robot". In: *IEEE Robotics and Automation Letters* 7.2, pp. 3563–3570.

Ai, Xiaojie, Anzhu Gao, Zecai Lin, Chong He, and Weidong Chen (July 2021). "A Multi-Contact-Aided Continuum Manipulator With Anisotropic Shapes". In: *IEEE Robotics and Automation Letters* 6.3, pp. 4560–4567.

Alambeigi, Farshid, Sahba Aghajani Pedram, Jason L. Speyer, Jacob Rosen, Iulian I. Iordachita, Russell H. Taylor, and Mehran Armand (Feb. 2020). "SCADE: Simultaneous Sensor Calibration and Deformation Estimation of FBG-Equipped Unmodeled Continuum Manipulators". In: *IEEE Transactions on Robotics* 36.1, pp. 222–239.

AlBeladi, Ali, Girish Krishnan, Mohamed-Ali Belabbas, and Seth Hutchinson (May 2021). "Vision-Based Shape Reconstruction of Soft Continuum Arms Using a Geometric Strain Parametrization". In: *Proceedings of the IEEE International Conference on Robotics and Automation (ICRA)*, pp. 11753–11759.

Alfalahi, Hessa, Federico Renda, and Cesare Stefanini (Aug. 2020). "Concentric Tube Robots for Minimally Invasive Surgery: Current Applications and Future Opportunities". In: *IEEE Transactions on Medical Robotics and Bionics* 2.3, pp. 410–424.

Aloi, Vincent A., Khoa T. Dang, Eric J. Barth, and Daniel Caleb Rucker (Oct. 2022). "Estimating Forces Along Continuum Robots". In: *IEEE Robotics and Automation Letters* 7.4, pp. 8877–8884.

Amanov, Ernar, Josephine Granna, and Jessica Burgner-Kahrs (May 2017). "Toward Improving Path Following Motion: Hybrid Continuum Robot Design". In: *Proceedings of the IEEE International Conference on Robotics and Automation (ICRA)*, pp. 4666–4672.

Amanov, Ernar, Thien-Dang Nguyen, and Jessica Burgner-Kahrs (Mar. 2015). "Additive manufacturing of patient-specific tubular continuum manipulators". In: *Proceedings of SPIE Medical Imaging: Image-Guided Procedures, Robotic Interventions, and Modeling*, 94151P.

— (Nov. 2021). "Tendon-Driven Continuum Robots with Extensible Sections—A Model-Based Evaluation of Path-Following Motions". In: *International Journal of Robotics Research* 40.1, pp. 7–23.

Anderson, Victor C. (1967). "Tenser Arm Manipulator Design". In: *Transactions of the ASME* 67, pp. 1–12.

Anor, Tomer, Joseph R. Madsen, and Pierre E. Dupont (May 2011). "Algorithms for Design of Continuum Robots Using the Concentric Tubes Approach: A Neurosurgical Example". In: *Proceedings of the IEEE International Conference on Robotics and Automation (ICRA)*, pp. 667–673.

Antman, Stuart S. (1995). *Nonlinear Problems of Elasticity*. Ne York, NY, USA: Springer-Verlag.

Armanini, Costanza, Frédéric Boyer, Anup Teejo Mathew, Christian Duriez, and Federico Renda (June 2023). "Soft Robots Modeling: A Structured Overview". In: *IEEE Transactions on Robotics* 39.3, pp. 1728–1748.

Azimian, Hamidreza, Peter Francis, Thomas Looi, and James M. Drake (Sept. 2014). "Structurally-redesigned Concentric-tube Manipulators with Improved Stability". In: *Proceedings of the IEEE/RSJ International Conference on Intelligent Robots and Systems (IROS)*, pp. 2030–2035.

Back, Junghwan, Lukas Lindenroth, Kawal Rhode, and Hongbin Liu (May 2017). "Model-Free Position Control for Cardiac Ablation Catheter Steering Using Electromagnetic Position Tracking and Tension Feedback". In: *Frontiers in Robotics and AI* 4.7, pp. 2296–9144.

Bartkowski, Piotr, Franciszek Gawinski, and Lukasz Pawliszak (Oct. 2022). "E-Morph as a New Adaptive Actuator for Soft Robotics". In: *IEEE Robotics and Automation Letters* 7.4, pp. 8831–8836.

Bertails-Descoubes, Florence, Alexandre Derouet-Jourdan, Victor Romero, and Arnaud Lazarus (Apr. 2018). "Inverse design of an isotropic suspended Kirchhoff rod: theoretical and numerical results on the uniqueness of the natural shape". In: *Mathematical, Physical and Engineering Sciences* 474.2212, p. 20170837.

Berthet-Rayne, Pierre, Gauthier Gras, Konrad Leibrandt, Piyamate Wisanuvej, Andreas Schmitz, Carlo A. Seneci, and Guang-Zhong Yang (June 2018a). "The I2snake Robotic Platform for Endoscopic Surgery". In: *Annals of Biomedical Engineering* 46.10, pp. 1663–1675.

Berthet-Rayne, Pierre, Konrad Leibrandt, Kiyoung Kim, Carlo A. Seneci, Jianzhong Shang, and Guang-Zhong Yang (Oct. 2018b). "Rolling-joint Design Optimization for Tendon Driven Snake-like Surgical Robots". In: *Proceedings of the IEEE/RSJ International Conference on Intelligent Robots and Systems (IROS)*, pp. 4964–4971.

Berthet-Rayne, Pierre, Seyed Mohammad Hadi Sadati, Georgios Petrou, Neel Patel, Stamatia Giannarou, Daniel Richard Leff, and Christos Bergeles (July 2021). "MAMMOBOT: A Miniature Steerable Soft Growing Robot for Early Breast Cancer Detection". In: *IEEE Robotics and Automation Letters* 6.3, pp. 5056–5063.

Bezawada, Harish, Cole Woods, and Vishesh Vikas (Oct. 2022). "Shape Reconstruction of Soft Manipulators Using Vision and IMU Feedback". In: *IEEE Robotics and Automation Letters* 7.4, pp. 9589–9596.

Bieze, Thor Morales, Frederick Largilliere, Alexandre Kruszewski, Zhongkai Zhang, Rochdi Merzouki, and Christian Duriez (June 2018). "Finite Element Method-Based Kinematics and Closed-Loop Control of Soft, Continuum Manipulators". In: *Soft Robotics* 5.3, pp. 348–364.

Bishop, Richard L. (Mar. 1975). "There is More than One Way to Frame a Curve". In: *The American Mathematical Monthly* 82.3, pp. 246–251.

Black, Caroline Bryson (2017). "Modeling, Analysis, Force Sensing and Control of Continuum Robots for Minimally Invasive Surgery". University of Tennessee. PhD thesis.

Black, Caroline Bryson, John Till, and Daniel Caleb Rucker (Feb. 2018). "Parallel Continuum Robots: Modeling, Analysis, and Actuation-based Force Sensing". In: *IEEE Transactions on Robotics* 34.1, pp. 29–47.

Bosman, Julien, Thor Morales Bieze, Othman Lakhal, Mario Sanz, Rochdi Merzouki, and Christian Duriez (May 2015). "Domain decomposition approach for FEM quasistatic modeling and control of Continuum Robots with rigid vertebras". In: *Proceedings of the IEEE International Conference on Robotics and Automation (ICRA)*, pp. 4373–4378.

Boyer, Frédéric, Vincent Lebastard, Fabien Candelier, and Federico Renda (June 2021). "Dynamics of Continuum and Soft Robots: A Strain Parameterization Based Approach". In: *IEEE Transactions on Robotics* 37.3, pp. 847–863.

— (Jan. 2022a). "Extended Hamilton's principle applied to geometrically exact Kirchhoff sliding rods". In: *Journal of Sound and Vibration* 516, p. 116511.

Boyer, Frédéric, Vincent Lebastard, Fabien Candelier, Federico Renda, and Mazen Alamir (Apr. 2022b). "Statics and Dynamics of Continuum Robots Based on Cosserat Rods and Optimal Control Theories". In: *IEEE Transactions on Robotics* 39.2, pp. 1544–1562.

Boyer, Frédéric, Mathieu Porez, and W. Khalil (Aug. 2006). "Macro-continuous computed torque algorithm for a three-dimensional eel-like robot". In: *IEEE Transactions on Robotics* 22.4, pp. 763–775.

Boyer, Frédéric, Mathieu Porez, and Alban Leroyer (Feb. 2010). "Poincare Cosserat Equations for the Lighthill Three-dimensional Large Amplitude Elongated Body Theory: Application to Robotics". In: *Journal of Nonlinear Science* 20.1, pp. 47–79.

Boyer, Frédéric and Dominique Primault (Dec. 2004). "Finite element of slender beams in finite transformations: a geometrically exact approach". In: *International Journal for Numerical Methods in Engineering* 59.5, pp. 669–702.

Bretl, Timothy and Zoe McCarthy (2013). "Equilibrium Configurations of a Kirchhoff Elastic Rod under Quasi-static Manipulation". In: *Algorithmic Foundations of Robotics X. Springer Tracts in Advanced Robotics*. Ed. by Emilio Frazzoli, Tomas Lozano-Perez, Nicholas Roy, and Daniela Rus. Heidelberg, Germany: Springer-Verlag, pp. 71–87.

— (Jan. 2014). "Quasi-Static Manipulation of a Kirchhoff Elastic Rod Based on a Geometric Analysis of Equilibrium Configurations". In: *International Journal of Robotics Research* 33.1, pp. 48–68.

Briot, Sébastien and Frédéric Boyer (Apr. 2023). "A Geometrically Exact Assumed Strain Modes Approach for the Geometrico- and Kinemato-Static Modelings of Continuum Parallel Robots". In: *IEEE Transactions on Robotics* 39.2, pp. 1527–1543.

Briot, Sébastien and Alexandre Goldsztejn (Feb. 2022). "Singularity Conditions for Continuum Parallel Robots". In: *IEEE Transactions on Robotics* 38.1, pp. 507–525.

Bryant, Micah, Connor Watson, and Tania K. Morimoto (Oct. 2022). "Tactile Perception for Growing Robots Via Discrete Curvature Measurements". In: *Proceedings of the IEEE/RSJ International Conference on Intelligent Robots and Systems (IROS)*, pp. 4257–4264.

Bryson, Caroline E. and Daniel Caleb Rucker (May 2014). "Toward Parallel Continuum Manipulators". In: *Proceedings of the IEEE International Conference on Robotics and Automation (ICRA)*, pp. 778–785.

Burgner, Jessica, Daniel Caleb Rucker, Hunter B. Gilbert, Philip J. Swaney, Paul T. Russell, Kyle D. Weaver, and Robert James Webster (June 2014). "A Telerobotic System for Transnasal Surgery". In: *IEEE/ASME Transactions on Mechatronics* 19.3, pp. 996–1006.

Burgner-Kahrs, Jessica, Daniel Caleb Rucker, and Howie Choset (Dec. 2015). "Continuum Robots for Medical Applications: A Survey". In: *IEEE Transactions on Robotics* 31.6, pp. 1261–1280.

Camarillo, David B., Christopher F. Milne, Christopher R. Carlson, Michael R. Zinn, and J. Kenneth Salisbury (Dec. 2008). "Mechanics Modeling of Tendon-Driven Continuum Manipulators". In: *IEEE Transactions on Robotics* 24.6, pp. 1262–1273.

Campisano, Federico, Simone Caló, Andria A. Remirez, James H. Chandler, Keith L. Obstein, Robert James Webster, and Pietro Valdastri (Mar. 2021). "Closed-Loop Control of Soft Continuum Manipulators under Tip Follower Actuation". In: *International Journal of Robotics Research* 40.6-7, pp. 923–938.

Campisano, Federico, Francesco Gramuglia, Imro R. Dawson, Christopher T. Lyne, Michelle L. Izmaylov, Sarthak Misra, Elena De Momi, Douglas R. Morgan, Keith L. Obstein, and Pietro Valdastri (June 2017). "Gastric Cancer Screening in Low-Income Countries: System Design, Fabrication, and Analysis for an Ultralow-Cost Endoscopy Procedure". In: *IEEE Robotics & Automation Magazine* 24.2, pp. 73–81.

Campisano, Federico, Andria A. Remirez, Simone Caló, James H. Chandler, Keith L. Obstein, Robert James Webster, and Pietro Valdastri (Apr. 2020). "Online Disturbance Estimation for Improving Kinematic Accuracy in Continuum Manipulators". In: *IEEE Robotics and Automation Letters* 5.2, pp. 2642–2649.

Cangan, Barnabas Gavin, Stefan Escaida Navarro, Yang Bai, Yu Zhang, Christian Duriez, and Robert Kevin Katzschmann (Oct. 2022). "Model-Based Disturbance Estimation for a Fiber-Reinforced Soft Manipulator Using Orientation Sensing". In: *Proceedings of the IEEE/RSJ International Conference on Intelligent Robots and Systems (IROS)*, pp. 9424–9430.

Cao, D. Q. and Robin W. Tucker (Jan. 2008). "Nonlinear Dynamics of Elastic Rods Using the Cosserat Theory: Modelling and Simulation". In: *International Journal of Solids and Structures* 45.2, pp. 460–477.

Cardona, Alberto and Michel Geradin (Nov. 1988). "A beam finite element non-linear theory with finite rotations". In: *International Journal for Numerical Methods in Engineering* 26.11, pp. 2403–2438.

Chacón, J. M., M. A. Caminero, E. García-Plaza, and P. J. Núñez (June 2017). "Additive Manufacturing of PLA Structures Using Fused Deposition Modelling: Effect of Process Parameters on Mechanical Properties And their Optimal Selection". In: *Materials & Design* 124, pp. 143–157.

Chen, Gang, Minh Tu Pham, and Tanneguy Redarce (2007). "A guidance control strategy for semi-autonomous colonoscopy using a continuum robot". In: *Recent Progress in Robotics: Viable Robotic Service to Human. Lecture Notes in Control and Information Sciences*. Ed. by Sukhan Lee, Il Hong Suh, and Mun Sang Kim. Heidelberg, Germany: Springer-Verlag, pp. 63–78.

Chen, Jianghua, Qingpeng Ding, Wanquan Yan, Kim Yan, Jibiao Chen, Jason Ying-Kuen Chan, and Shing Shin Cheng (Apr. 2022). "A Variable Length, Variable Stiffness Flexible Instrument for Transoral Robotic Surgery". In: *IEEE Robotics and Automation Letters* 7.2, pp. 3835–3842.

Chen, Yuyang, Baibo Wu, Jiabin Jin, and Kai Xu (Apr. 2021). "A Variable Curvature Model for Multi-Backbone Continuum Robots to Account for Inter-Segment Coupling and External Disturbance". In: *IEEE Robotics and Automation Letters* 6.2, pp. 1590–1597.

Cheong, Hyunmin, Mehran Ebrahimi, and Timothy Duggan (Apr. 2021). "Optimal Design of Continuum Robots With Reachability Constraints". In: *IEEE Robotics and Automation Letters* 6.2, pp. 3902–3909.

Chikhaoui, M. Taha, Amine Benouhiba, Patrick Rougeot, Kanty Rabenorosoa, Morvan Ouisse, and Nicolas Andreff (Apr. 2018). "Developments and Control of Biocompatible Conducting Polymer for Intracorporeal Continuum Robots". In: *Annals of Biomedical Engineering* 46.10, pp. 1511–1521.

Chikhaoui, M. Taha and Jessica Burgner-Kahrs (June 2018). "Control of Continuum Robots for Medical Applications: State of the Art". In: *Proceedings of the International Conference on New Actuators (ACTUATOR)*, pp. 154–164.

Chikhaoui, M. Taha, Amélie Cot, Kanty Rabenorosoa, Patrick Rougeot, and Nicolas Andreff (Oct. 2016a). "Design and closed-loop control of a tri-layer Polypyrrole based telescopic soft robot". In: *Proceedings of the IEEE/RSJ International Conference on Intelligent Robots and Systems (IROS)*, pp. 1145–1150.

Chikhaoui, M. Taha, Sven Lilge, Simon Kleinschmidt, and Jessica Burgner-Kahrs (Apr. 2019). "Comparison of Modeling Approaches for a Tendon Actuated Continuum Robot with Three Extensible Segments". In: *IEEE Robotics and Automation Letters* 4.2, pp. 989–996.

Chikhaoui, M. Taha, Kanty Rabenorosoa, and Nicolas Andreff (Oct. 2016b). "Kinematics and performance analysis of a novel concentric tube robotic structure with embedded soft microactuation". In: *Mechanism and Machine Theory* 104, pp. 234–254.

Chikhaoui, M. Taha and Benoît Rosa (2022). "Modeling and control strategies for flexible devices". In: *Endorobotics*. Ed. by Luigi Manfredi. New York, NY, USA: Academic Press Inc., pp. 187–213.

Chirikjian, Gregory S. (Jan. 1994). "Hyper-redundant manipulator dynamics: a continuum approximation". In: *Advanced Robotics* 9.3, pp. 217–243.

Chirikjian, Gregory S. and Joel W. Burdick (June 1994). "A modal approach to hyper-redundant manipulator kinematics". In: *IEEE Transactions on Robotics and Automation* 10.3, pp. 343–354.

— (Dec. 1995). "The kinematics of hyper-redundant robot locomotion". In: *IEEE Transactions on Robotics and Automation* 11.6, pp. 781–793.

Chitalia, Yash, Nancy Joanna Deaton, Seokhwan Jeong, Nahian Rahman, and Jaydev P. Desai (Apr. 2020). "Towards FBG-Based Shape Sensing for Micro-Scale and Meso-Scale Continuum Robots With Large Deflection". In: *IEEE Robotics and Automation Letters* 5.2, pp. 1712–1719.

Chitalia, Yash, Seokhwan Jeong, Kent K. Yamamoto, Joshua J. Chern, and Jaydev P. Desai (Apr. 2021). "Modeling and Control of a 2-DoF Meso-Scale Continuum Robotic Tool for Pediatric Neurosurgery". In: *IEEE Transactions on Robotics* 37.2, pp. 520–531.

Cianchetti, Matteo, Cecilia Laschi, Arianna Menciassi, and Paolo Dario (May 2018). "Biomedical applications of soft robotics". In: *Nature Reviews Materials* 3.6, pp. 143–153.

Cieślak, Radosław and Adam Morecki (Jan. 1999). "Elephant trunk type elastic manipulator - a tool for bulk and liquid materials transportation". In: *Robotica* 17.1, pp. 11–16.

Clark, Angus Benedict and Nicolas Rojas (Dec. 2022). "Malleable Robots: Reconfigurable Robotic Arms With Continuum Links of Variable Stiffness". In: *IEEE Transactions on Robotics* 38.6, pp. 3832–3849.

Cosserat, Eugène Maurice Pierre and François Cosserat (Dec. 1907). "Sur la statique de la ligne déformable". In: *Comptes Rendus de l'Académie des Sciences* 145.27, pp. 1409–1412.

— (1909). *Théorie des corps déformables*. Paris, France: Hermann & Cie.

Dario, Paolo, M. C. Carrozza, M. Marcacci, S. D'Attanasio, B. Magnami, O. Tonet, and G. Megali (Mar. 2000). "A novel mechatronic tool for computer-assisted arthroscopy". In: *IEEE Transactions on Information Technology in Biomedicine* 4.1, pp. 15–29.

Desai, Jaydev P., Jun Sheng, Shing Shin Cheng, Xuefeng Wang, Nancy Joanna Deaton, and Nahian Rahman (May 2019). "Toward Patient-specific 3d-printed Robotic Systems for Surgical Interventions". In: *IEEE Transactions on Medical Robotics and Bionics* 1.2, pp. 77–87.

Diezinger, Matyas A., Brahim Tamadazte, and Guillaume J. Laurent (Oct. 2022). "3D Curvature-Based Tip Load Estimation for Continuum Robots". In: *IEEE Robotics and Automation Letters* 7.4, pp. 10526–10533.

Ding, Jienan, Roger E. Goldman, Kai Xu, Peter K. Allen, Dennis L. Fowler, and Nabil Simaan (Oct. 2013). "Design and Coordination Kinematics of an Insertable Robotic Effectors Platform for Single-port Access Surgery". In: *IEEE/ASME Transactions on Mechatronics* 18.5, pp. 1612–1624.

Ding, Qingpeng, Yongkang Lu, Andre Kyme, and Shing Shin Cheng (May 2021). "Towards a Multi-imager Compatible Continuum Robot with Improved Dynamics Driven by Modular SMA". In: *Proceedings of the IEEE International Conference on Robotics and Automation (ICRA)*, pp. 11930–11937.

Dupont, Pierre E., Jesse Lock, Brandon Itkowitz, and Evan Butler (Apr. 2010). "Design and Control of Concentric-tube Robots". In: *IEEE Transactions on Robotics* 26.2, pp. 209–225.

Dupont, Pierre E., Nabil Simaan, Howie Choset, and Daniel Caleb Rucker (July 2022). "Continuum Robots for Medical Interventions". In: *Proceedings of the IEEE* 110.7, pp. 847–870.

Eugster, Simon R., Jonas Harsch, Max Bartholdt, Marco Herrmann, Mats Wiese, and Giuseppe Capobianco (Apr. 2022). "Soft Pneumatic Actuator Model Based on a Pressure-Dependent Spatial Nonlinear Rod Theory". In: *IEEE Robotics and Automation Letters* 7.2, pp. 2471–2478.

Exarchos, Ioannis, Karen Wang, Brian H. Do, Fabio Stroppa, Margaret M. Coad, Allison M. Okamura, and C. Karen Liu (May 2022). "Task-Specific Design Optimization and Fabrication for Inflated-Beam Soft Robots with Growable Discrete Joints". In: *Proceedings of the IEEE International Conference on Robotics and Automation (ICRA)*, pp. 7145–7151.

Fagogenis, Georgios, Christos Bergeles, and Pierre E. Dupont (Oct. 2016). "Adaptive nonparametric kinematic modeling of concentric tube robots". In: *Proceedings of the IEEE/RSJ International Conference on Intelligent Robots and Systems (IROS)*, pp. 4324–4329.

Falco, Iris De, Matteo Cianchetti, and Arianna Menciassi (Sept. 2017). "A soft multi-module manipulator with variable stiffness for minimally invasive surgery". In: *Bioinspiration & Biomimetics* 12.5, p. 056008.

Fang, Zhonggui, Chaoyi Huang, Yaxi Wang, Jiahao Xu, Jiyong Tan, Bin Li, Zichen Wang, Yige Wu, Anlun Huang, Juan Yi, Sicong Liu, and Zheng Wang (May 2022). "Multi-Dimensional Proprioception and Stiffness Tuning for Soft Robotic Joints". In: *Proceedings of the IEEE International Conference on Robotics and Automation (ICRA)*, pp. 10973–10979.

Fattahi, Javad S. and Davide Spinello (Oct. 2013). "Timoshenko Beam Model for Exploration and Sensing With a Continuum Centipede Inspired Robot". In: *Proceedings of the ASME Dynamic Systems and Control Conference (DSCC)*, p. 4103.

Featherstone, Roy (2007). *Rigid Body Dynamics Algorithms*. New York, NY, USA: Springer-Verlag.

Feng, Mei, Zhixue Ni, Yili Fu, Xingze Jin, Wei Liu, and Xiuquan Lu (May 2021). "Kinematic analysis of a flexible surgical instrument for robot-assisted minimally invasive surgery". In: *Proceedings of the IEEE International Conference on Robotics and Automation (ICRA)*, pp. 12229–12235.

Fiorini, Paolo, Ken Y. Goldberg, Yunhui Liu, and Russell H. Taylor (July 2022). "Concepts and Trends in Autonomy for Robot-Assisted Surgery". In: *Proceedings of the IEEE* 110.7, pp. 993–1011.

Francis, Peter, K. W. Eastwood, V. Bodani, Thomas Looi, and James M. Drake (May 2018). "Design, Modelling and Teleoperation of a 2 mm Diameter Compliant Instrument for the Da Vinci Platform". In: *Annals of Biomedical Engineering* 46.10, pp. 1437–1449.

Fried, Inbar, Janine Hoelscher, Mengyu Fu, Maxwell Emerson, Tayfun Efe Ertop, Margaret Rox, Josephine Granna, Alan Kuntz, Jason A. Akulian, Robert James Webster, and Ron Alterovitz (May 2021). "Design Considerations for a Steerable Needle Robot to Maximize Reachable Lung Volume". In: *Proceedings of the IEEE International Conference on Robotics and Automation (ICRA)*, pp. 1418–1425.

Gafford, Joshua B., Patrick L. Anderson, Scott Webster, S. Duke Herrell, Keith L. Obstein, Daniel Caleb Rucker, and Robert James Webster (2023). "Robotic Steerable Sheaths for Interventional Endoscopy: Design and Pre-Clinical Feasibility". In: *IEEE Transactions on Biomedical Engineering*. In Press, `https://www.researchgate.net/publication/359364722_Robotic_Steerable_Sheaths_for_Interventional_Endoscopy_Design_and_Pre-Clinical_Feasibility`.

Gafford, Joshua B., Michael Freeman, Loris Fichera, Jack Noble, Robert Labadie, and Robert James Webster (May 2020). "Eyes in Ears: A Miniature Steerable Digital Endoscope for Trans-Nasal Diagnosis of Middle Ear Disease". In: *Annals of Biomedical Engineering* 49.1, pp. 219–232.

Gafford, Joshua B., Scott Webster, Neal Dillon, Evan Blum, Richard J. Hendrick, Fabien Maldonado, Erin A. Gillaspie, Otis B. Rickman, S. Duke Herrell, and Robert James Webster (July 2019). "A Concentric Tube Robot System for Rigid Bronchoscopy: A Feasibility Study on Central Airway Obstruction Removal". In: *Annals of Biomedical Engineering* 48.1, pp. 181–191.

Gallardo, Oscar F., Benjamin Mauze, Redwan Dahmouche, Christian Duriez, and Guillaume J. Laurent (Sept. 2021). "Turning an Articulated 3-PPSR Manipulator into a Parallel Continuum Robot". In: *Proceedings of the IEEE/RSJ International Conference on Intelligent Robots and Systems (IROS)*, pp. 4955–4960.

Gan, Lucia T., Laura H. Blumenschein, Zhe Huang, Allison M. Okamura, Elliot W. Hawkes, and Jonathan A. Fan (Apr. 2020). "3D Electromagnetic Reconfiguration Enabled by Soft Continuum Robots". In: *IEEE Robotics and Automation Letters* 5.2, pp. 1704–1711.

Gao, Xiao-Shan, Xiao-Rong Hou, Jianliang Tang, and Hang-Fei Cheng (Aug. 2003). "Complete Solution Classification for the Perspective-Three-Point Problem". In: *IEEE Transactions on Pattern Analysis and Machine Intelligence* 25.8, pp. 930–943.

Gautreau, Elie, Juan Sandoval, Xavier Bonnet, Marc Arsicault, Said Zeghloul, and Med Amine Laribi (May 2022). "A New Bio-Inspired Hybrid Cable-Driven Robot (HCDR) to Design More Realistic Snakebots". In: *Proceedings of the IEEE International Conference on Robotics and Automation (ICRA)*, pp. 2134–2140.

Gazzola, M., L. H. Dudte, A. G. McCormick, and L. Mahadevan (June 2018). "Forward and inverse problems in the mechanics of soft filaments". In: *Royal Society Open Science* 5.6, p. 171628.

Gilbert, Hunter B., Richard J. Hendrick, and Robert James Webster (Feb. 2016a). "Elastic Stability of Concentric Tube Robots: A Stability Measure and Design Test". In: *IEEE Transactions on Robotics* 32.1, pp. 20–35.

Gilbert, Hunter B., Daniel Caleb Rucker, and Robert James Webster (2016b). "Concentric Tube Robots: The State of the Art and Future Directions". In: *Robotics Research. Springer Tracts in Advanced Robotics*. Ed. by Masayuki Inaba and Peter Corke. Heidelberg, Germany: Springer-Verlag, pp. 253–269.

Gilbert, Hunter B. and Robert James Webster (Jan. 2016). "Rapid, Reliable Shape Setting of Superelastic Nitinol for Prototyping Robots". In: *IEEE Robotics and Automation Letters* 1.1, pp. 98–105.

Giorelli, Michele, Federico Renda, Marcello Calisti, Andrea Arienti, Gabriele Ferri, and Cecilia Laschi (May 2015a). "Learning the inverse kinetics of an octopus-like manipulator in three-dimensional space". In: *Bioinspiration & Biomimetics* 10.3, p. 035006.

— (Aug. 2015b). "Neural Network and Jacobian Method for Solving the Inverse Statics of a Cable-Driven Soft Arm With Nonconstant Curvature". In: *IEEE Transactions on Robotics* 31.4, pp. 823–834.

Girerd, Cedric and Tania K. Morimoto (Aug. 2021). "Design and Control of a Hand-Held Concentric Tube Robot for Minimally Invasive Surgery". In: *IEEE Transactions on Robotics* 37.4, pp. 1022–1038.

Goldstein, Herbert, Charles Poole, and John Safko (2001). *Classical Mechanics*. Third. Reading, MA, USA: Addison Wesley.

Gonthina, Phanideep S., Apoorva D. Kapadia, Isuru S. Godage, and Ian. D. Walker (May 2019). "Modeling Variable Curvature Parallel Continuum Robots Using Euler Curves". In: *Proceedings of the IEEE International Conference on Robotics and Automation (ICRA)*, pp. 1679–1685.

Gonthina, Phanideep S., Michael B. Wooten, Isuru S. Godage, and Ian D. Walker (Apr. 2020). "Mechanics for Tendon Actuated Multisection Continuum Arms". In: *Proceedings of the IEEE International Conference on Robotics and Automation (ICRA)*, pp. 3896–3902.

Grassmann, Reinhard M. and Jessica Burgner-Kahrs (June 2019). "On the Merits of Joint Space and Orientation Representations in Learning the Forward Kinematics in SE(3)". In: *Proceedings of the Robotics: Science and Systems Conference (RSS)*, p17.

Grassmann, Reinhard M., Ryan Zeyuan Chen, Nan Liang, and Jessica Burgner-Kahrs (Oct. 2022). "A Dataset and Benchmark for Learning the Kinematics of Concentric Tube Continuum Robots". In: *Proceedings of the IEEE/RSJ International Conference on Intelligent Robots and Systems (IROS)*, pp. 9550–9557.

Grassmann, Reinhard M., Vincent Modes, and Jessica Burgner-Kahrs (Oct. 2018). "Learning the Forward and Inverse Kinematics of a 6-DOF Concentric Tube Continuum Robot in SE(3)". In: *Proceedings of the IEEE/RSJ International Conference on Intelligent Robots and Systems (IROS)*, pp. 5125–5132.

Graule, Moritz A., Clark Teeple, and Robert Wood (Oct. 2022). "Contact-Implicit Trajectory and Grasp Planning for Soft Continuum Manipulators". In: *Proceedings of the IEEE/RSJ International Conference on Intelligent Robots and Systems (IROS)*, pp. 9401–9408.

Gravagne, I. A., C. D. Rahn, and Ian D. Walker (June 2003). "Large deflection dynamics and control for planar continuum robots". In: *IEEE/ASME Transactions on Mechatronics* 8.2, pp. 299–307.

Gravagne, I. A. and Ian D. Walker (Apr. 2000a). "Kinematic transformations for remotely-actuated planar continuum robots". In: *Proceedings of the IEEE International Conference on Robotics and Automation (ICRA)*, pp. 19–26.

— (Apr. 2000b). "On the kinematics of remotely-actuated continuum robots". In: *Proceedings of the IEEE International Conference on Robotics and Automation (ICRA)*, pp. 2544–2550.

— (June 2002). "Manipulability, force, and compliance analysis for planar continuum manipulators". In: *IEEE Transactions on Robotics and Automation* 18.3, pp. 263–273.

Gu, Xiaoyi, Changsheng Li, Xiao Xiao, Chwee Ming Lim, and Hongliang Ren (Mar. 2019). "A Compliant Transoral Surgical Robotic System Based on a Parallel Flexible Mechanism". In: *Annals of Biomedical Engineering* 47.6, pp. 1329–1344.

Gulotta, Andrew James, Jesse Francisco D'Almeida, Joseph Ronald Bartone, and Nicholas Edward Pacheco (2020). "SCREAM 2.0: Super-elastic Continuum Robot for Endoscopic Articulation and Manipulation". Worcester Polytechnic Institute. MA thesis.

Ha, Junhyoung, Georgios Fagogenis, and Pierre E. Dupont (June 2017). "Effect of Path History on Concentric Tube Robot Model Calibration". In: *Proceedings of the Hamlyn Symposium on Medical Robotics (HSMR)*, pp. 77–78.

— (Apr. 2019). "Modeling Tube Clearance and Bounding the Effect of Friction in Concentric Tube Robot Kinematics". In: *IEEE Transactions on Robotics* 35.2, pp. 353–370.

Ha, Xuan Thao, Di Wu, Chun-Feng Lai, Mouloud Ourak, Gianni Borghesan, Arianna Menciassi, and Emmanuel Vander Poorten (Oct. 2022). "Contact Localization of Continuum and Flexible Robot Using Data-Driven Approach". In: *IEEE Robotics and Automation Letters* 7.3, pp. 6910–6917.

Haidegger, Tamas, Stefanie Speidel, Danail Stoyanov, and Richard M. Satava (July 2022). "Robot-Assisted Minimally Invasive Surgery—Surgical Robotics in the Data Age". In: *Proceedings of the IEEE* 110.7, pp. 835–846.

Harsch, Jonas, Simon Sailer, and Simon R. Eugster (Apr. 2023). "A total Lagrangian, objective and intrinsically locking-free Petrov-Galerkin SE(3) Cosserat rod finite element formulation". In: *International Journal for Numerical Methods in Engineering* 124.13, pp. 2965–2994.

Hawkes, Elliot W., Laura H. Blumenschein, Joseph D. Greer, and Allison M. Okamura (July 2017). "A soft robot that navigates its environment through growth". In: *Science Robotics* 2.8, eaan3028.

Hendrick, Richard J., Christopher R. Mitchell, S. Duke Herrell, and Robert James Webster (July 2015). "Hand-Held Transendoscopic Robotic Manipulators: A Transurethral Laser Prostate Surgery Case Study". In: *International Journal of Robotics Research* 34.13, pp. 1559–1572.

Hirose, Shigeo (1987). *Biologically Inspired Robots: Snake-Like Locomotors and Manipulators*. Oxford, U.K.: Oxford University Press.

Hong, Wuzhou, Andreas Schmitz, Weibang Bai, Pierre Berthet-Rayne, Le Xie, and Guang-Zhong Yang (May 2020). "Design and Compensation Control of a Flexible Instrument for Endoscopic Surgery". In: *Proceedings of the IEEE International Conference on Robotics and Automation (ICRA)*, pp. 1860–1866.

Hu, Yang, Wei Li, Lin Zhang, and Guang-Zhong Yang (Apr. 2019a). "Designing, Prototyping, and Testing a Flexible Suturing Robot for Transanal Endoscopic Microsurgery". In: *IEEE Robotics and Automation Letters* 4.2, pp. 1669–1675.

Hu, Yang, Lin Zhang, Wei Li, and Guang-Zhong Yang (Apr. 2019b). "Design and Fabrication of a 3-d Printed Metallic Flexible Joint for Snake-like Surgical Robot". In: *IEEE Robotics and Automation Letters* 4.2, pp. 1557–1563.

Hu, Yingbai, Jian Li, Yongquan Chen, Qiwen Wang, Chuliang Chi, Heng Zhang, Qing Gao, Yuanmin Lan, Zheng Li, Zonggao Mu, Zhenglong Sun, and Alois Knoll (Apr. 2022). "Design and Control of a Highly Redundant Rigid-flexible Coupling Robot to Assist the COVID-19 Oropharyngeal-Swab Sampling". In: *IEEE Robotics and Automation Letters* 7.2, pp. 1856–1863.

Huang, Xinjia, Xiangyang Zhu, and Guoying Gu (Dec. 2022). "Kinematic Modeling and Characterization of Soft Parallel Robots". In: *IEEE Transactions on Robotics* 38.6, pp. 3792–3806.

Hussaini, M. Yousuff, David A. Kopriva, and Anthony T. Patera (May 1989). "Spectral collocation methods". In: *Applied Numerical Mathematics* 5.3, pp. 177–208.

Hwang, Minho and Dong-Soo Kwon (Oct. 2019). "Strong Continuum Manipulator for Flexible Endoscopic Surgery". In: *IEEE/ASME Transactions on Mechatronics* 24.5, pp. 2193–2203.

Ibrahimbegović, Adnan and Mazen Al Mikdad (Mar. 1998). "Finite rotations in dynamics of beams and implicit time-stepping schemes". In: *International Journal for Numerical Methods in Engineering* 41.5, pp. 781–814.

Ikuta, Koji, Hironobu Ichikawa, Katsuya Suzuki, and Daisuke Yajima (May 2006). "Multi-degree of Freedom Hydraulic Pressure Driven Safety Active Catheter". In: *Proceedings of the IEEE International Conference on Robotics and Automation (ICRA)*, pp. 1553–1559.

Iordachita, Iulian I., Marc D. De Smet, Gerrit Naus, Mamoru Mitsuishi, and Cameron N. Riviere (July 2022). "Robotic Assistance for Intraocular Microsurgery: Challenges and Perspectives". In: *Proceedings of the IEEE* 110.7, pp. 893–908.

Janabi-Sharifi, Farrokh, Amir Jalali, and Ian D. Walker (2021). "Cosserat Rod-Based Dynamic Modeling of Tendon-Driven Continuum Robots: A Tutorial". In: *IEEE Access* 9, pp. 68703–68719.

Jayender, J., M. Azizian, and Rajni V. Patel (Aug. 2008). "Autonomous Image-Guided Robot-Assisted Active Catheter Insertion". In: *IEEE Transactions on Robotics* 24.4, pp. 858–871.

Jeong, Seokhwan, Yash Chitalia, and Jaydev P. Desai (July 2020). "Design, Modeling, and Control of a Coaxially Aligned Steerable (COAST) Guidewire Robot". In: *IEEE Robotics and Automation Letters* 5.3, pp. 4947–4954.

Jiang, Hao, Zhanchi Wang, Xinghua Liu, Xiaotong Chen, Yusong Jin, Xuanke You, and Xiaoping Chen (May 2017). "A two-level approach for solving the inverse kinematics of an extensible soft arm considering viscoelastic behavior". In: *Proceedings of the IEEE International Conference on Robotics and Automation (ICRA)*, pp. 6127–6133.

Jinno, Makoto and Iulian I. Iordachita (May 2022). "Microgripper Using Flexible Wire Hinge for Robotic Intraocular Snake". In: *Proceedings of the IEEE International Conference on Robotics and Automation (ICRA)*, pp. 6218–6224.

Jones, Bryan A., William McMahan, and Ian D. Walker (Sept. 2004). "Design and Analysis of a Novel Pneumatic Manipulator". In: *IFAC Proceedings Volumes* 37.14, pp. 687–692.

Jones, Bryan A. and Ian D. Walker (Feb. 2006a). "Kinematics for Multisection Continuum Robots". In: *IEEE Transactions on Robotics* 22.1, pp. 43–55.

— (Dec. 2006b). "Practical Kinematics for Real-time Implementation of Continuum Robots". In: *IEEE Transactions on Robotics* 22.6, pp. 1087–1099.

Kane, Thomas R. and David A. Levinson (1985). *Dynamics: Theaory and Applications*. New York, NY, USA: McGraw-Hill Inc.

Kang, Byungjeon, Risto Kojcev, and Edoardo Sinibaldi (Feb. 2016). "The First Interlaced Continuum Robot, Devised to Intrinsically Follow the Leader". In: *PLOS ONE* 11.2, e0150278.

Kazemipour, Amirhossein, Oliver Fischer, Yasunori Toshimitsu, Ki Wan Wong, and Robert Kevin Katzschmann (May 2022). "Adaptive Dynamic Sliding Mode Control of Soft Continuum Manipulators". In: *Proceedings of the IEEE International Conference on Robotics and Automation (ICRA)*, pp. 3259–3265.

Khadem, Mohsen, John O'Neill, Zisos Mitros, Lyndon da Cruz, and Christos Bergeles (Oct. 2020). "Autonomous Steering of Concentric Tube Robots via Nonlinear Model Predictive Control". In: *IEEE Transactions on Robotics* 36.5, pp. 1595–1602.

Kim, Jongwoo, Woo-Young Choi, Sungchul Kang, Chunwoo Kim, and Kyu-Jin Cho (Dec. 2019). "Continuously Variable Stiffness Mechanism Using Nonuniform Patterns on Coaxial Tubes for Continuum Microsurgical Robot". In: *IEEE Transactions on Robotics* 35.6, pp. 1475–1487.

Kim, Joonhwan, Michel de Mathelin, Koji Ikuta, and Dong-Soo Kwon (July 2022). "Advancement of Flexible Robot Technologies for Endoluminal Surgeries". In: *Proceedings of the IEEE* 110.7, pp. 909–931.

Kim, Sangbae, Cecilia Laschi, and Barry Trimmer (May 2013). "Soft robotics: a bioinspired evolution in robotics". In: *Trends in Biotechnology* 31.5, pp. 287–294.

Kim, Ji-Suk, Dae-Young Lee, Keri Kim, Sungchul Kang, and Kyu-Jin Cho (May 2014a). "Toward a Solution to the Snapping Problem in a Concentric-tube Continuum Robot: Grooved Tubes with Anisotropy". In: *Proceedings of the IEEE International Conference on Robotics and Automation (ICRA)*, pp. 5871–5876.

Kim, Yeongjin, Shing Shin Cheng, and Jaydev P. Desai (Feb. 2018). "Active Stiffness Tuning of a Spring-Based Continuum Robot for MRI-Guided Neurosurgery". In: *IEEE Transactions on Robotics* 34.1, pp. 18–28.

Kim, Yong-Jae, Shanbao Cheng, Sangbae Kim, and Karl Iagnemma (Apr. 2014b). "A Stiffness-adjustable Hyperredundant Manipulator Using a Variable Neutral-line Mechanism for Minimally Invasive Surgery". In: *IEEE Transactions on Robotics* 30.2, pp. 382–395.

Kirchhoff, G. (Jan. 1859). "Ueber das Gleichgewicht und die Bewegung eines unendlich dünnen elastischen Stabes". In: *Journal für die reine und angewandte Mathematik (Crelle's Journal)* 1859.56, pp. 285–313.

Kong, Yixuan, Shuang Song, Ning Zhang, Jiaole Wang, and Bing Li (Apr. 2022). "Design and Kinematic Modeling of In-Situ Torsionally-Steerable Flexible Surgical Robots". In: *IEEE Robotics and Automation Letters* 7.2, pp. 1864–1871.

Kuntz, Alan, Armaan Sethi, Robert James Webster, and Ron Alterovitz (May 2020). "Learning the Complete Shape of Concentric Tube Robots". In: *IEEE Transactions on Medical Robotics and Bionics* 2.2, pp. 140–147.

Kutzer, Michael D. M., Sean M. Segreti, Christopher Y. Brown, Mehran Armand, Russell H. Taylor, and Simon C. Mears (May 2011). "Design of a new cable-driven manipulator with a large open lumen: Preliminary applications in the minimally-invasive removal of osteolysis". In: *Proceedings of the IEEE International Conference on Robotics and Automation (ICRA)*, pp. 2913–2920.

Kwok, Ka-Wai, Helge Würdemann, Alberto Arezzo, Arianna Menciassi, and Kaspar Althoefer (July 2022). "Soft Robot-Assisted Minimally Invasive Surgery and Interventions: Advances and Outlook". In: *Proceedings of the IEEE* 110.7, pp. 871–892.

Langer, Marlene, Ernar Amanov, and Jessica Burgner-Kahrs (June 2018). "Stiffening Sheaths for Continuum Robots". In: *Soft Robotics* 5.3, pp. 291–303.

Laschi, Cecilia, Matteo Cianchetti, Barbara Mazzolai, Laura Margheri, Maurizio Follador, and Paolo Dario (Apr. 2012). "Soft Robot Arm Inspired by the Octopus". In: *Advanced Robotics* 26.7, pp. 709–727.

Lee, Dae-Young, Jongwoo Kim, Ji-Suk Kim, Changyeob Baek, Gunwoo Noh, Do-Nyun Kim, Keri Kim, Sungchul Kang, and Kyu-Jin Cho (Dec. 2015). "Anisotropic Patterning to Reduce Instability of Concentric-tube Robots". In: *IEEE Transactions on Robotics* 31.6, pp. 1311–1323.

Legrand, Julie, Mouloud Ourak, Tom Vandebroek, and Emmanuel Vander Poorten (May 2021). "A Large Displacement Model for Superelastic Material Side-Notched Tube Instruments". In: *International Journal of Mechanical Sciences* 197, p. 106329.

Leibrandt, Konrad, Christos Bergeles, and Guang-Zhong Yang (Sept. 2017). "Implicit Active Constraints for Concentric Tube Robots Based on Analysis of the Safe and Dexterous Workspace". In: *Proceedings of the IEEE/RSJ International Conference on Intelligent Robots and Systems (IROS)*, pp. 193–200.

Li, Changquing and Christopher D. Rahn (May 2002). "Design of Continuous Backbone, Cable-Driven Robots". In: *Journal of Mechanical Design* 124.2, pp. 265–271.

Li, Jianhua, Fangmin Zhang, Zhenguo Yang, Zhenming Jiang, Zhidong Wang, and Hao Liu (Apr. 2022). "Shape Sensing for Continuum Robots by Capturing Passive Tendon Displacements with Image Sensors". In: *IEEE Robotics and Automation Letters* 7.2, pp. 3130–3137.

Li, Minhan, Rongjie Kang, David T. Branson, and Jian S. Dai (Feb. 2018). "Model-Free Control for Continuum Robots Based on an Adaptive Kalman Filter". In: *IEEE/ASME Transactions on Mechatronics* 23.1, pp. 286–297.

Li, Wen-Bo, Xin-Yu Guo, Fu-Yi Fang, and Wen-Ming Zhang (May 2021). "Amplifying Laminar Jamming for Soft Robots by Geometry-Induced Rigidity". In: *Proceedings of the IEEE International Conference on Robotics and Automation (ICRA)*, pp. 11907–11912.

Li, Zheng, Liao Wu, Hongliang Ren, and Haoyong Yu (Jan. 2017). "Kinematic Comparison of Surgical Tendon-driven Manipulators and Concentric Tube Manipulators". In: *Mechanism and Machine Theory* 107, pp. 148–165.

Liang, Nan, Reinhard M. Grassmann, Sven Lilge, and Jessica Burgner-Kahrs (May 2021). "Learning-based Inverse Kinematics from Shape as Input for Concentric Tube Continuum Robots". In: *Proceedings of the IEEE International Conference on Robotics and Automation (ICRA)*, pp. 1387–1393.

Lilge, Sven and Jessica Burgner-Kahrs (Apr. 2023). "Kinetostatic Modeling of Tendon-Driven Parallel Continuum Robots". In: *IEEE Transactions on Robotics* 39.2, pp. 1563–1579.

Lin, Botao, Jiaole Wang, Shuang Song, Bing Li, and Max Q.-H. Meng (Apr. 2022a). "A Modular Lockable Mechanism for Tendon-Driven Robots: Design, Modeling and Characterization". In: *IEEE Robotics and Automation Letters* 7.2, pp. 2023–2030.

Lin, Daojing, Niandong Jiao, Zhidong Wang, and Lianqing Liu (Apr. 2021). "A Magnetic Continuum Robot With Multi-Mode Control Using Opposite-Magnetized Magnets". In: *IEEE Robotics and Automation Letters* 6.2, pp. 2485–2492.

Lin, Jui-Te, Cedric Girerd, Jiayao Yan, John T. Hwang, and Tania K. Morimoto (Dec. 2022b). "A Generalized Framework for Concentric Tube Robot Design Using Gradient-Based Optimization". In: *IEEE Transactions on Robotics* 38.6, pp. 3774–3791.

Lin, Zecai, Hao Wu, Huan Jia, Huanghua Liu, Xiaojie Ai, Yun Zou, Zhenglong Sun, Weidong Chen, Guang-Zhong Yang, and Anzhu Gao (May 2022c). "Fixed and Sliding FBG Sensors-Based Triaxial Tip Force Sensing for Cable-Driven Continuum Robots". In: *Proceedings of the IEEE International Conference on Robotics and Automation (ICRA)*, pp. 9593–9599.

Lis, Patrick, Achraj Sarma, Grace Trimpe, Timothy A. Brumfiel, Ronghuai Qi, and Jaydev P. Desai (May 2022). "Design and Modeling of a Compact Advancement Mechanism for a Modified COAST Guidewire Robot". In: *Proceedings of the IEEE International Conference on Robotics and Automation (ICRA)*, pp. 1176–1182.

Liu, Yang and Farshid Alambeigi (Apr. 2021). "Effect of External and Internal Loads on Tension Loss of Tendon-Driven Continuum Manipulators". In: *IEEE Robotics and Automation Letters* 6.2, pp. 1606–1613.

— (Apr. 2022). "Impact of Generic Tendon Routing on Tension Loss of Tendon-Driven Continuum Manipulators with Planar Deformation". In: *IEEE Robotics and Automation Letters* 7.2, pp. 3624–3631.

Lloyd, Peter, Onaizah Onaizah, Giovanni Pittiglio, Damith Katudampe Vithanage, James H. Chandler, and Pietro Valdastri (Oct. 2022). "Magnetic Soft Continuum Robots With Braided Reinforcement". In: *IEEE Robotics and Automation Letters* 7.4, pp. 9770–9777.

Lock, Jesse, Genevieve Laing, Mohsen Mahvash, and Pierre E. Dupont (Oct. 2010). "Quasistatic modeling of concentric tube robots with external loads". In: *Proceedings of the IEEE/RSJ International Conference on Intelligent Robots and Systems (IROS)*, pp. 2325–2332.

Luo, Kevin Ai Xin Jue, Thomas Looi, Saba Sabetian, and James M. Drake (Oct. 2018). "Designing Concentric Tube Manipulators for Stability Using Topology Optimization". In: *Proceedings of the IEEE/RSJ International Conference on Intelligent Robots and Systems (IROS)*, pp. 1764–1769.

Lynch, Kevin M. and Frank C. Park (2017). *Modern Robotics*. Cambridge, U.K.: Cambridge University Press.

Ma, Guoyu, Siyang Zuo, and Jianbin Liu (Sept. 2021). "Design of Low-Cost Endoscope Based on Novel Wire-Driven Rotary Valve and Water-Jet Mechanism". In: *Journal of Medical Devices* 15.4, p. 044501.

Ma, Xin, Xuchen Wang, Rui Cao, and K. W. Samuel Au (Oct. 2022). "Design, Teleoperation Control and Experimental Validation of a Dexterous Robotic Flexible Endoscope for Laparoscopic Surgery". In: *Proceedings of the IEEE/RSJ International Conference on Intelligent Robots and Systems (IROS)*, pp. 5937–5944.

MacDonald, J. K. L. (May 1933). "Successive Approximations by the Rayleigh-Ritz Variation Method". In: *Physical Review* 43.10, pp. 830–833.

Mahl, Tobias, Annika E. Mayer, Alexander Hildebrandt, and Oliver Sawodny (June 2013). "A variable curvature modeling approach for kinematic control of continuum manipulators". In: *Proceedings of the IEEE American Control Conference (ACC)*, pp. 4945–4950.

Mahoney, Arthur W., Hunter B. Gilbert, and Robert James Webster (2018). "A Review of Concentric Tube Robots: Modeling, Control, Design, Planning, and Sensing". In: *The Encyclopedia of Medical Robotics*. Ed. by Rajni Patel. Singapore: World Scientific, pp. 181–202.

Mahvash, Mohsen and Pierre E. Dupont (Apr. 2011). "Stiffness Control of Surgical Continuum Manipulators". In: *IEEE Transactions on Robotics* 27.2, pp. 334–345.

Maloisel, Guirec, Espen Knoop, Christian Schumacher, and Moritz Bacher (June 2021). "Automated Routing of Muscle Fibers for Soft Robots". In: *IEEE Transactions on Robotics* 37.3, pp. 996–1008.

Marechal, Luc, Pascale Balland, Lukas Lindenroth, Fotis Petrou, Christos Kontovounisios, and Fernando Bello (June 2021). "Toward a Common Framework and Database of Materials for Soft Robotics". In: *Soft Robotics* 8.3, pp. 284–297.

Marsden, Jerrold E., Sergey Pekarsky, and Steve Shkoller (Oct. 1999). "Discrete Euler-Poincaré and Lie-Poisson equations". In: *Nonlinearity* 12.6, pp. 1647–1662.

Marsden, Jerrold E. and Tudor S. Ratiu (1999). *Introduction to mechanics and symmetry*. Second. New York, NY, USA: Springer-Verlag.

Mattmann, Michael, Quentin Boehler, Xiang-Zhong Chen, Salvador Pané, and Bradley J. Nelson (Oct. 2022). "Shape Memory Polymer Variable Stiffness Magnetic Catheters with Hybrid Stiffness Control". In: *Proceedings of the IEEE/RSJ International Conference on Intelligent Robots and Systems (IROS)*, pp. 9589–9595.

McMahan, William, V. Chitrakaran, Matthew A. Csencsits, D. Dawson, Ian D. Walker, Bryan A. Jones, M. Pritts, D. Dienno, M. Grissom, and C. D. Rahn (May 2006). "Field trials and testing of the OctArm continuum manipulator". In: *Proceedings of the IEEE International Conference on Robotics and Automation (ICRA)*, pp. 2336–2341.

Meisel, Nicholas A., Amelia M. Elliott, and Christopher B. Williams (July 2014). "A Procedure for Creating Actuated Joints Via Embedding Shape Memory Alloys in PolyJet 3d Printing". In: *Journal of Intelligent Material Systems and Structures* 26.12, pp. 1498–1512.

Misra, Shivangi and Cynthia Sung (May 2022). "Forward Kinematics and Control of a Segmented Tunable-Stiffness 3-D Continuum Manipulator". In: *Proceedings of the IEEE International Conference on Robotics and Automation (ICRA)*, pp. 3238–3244.

Mitros, Zisos, Seyed Mohammad Hadi Sadati, Ross Henry, Lyndon Da Cruz, and Christos Bergeles (May 2022a). "From Theoretical Work to Clinical Translation: Progress in Concentric Tube Robots". In: *Annual Review of Control, Robotics, and Autonomous Systems* 5.1, pp. 335–359.

Mitros, Zisos, Seyed Mohammad Hadi Sadati, Sotirios Nousias, Lyndon da Cruz, and Christos Bergeles (May 2022b). "Design and Quasistatic Modelling of Hybrid Continuum Multi-Arm Robots". In: *Proceedings of the IEEE International Conference on Robotics and Automation (ICRA)*, pp. 9607–9613.

Mitros, Zisos, Seyed Mohammad Hadi Sadati, Carlo A. Seneci, Edward Bloch, Konrad Leibrandt, Mohsen Khadem, Lyndon da Cruz, and Christos Bergeles (July 2020). "Optic Nerve Sheath Fenestration With a Multi-Arm Continuum Robot". In: *IEEE Robotics and Automation Letters* 5.3, pp. 4874–4881.

Mochiyama, Hiromi (Nov. 2005). "Hyper-flexible robotic manipulators". In: *Proceedings of the IEEE International Symposium on Micro-NanoMechatronics and Human Science (MHS)*, pp. 41–46.

Morimoto, Tania K. and Allison M. Okamura (Dec. 2016). "Design of 3-d Printed Concentric Tube Robots". In: *IEEE Transactions on Robotics* 32.6, pp. 1419–1430.

Moses, Matthew S., Michael D. M. Kutzer, Hans Ma, and Mehran Armand (May 2013). "A Continuum Manipulator Made of Interlocking Fibers". In: *Proceedings of the IEEE International Conference on Robotics and Automation (ICRA)*, pp. 4008–4015.

Murray, Richard M. (1994). *A Mathematical Introduction to Robotic Manipulation*. Bocca Raton, FL, USA: CRC Press Inc.

Nelson, Bradley J., Simone Gervasoni, Philip Wai Yan Chiu, Li Zhang, and Ajmal Zemmar (July 2022). "Magnetically Actuated Medical Robots: An in vivo Perspective". In: *Proceedings of the IEEE* 110.7, pp. 1028–1037.

Neppalli, Srinivas, Matthew A. Csencsits, Bryan A. Jones, and Ian D. Walker (Jan. 2009). "Closed-form Inverse Kinematics for Continuum Manipulators". In: *Advanced Robotics* 23.15, pp. 2077–2091.

Neumann, Maria and Jessica Burgner-Kahrs (May 2016). "Considerations for Follow-the-leader Motion of Extensible Tendon-driven Continuum Robots". In: *Proceedings of the IEEE International Conference on Robotics and Automation (ICRA)*, pp. 917–923.

Nguyen, Chi Cong, Timotius Teh, Mai Thanh Thai, Phuoc Thien Phan, Trung Thien Hoang, Harrison Low, James Davies, Emanuele Nicotra, Nigel H. Lovell, and Thanh Nho Do (May 2022a). "Bidirectional Soft Robotic Catheter for Arrhythmia Treatment". In: *Proceedings of the IEEE International Conference on Robotics and Automation (ICRA)*, pp. 9579–9585.

Nguyen, Dang-Viet-Anh, Cedric Girerd, Quentin Boyer, Patrick Rougeot, Olivier Lehmann, Laurent Tavernier, Jérôme Szewczyk, and Kanty Rabenorosoa (Jan. 2022b). "A Hybrid Concentric

Tube Robot for Cholesteatoma Laser Surgery". In: *IEEE Robotics and Automation Letters* 7.1, pp. 462–469.

Nguyen, Thien-Dang and Jessica Burgner-Kahrs (Sept. 2015). "A Tendon-driven Continuum Robot with Extensible Sections". In: *Proceedings of the IEEE/RSJ International Conference on Intelligent Robots and Systems (IROS)*, pp. 2130–2135.

Noonan, David P., Valentina Vitiello, Jianzhong Shang, Christopher J. Payne, and Guang-Zhong Yang (Sept. 2011). "A Modular, Mechatronic Joint Design for a Flexible Access Platform for MIS". In: *Proceedings of the IEEE/RSJ International Conference on Intelligent Robots and Systems (IROS)*, pp. 949–954.

O'Reilly, Oliver M. (2017). "Kirchhoff's Rod Theory". In: *Modeling Nonlinear Problems in the Mechanics of Strings and Rods. Interaction of Mechanics and Mathematics*. Cham, Switzerland: Springer International Publishing AG, pp. 187–268.

Oliver-Butler, Kaitlin (2021). "Mechanics and Design of Stiffness-Modified Continuum Robots and Endoscopic Instruments". University of Tennessee. PhD thesis.

Oliver-Butler, Kaitlin, Jake A. Childs, Adam Daniel, and Daniel Caleb Rucker (Apr. 2022). "Concentric Push–Pull Robots: Planar Modeling and Design". In: *IEEE Transactions on Robotics* 38.2, pp. 1186–1200.

Oliver-Butler, Kaitlin, Zane H. Epps, and Daniel Caleb Rucker (Mar. 2017). "Concentric Agonist-antagonist Robots for Minimally Invasive Surgeries". In: *Proceedings of SPIE Medical Imaging: Image-Guided Procedures, Robotic Interventions, and Modeling*, p. 1013511.

Oliver-Butler, Kaitlin, John Till, and Daniel Caleb Rucker (Apr. 2019). "Continuum Robot Stiffness under External Loads and Prescribed Tendon Displacements". In: *IEEE Transactions on Robotics* 35.2, pp. 403–419.

Orekhov, Andrew L., Elan Z. Ahronovich, and Nabil Simaan (June 2023). "Lie Group Formulation and Sensitivity Analysis for Shape Sensing of Variable Curvature Continuum Robots With General String Encoder Routing". In: *IEEE Transactions on Robotics* 39.3, pp. 2308–2324.

Orekhov, Andrew L., Vincent A. Aloi, and Daniel Caleb Rucker (May 2017). "Modeling Parallel Continuum Robots with General Intermediate Constraints". In: *Proceedings of the IEEE International Conference on Robotics and Automation (ICRA)*, pp. 6142–6149.

Orekhov, Andrew L., Caroline Bryson Black, John Till, Scotty Chung, and Daniel Caleb Rucker (July 2016). "Analysis and Validation of a Teleoperated Surgical Parallel Continuum Manipulator". In: *IEEE Robotics and Automation Letters* 1.2, pp. 828–835.

Orekhov, Andrew L. and Nabil Simaan (Oct. 2020). "Solving Cosserat Rod Models via Collocation and the Magnus Expansion". In: *Proceedings of the IEEE/RSJ International Conference on Intelligent Robots and Systems (IROS)*, pp. 8653–8660.

Pacheco, Nicholas Edward, Joshua B. Gafford, Mostafa A. Atalla, Robert James Webster, and Loris Fichera (Sept. 2021). "Beyond Constant Curvature: A New Mechanics Model for Unidirectional Notched-Tube Continuum Wrists". In: *Journal of Medical Robotics Research* 6.1, p. 2140004.

Patesson, René, Eric Brangier, Xavier Bollen, and Matthias Tummers (Aug. 2018). "How to Implement a High-Fidelity Prototyping Approach in a Cardiac Surgery Device?" In: *Proceedings of the Congress of the International Ergonomics Association (IEA)*, pp. 291–302.

Peyron, Quentin, Quentin Boehler, Patrick Rougeot, Pierre Roux, Bradley J. Nelson, Nicolas Andreff, Kanty Rabenorosoa, and Pierre Renaud (Apr. 2022). "Magnetic concentric tube robots: Introduction and analysis". In: *The International Journal of Robotics Research* 41.4, pp. 418–440.

Peyron, Quentin, Kanty Rabenorosoa, Nicolas Andreff, and Pierre Renaud (Feb. 2019). "A numerical framework for the stability and cardinality analysis of concentric tube robots: Introduction and application to the follow-the-leader deployment". In: *Mechanism and Machine Theory* 132, pp. 176–192.

Pogue, Chloe, Priyanka Rao, Quentin Peyron, Jongwoo Kim, Jessica Burgner-Kahrs, and Eric D. Diller (Oct. 2022). "Multiple Curvatures in a Tendon-Driven Continuum Robot Using a Novel Magnetic Locking Mechanism". In: *Proceedings of the IEEE/RSJ International Conference on Intelligent Robots and Systems (IROS)*, pp. 472–479.

Ponten, Ryan (2017). "Design of a Robotic Instrument Manipulator for Endoscopic Deployment". University of Tennessee. MA thesis.

Press, William H., Saul A. Teukolsky, William T. Vetterling, and Brian P. Flannery (2007). *Numerical Recipes. The Art of Scientific Computing*. Third. Cambridge, U.K.: Cambridge University Press.

Rao, Priyanka, Quentin Peyron, and Jessica Burgner-Kahrs (May 2021a). "Using Euler Curves to Model Continuum Robots". In: *Proceedings of the IEEE International Conference on Robotics and Automation (ICRA)*, pp. 1402–1408.

— (Oct. 2022). "Shape Representation and Modeling of Tendon-Driven Continuum Robots Using Euler Arc Splines". In: *IEEE Robotics and Automation Letters* 7.3, pp. 8114–8121.

Rao, Priyanka, Quentin Peyron, Sven Lilge, and Jessica Burgner-Kahrs (Feb. 2021b). "How to Model Tendon-Driven Continuum Robots and Benchmark Modelling Performance". In: *Frontiers in Robotics and AI* 7.2, pp. 223–243.

Remirez, Andria A. and Robert James Webster (Mar. 2016). "Endoscopes and Robots for Tight Surgical Spaces: Use of Precurved Elastic Elements to Enhance Curvature". In: *Proceedings of SPIE Medical Imaging: Image-Guided Procedures, Robotic Interventions, and Modeling*, 97860R.

Renda, Federico, Costanza Armanini, Vincent Lebastard, Fabien Candelier, and Frédéric Boyer (July 2020). "A Geometric Variable-Strain Approach for Static Modeling of Soft Manipulators With Tendon and Fluidic Actuation". In: *IEEE Robotics and Automation Letters* 5.3, pp. 4006–4013.

Renda, Federico, Costanza Armanini, Anup Teejo Mathew, and Frédéric Boyer (Oct. 2022). "Geometrically-Exact Inverse Kinematic Control of Soft Manipulators With General Thread-like Actuators' Routing". In: *IEEE Robotics and Automation Letters* 7.3, pp. 7311–7318.

Renda, Federico, Matteo Cianchetti, Michele Giorelli, Andrea Arienti, and Cecilia Laschi (May 2012). "A 3D steady-state model of a tendon-driven continuum soft manipulator inspired by the octopus arm". In: *Bioinspiration & Biomimetics* 7.2, p. 025006.

Renda, Federico, Michele Giorelli, Marcello Calisti, Matteo Cianchetti, and Cecilia Laschi (Oct. 2014). "Dynamic Model of a Multibending Soft Robot Arm Driven by Cables". In: *IEEE Transactions on Robotics* 30.5, pp. 1109–1122.

Renda, Federico, Conor Messer, Daniel Caleb Rucker, and Frédéric Boyer (Apr. 2021). "A Sliding-Rod Variable-Strain Model for Concentric Tube Robots". In: *IEEE Robotics and Automation Letters* 6.2, pp. 3451–3458.

Riojas, Katherine E., Robert James Webster, Daniel Caleb Rucker, Kaitlin Oliver Butler, and Ryan Ponten (2019). *Surgical Device Tip with Deflectable Joint*. Patent: US 2019/0133705 A1.

Ritz, Von Herrn Walter (1909). "Über eine neue Methode zur Lösung gewisser Variationsprobleme der mathematischen Physik". In: *Journal für die reine und angewandte Mathematik (Crelle's Journal)* 135, pp. 1–61.

Roozing, Wesley, Stefan S. Groothuis, and Stefano Stramigioli (May 2020). "Energy-Based Safety in Series Elastic Actuation". In: *Proceedings of the IEEE International Conference on Robotics and Automation (ICRA)*, pp. 914–920.

Rox, Margaret, Aidan Copinga, Robert P. Naftel, Robert James Webster, and Alan Kuntz (June 2022). "Optimizing Continuum Robot Tendon Routing for Minimally Invasive Brain Surgery". In: *Proceedings of the Hamlyn Symposium on Medical Robotics (HSMR)*, pp. 145–146.

Rox, Margaret, Katherine E. Riojas, Maxwell Emerson, Kaitlin Oliver-Butler, Daniel Caleb Rucker, and Robert James Webster (June 2018). "Luminal Robots Small Enough to Fit Through Endoscope Ports: Initial Tumor Resection Experiments in the Airways". In: *Proceedings of the Hamlyn Symposium on Medical Robotics (HSMR)*, pp. 63–64.

Rucker, Daniel Caleb (2011). "The Mechanics of Continuum Robots: Model-based Sensing and Control". Vanderbilt University. PhD thesis.

— (Oct. 2018). "Integrating Rotations Using Nonunit Quaternions". In: *IEEE Robotics and Automation Letters* 3.4, pp. 2979–2986.

Rucker, Daniel Caleb, Eric J. Barth, Joshua Gaston, and James C. Gallentine (Oct. 2022a). "Task-Space Control of Continuum Robots Using Underactuated Discrete Rod Models". In: *Proceedings of the IEEE/RSJ International Conference on Intelligent Robots and Systems (IROS)*, pp. 10967–10974.

Rucker, Daniel Caleb, Jake A. Childs, Parsa Molaei, and Hunter B. Gilbert (Apr. 2022b). "Transverse Anisotropy Stabilizes Concentric Tube Robots". In: *IEEE Robotics and Automation Letters* 7.2, pp. 2407–2414.

Rucker, Daniel Caleb, Bryan A. Jones, and Robert James Webster (Oct. 2010a). "A Geometrically Exact Model for Externally Loaded Concentric-Tube Continuum Robots". In: *IEEE Transactions on Robotics* 26.5, pp. 769–780.

— (May 2010b). "A model for concentric tube continuum robots under applied wrenches". In: *Proceedings of the IEEE International Conference on Robotics and Automation (ICRA)*, pp. 1047–1052.

Rucker, Daniel Caleb and Robert James Webster (Oct. 2008). "Mechanics-based modeling of bending and torsion in active cannulas". In: *Proceedings of the IEEE RAS/EMBS International Conference on Biomedical Robotics and Biomechatronics (BioRob)*, pp. 704–709.

— (May 2011a). "Computing Jacobians and compliance matrices for externally loaded continuum robots". In: *Proceedings of the IEEE International Conference on Robotics and Automation (ICRA)*, pp. 945–950.

— (Dec. 2011b). "Statics and Dynamics of Continuum Robots with General Tendon Routing and External Loading". In: *IEEE Transactions on Robotics* 27.6, pp. 1033–1044.

Rus, Daniela and Michael T. Tolley (May 2015). "Design, fabrication and control of soft robots". In: *Nature* 521.7553, pp. 467–475.

Russo, Matteo, Natthapol Sriratanasak, Weiming Ba, Xin Dong, Abdelkhalick Mohammad, and Dragos Axinte (Apr. 2022). "Cooperative Continuum Robots: Enhancing Individual Continuum Arms by Reconfiguring into a Parallel Manipulator". In: *IEEE Robotics and Automation Letters* 7.2, pp. 1558–1565.

Sadati, Seyed Mohammad Hadi, Zisos Mitros, Ross Henry, Lingyun Zeng, Lyndon da Cruz, and Christos Bergeles (Apr. 2022). "Real-Time Dynamics of Concentric Tube Robots with Reduced-Order Kinematics Based on Shape Interpolation". In: *IEEE Robotics and Automation Letters* 7.2, pp. 5671–5678.

Sadati, Seyed Mohammad Hadi, Seyedeh Elnaz Naghibi, Ali Shiva, Brendan Michael, Ludovic Renson, Matthew Howard, Daniel Caleb Rucker, Kaspar Althoefer, Thrishantha Nanayakkara, Steffen Zschaler, Christos Bergeles, Helmut Hauser, and Ian D. Walker (Jan. 2020). "TMTDyn: A Matlab Package for Modeling and Control of Hybrid Rigid-Continuum Robots Based on Discretized Lumped Systems and Reduced-Order Models". In: *International Journal of Robotics Research* 40.1, pp. 296–347.

Sadati, Seyed Mohammad Hadi, Seyedeh Elnaz Naghibi, Ali Shiva, Ian D. Walker, Kaspar Althoefer, and Thrishantha Nanayakkara (July 2017). "Mechanics of continuum manipulators, a comparative study of five methods with experiments". In: *Proceedings of the Conference Towards Autonomous Robotic Systems (TAROS)*, pp. 686–702.

Sadati, Seyed Mohammad Hadi, Ali Shiva, Seyedeh Elnaz Naghibi, Daniel Caleb Rucker, Ludovic Renson, Christos Bergeles, Kaspar Althoefer, Thrishantha Nanayakkara, Helmut Hauser, and Ian D. Walker (June 2019). "Reduced Order vs. Discretized Lumped System Models with Absolute and Relative States for Continuum Manipulators". In: *Proceedings of the Robotics: Science and Systems Conference (RSS)*, p76.

Santina, Cosimo Della and Daniela Rus (Apr. 2020). "Control Oriented Modeling of Soft Robots: The Polynomial Curvature Case". In: *IEEE Robotics and Automation Letters* 5.2, pp. 290–298.

Sartoretti, Guillaume, Tianyu Wang, Gabriel Chuang, Qingyang Li, and Howie Choset (May 2021). "Autonomous Decentralized Shape-Based Navigation for Snake Robots in Dense Environments". In: *Proceedings of the IEEE International Conference on Robotics and Automation (ICRA)*, pp. 9276–9282.

Schlenk, Christopher, Julian Klodmann, Katharina Hagmann, Alexander Kolb, Anja Hellings-Kus, Florian Steidle, Dominik Schoeb, Thorsten Jurgens, Arkadiusz Miernik, and Alin Albu-Schaffer (Oct. 2022). "A Robotic System for Solo Surgery in Flexible Ureterorenoscopy". In: *IEEE Robotics and Automation Letters* 7.4, pp. 10558–10565.

Schultz, Joshua A., Haley Sanders, Phuc Duc Hong Bui, Brett Layer, and Marc Killpack (May 2022). "Modeling the Dynamics of Soft Robots by Discs and Threads". In: *Proceedings of the IEEE International Conference on Robotics and Automation (ICRA)*, pp. 3223–3229.

Sears, Patrick and Pierre E. Dupont (Oct. 2006). "A Steerable Needle Technology Using Curved Concentric Tubes". In: *Proceedings of the IEEE/RSJ International Conference on Intelligent Robots and Systems (IROS)*, pp. 2850–2856.

Sefati, Shahriar, Rachel Hegeman, Iulian I. Iordachita, Russell H. Taylor, and Mehran Armand (Apr. 2022). "A Dexterous Robotic System for Autonomous Debridement of Osteolytic Bone Lesions in Confined Spaces: Human Cadaver Studies". In: *IEEE Transactions on Robotics* 38.2, pp. 1213–1229.

Shao, Shicong, Botian Sun, Qingpeng Ding, Wanquan Yan, Wenjia Zheng, Kim Yan, Yilun Hong, and Shing Shin Cheng (Apr. 2020). "Design, Modeling, and Control of a Compact SMA-Actuated MR-Conditional Steerable Neurosurgical Robot". In: *IEEE Robotics and Automation Letters* 5.2, pp. 1381–1388.

Sheng, Jun, Xuefeng Wang, Timm-Michael L. Dickfeld, and Jaydev P. Desai (Oct. 2018). "Towards the Development of a Steerable and MRI-compatible Cardiac Catheter for Atrial Fibrillation Treatment". In: *IEEE Robotics and Automation Letters* 3.4, pp. 4038–4045.

Shiva, Ali, Seyed Mohammad Hadi Sadati, Yohan Noh, Jan Fraś, Ahmad Ataka, Helge Würdemann, Helmut Hauser, Ian D. Walker, Thrishantha Nanayakkara, and Kaspar Althoefer (Apr. 2019). "Elasticity Versus Hyperelasticity Considerations in Quasistatic Modeling of a Soft Finger-Like Robotic Appendage for Real-Time Position and Force Estimation". In: *Soft Robotics* 6.2, pp. 228–249.

Simaan, Nabil (Apr. 2005). "Snake-like Units Using Flexible Backbones and Actuation Redundancy for Enhanced Miniaturization". In: *Proceedings of the IEEE International Conference on Robotics and Automation (ICRA)*, pp. 3012–3017.

Simaan, Nabil, Russell H. Taylor, and Paul Flint (Apr. 2004). "A Dexterous System for Laryngeal Surgery". In: *Proceedings of the IEEE International Conference on Robotics and Automation (ICRA)*, pp. 351–357.

Simaan, Nabil, Kai Xu, Wei Wei, Ankur Kapoor, Peter Kazanzides, Russell H. Taylor, and Paul Flint (May 2009). "Design and Integration of a Telerobotic System for Minimally Invasive Surgery of the Throat". In: *International Journal of Robotics Research* 28.9, pp. 1134–1153.

Simo, Juan Carlo (May 1985). "A Finite-Strain Beam Formulation. The Three-Dimensional Dynamic Problem - Part I". In: *Computer Methods in Applied Mechanics and Engineering* 49.1, pp. 55–70.

Simo, Juan Carlo and L. Vu-Quoc (Oct. 1986). "A Three-Dimensional Finite-Strain Rod Model - Part II - Computational Aspects". In: *Computer Methods in Applied Mechanics and Engineering* 58.1, pp. 79–116.

— (Feb. 1988). "On the dynamics in space of rods undergoing large motions — A geometrically exact approach". In: *Computer Methods in Applied Mechanics and Engineering* 66.2, pp. 125–161.

Šittner, Petr, Ludek Heller, Jan Pilch, Caroline Curfs, Thiery Alonso, and Denis Favier (Apr. 2014). "Young's Modulus of Austenite and Martensite Phases in Superelastic NiTi Wires". In: *Journal of Materials Engineering and Performance* 23.7, pp. 2303–2314.

Sonneville, Valentin, Alberto Cardona, and Olivier Brüls (Jan. 2014). "Geometrically exact beam finite element formulated on the special Euclidean group". In: *Computer Methods in Applied Mechanics and Engineering* 268, pp. 451–474.

Spinelli, Filippo Alberto and Robert Kevin Katzschmann (Oct. 2022). "A Unified and Modular Model Predictive Control Framework for Soft Continuum Manipulators under Internal and External Constraints". In: *Proceedings of the IEEE/RSJ International Conference on Intelligent Robots and Systems (IROS)*, pp. 9393–9400.

Starke, Julia, Ernar Amanov, M. Taha Chikhaoui, and Jessica Burgner-Kahrs (Sept. 2017). "On the Merits of Helical Tendon Routing in Continuum Robots". In: *Proceedings of the IEEE/RSJ International Conference on Intelligent Robots and Systems (IROS)*, pp. 6470–6476.

Stella, Francesco, Nana Obayashi, Cosimo Della Santina, and Josie Hughes (Oct. 2022). "An Experimental Validation of the Polynomial Curvature Model: Identification and Optimal Control of a Soft Underwater Tentacle". In: *IEEE Robotics and Automation Letters* 7.4, pp. 11410–11417.

Su, Hao, Ka-Wai Kwok, Kevin Cleary, Iulian I. Iordachita, M. Cenk Cavusoglu, Jaydev P. Desai, and Gregory S. Fischer (July 2022). "State of the Art and Future Opportunities in MRI-Guided Robot-Assisted Surgery and Interventions". In: *Proceedings of the IEEE* 110.7, pp. 968–992.

Sun, Jiefeng and Jianguo Zhao (Apr. 2022). "Physics-Based Modeling of Twisted-and-Coiled Actuators Using Cosserat Rod Theory". In: *IEEE Transactions on Robotics* 38.2, pp. 779–796.

Swaney, Philip J., Peter A. York, Hunter B. Gilbert, Jessica Burgner-Kahrs, and Robert James Webster (Dec. 2016). "Design, Fabrication, and Testing of a Needle-sized Wrist for Surgical Instruments". In: *Journal of Medical Devices* 11.1, p. 014501.

Szewczyk, Jérôme, V. de Sars, Ph. Bidaud, and G. Dumont (2001). "An active tubular polyarticulated micro-system for flexible endoscope". In: *Experimental Robotics. Springer Tracts in Advanced Robotics*. Ed. by Daniella Rus and S. Singh. Heidelberg, Germany: Springer-Verlag, pp. 179–188.

Szewczyk, Jérôme, Emilie Marchandise, Patrice Flaud, Laurent Royon, and Raphaël Blanc (Feb. 2011). "Active Catheters for Neuroradiology". In: *Journal of Robotics and Mechatronics* 23.1, pp. 105–115.

Taylor, Russell H., Nabil Simaan, Arianna Menciassi, and Guang-Zhong Yang (July 2022). "Surgical Robotics and Computer-Integrated Interventional Medicine". In: *Proceedings of the IEEE* 110.7, pp. 823–834.

Thuruthel, Thomas George, Egidio Falotico, Federico Renda, and Cecilia Laschi (Feb. 2019). "Model-Based Reinforcement Learning for Closed-Loop Dynamic Control of Soft Robotic Manipulators". In: *IEEE Transactions on Robotics* 35.1, pp. 124–134.

Till, John (2019). "On the Statics, Dynamics, and Stability of Continuum Robots: Model Formulations and Efficient Computational Schemes". University of Tennessee. PhD thesis.

Till, John, Vincent A. Aloi, and Daniel Caleb Rucker (Apr. 2019). "Real-Time Dynamics of Soft and Continuum Robots Based on Cosserat Rod Models". In: *International Journal of Robotics Research* 38.6, pp. 723–746.

Till, John, Caroline E. Bryson, Scotty Chung, Andrew L. Orekhov, and Daniel Caleb Rucker (May 2015). "Efficient computation of multiple coupled Cosserat rod models for real-time simulation and control of parallel continuum manipulators". In: *Proceedings of the IEEE International Conference on Robotics and Automation (ICRA)*, pp. 5067–5074.

Torres, Luis G., Cenk Baykal, and Ron Alterovitz (May 2014). "Interactive-rate motion planning for concentric tube robots". In: *Proceedings of the IEEE International Conference on Robotics and Automation (ICRA)*, pp. 1915–1921.

Torres, Luis G., Alan Kuntz, Hunter B. Gilbert, Philip J. Swaney, Richard J. Hendrick, Robert James Webster, and Ron Alterovitz (May 2015). "A motion planning approach to automatic obstacle avoidance during concentric tube robot teleoperation". In: *Proceedings of the IEEE International Conference on Robotics and Automation (ICRA)*, pp. 2361–2367.

Trefethen, Lloyd N. (2000). *Spectral methods in MATLAB*. Philadelphia, PA, USA: SIAM.

Treratanakulchai, Shen, Enrico Franco, Arnau Garriga-Casanovas, Minghao Hu, Panagiotis Kassanos, and Ferdinando Rodriguez y Baena (Oct. 2022). "Development of a 6 DOF Soft Robotic

Manipulator with Integrated Sensing Skin". In: *Proceedings of the IEEE/RSJ International Conference on Intelligent Robots and Systems (IROS)*, pp. 6944–6951.

Trivedi, D., A. Lotfi, and C. D. Rahn (Aug. 2008). "Geometrically Exact Models for Soft Robotic Manipulators". In: *IEEE Transactions on Robotics* 24.4, pp. 773–780.

Troccaz, Jocelyne, Giulio Dagnino, and Guang-Zhong Yang (June 2019). "Frontiers of Medical Robotics: From Concept to Systems to Clinical Translation". In: *Annual Review of Biomedical Engineering* 21.1, pp. 193–218.

Tsabedze, Thulani, Christopher Mullen, Ryan Coulter, Scott Wade, and Jun Zhang (May 2020). "Helically Wrapped Supercoiled Polymer (HW-SCP) Artificial Muscles: Design, Characterization, and Modeling". In: *Proceedings of the IEEE International Conference on Robotics and Automation (ICRA)*, pp. 5862–5868.

Uppalapati, Naveen Kumar and Girish Krishnan (Apr. 2020). "VaLeNS: Design of a Novel Variable Length Nested Soft Arm". In: *IEEE Robotics and Automation Letters* 5.2, pp. 1135–1142.

Vanneste, Felix, Olivier Goury, and Christian Duriez (July 2022). "Calibration Method for Soft Robots Modeled With FEM: Application to Anisotropy". In: *IEEE Robotics and Automation Letters* 7.3, pp. 5904–5911.

Vanneste, Felix, Olivier Goury, Jonas Martinez, Sylvain Lefebvre, Herve Delingette, and Christian Duriez (Apr. 2020). "Anisotropic Soft Robots Based on 3D Printed Meso-Structured Materials: Design, Modeling by Homogenization and Simulation". In: *IEEE Robotics and Automation Letters* 5.2, pp. 2380–2386.

Walker, M. W. and D. E. Orin (Sept. 1982). "Efficient Dynamic Computer Simulation of Robotic Mechanisms". In: *Journal of Dynamic Systems, Measurement, and Control* 104.3, pp. 205–211.

Wang, Hao and Xuping Zhang (May 2021). "Modal Dynamic Modelling and Experimental Validation of a Curved Extensible Continuum Manipulator". In: *Proceedings of the IEEE International Conference on Robotics and Automation (ICRA)*, pp. 1958–1965.

Wang, Hao, Zhengxue Zhou, Xingyu Yang, and Xuping Zhang (May 2022a). "A Switchable Rigid-Continuum Robot Arm: Design and Testing". In: *Proceedings of the IEEE International Conference on Robotics and Automation (ICRA)*, pp. 5162–5169.

Wang, Jiaole, Junhyoung Ha, and Pierre E. Dupont (May 2019). "Steering a Multi-armed Robotic Sheath Using Eccentric Precurved Tubes". In: *Proceedings of the IEEE International Conference on Robotics and Automation (ICRA)*, pp. 9834–9840.

Wang, Jiaole, Joseph Peine, and Pierre E. Dupont (Feb. 2022b). "Eccentric Tube Robots as Multiarmed Steerable Sheaths". In: *IEEE Transactions on Robotics* 38.1, pp. 1–15.

Wang, Peiyi, Zhiqiang Tang, Wenci Xin, Zhexin Xie, Sheng Guo, and Cecilia Laschi (Oct. 2022c). "Design and Experimental Characterization of a Push-Pull Flexible Rod-Driven Soft-Bodied Robot". In: *IEEE Robotics and Automation Letters* 7.4, pp. 8933–8940.

Wang, Sicheng and Laura H. Blumenschein (Oct. 2022). "A Geometric Design Approach for Continuum Robots by Piecewise Approximation of Free-Form Shapes". In: *Proceedings of the IEEE/RSJ International Conference on Intelligent Robots and Systems (IROS)*, pp. 5416–5423.

Wang, Yuxin, Hesheng Wang, Fan Xu, Junzhi Yu, Weidong Chen, and Yun-Hui Liu (May 2021). "Towards Collision Detection, Localization and Force Estimation for a Soft Cable-driven

Robot Manipulator". In: *Proceedings of the IEEE International Conference on Robotics and Automation (ICRA)*, pp. 12222–12228.

Watson, Connor and Tania K. Morimoto (Apr. 2020). "Permanent Magnet-Based Localization for Growing Robots in Medical Applications". In: *IEEE Robotics and Automation Letters* 5.2, pp. 2666–2673.

Webster, Robert James and Bryan A. Jones (June 2010). "Design and Kinematic Modeling of Constant Curvature Continuum Robots: A Review". In: *International Journal of Robotics Research* 29.13, pp. 1661–1683.

Webster, Robert James, Joseph M. Romano, and Noah J. Cowan (Feb. 2009a). "Mechanics of Precurved-tube Continuum Robots". In: *IEEE Transactions on Robotics* 25.1, pp. 67–78.

Webster, Robet James, John P. Swensen, Joseph M. Romano, and Noah J. Cowan (2009b). "Closed-Form Differential Kinematics for Concentric-Tube Continuum Robots with Application to Visual Servoing". In: *Experimental Robotics. Springer Tracts in Advanced Robotics*. Ed. by Oussama Khatib, Vijay Kumar, and George J. Pappas. Heidelberg, Germany: Springer-Verlag, pp. 485–494.

Wei, Hang, Yu Shan, Yanzhi Zhao, Lizhe Qi, and Xilu Zhao (Dec. 2022). "A Soft Robot With Variable Stiffness Multidirectional Grasping Based on a Folded Plate Mechanism and Particle Jamming". In: *IEEE Transactions on Robotics* 38.6, pp. 3821–3831.

Wenlong, Yang, Dong Wei, and Du Zhijiang (Nov. 2013). "Mechanics-based kinematic modeling of a continuum manipulator". In: *Proceedings of the IEEE/RSJ International Conference on Intelligent Robots and Systems (IROS)*, pp. 5052–5058.

Wiese, Mats, Benjamin-Hieu Cao, and Annika Raatz (Oct. 2022). "Towards Accurate Modeling of Modular Soft Pneumatic Robots: From Volume FEM to Cosserat Rod". In: *Proceedings of the IEEE/RSJ International Conference on Intelligent Robots and Systems (IROS)*, pp. 9371–9378.

Wockenfuß, Wilhelm Richard, Viktor Brandt, Linda Weisheit, and Welf-Guntram Drossel (Apr. 2022). "Design, Modeling and Validation of a Tendon-Driven Soft Continuum Robot for Planar Motion Based on Variable Stiffness Structures". In: *IEEE Robotics and Automation Letters* 7.2, pp. 3985–3991.

Wolf, A., H. B. Brown, R. Casciola, A. Costa, M. Schwerin, E. Shamas, and Howie Choset (Oct. 2003). "A mobile hyper redundant mechanism for search and rescue tasks". In: *Proceedings of the IEEE/RSJ International Conference on Intelligent Robots and Systems (IROS)*, pp. 2889–2895.

Wooten, Michael B. and Ian D. Walker (Oct. 2022). "Environmental Interaction with Continuum Robots Exploiting Impact". In: *IEEE Robotics and Automation Letters* 7.4, pp. 10136–10143.

Wu, Liao, Ross Crawford, and Jonathan Roberts (Apr. 2017). "Dexterity Analysis of Three 6-DOF Continuum Robots Combining Concentric Tube Mechanisms and Cable-driven Mechanisms". In: *IEEE Robotics and Automation Letters* 2.2, pp. 514–521.

Wu, Shirui, Jiwen Zhang, and Dan Wu (Oct. 2022). "Equilibrium Manipulation Planning for a Soft Elastic Rod Considering an External Distributed Force and Intrinsic Curvature". In: *IEEE Robotics and Automation Letters* 7.4, pp. 11442–11449.

Wu, Zicong, Chuqian Lou, Zhu Jin, Shaoping Huang, Ning Liu, Yun Zou, Mirko Kovac, Anzhu Gao, and Guang-Zhong Yang (May 2021). "Robotic Electrospinning Actuated by Non-Circular

Joint Continuum Manipulator for Endoluminal Therapy". In: *Proceedings of the IEEE International Conference on Robotics and Automation (ICRA)*, pp. 1473–1479.

Xu, Fan, Hesheng Wang, Weidong Chen, and Yanzi Miao (July 2021). "Visual Servoing of a Cable-Driven Soft Robot Manipulator With Shape Feature". In: *IEEE Robotics and Automation Letters* 6.3, pp. 4281–4288.

Xu, Kai and Nabil Simaan (May 2006). "Actuation Compensation for Flexible Surgical Snake-like Robots with Redundant Remote Actuation". In: *Proceedings of the IEEE International Conference on Robotics and Automation (ICRA)*, pp. 4148–4154.

— (June 2008). "An Investigation of the Intrinsic Force Sensing Capabilities of Continuum Robots". In: *IEEE Transactions on Robotics* 24.3, pp. 576–587.

— (Feb. 2010). "Analytic Formulation for Kinematics, Statics, and Shape Restoration of Multi-backbone Continuum Robots Via Elliptic Integrals". In: *Journal of Mechanisms and Robotics* 2.1, p. 011006.

Xu, Kai, Jiangran Zhao, and Minxiao Fu (Oct. 2015). "Development of the SJTU Unfoldable Robotic System (SURS) for Single Port Laparoscopy". In: *IEEE/ASME Transactions on Mechatronics* 20.5, pp. 2133–2145.

Yang, Jingzhou, Esteban Peña Pitarch, Jason Potratz, Steven Beck, and Karim Abdel-Malek (Jan. 2006). "Synthesis and analysis of a flexible elephant trunk robot". In: *Advanced Robotics* 20.6, pp. 631–659.

Yang, Yang, Zhicheng Liu, Yanhan Wang, Shuai Liu, and Michael Yu Wang (May 2020). "A Compact and Low-Cost Robotic Manipulator Driven by Supercoiled Polymer Actuators". In: *Proceedings of the IEEE International Conference on Robotics and Automation (ICRA)*, pp. 1827–18533.

Yang, Zhengxin, Haojin Yang, Yanfei Cao, Yaoyao Cui, and Li Zhang (June 2023). "Magnetically Actuated Continuum Medical Robots: A Review". In: *Advanced Intelligent Systems* 5.6, p. 2200416.

Yekutieli, Yoram, Roni Sagiv-Zohar, Ranit Aharonov, Yaakov Engel, Binyamin Hochner, and Tamar Flash (Aug. 2005). "Dynamic Model of the Octopus Arm. I. Biomechanics of the Octopus Reaching Movement". In: *Journal of Neurophysiology* 94.2, pp. 1443–1458.

Yin, Zhanpeng, Yan Hong, Xiaoyu Sun, Zhiyuan Shen, Yingxuan Zhang, Feng Ju, and Bruce W. Drinkwater (Oct. 2022). "A Miniature Continuum Robot with Integrated Piezoelectric Beacon Transducers and its Ultrasonic Shape Detection in Robot-Assisted Minimally Invasive Surgeries". In: *Proceedings of the IEEE/RSJ International Conference on Intelligent Robots and Systems (IROS)*, pp. 5945–5950.

Yip, Michael C., Jake A. Sganga, and David B. Camarillo (Feb. 2017). "Autonomous Control of Continuum Robot Manipulators for Complex Cardiac Ablation Tasks". In: *Journal of Medical Robotics Research* 2.1, p. 1750002.

Yoon, Hyun-Soo, Hyo-Jeong Cha, Jaeheon Chung, and Byung-Ju Yi (Nov. 2013). "Compact Design of a Dual Master-Slave System for Maxillary Sinus Surgery". In: *Proceedings of the IEEE/RSJ International Conference on Intelligent Robots and Systems (IROS)*, pp. 5027–5032.

York, Peter A., Philip J. Swaney, Hunter B. Gilbert, and Robert James Webster (May 2015). "A Wrist for Needle-sized Surgical Robots". In: *Proceedings of the IEEE International Conference on Robotics and Automation (ICRA)*, pp. 1776–1781.

Yu, Haibo, Liao Wu, Keyu Wu, and Hongliang Ren (July 2016). "Development of a Multi-channel Concentric Tube Robotic System with Active Vision for Transnasal Nasopharyngeal Carcinoma Procedures". In: *IEEE Robotics and Automation Letters* 1.2, pp. 1172–1178.

Yu, Hong-Jian, Wen-Long Yang, Zheng-Xin Yang, Wei Dong, Zhi-Jiang Du, and Zhi-Yuan Yan (June 2018). "Hysteresis analysis of a notched continuum manipulator driven by tendon". In: *Mechanical Sciences* 9.1, pp. 211–219.

Yuan, Han, Zuan Li, and Wenfu Xu (May 2021). "Kinetostatics for variable cross-section continuum manipulators". In: *Proceedings of the IEEE International Conference on Robotics and Automation (ICRA)*, pp. 11878–11883.

Zaccaria, Federico, Edoardo Ida, Sébastien Briot, and Marco Carricato (Apr. 2022). "Workspace Computation of Planar Continuum Parallel Robots". In: *IEEE Robotics and Automation Letters* 7.2, pp. 2700–2707.

Zanaty, Mohamed, Thomas Fussinger, Arno Rogg, Andrea Lovera, David Lambelet, Ilan Vardi, Thomas J. Wolfensberger, Charles Baur, and Simon Henein (Mar. 2019). "Programmable Multistable Mechanisms for Safe Surgical Puncturing". In: *Journal of Medical Devices* 13.2, p. 021002.

Zeng, Wenhui, Junyan Yan, Xu Huang, and Shing Shin Cheng (May 2021). "Motion Coupling Analysis for the Decoupled Design of a Two-segment Notched Continuum Robot". In: *Proceedings of the IEEE International Conference on Robotics and Automation (ICRA)*, pp. 7665–7671.

Zhang, Heng, Qiwen Wang, Chuliang Chi, Yongquan Chen, Zonggao Mu, Zheng Li, Yuanmin Lan, and Aidong Zhang (May 2021a). "Design and Implementation of a Novel, Intrinsically Safe Rigid-Flexible Coupling Manipulator for COVID-19 Oropharyngeal Swab Sampling". In: *Proceedings of the IEEE International Conference on Robotics and Automation (ICRA)*, pp. 12282–12288.

Zhang, Jingting, Xiaotian Chen, Paolo Stegagno, and Chengzhi Yuan (Oct. 2022). "Nonlinear Dynamics Modeling and Fault Detection for a Soft Trunk Robot: An Adaptive NN-Based Approach". In: *IEEE Robotics and Automation Letters* 7.3, pp. 7534–7541.

Zhang, Shu'an, Qi Li, Haozhe Yang, Jiangran Zhao, and Kai Xu (Oct. 2019a). "Configuration Transition Control of a Continuum Surgical Manipulator for Improved Kinematic Performance". In: *IEEE Robotics and Automation Letters* 4.4, pp. 3750–3757.

Zhang, Tieshan, Liu Yang, Xiong Yang, Rong Tan, Haojian Lu, and Yajing Shen (Nov. 2021b). "Millimeter-Scale Soft Continuum Robots for Large-Angle and High-Precision Manipulation by Hybrid Actuation". In: *Advanced Intelligent Systems* 3.2, p. 2000189.

Zhang, Xue, Weibing Li, Wing Yin Ng, Yisen Huang, Yitian Xian, Philip Wai Yan Chiu, and Zheng Li (May 2021c). "An Autonomous Robotic Flexible Endoscope System with a DNA-inspired Continuum Mechanism". In: *Proceedings of the IEEE International Conference on Robotics and Automation (ICRA)*, pp. 12055–12060.

Zhang, Yaru, Huali Sun, Yue Jia, Dan Huang, Ruyu Li, Zhuolin Mao, Yida Hu, Jianbo Chen, Shaolong Kuang, Jie Tang, Xinru Xiao, and Baiquan Su (June 2018). "A Continuum Robot with Contractible and Extensible Length for Neurosurgery". In: *Proceedings of the International Conference on Control and Automation (ICCA)*, pp. 1150–1155.

Zhang, Zhengyou (Nov. 2000). "A Flexible New Technique for Camera Calibration". In: *IEEE Transactions on Pattern Analysis and Machine Intelligence* 22.11, pp. 1330–1334.

Zhang, Zhongkai, Jeremie Dequidt, Junghwan Back, Hongbin Liu, and Christian Duriez (Apr. 2019b). "Motion Control of Cable-Driven Continuum Catheter Robot Through Contacts". In: *IEEE Robotics and Automation Letters* 4.2, pp. 1852–1859.

Zhao, Bin, Lingyun Zeng, Baibo Wu, and Kai Xu (Apr. 2020). "A Continuum Manipulator with Closed-Form Inverse Kinematics and Independently Tunable Stiffness". In: *Proceedings of the IEEE International Conference on Robotics and Automation (ICRA)*, pp. 1847–1853.

Zheng, Tianjiang, David T. Branson, Rongjie Kang, Matteo Cianchetti, Emanuele Guglielmino, Maurizio Follador, Gustavo A. Medrano-Cerda, Isuru S. Godage, and Darwin G. Caldwell (May 2012). "Dynamic continuum arm model for use with underwater robotic manipulators inspired by octopus vulgaris". In: *Proceedings of the IEEE International Conference on Robotics and Automation (ICRA)*, pp. 5289–5294.

Zhong, Yong, Ruxu Du, Liao Wu, and Haoyong Yu (May 2020). "A Novel Articulated Soft Robot Capable of Variable Stiffness through Bistable Structure". In: *Proceedings of the IEEE International Conference on Robotics and Automation (ICRA)*, pp. 2939–2945.

Zienkiewicz, O. C., R. L. Taylor, and J. Z. Zhu (2005). *The Finite Element Method: Its Basis and Fundamentals*. Sixth. Oxford, U.K.: Butterworth-Heinemann.

Cosserat Rod Modeling of Continuum Robots: Application to Concentric Agonist-Antagonist Robots

Matthias Tummers – 2023

Cosserat Rod Modeling of Continuum Robots: Application to Concentric Agonist-Antagonist Robots

Abstract:

Since roughly 40 years, medical robotics combines advancements in robotics and healthcare to improve patient outcomes. Today, most clinical robots are rigid-link robots with limited degrees-of-freedom. Yet recently, there has been a growing trend towards the development of more compliant robots that offer increased dexterity and can access the body through natural orifices. This has led to the advent of continuum robots in the medical robotics field, which are composed of elastic materials and provide infinite degrees of freedom.

This dissertation investigates the design and modeling of a novel continuum robot structure called concentric agonist-antagonist robot (CAAR), showing great potential for medical applications. In order to deploy CAARs, a precise mechanical model was yet to be derived. This thesis proposes such a model based on the Cosserat rod theory. The derived model is experimentally validated with various CAAR prototypes, in free-space and with applied external forces.

Keywords:

Continuum robots, Mechanical modeling, Concentric push-pull robots, Medical robotics, Cosserat rod, Tendon-actuated continuum robots

Modélisation de Robots Continus par la Théorie de Cosserat : Application aux Robots Concentriques Agonistes-Antagonistes

Résumé :

Depuis une quarantaine d'années, la robotique médicale associe la robotique et les soins de santé au bénéfice du patient. Aujourd'hui, la plupart des robots cliniques sont rigides et ont des degrés de liberté limités. Pourtant, on observe depuis peu une tendance au développement de robots plus souples offrant plus de dextérité et pouvant accéder au corps par des orifices naturels. Cela a conduit à l'avènement de robots continus dans le domaine de la robotique médicale, qui sont composés de matériaux élastiques et offrent une infinté de degrés de liberté.

Cette thèse étudie la conception et la modélisation d'une nouvelle structure de robots continus, appelée robot concentrique agoniste-antagoniste (RCAA), ayant du potentiel pour les applications médicales. Afin de développer les RCAA, un modèle mécanique précis manquait. Cette thèse propose un tel modèle basé sur la théorie de Cosserat. Le modèle est validé expérimentalement sur différents prototypes, avec et sans forces externes.

Mots-clefs :

Robots continus, Modélisation mécanique, Robots concentriques agonistes-antagonistes, Robotique médicale, Théorie Cosserat, Robots continus actionnés par câbles